Final Report

Cooperative Agreement S11AC20005
United States Office of Surface Mining

Low-pH Fe(II) Oxidation for Passive Treatment of Coal Mine Drainage

November 4, 2014

William D. Burgos*,[1]
Jennifer L. Macalady[2]

[1] The Pennsylvania State University,
Department of Civil and Environmental Engineering
[2] The Pennsylvania State University,
Department of Geosciences

*Principal Investigator – address: Department of Civil and Environmental Engineering, The Pennsylvania State University, 212 Sackett Building, University Park, PA, 16802-1408; telephone: 814-863-0578; fax: 814-863-7304: e-mail: wdb3@psu.edu

LOW-PH FE(II) OXIDATION FOR PASSIVE TREATMENT OF COAL MINE DRAINAGE

Bill Burgos, Professor, Department of Civil and Environmental Engineering, The Pennsylvania State University, University Park, PA
Jenn Macalady, Associate Professor, Department of Geosciences, The Pennsylvania State University, University Park, PA

1. Introduction

This OSM Applied Science project began in January 2011 and concluded in December 2013. The motivation for this project was to better understand the biogeochemistry of so-called terraced iron formations (TIFs) that facilitate low-pH Fe(II) oxidation. Low-pH Fe(II) oxidation has been found to occur with no human intervention and can lead to the removal of considerable amounts of dissolved iron found in acid mine drainage (AMD). Low-pH, high-metal AMD discharges are often classified as "untreatable" in decision trees used for the selection of appropriate passive treatment technologies. However, removal of high metal/iron sufficiently changes the classification of the AMD, e.g. now to low-pH, low-metal, such that conventional passive treatment options could become viable. Thus, low-pH Fe(II) oxidation should be considered as a passive "pretreatment" technology.

Cost-effective treatment technologies for the remediation of AMD are needed. In Appalachia, the removal of iron is probably the most important aspect of AMD treatment. Biological low-pH Fe(II) oxidation can improve the performance of conventional passive limestone treatment systems. Limestone dissolution neutralizes acidic water and promotes the precipitation of Fe(III) (hydr)oxides. Unfortunately, these Fe(III) oxides chemically coat limestone surfaces (commonly called "armoring"), limiting further limestone dissolution and neutralization capacity, and, more importantly, hydraulically clog the limestone bed.

To limit armoring and clogging, dissolved Fe may be removed from AMD before waters are neutralized with limestone. In the pH range typical of acidic Appalachian mine drainage (2.5 – 4.5), the abiotic oxidation of Fe(II) is kinetically limited, but hydrolysis and precipitation of Fe(III) will still occur (Figure 1). Under such conditions, acidophilic Fe(II)-oxidizing bacteria (Fe(II)OB) may catalyze Fe(II) oxidation, allowing for the oxidative precipitation of Fe from AMD discharges at low-pH. This water may then be neutralized using limestone before it is released into nearby streams. The spatial separation of iron oxidation and precipitation from alkalinity addition would improve the operation and maintenance of limestone beds and reduce the associated costs. This spatial separation can be achieved by promoting low-pH Fe(II) oxidation across natural iron mounds (commonly found immediately downstream of emergent acidic mine discharges) before conveying the water to a limestone treatment bed.

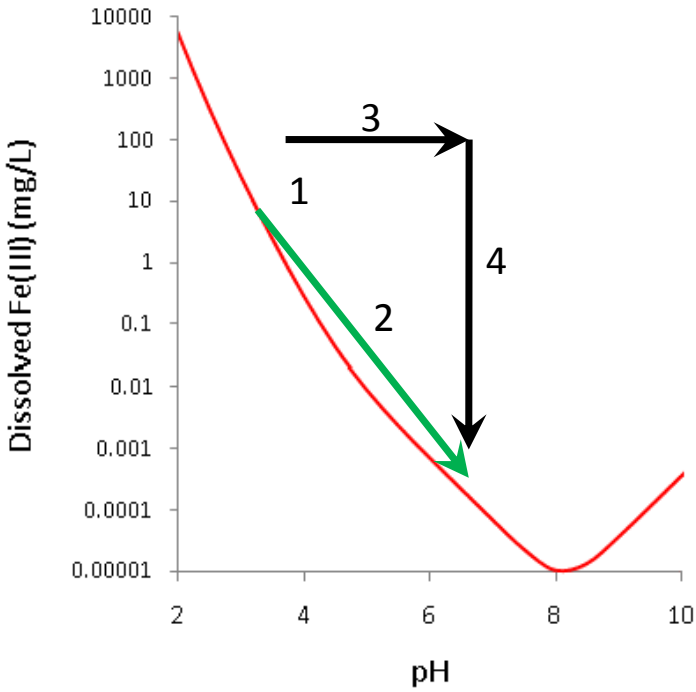

Figure 1. Low-pH Fe(II) oxidation with respect to the solubility of Fe(III). The red line represents the solubility of $Fe(OH)_3(s)$ as a function of pH. The star represents a hypothetical AMD discharge at pH 4.0 with 100 mg/L Fe(II). Line 1 represents the reaction path followed during biological low-pH Fe(II) oxidation. The pH decreases because of the precipitation of $Fe(OH)_3(s)$. Line 2 represents the reaction path when the water discharged from the iron mound is conveyed through a limestone bed. Lines 3 and 4 represent the combined processes of alkalinity addition, abiotic Fe(II) oxidation, and Fe(III) precipitation. A considerably greater load of Fe will be precipitated in the limestone bed via this conventional treatment scheme.

The PIs have been studying biological low-pH Fe(II) oxidation since 2007. In their initial work, funded by PADEP BAMR, they studied this process at Fridays-2 near Hollywood, PA, Gum Boot Run in McKean County, and Hughes Borehole near Portage, PA. A few years later they began to study Lower Red Eyes in Prince Gallitzin State Forest in Somerset County. While the geochemistry and hydrology of all of these sites varied considerably, common geochemical gradients downstream of the AMD sources were observed. In all cases, O_2 in-gassed into the sub-oxic AMD which promoted biological Fe(II) oxidation. Simultaneously, dissolved Fe(II), total Fe, and pH all decreased with downstream distance. These geochemical changes were consistent with the oxidative precipitation of iron hydroxides, an alkalinity-consuming reaction.

Laboratory experiments were conducted in so-called "chunk reactors." Intact pieces of TIF sediments were carefully removed and cut and shaped to fit snugly into the bottom of plastic containers. Large quantities of emergent AMD were also collected. The sediment-containing containers were then plumbed with influent and effluent ports. The collected AMD was filtered and then pumped across the sediment chunk in a shallow sheet-flow mode to mimic the most common hydrodynamic conditions observed at these TIF sites. An empirical zero-order land area-based performance criteria of grams of Fe removed per day per square meter of plan area (GDM; g Fe d^{-1} m^{-2}) was used to evaluate these reactors. Surprisingly, similar rates of Fe removal were measured for most of these sites. In this case, GDM values

of 1 to 6 g Fe d^{-1} m^{-2} were measured. In comparison, design guidelines for iron removal from net acid coal mine drainage using aerobic wetlands range from 2 to 5 g Fe d^{-1} m^{-2}.

2. Research Objectives

The goals of this project were to (1) expand the number of sites to confirm if the previously measured GDM criteria are broadly applicable to most AMD discharges, (2) determine how laboratory rates correlate to field rates, and (3) study the microbial communities and mineralogy associated with low-pH Fe(II) oxidation in order to fully exploit this process for AMD passive treatment. Reliable performance criteria will allow the incorporation of low-pH Fe(II) oxidation into more passive treatment systems.

3. Results

Five peer-reviewed publications acknowledging partial support from Cooperative Agreement S11AC20005 were generated from this research. Results from most of these are summarized below.

Burgos, W.D., T. Borch, L.D. Troyer, F. Luan, L.N. Larson, J.F. Brown, J. Lambson and M. Shimizu. (2012) "Schwertmannite and Fe oxides formed by biological low-pH Fe(II) oxidation versus abiotic neutralization: Impact on trace metal sequestration." *Geochimica Cosmochimica Acta*. 76:29-44.
Larson, L.N., M. Fitzgerald, K. Singha, M.N. Gooseff, J.L. Macalady, and W.D. Burgos. (2013) "Hydrogeochemical changes associated with hyporheic exchange beneath an acid mine drainage-contaminated stream." *Journal of Hydrology* 501:163-174.
Macalady, J.L., T.L. Hamilton, C.L. Grettenberger, D.S. Jones, L.E. Tsao and W.D. Burgos. (2013) "Energy, ecology, and the distribution of microbial life." *Philosophical Transactions of the Royal Society B*. 368: 1622 20120253.
Larson, L.N., J. Sanchez-España, J.L. Macalady and W.D. Burgos. (2014a) "Comparison of field and laboratory rates of low-pH biological Fe(II) oxidation in Appalachian coal fields and Iberian Pyrite Belt." *Applied Geochemistry*. 47:85-98.
Larson, L.N., J.Sánchez-España, B. Kaley, Y. Sheng, K. Bibby and W.D. Burgos. (2014b) "Thermodynamic Controls on the Kinetics of Microbial Low-pH Fe(II) Oxidation." *Environmental Science & Technology*. 48: 9246-9254.
Jones, D.S., C. Kohl, C. L. Grettenberger, L.N. Larson, W.D. Burgos and J.L. Macalady. (2014) "Geochemical niches of iron-oxidizing acidophiles in an acidic coal mine drainage." *Applied and Environmental Microbiology*. (Paper #AEM02919-14) Accepted October 2014.

Eight sites in the Appalachian Bituminous Coal Basin and three sites in the Iberian Pyrite Belt (IPB) in Spain were selected for this project (Figure 2; Table 1). Of the eight sites in the US (all in Pennsylvania and West Virginia), five were "natural" TIFs and three were "engineered" Fe(II) oxidation channels. These eight sites were sampled three to six times between September 2010 and May 2013. Laboratory chunk reactors were run for the five natural TIF sites. Of the three sites in the IPB, all were natural TIFs and they were sampled twice in March and May 2012 (during PI-Burgos's sabbatical in Spain). No laboratory tests were conducted with materials from the IPB.

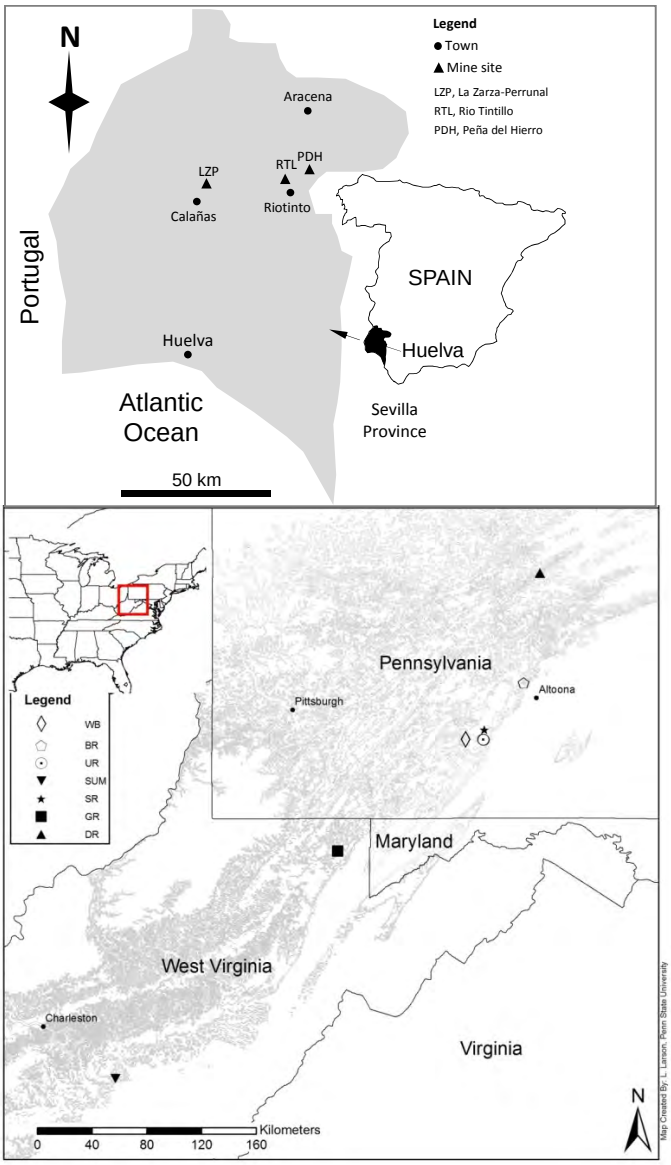

Figure 2. Sampling locations for TIF sites in the Appalachian Bituminous Coal Basin in the US and the Iberian Pyrite Belt in Spain. Light gray zones show the location of coal fields in western Pennsylvania and West Virginia. SUM-E and SUM-N are located approximately 20 m apart and are collectively labeled as 'SUM'. From Larson et al. (2014a).

Table 1. Geochemical characteristics of the emergent waters from the eleven acid mine drainage (AMD) study sites. Each site contained a terraced iron formation (TIF), either naturally occurring or engineered into an AMD passive treatment system. Values represent mean ± one standard deviation for n sampling events. From Larson et al. (2014a).

	United States - Appalachian Region								Spain – Iberian Pyrite Belt		
	Natural Sites					Engineered Sites			Natural Sites		
Parameter	Brubaker Run BR	Scalp Level SL	Sulphur Run SR	Summerlee SUM-N	Upper Red Eyes UR	Dents Run DR	Greens Run GR	Summerlee SUM-E	La Zarza LZP	Peña del Hierro PDH	Rio Tintillo RTL
Temp (°C)	11.0 +/- 0.26	13.3 +/- 0.67	10.4 +/- 0.15	14.6 +/- 0.64	9.38 +/- 0.46	11.2 +/- 12.6	14.5 +/- 7.5	17.3 +/- 5.0	26.5 +/- 0.4	16.9 +/- 2.1	24.3 +/- 0.3
DO (mg/L)	0.06 +/- 0.05	0.30 +/- 0.06	0.14 +/- 0.03	0.53 +/- 0.6	0.18 +/- 0.04		9.1 +/- 2.2	5.3 +/- 1.8	1.18 +/- 0.8	2.75 +/- 3.66	2.6 +/- 3.1
ORP (mV)	348 +/- 37	386 +/- 39	315 +/- 34	194 +/- 49	284 +/- 41	440 +/- 19	465 +/- 36	364 +/- 41	323 +/- 14	423 +/- 28	368 +/- 8.5
Conductivity (uS)	1,690 +/- 236	2,010 +/- 24	859 +/- 41	1,890 +/- 147	2,647 +/- 44		1,270 +/- 816	2,440 +/- 220	7,440 +/- 395		18,900 +/- 117
pH	3.37 +/- 0.15	2.89 +/- 0.08	3.48 +/- 0.07	4.32 +/- 0.64	4.04 +/- 0.03	2.47 +/- 0.08	3.13 +/- 0.88	3.38 +/- 0.88	3.13 +/- 0.04	2.36 +/- 0.12	2.96 +/- 0.01
Dissolved total Fe (mg/L)	118 +/- 27.9	97.4 +/- 9.43	105 +/- 6.4	278 +/- 57	395 +/- 8.4	302 +/- 32	379 +/- 331	236 +/- 64	2,930 +/- 294	1,220 +/- 32	2,640 +/- 151
Dissolved Fe(II) (mg/L)	114 +/- 28.4	92.3 +/- 11.9	102 +/- 6.5	275 +/- 57	383 +/- 20	135 +/- 27	210 +/- 166	230 +/- 75	2,740 +/- 229	1,090 +/- 61	2,310 +/- 50
Al (mg/L)	11.6 +/- 1.6	19.4 +/- 0.4	16.5 +/- 3.1	20.3 +/- 1.3	55.6 +/- 2.9	96 +/- 3.4	96 +/- 125	24.4 +/- 8.14	245 +/- 32	137 +/- 7.3	1,940 +/- 45
Mn (mg/L)	34.5 +/- 10.4	3.3 +/- 0.1	14.6 +/- 3.3	15.45 +/- 0.61	105 +/- 11	16.8 +/- 0.66	3.82 +/- 4.59	14.1 +/- 1.32	60.4 +/- 7.2	14.4 +/- 0.33	314 +/- 17
Co (mg/L)	0.69 +/- 0.15	0.045 +/- 0.003	0.64 +/- 0.12	0.22 +/- 0.01	3.82 +/- 0.36	0.24 +/- 0.00	0.32 +/- 0.39	0.23 +/- 0.04	1.12 +/- 0.08	1.01 +/- 0.04	9.6 +/- 0.35
Ni (mg/L)	1.47 +/- 1.10	0.16 +/- 0.06	1.67 +/- 1.23	0.48 +/- 0.24	9.01 +/- 6.07	0.56 +/- 0.008	1.26 +/- 1.71	0.33 +/- 0.07	0.68 +/- 0.07	0.05 +/- 0.005	5.72 +/- 0.18
Zn (mg/L)	1.75 +/- 0.32	0.23 +/- 0.03	2.13 +/- 0.39	0.39 +/- 0.02	12.2 +/- 0.66	1.02 +/- 0.02	1.17 +/- 1.51	0.46 +/- 0.04	46.4 +/- 8.96	54.2 +/- 9.4	385 +/- 127
SO_4^{2-} (mg S/L)	381 +/- 89	429 +/- 34	212 +/- 44	547 +/- 37	903 +/- 100	655	496 +/- 634	549 +/- 8	2,530	1,180	8,190
Si (mg/L)	10.4 +/- 0.3	16.5 +/- 1.14	14.4 +/- 1.2	14.2 +/- 0.16	13.9 +/- 0.21	38.9 +/- 1.5	23.4 +/- 26.4	16.8 +/- 2.1	52.3 +/- 0.29	52.1 +/- 3.5	55.3 +/- 5.1
PO_4^{3-} (mg P/L)	1.32 +/- 1.86	1.3 +/- 1.7	1.5 +/- 2.1	1.10 +/- 1.56	2.95 +/- 3.84	<.05	7.16 +/- 10.1	0.11 +/- 0.11	1.62	0.5	3.81
n (field chemistry)	7	4	5	5	5	3	5	4	2	2	2
n (trace metals)	3	2	2	2	2	2	2	2	2	2	2
Mean Acidity (mg/L as $CaCO_3$)*	360	357	325	642	1,220	1,420	1,410	609	6,910	3,310	16,400

At all field sites, a suite of geochemical parameters were measured as a function of distance downstream from each AMD source. The real innovation with this new field work was that water velocity was also measured at each sampling location. By measuring water velocity, concentration-versus-distance plots were transformed to concentration-versus-time plots. Field-based Fe(II) oxidation rates were then calculated assuming that each stream reach behaved as a plug flow reactor and that the rate of Fe(II) oxidation was first-order with respect to the dissolved Fe(II) concentration.

Rates of Fe(II) of Fe(II) oxidation were fastest at sites with the lowest emergent pH values (Figure 3). Sites with the fastest rates also displayed a unique geochemical gradient where the pH increased across the TIF. In all previous studies, and at nine of the 11 sites studied in this project, the pH decreased across the TIF. These results demonstrated that the fastest rates of Fe(II) oxidation occurred when little Fe(III) subsequently precipitated out of solution. This result highlights a treatment tradeoff where Fe(II) will be oxidized at sites with very low pH values (e.g., $pH < 3.0$) very quickly but not remove much total Fe. Fe(II) oxidation will be slower but substantial amounts of total Fe will be removed at site with moderate pH values (e.g., $3.5 < pH < 4.5$).

Engineered TIFs could be tailored to maximize both low-pH Fe(II) oxidation and total Fe removal by using natural TIFs followed with an alkaline channel (Figure 4). The alkalinity in this channel would not be sized to neutralize the influent acidity but instead to counterbalance the acidity generated by Fe(III) precipitation within the channel. The hydrodynamics of the channel would be similar to the shallow sheet flow commonly seen across natural TIFs. The natural TIF would provide the microbial seed to colonize the downstream alkaline channel. Conceptually, the relative sizes of the natural TIF and alkaline channel would be determined based on the thermodynamic favorability of the production of soluble Fe(III) versus the production of schwertmannite. If an emergent AMD source was extremely acidic such that rapid production of soluble Fe(III) was favored, an equal-sized alkaline channel would be helpful to raise the pH and promote Fe(III) precipitation (Figure 4A). If an emergent AMD source had a pH that favored the oxidative precipitation of Fe(III), a relatively smaller sized alkaline channel would be used to help promote the removal of correspondingly lower concentrations of Fe(III).

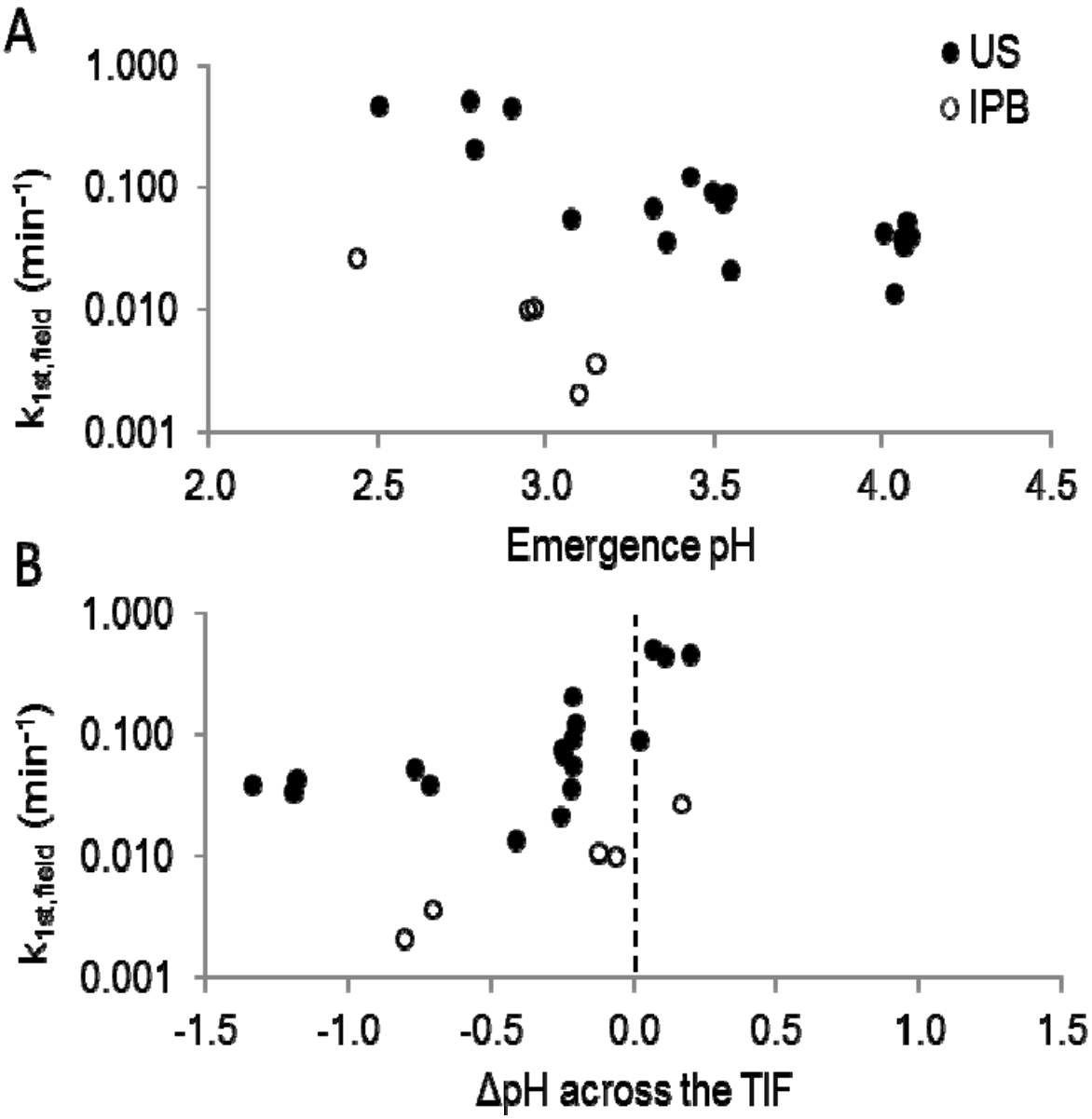

Figure 3. First-order field Fe(II) rate constants ($k_{1st,field}$) at the US and IPB field sites displayed with (A) emergent pH and (B) ΔpH across the TIF. Positive values for ΔpH denote a net pH increase across the TIF and negative ΔpH values indicate a net pH decrease. Positive values for ΔpH are consistent with the oxidation of Fe(II) to soluble Fe(III). Negative values for ΔpH are consistent with the oxidation of Fe(II) and precipitation of Fe(III). From Larson et al. (2014a).

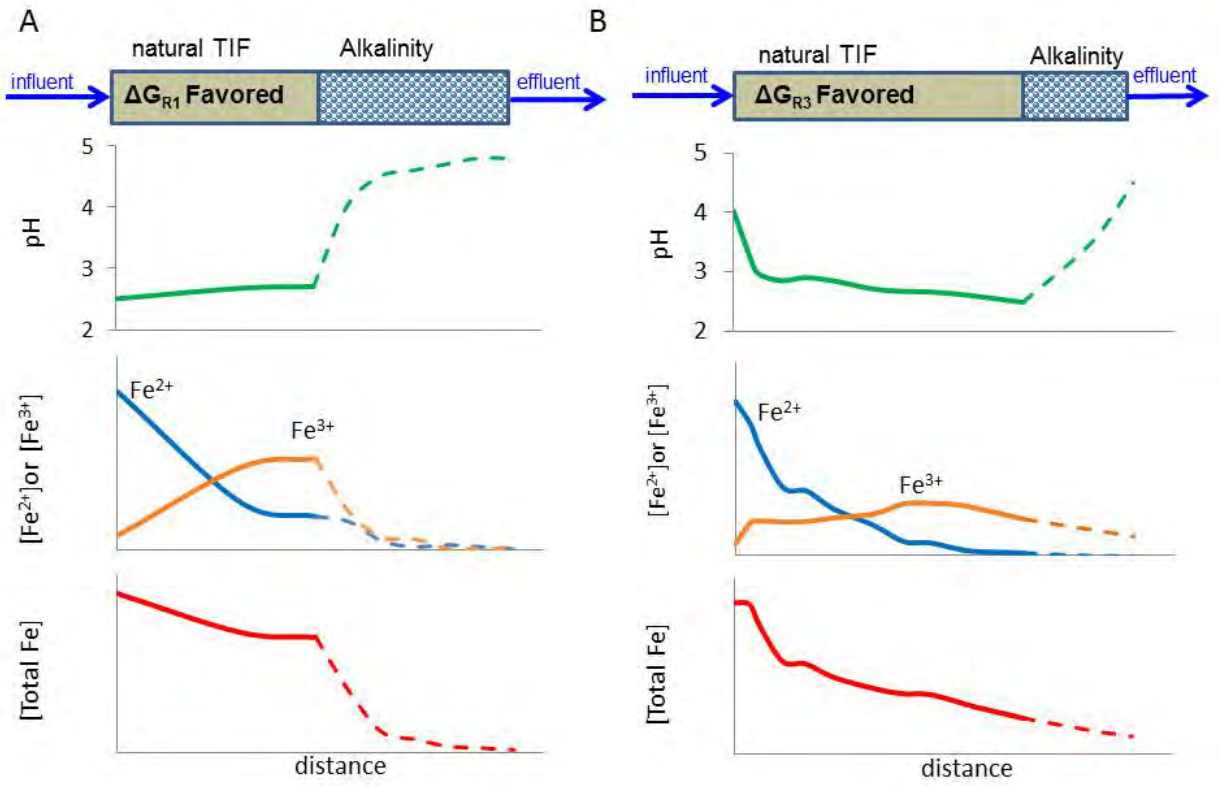

Figure 4. Conceptual schematics of passive treatment systems for anoxic, acidic, Fe(II)-rich acid mine drainage (AMD). An "engineered" terraced iron formation (TIF) would include a natural TIF followed by an alkaline channel. A) Configuration for an extremely acidic discharge where the oxidation of Fe(II) to soluble Fe(III) (reaction 1) would be thermodynamically favored. Solid lines are observations from Scalp Level, dashed lines are conceptual predictions. B) Configuration for a moderately acidic discharge where the oxidation of Fe(II) to insoluble Fe(III) (reaction 3) would be thermodynamically favored. Solid lines are observations from Upper Red Eyes. From Larson et al. (2014b).

An additional series of laboratory experiments were conducted with microbial enrichments from two sites in Pennsylvania. Flow-through, chemostatic (constant pH and temperature) bioreactors were operated through a series of set-points to measure rates of Fe(II) oxidation as a function of pH. Field rates and lab rates both displayed the same trend with respect to pH (Figure 5). A thermodynamic-based model was developed to explain why biological Fe(II) oxidation was fastest at lower pH values. Quite simply, a larger amount of free energy was available to the Fe(II)-oxidizing microbes at lower pH values. With more available energy ($\Delta G_{oxidation}$), microbes could oxidize Fe(II) more rapidly. This simple linkage between thermodynamics and microbial kinetics should be broadly applicable to many other biogeochemical systems.

Rates of total Fe removal were also measured in the chemostatic bioreactor laboratory experiments. Using the circular cross-section of the bioreactor vessel, GDM (g Fe d^{-1} m^{-2}) values were calculated for the various operational set points (Figure 6). Total Fe removal was remarkably high even at low-pH values. Total Fe removal increased with increasing influent Fe(II) concentrations. In the laboratory experiments, GDM for total Fe removal reached values as high as 150 to 400 g Fe d^{-1} m^{-2}. In comparison, GDM values measured from laboratory "chunk reactors" for these same sites were 2.6 to 5.0 g Fe d^{-1} m^{-2}. These results suggest that biological low-pH Fe(II) oxidation may be tremendously effective in active treatment bioreactor configuration. Currently, plans are being formulated with PADEP BAMR to pilot-test such a system at a low-pH, exceptionally high-Fe(II) discharge emerging from a coal refuse pile.

While the major focus of this project was on the parameterization of rates of Fe(II) oxidation and rates of total Fe removal, the microbial communities and mineralogy of the TIF sediments were also examined. The microbial community structure of two geochemically similar discharges in western Pennsylvania (Somerset County) known as Upper and Lower Red Eyes were studied in further detail. A molecular biological technique known as fluorescence in situ hybridization (FISH) was used to identify and quantify acidophilic Fe(II)-oxidizing bacteria found on the upper-most sediments of these TIFs. First, clone libraries were generated by sequencing the 16S rRNA gene to most confidently identify the predominant bacteria on these TIFs. Then, genus-level FISH probes were designed and used to detect these predominant bacteria. Flow across the TIFs promoted the oxygenation of AMD, Fe(II) oxidation, and a drop in pH as Fe(III) precipitated from solution. These geochemical gradients then controlled the evolution of the microbial community and the pattern was similar for both sites. A "hydrogeochemical niche" defined by the combination of the concentration of dissolved Fe(II) and pH selected the predominant bacterial species (Figure 7). At the genus-level, the microbial communities associated with these TIFs were shown to transition from *Gallionella* to *Ferrovum* to *Acidithiobacillus*.

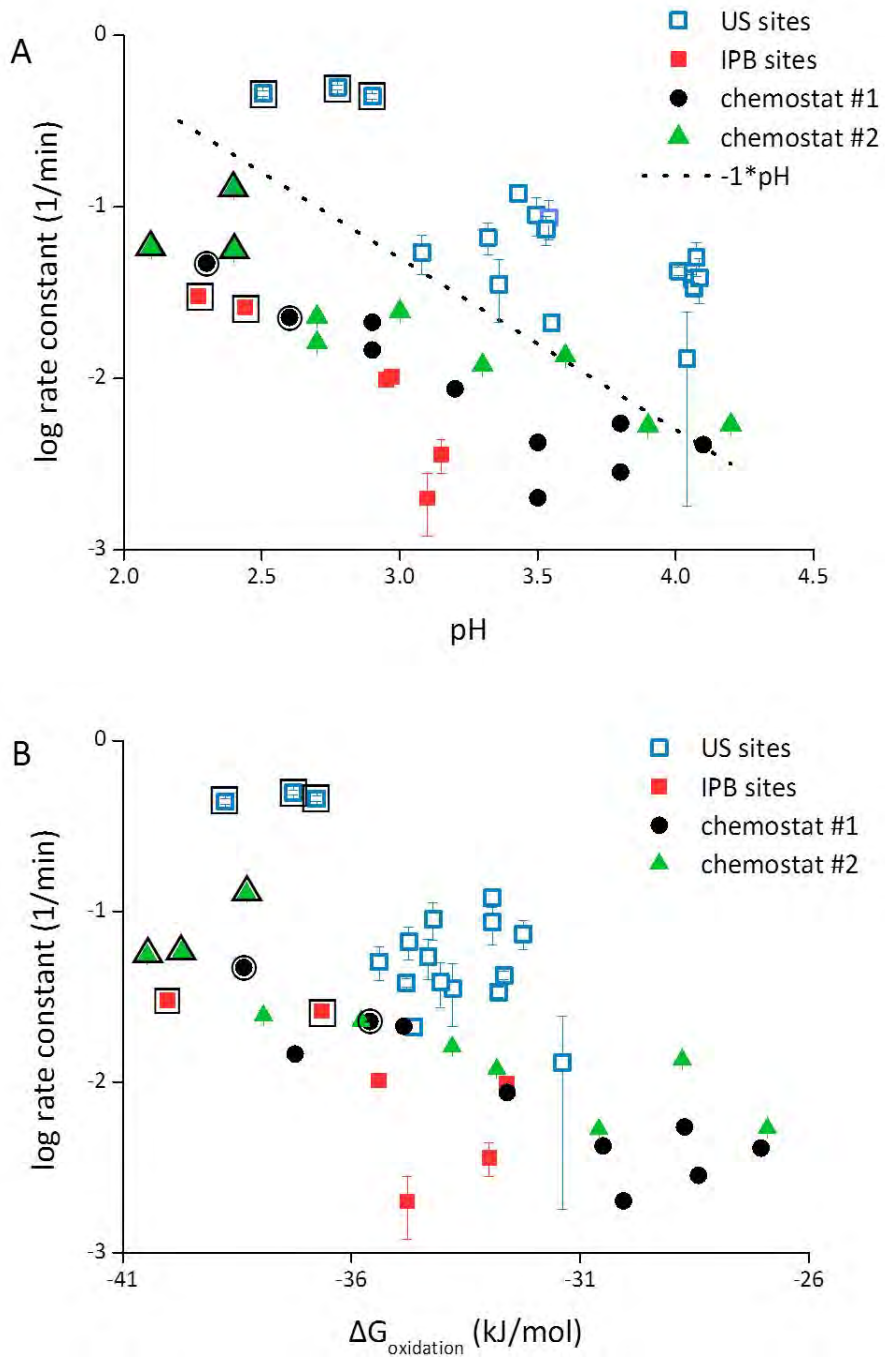

Figure 5. A) First-order rate constants for Fe(II) oxidation versus pH. The dotted line is included to show –1·pH dependency. Enlarged borders around select data points correspond to the same data in both panels A and B. Standard error shown with error bars, otherwise smaller than symbol. B) First-order rate constants for Fe(II) oxidation versus Gibbs free energy for microbial low-pH Fe(II) oxidation ($\Delta G_{oxidation}$). $\Delta G_{oxidation}$ values were calculated based on site- and condition-specific geochemical measurements. From Larson et al. (2014b).

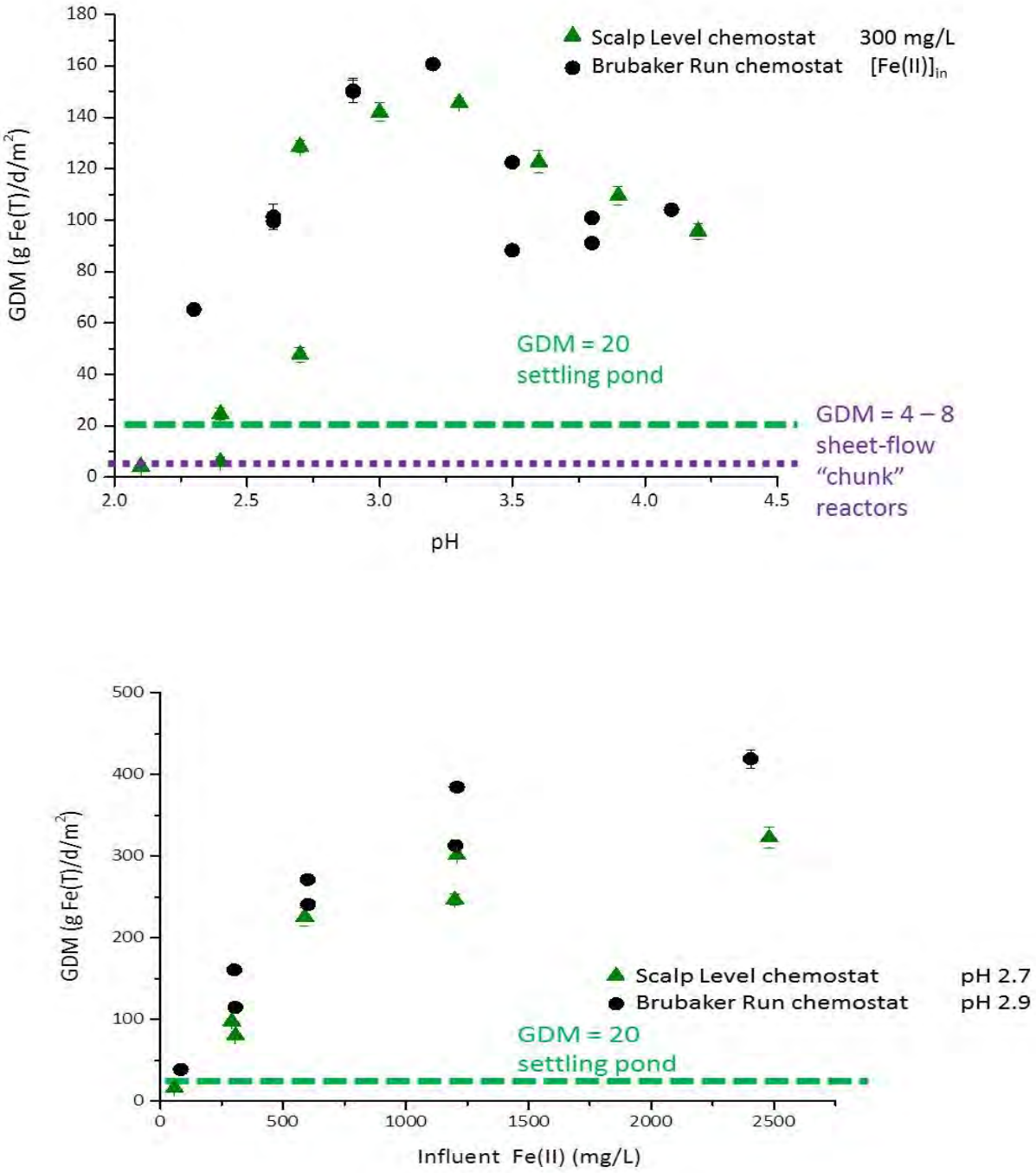

Figure 6. Total Fe removal during the operation of chemostatic, flow-through bioreactors. From Kaley, B. Low-pH Fe(II) Oxidation Using a Bioreactor for the Treatment of Acid Mine Drainage. MS Thesis, The Pennsylvania State University, University Park, PA, **2013**.

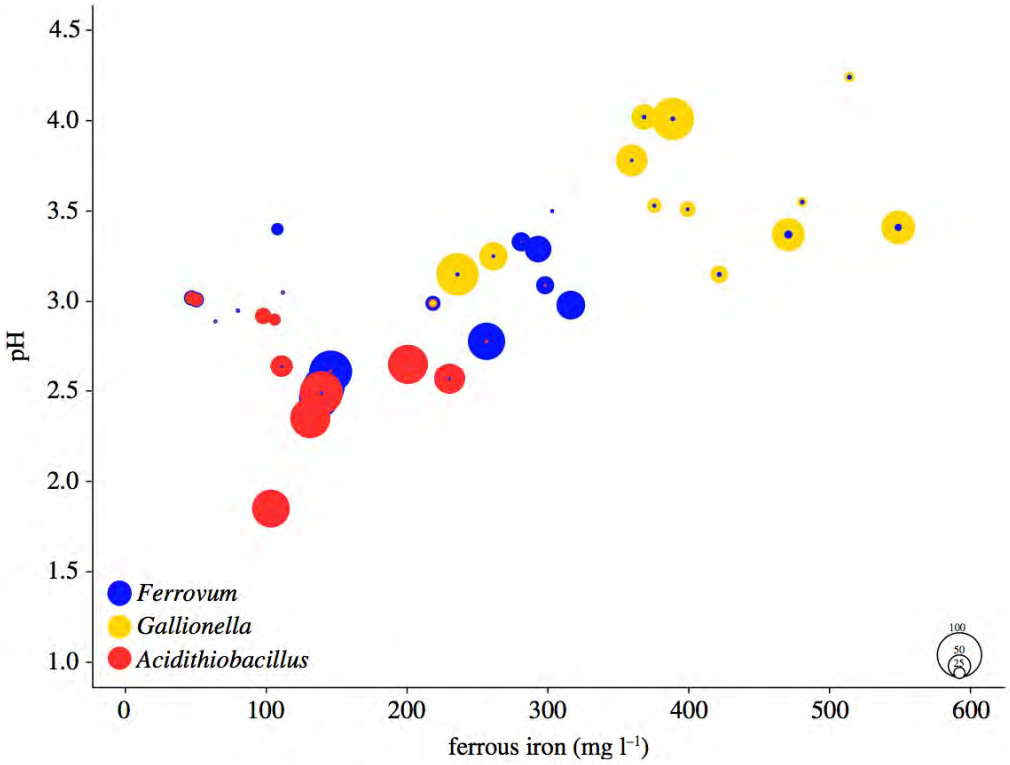

Figure 7. Predominance of various acidophilic Fe(II)-oxidizing bacteria across Upper and Lower Red Eyes. Colors indicate three genus-level taxa common in these communities. Symbol diameters are scaled to the percentage of the community represented by each genus as indicated by the key at lower right. Community compositions were determined using fluorescence in situ hybridization. From Macalady et al. (2013).

4. Conclusions

- Zero-order Fe(II) oxidation rates ranged from $8.60 – 81.3 \times 10^{-7}$ mol L^{-1} s^{-1} at the Appalachian sites and $13.1 – 67.9 \times 10^{-7}$ mol L^{-1} s^{-1} at the IPB sites.
- First-order Fe(II) oxidation rate constants ranged from $0.035 – 0.399$ min^{-1} at the Appalachian sites and $0.003 – 0.010$ min^{-1} at the IPB sites.
- First-order laboratory rate constants normalized to sediment biomass concentrations (measured by phospholipid fatty acids) were positively correlated to first-order field rate constants.
- Faster rates of Fe(II) oxidation were measured at two sites (one in Appalachia and one in IPB) where the emergent pH values were the lowest and little to no oxidative precipitation of Fe(III) occurred.
- Engineered TIFs could be tailored to maximize both low-pH Fe(II) oxidation and total Fe removal by using natural TIFs followed with an alkaline channel.
- A zero-order lab-based removal rate for dissolved Fe(T) was used to calculate area-based design criteria of $2.6 – 8.7$ g Fe day^{-1} m^{-2} (GDM) for both natural and engineered TIFs.
- The removal rate for dissolved Fe(T) measured in chemostatic, flow-through bioreactors was as high as 150 to 400 g Fe d^{-1} m^{-2}.
- The dominant Fe(II)-oxidizing bacteria found across these TIF sites were acidophilic *Gallionella*-like organisms, "*Ferrovum*" spp., and *Acidithiobacillus* spp.
- A "hydrogeochemical niche" defined by the combination of the concentration of dissolved Fe(II) and pH selected the predominant bacterial species.

Available online at www.sciencedirect.com

SciVerse ScienceDirect

Geochimica et Cosmochimica Acta xxx (2011) xxx–xxx

Geochimica et Cosmochimica Acta

www.elsevier.com/locate/gca

Schwertmannite and Fe oxides formed by biological low-pH Fe(II) oxidation versus abiotic neutralization: Impact on trace metal sequestration

William D. Burgos [a,*], Thomas Borch [b,c], Lyndsay D. Troyer [c], Fubo Luan [a], Lance N. Larson [a], Juliana F. Brown [a], Janna Lambson [d], Masayuki Shimizu [b]

[a] Department of Civil and Environmental Engineering, The Pennsylvania State University, University Park, PA 16802, United States
[b] Department of Chemistry, Colorado State University, Fort Collins, CO 80523-1872, United States
[c] Department of Soil and Crop Sciences, Colorado State University, Fort Collins, CO 80523-1170, United States
[d] Department of Biology, Washington University in St. Louis, St. Louis, MO 63105, United States

Received 3 May 2011; accepted in revised form 6 October 2011

Abstract

Three low-pH coal mine drainage (CMD) sites in central Pennsylvania were studied to determine similarities in sediment composition, mineralogy, and morphology. Water from one site was used in discontinuous titration/neutralization experiments to produce Fe(III) minerals by abiotic oxidative hydrolysis for comparison with the field precipitates that were produced by biological low-pH Fe(II) oxidation. Even though the hydrology and concentration of dissolved metals of the CMD varied considerably between the three field sites, the mineralogy of the three iron mounds was very similar. Schwertmannite was the predominant mineral precipitated at low-pH (2.5–4.0) along with lesser amounts of goethite. Trace metals such as Zn, Ni and Co were only detected at μmol/g concentrations in the field sediments, and no metals (other than Fe) were removed from the CMD at any of the field sites. Metal cations were not lost from solution in the field because of unfavorable electrostatic attraction to the iron mound minerals. Ferrihydrite was the predominant mineral formed by abiotic neutralization (pH 4.4–8.4, 4 d aging) with lesser amounts of schwertmannite and goethite. In contrast to low-pH precipitation, substantial metal removal occurred in the neutralized CMD. Al was likely removed as hydrobasaluminite and $Al(OH)_3$, and as a co-precipitate into schwertmannite or ferrihydrite. Zn, Ni and Co were likely removed via adsorption onto and co-precipitation into the freshly formed Fe and Al solids. Mn was likely removed by co-precipitation and, at the highest final pH values, as a Mn oxide. Biological low-pH Fe(II) oxidation can be cost-effectively used to pretreat CMD and remove Fe and acidity prior to conventional neutralization techniques. A further benefit is that solids formed under these conditions may be of industrial value because they do not contain trace metal or metalloid contaminants.
© 2011 Elsevier Ltd. All rights reserved.

1. INTRODUCTION

Pennsylvania is currently the fourth largest coal producing state in the United States and has produced more than 25% of the total coal mined in the US during the past 200 years (USGS, 2008). These practices, though, have left their mark on the environment. Coal mine drainage (CMD) is a severe environmental threat to much of the Appalachian region of the US. Commonly referred to as acid mine drainage (AMD), CMD is marked by high concentrations of Fe and acidity. More than 10,000 km of streams in the Appalachian region are contaminated by AMD, with greater than 2000 km of those in Pennsylvania (Herlihy et al.,

* Corresponding author.
E-mail addresses: WDB3@engr.psu.edu, wdb3@psu.edu (W.D. Burgos).

0016-7037/$ - see front matter © 2011 Elsevier Ltd. All rights reserved.
doi:10.1016/j.gca.2011.10.015

1990). The cost of reclamation of contaminated watersheds in Pennsylvania alone is estimated between $5 and $15 billion (USGS, 2008).

Fe(III)-containing precipitates, often referred to as "yellowboy", are found at CMD sites coating rocks and streambeds. In certain settings where AMD springs emerge with elevated concentrations of Fe(II), biological low-pH Fe(II) oxidation produces terraced mounds of Fe(III) minerals that can be meters thick (DeSa et al., 2010). Most of these phases are amorphous; however, schwertmannite ($Fe_8O_8(OH)_x(SO_4)_y$; $x = 8 - 2y$, $1 < y < 1.75$), appears to be the predominant phase for low-pH water with high concentrations of sulfate while goethite can also be present in minor amounts (Bigham et al., 1990, 1996; Acero et al., 2006). Schwertmannite is metastable with respect to goethite and is often found on fresh depositional surfaces of AMD sites while goethite is found to increase with depth (Acero et al., 2006; Kumpulainen et al., 2007; Burton et al., 2008; Peretyazhko et al., 2009). The stability of schwertmannite can be enhanced by elevated concentrations of silica, phosphorus, and natural organic matter (Collins et al., 2010).

In order to offset the high costs associated with CMD treatment, it may be possible to collect the large amounts of Fe(III) precipitates at CMD sites for industrial reuse. Hedin et al. (1994) showed that Fe(III) precipitates formed at circumneutral pH and collected at CMD sites were similar to those mined for use as pigments. Since these pigments may be used in products such as cosmetics and ceramic serving ware, the incorporation of trace metals in the Fe(III) mineral is a potential concern. Due to kinetic limitations on abiotic Fe(II) oxidation at low pH, it is widely believed that acidophilic Fe(II)-oxidizing microorganisms are responsible for the majority of Fe(II) oxidation and subsequent precipitation of Fe(III) at AMD sites (Lane et al., 1992; Johnson et al., 2005; Senko et al., 2008). It is likely that the mineralogy and elemental composition of biogenic precipitates formed at low-pH CMD sites differ from those formed as a result of abiotic precipitation after neutralization of CMD.

There has been a great deal of research on the characterization of schwertmannite precipitation at low-pH and ferrihydrite precipitation at circumneutral-pH, as well as the conversion of schwertmannite to goethite (Bigham et al., 1996; Schwertmann and Carlson, 2005; Acero et al., 2006; Burton et al., 2008). However, little research has compared the incorporation of trace metal cations during low-pH biologically mediated precipitation to abiotic precipitation at higher pH. This is an important consideration for the remediation of heavy metal-laden AMD and industrial reuse of Fe(III) precipitates. The objectives of this study were to identify the mineral phases present and the extent of trace metal incorporation into precipitates formed in the field via low-pH Fe(II) oxidation at three AMD sites as compared to precipitates formed in the laboratory via abiotic neutralization at pH 4.38–8.35. The neutralization experiments were designed to mimic geochemical conditions encountered during alkali addition in a conventional AMD active treatment system.

2. MATERIALS AND METHODS

2.1. Site descriptions

Three CMD sites in western Pennsylvania were included in the current study: Lower Red Eyes in Somerset County, PA; Fridays-2 in Clearfield County, PA; and, Hughes Borehole in Cambria County, PA (Fig. 1). Physical characteristics and water chemistry for each site are provided in Table 1 and site schematics are provided in the Electronic Annex (Figs. EA-1–EA-3). Lower Red Eyes is a low flow (<1 L/s) CMD artesian spring that emerges within the Prince Gallitzin State Forest near Windber, PA (40° 14′←25″ N; 78° 44′←49″←W). The CMD is believed to originate from a nearby surface mine operated from the 1970s into the 2000s, and located along the Clarion, Brookville, and Kittanning coal seams. The CMD flows downstream across a spectacular series of iron terraces and pools (Fig. 1a) before eventually seeping back into the ground (150 m downstream of spring). This site is unique to the other two field sites in that the CMD is never hydrologically captured by a larger receiving stream, establishing a more extensive geochemical gradient. The CMD at this site is characterized by higher acidity, dissolved metals, and sulfate as compared to the other two field sites (Table 1).

Fridays-2 is the smaller of two CMD discharges (2.3 L/s) that drain the underground Fridays Mine complex. Fridays Mine is located in Hollywood, PA (41° 14′←34″ N; 78° 32′←28″←W) along the Kittanning coal seam and was first mined in the late 1800s (PA DEP, 2006). Fridays-2 emerges as an artesian spring at a collapsed mine entry, and flows 5–15 m over an iron mound before discharging to an unnamed tributary of Bennett Branch. The CMD flows over the mound as shallow (ca. 1 cm) sheet flow, and drops over a ca. 1 m tall terrace before immediately joining the tributary. The tall terrace contains unique stalactite-like Fe precipitates (Fig. 1d). Because of the higher flow rate and shorter path length across the iron mound, leading to a much shorter hydraulic residence time, the extent of Fe(II) oxidation at Fridays-2 is much less as compared to Lower Red Eyes (Table 1 and Fig. 2).

Hughes Borehole is a high flow (63 L/s) artesian spring that was purposefully drilled to drain a very large underground mine complex (2900 ha) near Portage, PA (40° 24′←31″←N; 78° 39′←17″ W) (DeSa et al., 2010). The CMD emerges near, and later flows into, the Little Conemaugh River. The CMD emergence is surrounded by a 0.61 ha iron mound that is up to 2 m deep. The CMD flows across the iron mound through relatively deep channels (ca. 0.6 m deep; captures most of the flow from the borehole) and as shallow sheet flow (ca. 1 cm deep) before discharging off the iron mound ca. 60 m downstream of the borehole.

2.2. Field sampling

Sampling locations were established as a function of distance downstream of each source along a single flow path that conveyed the majority of the water across each iron mound. Sediments were collected at different downstream distances to obtain solids that had formed under varying

Please cite this article in press as: Burgos W. D., et al. Schwertmannite and Fe oxides formed by biological low-pH Fe(II) oxidation versus abiotic neutralization: Impact on trace metal sequestration. *Geochim. Cosmochim. Acta* (2011), doi:10.1016/j.gca.2011.10.015

Fig. 1. Field photographs of the AMD sites. Upstream view of pool and terraces at Lower Red Eyes (a). Upstream view of iron mound at Fridays-2 with large ledge in the bottom left corner (b). Downstream view of scoured channels on the iron mound at Hughes Borehole (c). Detail view of the large ledge at Fridays-2 where samples H1 and H4 were collected – note 50 mL tube (d).

geochemical conditions. Sediments were collected from areas of relatively fast and slow water velocities to obtain solids that been deposited under varying hydrological conditions. Sediments were collected from terraces, pools, and microterracettes to obtain solids from unique depositional *facies* (Fouke et al., 2000; Brown et al., 2010). Six to twelve sediment samples were collected from each site to capture any variances caused by these geochemical, hydrological, and geomorphological differences. Sediments were collected from the top 2 cm of the iron mounds, transported on ice, and stored under atmospheric conditions at 4 °C until analysis.

Two core samples (designated as H1 and H4) were collected horizontally into the vertical face of the tall terrace (ca. 6 cm penetration depth) that marked one edge of the iron mound at Fridays-2 (Fig. 1b and d). Photographs of the collected sediment cores are included in the Electronic Annex (Fig. EA-4). Location H1 was collected from the terrace directly below the primary flowpath from the borehole, while H4 was collected from the terrace ca. 1 m to the right/downhill of H1. The soil cores were plugged with rubber stoppers and immediately stored in an airtight, N_2-flushed ammunition box, and then kept at 4 °C. The box was opened in an anaerobic chamber (95:5% N_2:H_2) and the soil cores were divided into three sections, each approximately 2 cm long, and dried in the chamber prior to analysis.

Dissolved oxygen (DO) was measured using an Oakton DO 300 Series field meter; temperature, pH, and oxidation–reduction potential (ORP) were measured with Beckman Φ265 pH/Temp/mV meters; and conductivity was measured using an Oakton CON 400 series field meter. Filtered (0.45 μm) water samples were preserved in the field with HCl (for dissolved Fe(II) analysis) or HNO_3 (for dissolved metals analysis by inductively coupled plasma-atomic emission spectroscopy, ICP-AES). Samples for sulfate analysis were neither filtered nor acidified. All water samples were transported on ice and stored at 4 °C until analysis.

2.3. Laboratory abiotic neutralization experiments

Water was collected from the emergent Lower Red Eyes spring by completely submerging 10 L high density polyethylene (HDPE) plastic containers ca. 10 cm below the water surface. DO was below detection (<0.5 μM), pH was 4, and ORP was 225 mV at both times of collection (July 2009, October 2010). Containers were filled underwater with no headspace, capped underwater, and then stored on ice during transport. The water was then filtered (0.45 μm) and stored in another plastic container with no headspace at 4 °C. No attempt was made to maintain anoxic conditions after filtration.

The filtered Lower Red Eyes water was used in discontinuous titration/neutralization experiments to produce Fe(III) precipitates via abiotic reactions at a number of elevated pH values. The theoretical total acidity of the Lower Red Eyes water was calculated based on pH and measured concentrations of dissolved Fe(II), Fe(III), Mn, and Al according to Kirby and Cravotta (2005), and found to equal 28.3 meq/L. Four acid-washed HDPE plastic bottles were filled with 250 mL of Lower Red Eyes water. NaOH was titrated into Lower Red Eyes water in aliquots equivalent to ¼ of the theoretical total acidity of the water, until the pH of the system reached pH 8.3. This amounted to first adding 17.8 mL of 0.10 N NaOH to each bottle of Lower Red Eyes water (i.e., to complete 25% of the neutralization). The bottles were stirred to maintain a small vortex

Please cite this article in press as: Burgos W. D., et al. Schwertmannite and Fe oxides formed by biological low-pH Fe(II) oxidation versus abiotic neutralization: Impact on trace metal sequestration. *Geochim. Cosmochim. Acta* (2011), doi:10.1016/j.gca.2011.10.015

Table 1
Water chemistry of the emergent springs at Lower Red Eyes, Fridays-2, and Hughes Borehole.

	Lower Red Eyes	Fridays-2	Hughes Borehole
Flow (L/s)	0.4	2.3	20–125
Temp. (°C)	9.4 ± 0.7	9.8 ± 0.1	12.7 ± 0.6
	$N = 7$	$N = 4$	$N = 30$
DO (μM)	<0.5	11.3 ± 13.4	34.4 ± 25.0
	$N = 2$	$N = 4$	$N = 21$
Conductivity (mS/cm)	4.36 ± 0.16	0.772 ± 0.001	1.08 ± 0.1
	$N = 7$	$N = 2$	$N = 23$
pH	4.04 ± 0.25	4.1 ± 0.2	3.96 ± 0.25
	$N = 7$	$N = 4$	$N = 29$
Dissolved total Fe[a] (μM)	9620 ± 387	865 ± 105	1590 ± 6
	$N = 5$	$N = 4$	$N = 7$
Dissolved Fe(II)[a] (μM)	9720 ± 326	840 ± 108	1790 ± 312
	$N = 5$	$N = 5$	$N = 25$
Al (μM)	1590 ± 43	741 ± 89	304 ± 14
	$N = 3$	$N = 6$	$N = 7$
Mn (μM)	2060 ± 53	24 ± 2	44 ± 0.4
	$N = 3$	$N = 6$	$N = 7$
Co (μM)	2060 ± 53	n.a.	3.22 ± 0.17
	$N = 3$		$N = 7$
Ni (μM)	138 ± 83	n.a.	6.82 ± 0.17
	$N = 3$		$N = 7$
Zn (μM)	199 ± 23	n.a.	4.13 ± 0.15
	$N = 3$		$N = 7$
As (μM)	<0.67	n.a.	<0.13
	$N = 3$		$N = 7$
SO_4^{2-} (μM)	31,170 ± 3833	3410 ± 770	5970 ± 660
	$N = 12$	$N = 4$	$N = 5$
Acidity(mM $CaCO_3$/L)	14.2 ± 0.05	2.07 ± 0.05	2.3 ± 0.05
	$N = 2$	$N = 4$	$N = 7$
Si (μM)	423 ± 5.1	792 ± 143	630 ± 8.5
	$N = 2$	$N = 4$	$N = 7$
TOC (μM)	91.7	167 ± 100	72.5 ± 18
		$N = 3$	$N = 3$
PO_4^{3-} (μM)	5.3 ± 0.7	n.a.	6.2 ± 3.2
	$N = 3$		$N = 3$

[a] Dissolved total Fe measured by ICP-AES, dissolved total Fe(II) measured by ferrozine.

and purged continuously with compressed air for 1 h, and then refrigerated overnight. The following day, the bottles were removed from the refrigerator to come to room temperature, the pH was measured in the overlying water in all four bottles, and one bottle was returned to the refrigerator (pH 5.18). For the remaining three bottles, another 17.8 mL of 0.10 N NaOH was added to each bottle and identical procedures were followed over the next three days to produce suspensions equivalent to 50 (pH 5.36), 75 (pH 6.21), and 100% neutralization (pH 8.34). One day after the 100% neutralization suspension was produced; all of the suspensions were transferred to centrifuge tubes and centrifuged at 8000 rpm for 10 min. Supernatant samples were collected and preserved with HNO_3 for dissolved metals analysis by ICP-AES, and concentrations were calculated to account for sample dilution with NaOH. Pelletized precipitates were rinsed once with distilled–deionized water, and air-dried for SEM analysis or dried under nitrogen for XRD analysis.

This experiment was repeated with the October 2010 water to generate solids for Fe K-edge EXAFS analysis. During this repeat experiment pH and ORP were monitored continuously over the four days allowed for precipitates to form. ORP was measured after calibrating with a freshly prepared +228 mV Zobel standard solution. Suspensions were mixed and bubbled with air continuously, and maintained at room temperature (22–25 °C) over the four days. For suspensions with NaOH added equivalent to 25%, 50%, 75% and 100% neutralization, final pH values were 4.38, 4.40, 7.03 and 8.35, respectively. An additional sample was prepared where NaOH was added equivalent to 100% neutralization in one single aliquot (71.2 mL 0.1 N NaOH to 250 mL of Lower Red Eyes water). The final pH for this suspension was 8.13. Supernatant and solid samples were prepared as described above.

2.4. Analytical methods

Dissolved metal concentrations were analyzed on a Perkin-Elmer Optima 5300 ICP-AES. Dissolved Fe(II) concentrations were measured by ferrozine. Field sediments and laboratory precipitates were sieved (<1-mm) and ground into fine powders. The composition of metal oxides was determined for field sediments via ICP-AES, after lithium

Please cite this article in press as: Burgos W. D., et al. Schwertmannite and Fe oxides formed by biological low-pH Fe(II) oxidation versus abiotic neutralization: Impact on trace metal sequestration. *Geochim. Cosmochim. Acta* (2011), doi:10.1016/j.gca.2011.10.015

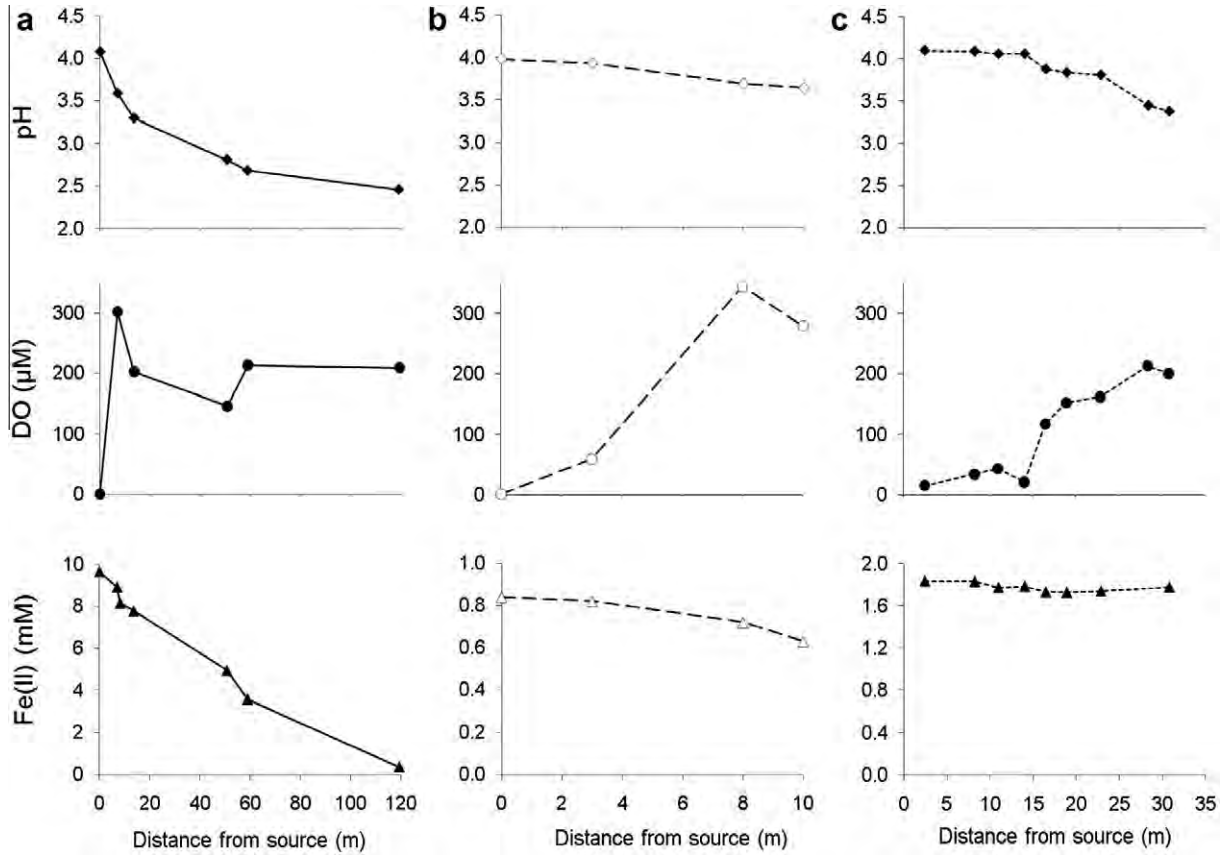

Fig. 2. Water chemistry trends for Lower Red Eyes (July 2009) (a), Fridays-2 (July 2006) (b), and Hughes Borehole (August 2007) (c).

metaborate fusion at 1000 °C. Laboratory precipitates produced from Lower Red Eyes water and field samples collected from the Lower Red Eyes iron mound were dissolved in ammonium oxalate (28 g/L ammonium oxalate + 15 g/L oxalic acid, pH ~2.7) and 6 N HCl, respectively, to operationally distinguish poorly crystalline iron oxides (schwertmannite and ferrihydrite) from less soluble crystalline iron oxides (goethite) (Peretyazhko et al., 2009). Fifty mg dried solids were reacted with 50 mL of each reagent for 1 h, then centrifuged and supernatant samples were preserved with HNO_3 prior to analysis by ICP-AES.

Sediment samples were prepared for scanning electron microscopy (SEM) following procedures described by Zhang et al. (2007). Samples were preserved in the field with 2.5% glutaraldehyde and prepared for imaging with a series of ethanol dehydrations followed by critical point drying. Dried samples were mounted onto carbon SEM stubs and imaged on an FEI Quanta 200 environmental SEM under low vacuum. Higher magnification images were collected using a Jeol JSM-6700F field emission SEM with a working distance of 3 mm.

Powder X-ray diffraction patterns were collected using a Rigaku D/Max Rapid II X-ray diffractometer (XRD) with a Mo X-ray tube and a 0.3 mm collimator. Intensities were measured with the omega axis fixed at 0° and phi axis oscillation between −20° and +20° with a 10 min exposure time. Data was integrated from 0° to 360° with a step size of 0.02 using AreaMax software and all data analysis was performed using Jade 7 software.

Dry samples for X-ray absorption spectroscopic analyses were diluted with boron nitride and packed in Teflon sample holders and sealed with a Kapton polyimide film to prevent oxidation while minimizing X-ray absorption. The structural environment of Fe was determined using extended X-ray absorption fine structure (EXAFS) spectroscopy at the Stanford Synchrotron Radiation Lightsource (SSRL). Data were collected for the Fridays-2 samples on beamline 10-2 (26-pole wiggler). The storage ring was operated at 3.0 GeV and at currents between 60 and 100 mA. Data for the abiotic precipitation samples were collected on beamline 4-3 (20-pole wiggler). The storage ring was operated at 3.0 GeV at a current of 300 mA. The Fe EXAFS analytical procedures used here were similar to those described previously (Borch et al., 2006; Jacquat et al., 2009; Moberly et al., 2009). Energy selection was accomplished with a Si (1 1 1) monochromator and spectra were recorded in X-ray transmission mode using ion chambers. A set of Fe reference compounds was used to perform linear combination (LC) k^3-weighted EXAFS spectral fitting using the SIXPACK interface to IFEFFIT (Webb, 2005). Principal component analysis was performed on sample spectra to estimate the number of reference compounds required for LC fitting. Fe EXAFS reference spectra for ferrihydrite, schwertmannite and goethite are included in the Electronic Annex (Fig. EA-5). The appropriate Fe reference

Please cite this article in press as: Burgos W. D., et al. Schwertmannite and Fe oxides formed by biological low-pH Fe(II) oxidation versus abiotic neutralization: Impact on trace metal sequestration. *Geochim. Cosmochim. Acta* (2011), doi:10.1016/j.gca.2011.10.015

spectra were identified using target transformation (TT) testing. Based on the SPOIL value from TT testing, preliminary LC fitting, appearance in XRD patterns, and their likelihood of formation based on reaction path modeling; schwertmannite, goethite and ferrihydrite were specifically selected as reference compounds. The SPOIL values for schwertmannite and ferrihydrite were greatly different from each other, which implies that these reference spectra are different from each other (Fig. EA-5). Reference compounds were included in the fit only if they contributed more than 5% mol/mol, equivalent to our detection limit for minor constituents (Hansel et al., 2003). Linear combinations of the reference compounds were optimized and the only variable parameters were the mole fractions of each reference compound.

3. RESULTS

3.1. AMD chemistry

The three field sites we studied all contained iron mounds that formed via biological low-pH Fe(II) oxidation (Fig. 1), while the water chemistry (Table 1), geochemical gradients (Fig. 2), and hydrodynamics across the iron mounds varied considerably. The importance of biological Fe(II) oxidation was confirmed through a series of laboratory experiments using live and sterilized sediments from Lower Red Eyes (Brown et al., 2010), Fridays-2 (Lucas, 2008) and Hughes Borehole (DeSa et al., 2010). Lower Red Eyes had the highest concentrations of metals, acidity, and sulfate, the lowest flow rate, and the longest residence time across its iron mound (Table 1). The influx and saturation of DO, and decreases in pH, dissolved Fe(II) and dissolved Fe are consistent with biologically-mediated low-pH Fe(II) oxidation and Fe(III) hydrolysis and precipitation (Fig. 2a). Fridays-2 had the lowest concentration of Fe(II), acidity, and sulfate, an intermediate flow rate, and likely the shortest residence time across its iron terrace. Hughes Borehole had intermediate concentrations of Fe(II), acidity, and sulfate, an extremely high flow rate, and variable residence times across its iron mound because of a combination of flow along scoured channels or across shallow microterracettes. Even though dissolved Fe(II) and dissolved total Fe concentrations did not drop dramatically across the Hughes Borehole iron mound (Fig. 2c), Fe precipitation over the past several decades has produced mound sediments 1–2 m deep.

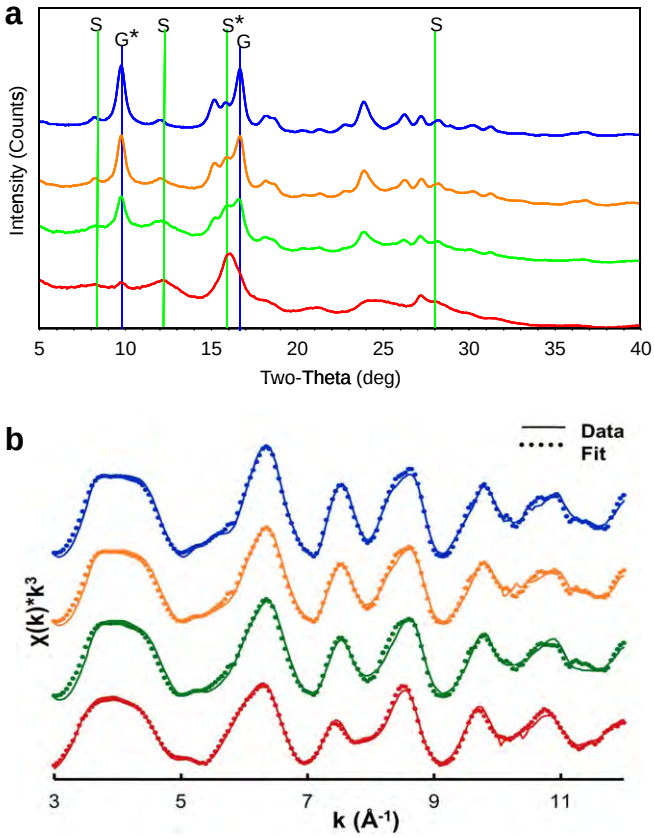

Fig. 3. X-ray diffraction patterns (a) and Fe K-edge EXAFS spectra (b) from field samples collected from Fridays-2. Samples were collected 10 m downstream of emergent AMD spring from the vertical face of a large ledge. Core samples (6 cm penetration depth) were collected horizontally into the ledge face at two locations, H1 and H4. H1 was directly below the primary flowpath while H4 was 1 m to the right/downhill of H1. Patterns are arranged top to bottom, respectively, for samples with highest to lowest goethite contents and are in identical order in (a) and (b). Top pattern from H1 0–2 cm depth, 2nd pattern from H1 4–6 cm depth, 3rd pattern from H4 0–2 cm depth, and bottom pattern from H4 4–6 cm depth. In (a) G = goethite, S = schwertmannite, and ∗ designates peak with greatest intensity in reference pattern. Details for fits of the Fe K-edge EXAFS spectra in (b) are provided in Table 2.

Please cite this article in press as: Burgos W. D., et al. Schwertmannite and Fe oxides formed by biological low-pH Fe(II) oxidation versus abiotic neutralization: Impact on trace metal sequestration. *Geochim. Cosmochim. Acta* (2011), doi:10.1016/j.gca.2011.10.015

3.2. Mineralogy of natural sediments produced via biological low-pH Fe(II) oxidation

Iron precipitates varied across these sites with respect to their physical features and morphology. For example, at Lower Red Eyes, the iron mound was classified into unique depositional *facies* such as terraces, pools, and microterracettes (Fouke et al., 2000; Brown et al., 2010). Terraces consisted of vertical drops greater than 5 cm, pools with diameters of 1–2 m contained quiescent water, and microterracettes consisted of vertical drops less than 2 cm. At Fridays-2, the predominant depositional *facie* was microterracettes, but there was one tall terrace (1 m) that the CMD ran over before entering the adjacent unnamed tributary. At Hughes Borehole, the predominant depositional *facie* was microterracettes, however, the majority of the CMD was conveyed along deep (0.5 m), narrow (1 m wide) scoured channels. We found that schwertmannite was the predominant mineral across these iron mounds while goethite was found in smaller amounts (Figs. 3 and 4).

Based on comparisons of XRD patterns and LC fitting of Fe K-edge EXAFS spectra (Fig. 3 and Table 2), we qualitatively ranked the goethite content of all of the sediments based on the XRD peak intensity at 9.73° two theta. From this we then arranged all of the XRD patterns from each site (6–12) in order of highest to lowest goethite content. In Figs. 3a and 4 we selected four patterns from each site that captured the whole range of schwertmannite-to-goethite ratios observed for each site. We found that there were no observable systematic trends in iron mineralogy with respect to location on the iron mound (i.e., along a geochemical gradient), or with respect to the sample location's water velocity (i.e., across a hydrodynamic gradient), or with respect to the depositional *facies* where the sediments were formed. No mineralogical phases other than schwertmannite and goethite were detected at any field site. SEM analysis of all field samples also revealed a predominance of spherical particles (1–2 μm diameter) with a "hedgehog" morphology characteristic of schwertmannite (Fig. 5a–d). The average Fe/S molar ratio in the Lower Red Eyes sediments was 5.42 ± 0.83 ($n = 4$) (based on HCl digestions, Table 3), corresponding to a schwertmannite stoichiometry of $Fe_8O_8(OH)_5(SO_4)_{1.5}$ (with reported values of $1 < SO_4 < 1.75$).

Based on LC fitting of Fe K-edge EXAFS spectra, goethite decreased with horizontal distance into the tall terrace at Fridays-2 (Fig. 3b and Table 2). The surface section of sample H1 (0–2 cm horizontal penetration into the vertical

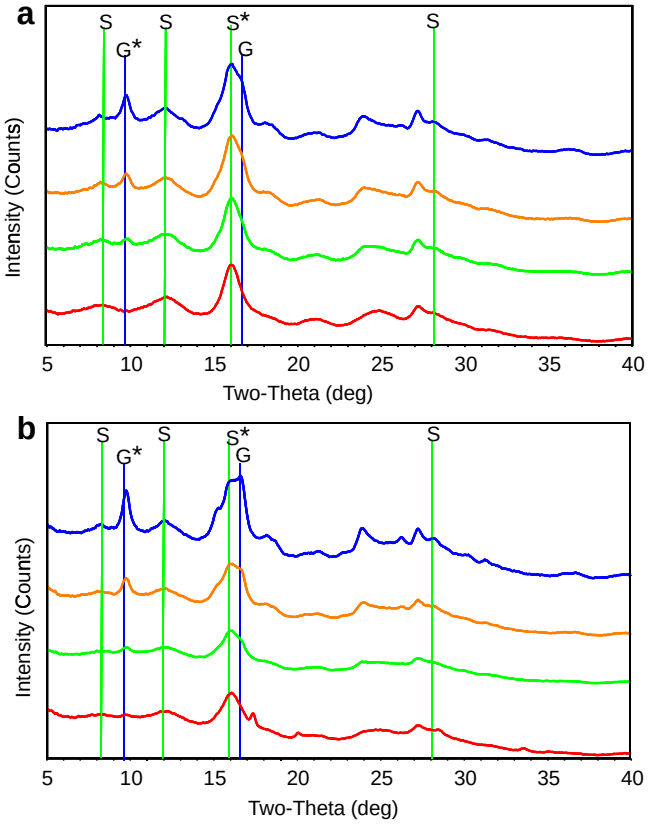

Fig. 4. X-ray diffraction patterns from samples collected from Lower Red Eyes (a) and Hughes Borehole (b). In both panels, patterns are arranged top to bottom, respectively, for samples with highest to lowest goethite contents. (a) Top pattern from pool *facies* 59 m downstream of Lower Red Eyes spring, 2nd pattern from terrace 62 m downstream, 3rd pattern from terrace 52 m downstream, and bottom pattern from pool 14 m downstream. (b) Top pattern from the main scoured channel 8 m downstream of Hughes Borehole, 2nd pattern from terrace *facies* 60 m downstream, 3rd pattern from microterracette 31 m downstream, and bottom pattern from pool 55 m downstream. G = goethite, S = schwertmannite, and ∗ designates peak with greatest intensity in reference pattern.

Please cite this article in press as: Burgos W. D., et al. Schwertmannite and Fe oxides formed by biological low-pH Fe(II) oxidation versus abiotic neutralization: Impact on trace metal sequestration. *Geochim. Cosmochim. Acta* (2011), doi:10.1016/j.gca.2011.10.015

Table 2
Mineralogical composition of samples based on linear combination fitting of Fe K-edge EXAFS spectra. Field samples were collected from Fridays-2 (H1, H4) and solids were formed in the laboratory via abiotic neutralization/precipitation from Lower Red Eyes water. Precision of fits is ca. 5 mol%.

Sample	Schwertmannite mol% Fe	Goethite mol% Fe	Ferrihydrite mol% Fe	Red. χ^2
H1 0–2 cm depth	44.6	55.4	–	0.08
H1 4–6 cm depth	55.7	44.3	–	0.08
H4 0–2 cm depth	58.9	41.1	–	0.11
H4 4–6 cm depth	68.3	31.7	–	0.17
Abiotic precipitate pH 4.38	38.1	16.8	45.1	0.19
Abiotic precipitate pH 4.40	33.2	17.1	49.7	0.11
Abiotic precipitate pH 7.03	30.2	10.0	59.8	0.10
Abiotic precipitate pH 8.13	20.5	10.1	69.4	0.16
Abiotic precipitate pH 8.35	21.9	7.0	71.1	0.11

terrace face) consisted of 45% schwertmannite, 55% goethite, while the deeper section (4–6 cm horizontal penetration) consisted of 56% schwertmannite and 44% goethite (all estimates ±5%). A similar difference along the horizontal penetration depth into the terrace was found in sample H4. The first 0–2 cm into the ledge was composed of 59% schwertmannite and 41% goethite, while the sample 4–6 cm into the ledge was composed of 68% schwertmannite and 32% goethite. Because schwertmannite is metastable with respect to goethite, sample locations with high schwertmannite-to-goethite ratios should reflect conditions that stabilize schwertmannite. The Lower Red Eyes AMD contained the highest sulfate concentration which should favor the stabilization of schwertmannite, while the Fridays-2 AMD contained the lowest sulfate concentration which could favor the conversion of schwertmannite to goethite. In addition to sulfate, silica, phosphorus and dissolved organic carbon (DOC) have been shown to stabilize schwertmannite with respect to Fe(II)-catalyzed conversion to goethite (Jones et al., 2009). At these three sites, dissolved Si concentrations ranged from 420 to 790 μM, dissolved phosphate concentrations were around 5–6 μM (but less downstream of the springs), and DOC concentrations ranged from 70 to 170 μM (Table 1). Jones et al. (2009) showed that 1 mM dissolved Si completely stabilized schwertmannite while 25 mg/L Suwannee River fulvic acid (equivalent to ca. 1 mM DOC) partially stabilized schwertmannite. We speculate that Si concentrations below 1 mM, rather than P or DOC, stabilized schwertmannite at our field sites.

3.3. Mineralogy from abiotic precipitation experiments

Discontinuous titration/neutralization experiments were conducted with Lower Red Eyes water to produce solids that formed at elevated pH values (pH 4.4–8.4) as compared to field conditions (emergent pH 4.0 declined to pH 2.5; Fig. 1a). Our motivation for conducting these experiments was to examine trace metal partitioning under relatively high pH conditions encountered in AMD active treatment systems as compared to natural low-pH iron mound sediments. We conducted these experiments on two different occasions with water collected in July 2009 and October 2010, however, the water chemistry of the emergent Lower Red Eyes spring was essentially identical. In our first experiment, the discontinuous titration process yielded precipitates that formed at final pH values of 5.18, 5.36, 6.21, and 8.34. After the first aliquot of NaOH was added (day 0), an orange precipitate formed and its color remained unchanged for the whole 4 d reaction period (final pH 5.18). After the second aliquot of NaOH was added (day 1), a dark green precipitate formed initially but then became orange after 1 h (final pH 5.36). After the third aliquot of NaOH was added (day 2) a green precipitate formed initially but then became orange-brown (final pH 6.21). After the fourth and final aliquot of NaOH was added (day 3), an orange precipitate formed and its color remained unchanged for the remainder of the reaction period (final pH 8.34).

During our second experiment we continuously monitored the pH and ORP of the suspensions during the whole 4 d reaction period (Fig. 6). In this repeat experiment, the discontinuous titration process yielded precipitates that formed at final pH values of 4.38, 4.40, 7.03, and 8.35. In contrast to the first experiment where we mixed and aerated the suspensions for 1 h after NaOH addition and then stored the suspension at 4 °C until the next day, in this repeat experiment we continuously mixed and aerated the suspensions so that we could continuously monitor pH and ORP. Continuous aeration promoted greater Fe(II) oxidation in the first two suspensions (i.e., one and two additions of NaOH), and the subsequent precipitation of more Fe(III) decreased the final pH values to 4.38 and 4.40 (as compared to final pH values of 5.18 and 5.36 in the first experiment). Continuous monitoring of pH and ORP in these suspensions clearly showed that the geochemical conditions varied much more than just the differences between the initial and final conditions. For example, while we designated the first suspension as "abiotic precipitate pH 4.38", over its 4 d reaction period the suspension pH varied from pH 3.72 to 5.89 and the ORP varied from –9 to +300 mV (Fig. 6a). In the first 10 min (inset in Fig. 6a), the pH increased quickly because of the instantaneous dosing of NaOH while the ORP decreased because the initial oxidation rate of Fe(II) exceeded the mass transfer rate of O_2. The subsequent decrease in pH was caused by hydrolysis of the Fe(III) that had been produced while the subsequent increase in ORP demonstrated that the mass transfer rate of O_2 began to exceed the oxidation rate of Fe(II). Similarly, for the suspension that was discontinuously dosed with four aliquots of NaOH and designated

Please cite this article in press as: Burgos W. D., et al. Schwertmannite and Fe oxides formed by biological low-pH Fe(II) oxidation versus abiotic neutralization: Impact on trace metal sequestration. *Geochim. Cosmochim. Acta* (2011), doi:10.1016/j.gca.2011.10.015

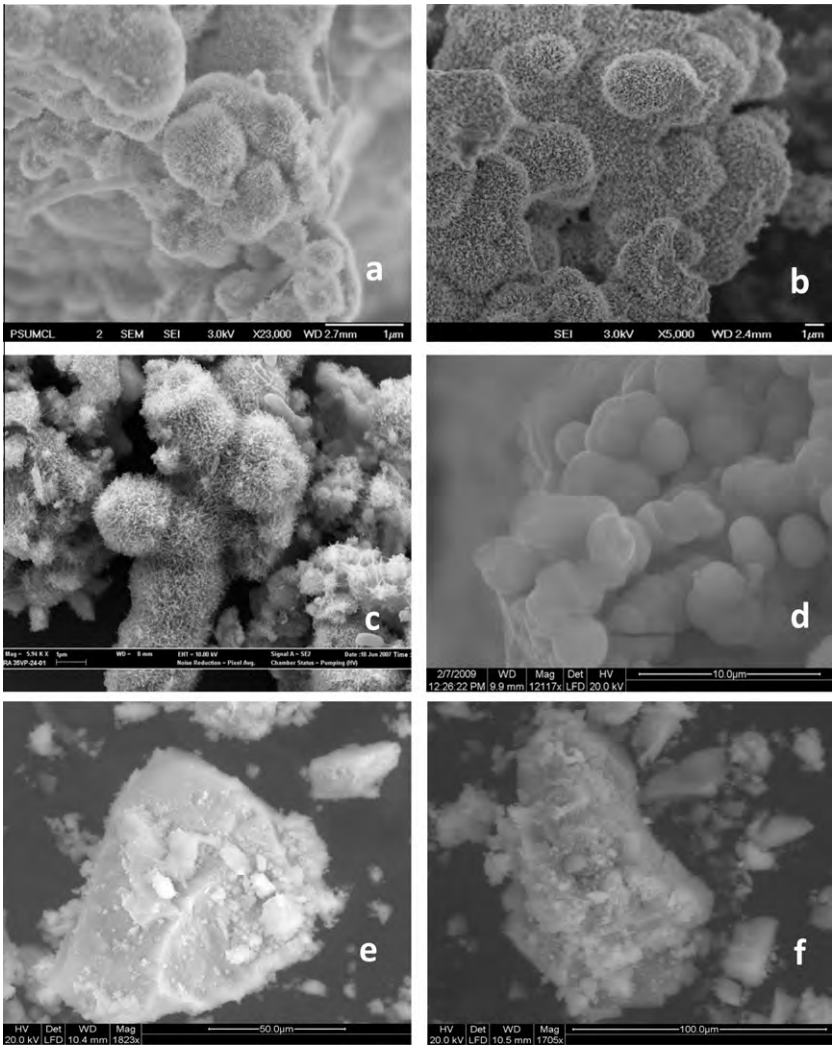

Fig. 5. SEM images of representative samples from: Lower Red Eyes at the AMD source (a); Lower Red Eyes at a downstream pool (b); Fridays-2 (c); Hughes Borehole (d); and solids formed in the lab from Lower Red Eyes water via abiotic neutralization/precipitation at final pH 4.38 (e) and final pH 8.13 (f).

as "abiotic precipitate pH 8.35", over its 4 d reaction period the suspension pH varied from pH 3.72 to 9.38 while its ORP varied from –100 to +300 mV (Fig. 6b). These large changes in pH and pe (i.e., ORP) span mineral stability fields of schwertmannite, goethite and ferrihydrite. In other words, all of these minerals could have potentially formed as the water chemistry evolved over the different reaction periods (e.g., as reaction path "trajectories" plotted on a pe-pH diagrams; Figs. EA-6 and EA-7 in the Electronic Annex; generated using Geochemists Workbench and the water chemistry of Lower Red Eyes in Table 1).

Based on XRD patterns (Fig. 7a) and LC fitting of the Fe K-edge EXAFS spectra (Fig. 7b and Table 2), a combination of schwertmannite, goethite, and ferrihydrite were identified in all of the precipitates formed via abiotic neutralization. We found that abiotic precipitates formed at pH 4.38 contained 38% schwertmannite, 17% goethite, and 45% ferrihydrite, similar to LC fitting results for the solids formed at pH 4.40. As the final pH of the abiotic precipitates increased, the mole fractions of schwertmannite and goethite decreased while the fraction of ferrihydrite increased. Abiotic precipitates formed at pH 8.35 contained 22% schwertmannite, 7% goethite, and 71% ferrihydrite. SEM analysis of the neutralized precipitates revealed distinctly different particle morphologies (Fig. 5e and f) as compared to field samples (Fig. 5a–d). Instead of spheres with a hedgehog texture, neutralized precipitates appeared as laths fused into much larger particles. Characteristic dimensions of these laths were difficult to generalize from these SEM micrographs. This altered morphology was similar to observations reported by Acero et al. (2006) coincident with schwertmannite transformation into goethite in aging experiments (353 d) where the pH decreased from pH 3.07 to 1.74.

Higher amounts of schwertmannite at pH 4.38 and 4.40 were consistent with higher solid-phase S/Fe ratios measured in these precipitates as compared to precipitates formed at pH > 7 (Table 3). It is important to note that

Please cite this article in press as: Burgos W. D., et al. Schwertmannite and Fe oxides formed by biological low-pH Fe(II) oxidation versus abiotic neutralization: Impact on trace metal sequestration. *Geochim. Cosmochim. Acta* (2011), doi:10.1016/j.gca.2011.10.015

ARTICLE IN PRESS

Table 3
Metal content of solids formed via abiotic neutralization/precipitation in the laboratory, and for sediments collected from Lower Red Eyes and Hughes Borehole. Solids were dissolved in 6 N HCl and ammonium oxalate.

Sample ID	Fe_{HCl} (mmol/g)	Fe_{ox} (mmol/g)	S_{HCl} (mmol/g)	S_{ox} (mmol/g)	Al_{HCl} (μmol/g)	Al_{ox} (μmol/g)	Mn_{HCl} (μmol/g)	Mn_{ox} (μmol/g)	Co_{HCl} (μmol/g)	Co_{ox} (μmol/g)	Ni_{HCl} (μmol/g)	Ni_{ox} (μmol/g)	Si_{HCl} (μmol/g)	Si_{ox} (μmol/g)	Zn_{HCl} (μmol/g)	Zn_{ox} (μmol/g)
Abiotic precipitate pH 4.38	6.06	4.19	1.73	1.23	3380	2380	3	1.6	5	3.7	14	11	159	81	30	22
Abiotic precipitate pH 4.40	6.15	5.12	1.01	0.96	1380	1200	2	1.9	3	3.0	13	11	114	75	34	30
Abiotic precipitate pH 7.03	6.80	6.36	0.57	0.53	1180	1080	141	140	37	36	61	59	288	260	150	144
Abiotic precipitate pH 8.13	5.55	5.58	0.37	0.35	950	930	1160	1150	42	42	55	56	255	235	124	125
Abiotic precipitate pH 8.35	5.76	5.22	0.33	0.35	1010	990	1260	1250	44	44	59	59	269	233	132	127
Lower Red Eyes upper pool[a]	7.89	0.42	1.72	0.03	29	2.6	2.3	0.4	1.9	0.00	0.78	0.10	41.8	2.0	0.95	3.8
Lower Red Eyes upper terrace[a]	8.55	1.27	1.78	0.41	22	2.7	2.3	1.1	2.3	0.03	1.2	0.12	46.7	5.0	2.1	0.8
Lower Red Eyes lower pool[a]	7.43	0.73	1.22	0.26	14	3.9	1.9	1.1	0.21	0.02	0.16	0.12	26.7	4.2	1.2	0.8
Lower Red Eyes lower terrace[a]	8.56	1.15	1.39	0.42	10	1.5	1.8	1.1	2.4	0.04	2.2	0.12	50.8	4.1	3.5	1.4

[a] Lower Red Eyes sediment sampling locations refer to depositional *facies* where samples were collected. Upper terrace and pool sediments were collected 27 m downstream from the emergent AMD spring, lower terrace and pool sediments were collected 60 m downstream, emergent pool was collected 0 m downstream, and top terrace was collected 11 m downstream.

Please cite this article in press as: Burgos W. D., et al. Schwertmannite and Fe oxides formed by biological low-pH Fe(II) oxidation versus abiotic neutralization: Impact on trace metal sequestration. *Geochim. Cosmochim. Acta* (2011), doi:10.1016/j.gca.2011.10.015

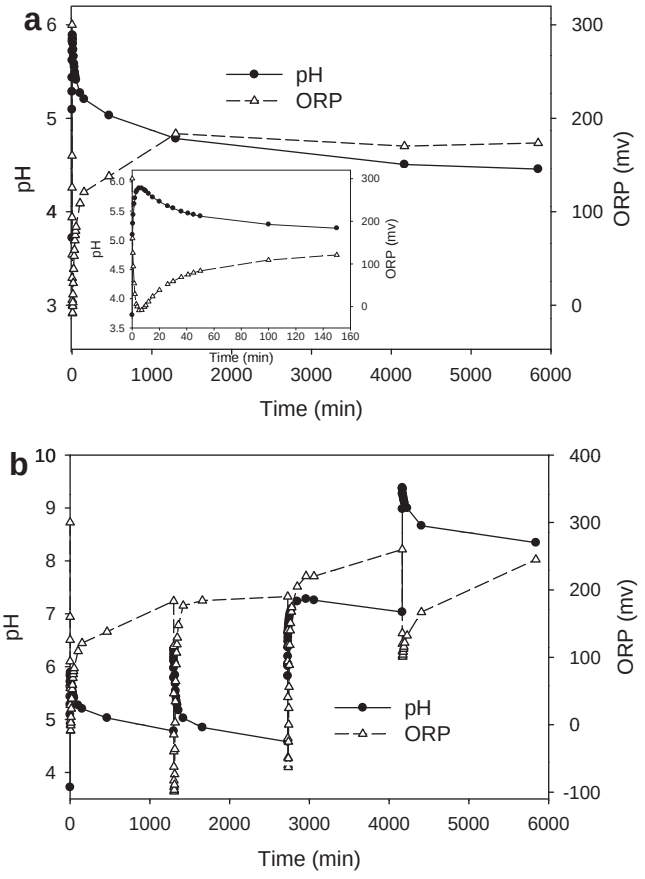

Fig. 6. Kinetics of pH and oxidation–reduction potential (ORP) changes in Lower Red Eyes water during abiotic neutralization/precipitation experiments. Results shown after addition of one aliquot of NaOH that yielded a final suspension of pH 4.38 (a). Inset in (a) details initial kinetics. Results shown for complete discontinuous neutralization where four aliquots of NaOH were added over four days and yielded a final suspension of pH 8.35 (b). Note that ORP values are relative to a +228 mV Zobel solution.

we did rinse these solids with distilled–deionized water before drying and digesting. Sulfate and other weakly adsorbed elements were likely removed to some unquantified extent by this water rinsing. Based on solid-phase Fe and S concentrations measured in ammonium oxalate and HCl digestions, the crystalline mineral fraction was highest for the precipitates formed at pH 4.38 and 4.40 (Table 3), consistent with higher estimated fractions of goethite for these samples (based on Fe EXAFS LC fitting; Table 2). For precipitates formed above pH 7, concentrations of Fe and S measured in the oxalate and HCl digestions were near equal, consistent with higher proportions of poorly crystalline minerals (i.e., schwertmannite and ferrihydrite). In contrast, S and Fe concentrations measured in the field sediments were much higher in the HCl digestions as compared to the oxalate digestions (Table 3). XRD peaks from field sediments (Figs. 3a and 4) could have been broadened by nanocrystalline phases (i.e., short-range ordered phases resistant to oxalate dissolution) of schwertmannite and goethite thereby confounding our operational distinction of crystalline versus poorly crystalline phases for certain samples.

The mineralogy of the abiotic precipitates formed from Lower Red Eyes water clearly differed from the natural sediments collected from Lower Red Eyes (compare Fig. 4a with 7a), and clearly differed from the natural sediments collected from Fridays-2 (Table 2). The large fraction of ferrihydrite found in the abiotic precipitates formed at high pH is consistent with other studies (Bigham et al., 1996; Murad and Rojik, 2003). The formation of ferrihydrite over a more crystalline phase such as goethite or lepidocrocite could be promoted by dissolved species in the Lower Red Eyes water. For example, the presence of Si or Al favors the formation of ferrihydrite over lepidocrocite during oxidative hydrolysis of Fe(II) (Schwertmann and Thalmann, 1976; Taylor and Schwertmann, 1978). Both of these elements were present at high concentrations in the Lower Red Eyes water (Table 1), where Al was 1590 μM (Al/Fe(II) = 0.16) and Si was 423 μM (Si/Fe(II) = 0.04).

The incorporation of Al and Fe into the abiotic precipitates was confirmed by measuring the loss from solution of these elements from the supernatant of the neutralized suspensions (R-hand portions of Fig. 8). In the abiotic experiments, at final pH values of 4.38 and 4.40, Al ($C_i = 1.6$ mM) was removed to a greater relative extent ($C_{final\ pH}/C_i = 0.083$–$0.22$; i.e., 91.7–88% removal) as compared to Fe ($C_i = 8.9$ mM; $C_{final\ pH}/C_i = 0.29$–0.67). At fi-

Please cite this article in press as: Burgos W. D., et al. Schwertmannite and Fe oxides formed by biological low-pH Fe(II) oxidation versus abiotic neutralization: Impact on trace metal sequestration. *Geochim. Cosmochim. Acta* (2011), doi:10.1016/j.gca.2011.10.015

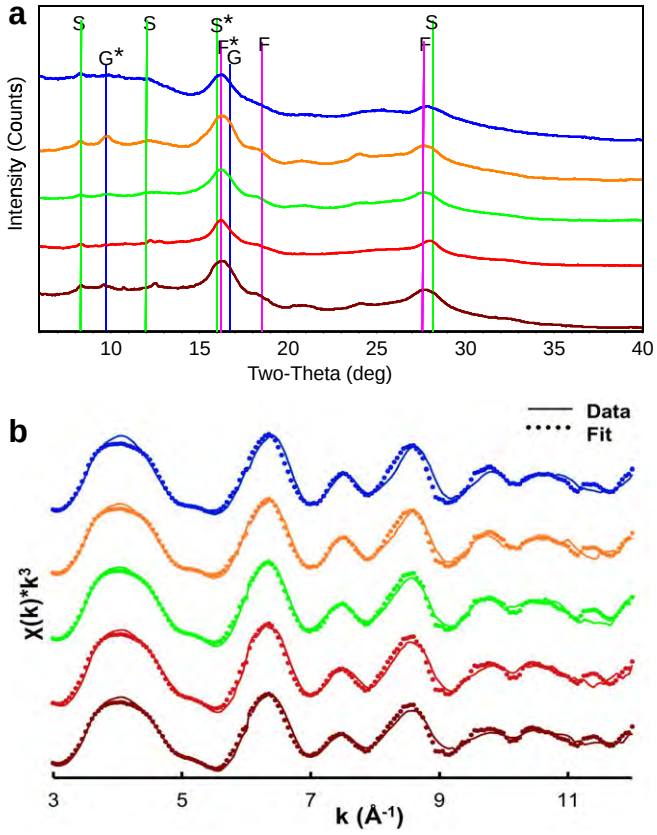

Fig. 7. X-ray diffraction patterns (a) and Fe K-edge EXAFS spectra (b) from solids formed in the lab from Lower Red Eyes water via abiotic neutralization/precipitation. Patterns are arranged top to bottom, respectively, for samples with lowest to highest final pH values and are in identical order in (a) and (b). Top pattern from pH 4.38 suspension, 2nd pattern from pH 4.40 suspension, 3rd pattern from pH 7.03 suspension, 4th pattern from pH 8.13 suspension, and bottom pattern from pH 8.35 suspension. In (a) F = ferrihydrite, G = goethite, S = schwertmannite, and * designates peak with greatest intensity in reference pattern. Details for fits of the Fe K-edge EXAFS spectra in (b) are provided in Table 2.

nal pH values >7, dissolved Fe and Al concentrations were always <50 μg/L.

We include dissolved metal concentrations as a function of pH on the iron mound in the L-hand portions of Fig. 8 to compare metal loss from solution in the field with the abiotic precipitates formed in the laboratory. In this unconventional plot, the dashed vertical line represents the emergent CMD spring, while points to the left represent sample sites further downstream of the CMD spring (where pH values continue to decline due to greater biological Fe(II) oxidation and Fe(III) hydrolysis) and points to the right represent laboratory samples with more NaOH addition. No metals other than Fe were removed across the Lower Red Eyes iron mound (L-hand portions of Fig. 8). Metal cations were not lost from surface waters in the field because of unfavorable electrostatic attraction to the iron mound minerals (i.e., schwertmannite). The pH of the surface waters decreased from ca. pH 4.0 to 2.5 across the iron mounds. The pH of zero point of charge (pH_{zpc}) of schwertmannite has been reported to be 7.2 (Johnson et al., 2005), thus metal cations would not be strongly attracted to the surface of schwertmannite at the low pH values found in the field. This result is consistent with other related field studies (Sidenko and Sherriff, 2005; Nagano et al., 2011).

Zinc, nickel and cobalt were the trace metals detected at the highest concentrations in the emergent AMD spring at Lower Red Eyes (Table 1). The removal of these metals from solution via NaOH addition was similar to the behavior of Fe and Al. At final pH values of 4.38–4.40, Ni was removed to a greater extent ($C_i = 233$ μM; $C_{final\ pH}/C_i = 0.33$–0.37) as compared to Zn ($C_i = 199$ μM; $C_{final\ pH}/C_i = 0.84$–0.98), and as compared to Co ($C_i = 70$ μM; $C_{final\ pH}/C_i = 0.95$–1.0). At final pH values >5, $C_{final\ pH}/C_i$ ratios were 0.042 ± 0.030 for Ni ($n = 7$), 0.015 ± 0.013 for Zn, and 0.10 ± 0.10 ($n = 7$) for Co. Greater removal of these metals at pH values >5 was confirmed based on corresponding increased solid-phase concentrations (Table 3). Based on oxalate and HCl digestions, the majority of these trace metals were associated with poorly crystalline minerals, especially for solids formed above pH 7.

4. DISCUSSION

The remediation of CMD focuses primarily on the removal of metals and acidity. Active CMD treatment refers to the continuous addition of chemicals and collection of metal precipitates. The most common active treatment processes are aeration and alkali addition to neutralize acidity

Please cite this article in press as: Burgos W. D., et al. Schwertmannite and Fe oxides formed by biological low-pH Fe(II) oxidation versus abiotic neutralization: Impact on trace metal sequestration. *Geochim. Cosmochim. Acta* (2011), doi:10.1016/j.gca.2011.10.015

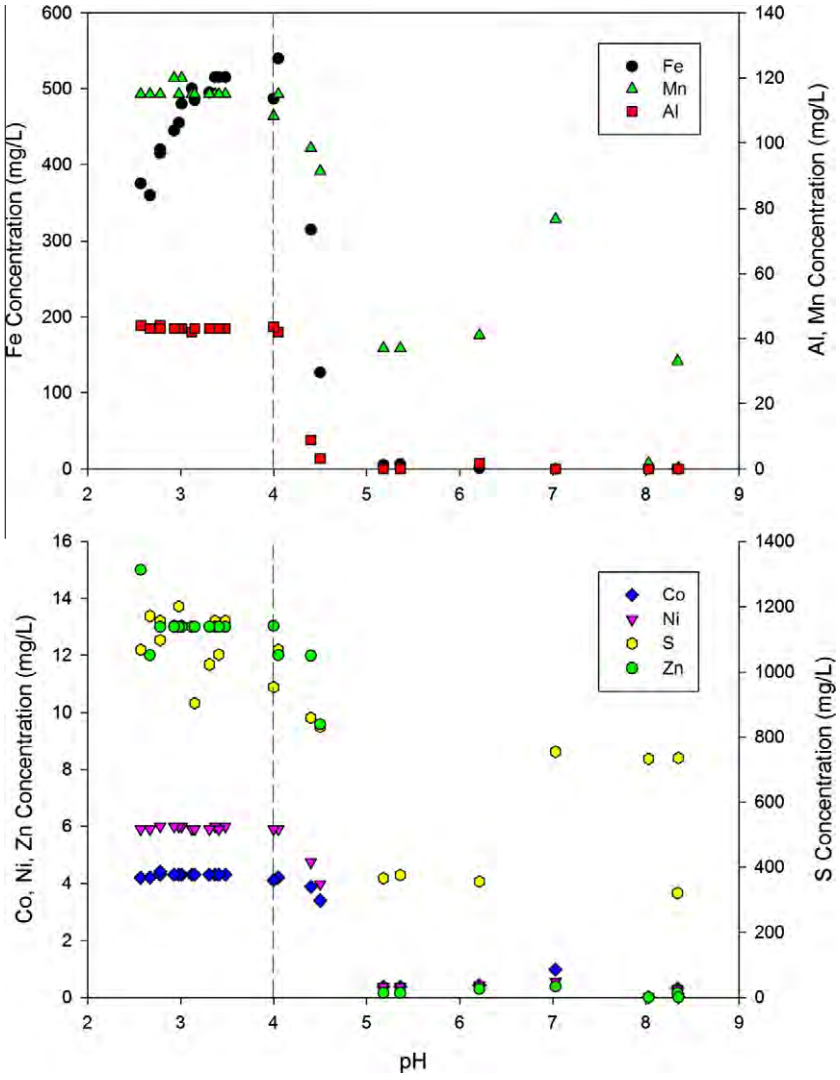

Fig. 8. Concentrations of dissolved elements in Lower Red Eyes water plotted as a function of pH. The dashed line indicates conditions at the emergent AMD spring. Left of the dashed line corresponds to field conditions downstream of the spring. Right of the dashed line corresponds to abiotic neutralization/precipitation in the laboratory. Note secondary axes for certain elements.

and promote rapid oxidation of Fe^{2+} and precipitation of Fe^{3+}, Al^{3+} and other metal contaminants. Depending on alkali dosing conditions, effective removal of Mn via oxidative hydrolysis of Mn^{2+} may or may not occur. Sodium hydroxide and calcium oxide are the most commonly used neutralizing agents for CMD active treatment. Alkali dosing is targeted to slightly exceed the total load (flow $*$ concentration) of hot peroxide acidity of the influent CMD and results in abrupt geochemical changes. For example, it is not uncommon to see blue-green Fe(II)-rich and/or $Fe(OH)_2$(s)-containing water immediately downstream of the alkali dosing location. Even with settling ponds open to the atmosphere, the oxygen demand caused by high Fe(II) concentrations can allow reducing conditions to persist for some time. As aeration continues, the blue-green water eventually converts to an orange-red color indicative of Fe(III)-rich and/or $Fe(OH)_3$(s)-containing water. We describe these field observations because our laboratory neutralization experiments essentially mimicked geochemical conditions encountered during CMD active treatment.

A number of studies have examined the stability of Fe precipitates formed in AMD and the corresponding controls on trace metals and metalloids. A portion of these studies began their experiments with minerals pre-formed in the field and/or via laboratory synthesis and monitored phase transformations and metal release/uptake as a function of time or as a function of solution chemistry (Bigham et al., 1996; Jönsson et al., 2005; Kumpulainen et al., 2008; Paikaray and Peiffer, 2010). At pH 2.5–4.0 goethite is often the sole transformation product of schwertmannite, while at pH >4.5–6.0 ferrihydrite and goethite are both produced (Bigham et al., 1996; Sánchez-España et al., 2011). Schwertmannite transformation to goethite is slow, often requiring hundreds of days, but conflicting results have been reported regarding the effect of pH. Two studies have reported that transformation to goethite was faster at high pH as com-

Please cite this article in press as: Burgos W. D., et al. Schwertmannite and Fe oxides formed by biological low-pH Fe(II) oxidation versus abiotic neutralization: Impact on trace metal sequestration. *Geochim. Cosmochim. Acta* (2011), doi:10.1016/j.gca.2011.10.015

pared to low pH (Regenspurg et al., 2004; Jönsson et al., 2005; Schwertmann and Carlson, 2005), while one study reported that transformation was faster at low pH (Kumpulainen et al., 2008). These conflicting reports are likely caused by differing concentrations of constituents that can stabilize schwertmannite (e.g., Si, P, TOC – Jones et al., 2009; SO_4 – Knorr and Blodau, 2007) and/or Fe speciation that can control the importance of Fe(II)-induced conversion of schwertmannite (Burton et al., 2008).

Another group of studies more similar to our laboratory experiments involved using metal-rich solutions that abruptly became supersaturated due to aeration (Johnston et al., 2011) or neutralization (Lee et al., 2002; Sánchez-España et al., 2011) and then were monitored for phase transformations and release/uptake of metals and metalloids. Under these conditions trace metals can be removed from solution via (i) adsorption onto freshly formed mineral surface(s), (ii) co-precipitation into the mineral structure(s), and/or (iii) precipitation as "discrete" trace metal solid phases (e.g., $Me(OH)_x(s)$). The partitioning of adsorbed or co-precipitated trace metals can be subsequently affected by any phase transformation of the initial precipitate (e.g., schwertmannite) into secondary products (e.g., goethite). These studies have also focused on arsenic because it is a key contaminant of concern in the Iberian Pyrite Belt (Sánchez-España et al., 2011) and in Australian coastal lowland acid sulfate soils (Johnston et al., 2011). Arsenic, however, is not an important contaminant in Appalachian CMD. For example, in one survey of 156 CMD sources in Pennsylvania, the median As concentration was 0 μg/L (no detection limit reported; Watzlaf et al., 2002). In another survey of 99 CMD sources in the bituminous coal mining region of Pennsylvania (same as current study), the median As concentration was 2.0 μg/L (Cravotta, 2008).

Instead of arsenic, Fe, Al, Mn and acidity are the primary contaminants of concern in CMD. Active treatment using aeration and NaOH addition was clearly effective in removing Fe and Al (and Mn at highest pH values) from Lower Red Eyes water (Fig. 8). Based on reaction path modeling for Fe, schwertmannite would precipitate at pH >4.5 and ferrihydrite would precipitate at pH >6.2 if goethite precipitation was suppressed within the model (Electronic Annex, Fig. EA-6). If goethite precipitation was not suppressed, then it became thermodynamically stable throughout the entire pe-pH range over schwertmannite and ferrihydrite, indicating that all three Fe(III) minerals could form under these geochemical conditions. The simultaneous occurrence of schwertmannite, ferrihydrite, goethite and lepidocrocite (near pH 5.5) was observed in similar AMD titrations (Jönsson et al., 2006). Based on Fe EXAFS (Table 2), schwertmannite, goethite and ferrihydrite were all present in the abiotic precipitates, including those collected at final pH values >4.5. We speculate that both schwertmannite and ferrihydrite were the initial Fe phases to nucleate in these suspensions (Bigham et al., 1996; Schwertmann and Carlson, 2005) while goethite formed as a secondary product from schwertmannite (Regenspurg et al., 2004; Burton et al., 2008).

Based on reaction path modeling for Al, hydrobasaluminite ($Al_4(SO_4)(OH)_{10} \cdot 15H_2O$) would precipitate near pH 4.0 and was predicted to be the predominant solid Al phase throughout the entire pe-pH range of our experiments if $Al(OH)_3$ precipitation was suppressed in the model (Electronic Annex, Fig. EA-7). Inclusion of basaluminite instead of hydrobasaluminite yielded similar model predictions but we chose hydrobasaluminite because no dehydration to basaluminite would be expected to occur in these fresh, fully hydrated suspensions. If $Al(OH)_3$ precipitation was not suppressed, then it became predominant throughout the entire pe-pH range over hydrobasaluminite indicating that both hydrobasaluminite and $Al(OH)_3$ could form in our experiments. In Australian coastal lowland acid sulfate soils, a combination of basaluminite and amorphous $Al(OH)_3$ were found to control dissolved Al^{3+} concentrations between pH 3–7 (Jones et al., 2011). In Pennsylvanian coal mine drainage, a combination of amorphous $Al(OH)_3$ and a poorly crystalline aluminum hydroxysulfate were found to control dissolved Al^{3+} concentrations above pH 5 (Pu et al., 2010). In our experiments, Al was detected in the abiotic precipitates by SEM-EDS but we were unable to resolve whether the Al signal originated from morphologically unique particles (i.e., as Al solids vs. co-precipitated with Fe solids). However, because Al solids were predicted to form at pH values lower than when Fe solids were first predicted to form, Al was likely removed both as hydrobasaluminite (especially at low pH), amorphous $Al(OH)_3$, and/or as a co-precipitate into schwertmannite or ferrihydrite. It was unclear whether jurbanite ($Al(OH)SO_4$) formed in our neutralization experiments, however, suppression of jurbanite substantially increased the accuracy of our reaction path modeling. In contrast to field sediments collected from Lower Red Eyes, Al concentrations were two to three orders of magnitude higher in the abiotic precipitates (Table 3).

Reaction path modeling for Zn, Ni and Co showed that these trace metals would not be removed from solution as their corresponding $Me(OH)_2(s)$ phases at the pH values that we observed for their removal. Therefore, adsorption to or co-precipitation in schwertmannite, ferrihydrite, and hydrobasaluminite were the predominant trace metal removal mechanisms in our experiments. This interpretation is supported by the results from the oxalate and HCl digestions, where the majority of trace metals were associated with poorly crystalline minerals (Table 3). Similar results have been reported by Lee et al. (2002) using AMD generated from the mining of massive sulfide ore deposits in eastern Tennessee. Using one fully oxidized, Fe-rich AMD sample (pH 2, 12 mM Fe, 21 mM SO_4^{2-}) that was similar to Lower Red Eyes CMD, they found that Fe was removed from solution at pH >3, Al was removed at pH >5, and Mn was removed at pH >8. The removal of Cd, Co, Cu, Pb and Zn occurred fairly sharply over different pH ranges for each metal but complete removal of all metals did not occur until pH >8. In the current study, we found that removal of Fe, Al, Co, Ni and Zn all occurred fairly sharply and somewhat simultaneously at pH >5 (Fig. 8). As noted above, removal of metal cations (except Fe) did not occur in the field be-

Please cite this article in press as: Burgos W. D., et al. Schwertmannite and Fe oxides formed by biological low-pH Fe(II) oxidation versus abiotic neutralization: Impact on trace metal sequestration. *Geochim. Cosmochim. Acta* (2011), doi:10.1016/j.gca.2011.10.015

cause of limited sorption at pH <4 (Sidenko and Sherriff, 2005; Nagano et al., 2011).

Biological low-pH Fe(II) oxidation could be a very useful pre-treatment step in the remediation of AMD. Fe and acidity loads could be decreased before conventional active or passive treatment processes, thereby decreasing the size and cost of these units. Removal of any iron and acidity before passive treatment limestone beds will improve performance by decreasing limestone armoring, decreasing hydraulic clogging by Fe precipitates, and decreasing the acidity load. Removal of any iron and acidity before active treatment via neutralization will reduce costs by decreasing alkali chemical requirements and decreasing Fe sludge production. Furthermore, in portions of the Appalachian coal mining region where As or other anionic contaminants such as Se are present at only exceptional low concentrations, the Fe(III) precipitates should be essentially free of trace metal and metalloid contaminants. The mineral composition of iron mounds produced by low-pH Fe(II) oxidation of Appalachian CMD appeared to be similar at all of the field sites we studied both spatially across any one site and comparatively between any two sites. Based on metal oxide contents measured after lithium metaborate fusion (Electronic Annex, Table EA-1), Fe_2O_3 contents of 50–67% approached values of Fe ore bodies (Hedin, 2003). Because of their high Fe content, mineralogical purity and absence of trace contaminants, these iron mound sediments could prove to be of considerable economic value (Janneck et al., 2010).

Iron mounds and low-pH Fe(II) oxidation are often underappreciated by watershed professionals responsible for designing AMD remediation systems. In many cases significant amounts of Fe and associated acidity are naturally and passively removed by these mounds. Assuming that we can better understand the biogeochemistry of this process, we should be able to exploit and engineer it for even greater treatment. Water discharged from these mounds would still have to be neutralized to remove acidity and trace metals but the iron and acidity loads going into downstream systems could be dramatically reduced. If the iron mound sediments were periodically collected and sold for some industrial purpose (e.g., anion adsorbents, pigments, ceramics) then any profit could be invested back into additional AMD treatment systems. Future research will hopefully develop the economic and environmental sustainability of these efforts.

ACKNOWLEDGMENTS

This work was supported by the National Science Foundation (NSF) under Grant No. CHE-0431328, by the Pennsylvania Department of Environmental Protection, Bureau of Abandoned Mine Reclamation, by the Office of Surface Mining under Cooperative Agreement S11AC20005, and by an NSF CAREER Award (EAR 0847683) to Thomas Borch. Janna Lambson was supported by NSF EAR 0525503 (REU Supplement) to Jenn L. Macalady. Portions of this research were carried out at the Stanford Synchrotron Radiation Lightsource (SSRL), a national user facility operated by Stanford University on behalf of the U.S. Department of Energy, Office of Basic Energy Sciences. We thank Brent Means from the US Office of Surface Mining, and Malcolm Crittenden from the Pennsylvania Department of Environmental Protection for directing us to the Lower Red Eyes site. We thank the associate editor and three anonymous reviewers for the helpful suggestions to improve this work.

APPENDIX A. SUPPLEMENTARY DATA

Supplementary data associated with this article can be found, in the online version, at doi:10.1016/j.gca.2011.10.015.

REFERENCES

Acero P., Ayora C., Torrentó C. and Nieto J.-M. (2006) The behavior of trace elements during schwertmannite precipitation and subsequent transformation into goethite and jarosite. *Geochim. Cosmochim. Acta* **70**, 4130–4139.

Bigham J. M., Schwertmann U., Carlson L. and Murad E. (1990) A poorly crystallized oxyhydroxysulfate of iron formed by bacterial oxidation of Fe(II) in acid mine waters. *Geochim. Cosmochim. Acta* **54**, 2743–2758.

Bigham J. M., Schwertmann U., Traina S. J., Winland R. L. and Wolf M. (1996) Schwertmannite and the chemical modeling of iron in acid sulfate waters. *Geochim. Cosmochim. Acta* **60**, 2111–2121.

Borch T., Masue Y., Kukkadapu R. K. and Fendorf S. (2006) Phosphate imposed limitations on biological reduction and alteration of ferrihydrite. *Environ. Sci. Technol.* **41**, 166–172.

Brown J. F., Jones D. S., Mills D. B., Macalady J. L. and Burgos W. D. (2010) Application of a depositional *facies* model to an acid mine drainage site. *Appl. Environ. Microbiol.*. AEM.01550–01510.

Burton E. D., Bush R. T., Sullivan L. A. and Mitchell D. R. G. (2008) Schwertmannite transformation to goethite via the Fe(II) pathway: reaction rates and implications for iron-sulfide formation. *Geochim. Cosmochim. Acta* **72**, 4551–4564.

Collins R. N., Jones A. M. and Waite T. D. (2010) Schwertmannite stability in acidified coastal environments. *Geochim. Cosmochim. Acta* **74**, 482–496.

Cravotta C. A. (2008) Dissolved metals and associated constituents in abandoned coal-mine discharges, Pennsylvania, USA. Part 1: constituent quantities and correlations. *Appl. Geochem.* **23**, 166–202.

DeSa T., Brown J. and Burgos W. (2010) Laboratory and field-scale evaluation of low-pH Fe(II) oxidation at Hughes Borehole, Portage, Pennsylvania. *Mine Water Environ.* **29**, 239–247.

Fouke B. W., Farmer J. D., Des Marais D. J., Pratt L., Sturchio N. C., Burns P. C. and Discipulo M. K. (2000) Depositional *facies* and aqueous-solid geochemistry of travertine-depositing hot springs (Angel Terrace, Mammoth Hot Springs, Yellowstone National Park, USA). *J. Sediment. Res.* **70**, 565–585.

Hansel C. M., Benner S. G., Neiss J., Dohnalkova A., Kukkadapu R. K. and Fendorf S. (2003) Secondary mineralization pathways induced by dissimilatory iron reduction of ferrihydrite under advective flow. *Geochim. Cosmochim. Acta* **67**, 2977–2992.

Hedin R. S., Watzlaf G. R. and Nairn R. W. (1994) Passive treatment of acid mine drainage with limestone. *J. Environ. Qual.* **23**, 1338–1345.

Hedin R. S. (2003) Recovery of marketable iron oxide from mine drainage in the USA. *Land Contam. Reclaminat.* **11**, 93–97.

Herlihy A., Kaufmann P., Mitch M. and Brown D. (1990) Regional estimates of acid mine drainage impact on streams

in the mid-atlantic and Southeastern United States. *Water Air Soil Pollut.* **50**, 91–107.

Jacquat O., Voegelin A. and Kretzschmar R. (2009) Soil properties controlling Zn speciation and fractionation in contaminated soils. *Geochim. Cosmochim. Acta* **73**, 5256–5272.

Janneck E., Arnold I., Koch T., Meyer J., Burghardt D. and Ehinger S. (2010) Microbial synthesis of schwertmannite from lignite mine water and its utilization for removal of arsenic from mine waters and for production of iron pigments. Mine Water and Innovative Thinking, Sydney, NS.

Johnson D. B., Okibe N. and Hallberg K. B. (2005) Differentiation and identification of iron-oxidizing acidophilic bacteria using cultivation techniques and amplified ribosomal DNA restriction enzyme analysis. *J. Microbiol. Methods* **60**, 299–313.

Johnston S. G., Keene A. F., Burton E. D., Bush R. T. and Sullivan L. A. (2011) Iron and arsenic cycling in intertidal surface sediments during wetland remediation. *Environ. Sci. Technol.* **45**, 2179–2185.

Jones A. M., Collins R. N., Rose J. and Waite T. D. (2009) The effect of silica and natural organic matter on the Fe(II)-catalysed transformation and reactivity of Fe(III) minerals. *Geochim. Cosmochim. Acta* **73**, 4409–4422.

Jones A. M., Collins R. N. and Waite T. D. (2011) Mineral species control of aluminum solubility in sulfate-rich acidic waters. *Geochim. Cosmochim. Acta* **75**, 965–977.

Jönsson J., Persson P., Sjöberg S. and Lövgren L. (2005) Schwertmannite precipitated from acid mine drainage: phase transformation, sulphate release and surface properties. *Appl. Geochem.* **20**, 179–191.

Jönsson J., Jönsson J. and Lövgren L. (2006) Precipitation of secondary Fe(III) minerals from acid mine drainage. *Appl. Geochem.* **21**, 437–445.

Kirby C. S. and Cravotta Iii C. A. (2005) Net alkalinity and net acidity 1: theoretical considerations. *Appl. Geochem.* **20**, 1920–1940.

Knorr K.-H. and Blodau C. (2007) Controls on schwertmannite transformation rates and products. *Appl. Geochem.* **22**, 2006–2015.

Kumpulainen S., Carlson L. and Räisänen M.-L. (2007) Seasonal variations of ochreous precipitates in mine effluents in Finland. *Appl. Geochem.* **22**, 760–777.

Kumpulainen S., Raisanen M.-L., Von Der Kammer F. and Hofmann T. (2008) Ageing of synthetic and natural schwertmannites at pH 2–8. *Clay Mineral.* **43**, 437–448.

Lane D. J., Harrison, Jr., A. P., Stahl D., Pace B., Giovannoni S. J., Olsen G. J. and Pace N. R. (1992) Evolutionary relationships among sulfur- and iron-oxidizing eubacteria. *J. Bacteriol.* **174**, 269–278.

Lee G., Bigham J. M. and Faure G. (2002) Removal of trace metals by coprecipitation with Fe, Al and Mn from natural waters contaminated with acid mine drainage in the Ducktown Mining District, Tennessee. *Appl. Geochem.* **17**, 569–581.

Lucas M. A. (2008) The comparison of two acid mine drainage sites in central Pennsylvania: field site characterizations and batch reactor experiments. M. S. Thesis, The Pennsylvania State Univ., University Park, PA, USA, pp. 172.

Moberly J., Borch T., Sani R., Spycher N., Şengör S., Ginn T. and Peyton B. (2009) Heavy metal–mineral associations in Coeur d'Alene river sediments: a synchrotron-based analysis. *Water Air Soil Pollut.* **201**, 195–208.

Murad E. and Rojik P. (2003) Iron-rich precipitates in a mine drainage environment: influence of pH on mineralogy. *Am. Mineral.* **88**, 1915–1918.

Nagano T., Yanase N., Hanzawa Y., Takada M., Mitamura H., Sato T. and Naganawa H. (2011) Evaluation of the affinity of some toxic elements to schwertmannite in natural streams contaminated with acid mine drainage. *Water Air Soil Pollut.* **216**, 153–166.

Paikaray S. and Peiffer S. (2010) Dissolution kinetics of sulfate from schwertmannite under variable pH conditions. *Mine Water Environ.* **29**, 263–269.

Pennsylvania Department of Environmental Protection (PA DEP). (2006) The Development of a Mine Drainage Restoration Plan for Bennett Branch, Sinnemahoning Creek: Clearfield, Elk, and Cameron Counties, Pennsylvania.

Peretyazhko T., Zachara J. M., Boily J. F., Xia Y., Gassman P. L., Arey B. W. and Burgos W. D. (2009) Mineralogical transformations controlling acid mine drainage chemistry. *Chem. Geol.* **262**, 169–178.

Pu X., Vazquez O., Monnell J. D. and Neufeld R. D. (2010) Speciation of aluminum precipitates from acid rock discharges in Central Pennsylvania. *Environ. Eng. Sci.* **27**, 169–180.

Regenspurg S., Brand A. and Peiffer S. (2004) Formation and stability of schwertmannite in acidic mining lakes. *Geochim. Cosmochim. Acta* **68**, 1185–1197.

Sánchez-España J., Yusta I. and Diez-Ercilla M. (2011) Schwertmannite and hydrobasaluminite: a re-evaluation of their solubility and control on the iron and aluminium concentration in acidic pit lakes. *Appl. Geochem.* **26**, 1752–1774.

Schwertmann U. and Thalmann H. (1976) The influence of [Fe(II)], [Si], and pH on the formation of lepidocrocite and ferrihydrite during oxidation of aqueous $FeCl_2$ solutions. *Clay Mineral.* **11**, 189–200.

Schwertmann U. and Carlson L. (2005) The pH-dependent transformation of schwertmannite to goethite at 25 °C. *Clay Mineral.* **40**, 63–66.

Sidenko N. V. and Sherriff B. L. (2005) The attenuation of Ni, Zn and Cu, by secondary Fe phases of different crystallinity from surface and ground water of two sulfide mine tailings in Manitoba, Canada. *Appl. Geochem.* **20**, 1180–1194.

Senko J. M., Wanjugi P., Lucas M., Bruns M. A. and Burgos W. D. (2008) Characterization of Fe(II) oxidizing bacterial activities and communities at two acidic Appalachian coalmine drainage-impacted sites. *ISME J.* **2**, 1134–1145.

Taylor R. M. and Schwertmann U. (1978) The influence of aluminum on iron oxides: Part 1. The influence of Al on Fe oxide formation from the Fe(II) system. *Clays Clay Miner.* **26**, 373–383.

United States Geological Survey (USGS). (2008) Coal mine drainage projects in Pennsylvania. US Geological Survey. <http://pa.water.usgs.gov/projects/energy/amd/> (accessed May 2, 2011).

Watzlaf G. R., Schroeder K. T., Kleinmann R. L. P., Kairies C. L. and Nairn R. W. (2002) *The Passive Treatment of Coal Mine Drainage*. American Society of Mining and Reclamation, Lexington, Kentucky.

Webb S. M. (2005) SIXpack: a graphical user interface for XAS analysis using IFEFFIT. *Phys. Scr.* **2005**, 1011.

Zhang G., Dong H., Kim J. and Eberl D. D. (2007) Microbial reduction of structural Fe^{3+} in nontronite by a thermophilic bacterium and its role in promoting the smectite to illite reaction. *Am. Mineral.* **92**, 1411–1419.

Associate editor: Donald L. Sparks

Please cite this article in press as: Burgos W. D., et al. Schwertmannite and Fe oxides formed by biological low-pH Fe(II) oxidation versus abiotic neutralization: Impact on trace metal sequestration. *Geochim. Cosmochim. Acta* (2011), doi:10.1016/j.gca.2011.10.015

Journal of Hydrology 501 (2013) 163–174

Contents lists available at ScienceDirect

Journal of Hydrology

journal homepage: www.elsevier.com/locate/jhydrol

Hydrogeochemical niches associated with hyporheic exchange beneath an acid mine drainage-contaminated stream

Lance N. Larson [a], Michael Fitzgerald [b,c], Kamini Singha [d], Michael N. Gooseff [e], Jennifer L. Macalady [b], William Burgos [a,*]

[a] Department of Civil and Environmental Engineering, The Pennsylvania State University, University Park, PA 16802, USA
[b] Department of Geosciences, The Pennsylvania State University, University Park, PA 16802, USA
[c] Aquatics Team, National Ecological Observatory Network, Inc. (NEON, Inc.), Boulder, CO 80301, USA[1]
[d] Hydrologic Science and Engineering Program, Colorado School of Mines, Golden, CO 80401, USA[1]
[e] Department of Civil & Environmental Engineering, Colorado State University, Fort Collins, CO 80523, USA[1]

ARTICLE INFO

Article history:
Received 5 January 2013
Received in revised form 3 August 2013
Accepted 5 August 2013
Available online 14 August 2013
This manuscript was handled by Peter K. Kitanidis, Editor-in-Chief, with the assistance of Xunhong Chen, Associate Editor

Keywords:
Iron cycling
Hyporheic exchange
Coal mine drainage
In situ pore-water

SUMMARY

Biological low-pH Fe(II)-oxidation creates terraced iron formations (TIFs) that remove Fe(III) from solution. TIFs can be used for remediation of acid mine drainage (AMD), however, as sediment depth increases, Fe(III)-reduction in anoxic subsurface areas may compromise treatment effectiveness. In this study we used near-surface electrical resistivity imaging (ERI) and *in situ* pore-water samplers to spatially resolve bulk conductivity changes within a TIF formed in a stream emanating from a large abandoned deep clay mine in Cambria County, Pennsylvania, USA. Because of the high fluid electrical conductivity of the emergent AMD (1860 μS), fresh water (42 μS) was added as a dilution tracer to visualize the spatial and temporal extent of hyporheic exchange and to characterize subsurface flow paths. Distinct hydrogeochemical niches were identified in the shallow subsurface beneath the stream by overlaying relative groundwater velocities (derived from ERI) with pore-water chemistry profiles. Niches were classified based on relatively "fast" versus "slow" rates of hyporheic exchange and oxic versus anoxic conditions. Pore-water concentrations and speciation of iron, pH, and redox potential differed between subsurface flow regimes. The greatest extent of hyporheic exchange was beneath the center of the stream, where a shallower (<10 cm) Fe(II)-oxidizing zone was observed. Meanwhile, less hyporheic exchange was observed near the channel banks, concurrent with a more pronounced, deeper (>70 cm) Fe(II)-oxidizing zone. At these locations, relatively slower groundwater exchange may promote biotic Fe(II)-oxidation and improve the long-term stability of Fe sequestered in TIFs.

© 2013 Elsevier B.V. All rights reserved.

1. Introduction

Environmental impacts associated with active and historic coal mining activities impair or threaten ecosystems throughout much of the Appalachian region of the United States. The Appalachian coal fields extend over 1600 km in length from Alabama to Pennsylvania; however, a disproportionate number of mine-impacted streams are found in Pennsylvania because of the regional coal geology (PA DEP, 1998). Ecological impairment to downstream water bodies arise as sulfide-bearing coal seams and surrounding strata are subject to chemical and physical weathering processes that generate acidity, frequently referred to as acid mine drainage (AMD) or, more specifically, coal mine drainage (CMD). CMD is characterized by elevated concentrations of dissolved metals (primarily iron, aluminum and manganese) and sulfate, and high fluid electrical conductivity (Kirby and Cravotta, 2005; Cravotta, 2008). Depending on site geology and hydrogeology, the pH and acidity of CMD can vary from low-pH and net-acid to circumneutral-pH and net-alkaline.

Our research focuses on systems where anoxic, low-pH, Fe(II)-rich AMD emerges from artesian springs, enters a stream, and immediately begins to react with the atmosphere and stream water. In these hydrogeochemical settings, biological low-pH Fe(II) oxidation leads to the precipitation of Fe(III) in the form of ferric sulfate-(hydr)oxide minerals such as schwertmannite [$Fe_8O_8(OH)_6(SO_4)$] (Bigham et al., 1996) or ferric oxyhydroxides such as ferrihydrite. Biological low-pH Fe(II) oxidation, therefore,

* Corresponding author. Address: Department of Civil and Environmental Engineering, The Pennsylvania State University, 212 Sackett Building, University Park, PA 16802, USA. Tel.: +1 814 863 0578; fax: +1 814 863 7304.
E-mail address: wdb3@psu.edu (W. Burgos).
[1] Current address.

0022-1694/$ - see front matter © 2013 Elsevier B.V. All rights reserved.
http://dx.doi.org/10.1016/j.jhydrol.2013.08.007

is an attractive option for AMD remediation because it can remove substantial amounts of Fe(III) before conventional neutralization processes. For example, limestone beds are common in passive treatment systems; however armoring of limestone and/or clogging of the limestone beds due to precipitation of Fe(III) minerals limits performance, but can be minimized by first removing Fe(III) via low-pH Fe(II) oxidation. Furthermore, the process decreases pH, which can promote alkalinity generation from limestone.

In natural or engineered settings, biologically mediated low-pH Fe(II) oxidation will create terraced iron formations (TIFs). The morphology of these TIFs is dependent on site specific hydrodynamic conditions (Veysey Ii and Goldenfeld, 2008), water chemistry, and kinetics of Fe(II) oxidation and Fe(III) precipitation. Under certain conditions TIF sediment depth can become substantial. For example, Fe-rich sediments >1 m in depth have been reported for TIFs formed from CMD in Appalachia (DeSa et al., 2010) and AMD in the Iberian Pyrite Belt (Sánchez España et al., 2007). For TIFs to remain as part of an AMD treatment system, the immobilization of Fe (via oxidative precipitation at the surface) must exceed any possible remobilization in the subsurface (via reductive dissolution). Previous studies have shown that hydrodynamic conditions (velocity and shear) in surface streams control biofilm architecture (Bottacin-Busolin et al., 2009) and microbial community composition (Macalady et al., 2008). Geochemical conditions also exert an effect on microbial community composition, especially in extreme low-pH environments (Baker and Banfield, 2003). However, hydrodynamic or geochemical conditions alone often cannot fully explain microbial diversity (Flores et al., 2012). Hydrogeochemical niches can be identified by overlaying hydrodynamic and geochemical conditions, and may improve our ability to understand and predict microbial diversity. These data are relatively straightforward to obtain in surface streams but are far more difficult to obtain in the subsurface.

In-steam measurements, or measurements from limited available wells, make characterization of groundwater-surface water exchange processes difficult. Geophysical tools are starting to become commonly used in these systems; in particular, electrical resistivity is now frequently used to monitor exchange and understand flow paths (Ward et al., 2010; Cardenas and Markowski, 2010; Coscia et al., 2011; Toran et al., 2012; Doro et al., 2013). Electrical methods have long been used to image groundwater contamination associated with AMD (Merkel, 1972; Ebraheem et al., 1990; Rucker et al., 2009); however, application of these techniques to quantify hyporheic exchange in an AMD-impacted river, to the best of our knowledge, has not yet been considered. Here, we capitalize on this previous work in a new setting.

The objectives of the current study were to (1) resolve the spatial extent of oxic and anoxic conditions within a TIF, (2) to characterize the subsurface geochemistry in these zones, and (3) identify hydrogeochemical niches in the shallow subsurface. Geophysical techniques such as near-surface electrical resistivity imaging (ERI) used with a conductive tracer can visualize hyporheic exchange beneath a stream (e.g., Nyquist et al., 2008; Ward et al., 2010). In the current study, we used low conductivity water as the tracer because of the intrinsically high conductivity of the AMD-impacted stream. ERI methods coupled with a constant-rate, long-term tracer addition provided a 2-dimensional view of subsurface hydrodynamic conditions beneath the stream and the spatial and temporal extent of hyporheic exchange. Subsurface pore-water samplers were then deployed along electrode transects to measure geochemistry in areas of contrasting extent of hyporheic exchange. Combined, these approaches identified a variety of hydrogeochemical niches beneath the AMD-impacted stream.

2. Methods and materials

2.1. Site description

The AMD field site was located near Brubaker Run (BR) (40°37′1.42″N; 78°28′35.76″W), a small tributary of Clearfield Creek (Fig. 1); located approximately 3.2 km northwest of Altoona, PA and 2 km east of Dean, PA. The Dean Clay Mine was a 1,011,800 m^2 underground kaolinite mine that flooded after being abandoned (ca. 1950). The Dean Clay Mine now discharges AMD to Brubaker Run as a large artesian spring that was located above a former air shaft in the collapsed entry to the mine. Water flows downhill from the artesian spring across a large TIF (6000 m^2) in a highly uncontrolled, multi-directional manner, except for one large channel that was the former adit into the mine. This large channel was used for all tracer studies because of its well-constrained, uni-directional flow characteristics (Figs. 1 and 2). A second artesian spring (referred to as BR80) is located along the left-bank of this channel. All left and right-bank designations refer to a downstream orientation. The water chemistry of BR80 and the uphill artesian spring are essentially identical and BR80 is thought to emerge from the "toe" of the mine pool (versus up through the former air shaft). A large fraction of the water from the uphill spring is captured by the adit channel. The top of the uni-directional portion of this channel is approximately 20 m from the center of the uphill spring (and approximately 5 m lower in elevation). The uni-directional portion of the channel then runs for 60 m before dispersing in a multi-directional manner across a lower series of iron terraces.

Because of the high flow and high conductivity of the Dean Clay Mine discharge, a "dilution tracer" was selected containing low conductivity water collected from an adjacent headwater creek (see Table 1). Laurel Run is located near Dysart, PA, approximately 4.8 km from Brubaker Run and was never impacted by coal-mining activities. A water-hauling company was contracted to collect water from Laurel Run and deliver it via a 3000-gallon water truck parked at the test site. A coarse screen was placed on the hose during collection from Laurel Run, and the water was then pumped through 0.5 mm filter bags when fillingthe parked water truck. Water was pumped from the parked tanker through a Neptune flowmeter that was continuously monitored and maintained at 6.3–6.4 L/s for the complete 10 h tracer addition period. With no tracer addition, we estimated that approximately 3.5 L/s was entering the channel just upstream of the tracer addition zone (0 m datum), and we measured a flow of 15.8 L/s at the end of the uni-directional portion of the channel (60 m downstream). Water was pumped approximately 90 m (~10 m elevation gain) from the truck to the injection zone (BR100). The tracer addition zone was located essentially at the start of the uni-directional portion of the channel and is referred to as the 0 m datum for stream locations in this study. The injection zone consisted of a 55-gallon plastic drum equipped with a 3-in. diameter stand pipe positioned to deliver water to the bottom of the drum. Water then overfilled the drum, ran onto plywood placed beneath the drum and then into the channel (Fig. 2A). Wading surveys to measure stream flow, using a Marsh-McBirney velocimeter and wading rod, were conducted 60 m below the injection zone before and during tracer injection to evaluate how much of the tracer exited the uni-directional portion of the channel.

2.2. Electrical resistivity imaging

ERI data were collected on a network of electrodes installed in three transects oriented laterally across the stream channel using a 10-channel Syscal Pro Resistivity Meter (IRIS Instruments,

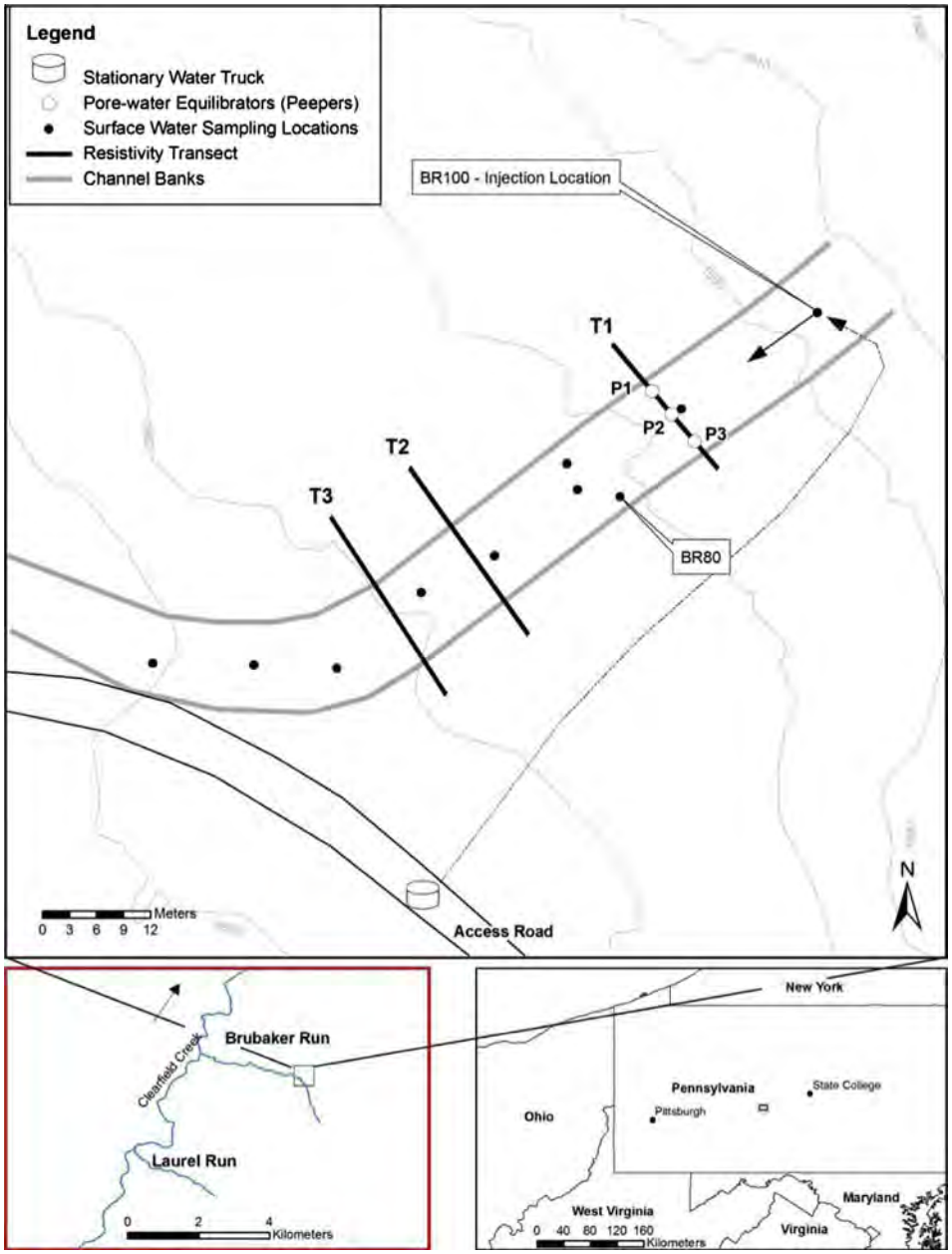

Fig. 1. Location and layout of experimental setup at Brubaker Run, near Dean, PA. Laurel Run was used for the fresh water dilution tracer. Acid mine drainage (AMD) from a large, underground clay mine emerges uphill of BR100 and flows down a channel formed from the former adit into the mine. An artesian spring at BR80 serves as a secondary source of AMD. Electrode transects for electrical resistivity imaging (ERI) were installed perpendicular to the AMD channel at T1, T2 and T3. Subsurface pore-water samplers were installed at T1 along the center of the channel. The fresh water tracer was pumped from a water truck parked on the access road to the injection location at BR100.

Orleans, France). Transects 1, 2 and 3 (T1, T2 and T3) were 20, 46, and 58 m, respectively, from the injection zone (Fig. 2B). BR80 was 30 m from the injection zone. Electrode spacing within each transect was approximately 1.0 m between electrodes in the transect center and increased to 1.5 m towards the end of each transect. Electrode positioning was selected to yield high-resolution measurements across the stream channel where change was anticipated to be greatest while also collecting measurements beyond the channel banks.

Electrodes were manufactured from ½-in. diameter schedule-40 PVC pipes approximately 0.75 m in length. Conductive foil tape was wrapped around the pipe about 10 cm from the bottom to create the electrode surface. An 18-gauge stranded wire connected the foil tape (contact surface below ground) to the trunk line of wires (solid strand 18-gauge), which connected to the ER switch box. Contact resistance of the electrodes was checked prior to the injection and ranged from 0.1 to 4.0 kOhms. The design of these foil-wrapped PVC pipes allowed the electrodes to be positioned in the subsurface without providing a direct conduit to the surface (e.g., via steel or copper pipe electrode).

A mixed dipole–dipole array with 323 measurements was used for data collection and the same sequence was utilized for all transects. The sequence was designed to maximize coverage in the stream center while minimizing the number of electrical injections to reduce temporal smearing during the test. Data collection took approximately 12 min per transect. All data were collected along individual transects; between-transect data were not collected in the interest of time.

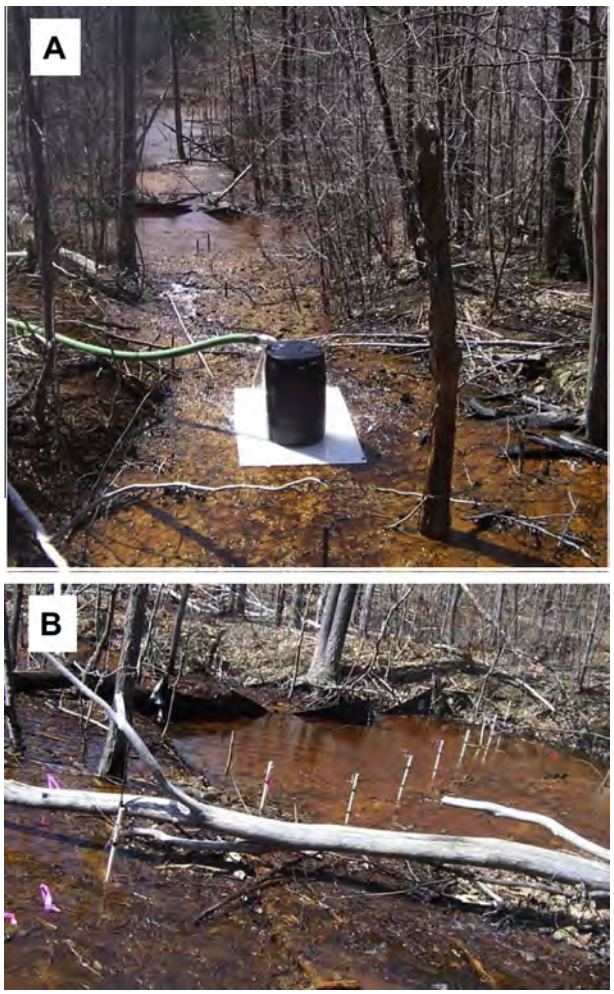

Fig. 2. Field photographs of the Brubaker Run site. (A) Downhill view of the tracer injection zone and the top of the channel (orientation for assignment of L and R bank locations). Fresh water was pumped from a truck and overfilled the barrel before flowing down the channel. (B) Electrode Transect 1 (T1) located 20 m downstream of injection zone. Twelve electrodes (placed 25 cm into the ground) were spaced 1.0–1.5 m apart and data were collected every 30–45 min during the 10 h constant-rate injection test.

Background resistivity measurements were collected across each transect three times before tracer addition, from 17:00 March 21 to 07:00 March 22, 2011. Background resistivity values for each transect were averaged from these three datasets and then used as the initial conditions to calculate relative changes in resistivity in the ERI tomograms. Resistivity measurements for T1, T2, and T3 were cycled approximately every 38 min over the entire sampling period. The tracer addition began at 08:00 and ended at 18:00 March 22, 2011. To monitor the storage and flushing of the tracer, ERI data collection continued for 60 min after the tracer addition ceased. Data quality was monitored during the tests and error was estimated using data stacking where a minimum of two measurements were collected, averaged, and standard deviation calculated on the set. Due to time constraints, reciprocal measurements were not collected. Mean stacking errors (coefficients of variation) for any transect never exceeded 0.1%, and were generally between 0.05% and 0.07%.

2.3. Surface water sampling

Before, during, and after tracer addition a series of in-stream locations were used to measure electrical conductivity of the surface water using an YSI Environmental EC 300 conductivity electrode (YSI, Yellow Springs, OH). In-stream conductivity measurements were made primarily along the center of the channel, typically in shallow pools where it was easy to fully immerse the probe.

Before and during the tracer experiment a series of in-stream locations were used to measure surface water chemistry up to 130 m downstream of the injection zone (including a section below the uni-directional portion of the channel). Portable field meters were used to measure pH and temperature [Beckman BKA57201], and oxidation–reduction potential (ORP) [Beckman A57197]. Water samples were collected at each location, filtered (0.2 μm), chemically preserved (analyte-dependent), and stored on ice before analysis. These measurements were made at 07:00 March 22, 2011 (before injection) and 14:00 March 22, 2011 (during injection), and a similar set of in-stream samples were collected on 12:00 July 28, 2011 when subsurface pore-water samplers were removed from the site (described below).

2.4. Subsurface pore-water sampling

Subsurface chemistry profiles were measured using *in situ* pore-water equilibration samplers (referred to as "peepers"), previously designed, built, and used by Johnston et al. (2009). Three peepers were installed across T1 (Fig. 1), one near each channel bank and one in the center of the channel. Peepers were constructed from solid 3-in. diameter high density polyethylene and had a series of 2.6 cm diameter holes cross-drilled horizontally through the peeper frame at a vertical spacing interval of 5 cm. Each peeper was 1.52 m in length and held 25 sample vials. Sample vials were 26 mm dia, 25 mL polypropylene vials that were fitted with a 47 mm dia., 0.2 μm Tuffryn® Membrane Filter (Pall Life Sciences, Ann Arbor, Michigan) and sealed with a 26 mm threaded "annulus" cap. The cap left a 12 mm dia membrane circle exposed to adjacent pore-water. Sample vials were filled with 100% N_2-purged, distilled and de-ionized (d–d) water, capped, and stored overnight in a d–d water bath continuously flushed with N_2 prior to field deployment. A portable bottle of nitrogen gas was used to flush the water bath as sample vials were transported to the field site (<1.5 h). Pre-labeled sample vials were quickly loaded into the peeper frame to minimize atmospheric O_2 exposure. We estimate that sample

Table 1
Geochemical characteristics of emergent acid mine drainage (AMD) into Brubaker Run and low conductivity tracer collected from Laurel Run.

	pH	ORP (mV)	Conductivity (μS/cm)	Temp (°C)	Discharge[a] (L/s)	Al	Ca	Co	Cu	Fe	K	Mg	Mn	Na	Ni	S	Zn
AMD Source (BR 80)	3.34	404	1863	11.0	7.8 ± 2.8	0.47	3.1	0.01	BDL	1.5	0.14	4.4	0.53	0.48	0.015	10.9	0.026
Injection Water (Laurel Run)	6.21	405	42	7.6	6.3 ± 0.3	0.004	0.052	BDL	BDL	BDL	0.02	0.03	0.002	0.05	BDL	0.07	BDL

BDL – Below Detection Limit.
All concentrations are mM.
% error weir/wading survey: 3.2–10.8%
[a] Estimated with weir calculations and wading surveys.

vials were exposed to the atmosphere for no more than 15 min before each peeper was pushed into the ground. Peepers were manually pushed into the streambed sediments to their complete depth, assisted in some cases with a post-hole driver, or embedded incompletely to the point of first refusal. Care was taken not to push the peepers too hard and possibly shear off the membranes in the sample vial caps. The peepers were installed on July 1, 2011 and removed on July 28, 2011. This 27 d equilibration period was similar to a recommended equilibration time of 30 d (Hesslein, 1976; Johnston et al., 2009).

The peepers were manually removed from the sediments and all sample vials were quickly transferred to portable glove bags (Aldrich® Atmosbag) that were constantly flushed with helium gas. The integrity of each sample vial membrane/cap was checked based on the absence of turbidity or the absence of any gas bubbles in the vials. Vials that failed this quality control check were not analyzed. The He-purged portable glove bags were sealed after all sample vials were removed from the peepers, transported back to our laboratory, and then opened inside an anoxic chamber (Coy, Grass Lakes, MI) supplied with a 95:5% N_2:H_2 gas mix. Samples were stored in the anoxic chamber until analysis (<1 d).

2.5. Analytical methods

Peeper vials were opened inside the anoxic chamber and split into multiple plastic sample bottles for various analyses. The remainder of sample was analyzed directly for pH (Mettler Toledo–InLab* Mini pH Electrode), ORP (Mettler Toledo–InLab*Redox Mini Electrode), and conductivity [Thermo Orion 105A+]. All ORP values are reported relative to an Ag/AgCl reference electrode. Samples were preserved with HCl and dissolved Fe(II) was measured using the ferrozine assay (Stookey, 1970). Samples for total dissolved iron were first reacted with 0.5 M hydroxylamine–HCl and then measured by ferrozine. Dissolved Fe(III) was operationally defined as the difference between total dissolved iron and dissolved Fe(II).

2.6. Electrical resistivity modeling methods

Electrical resistivity data inversion was completed using the code R2 (v2.6, Generalized 2-D Inversion of Resistivity Data, available online at: http://www.es.lancs.ac.uk/people/amb/Freeware/freeware.htm). The algorithm, which is based on Occam's inversion, is described in Binley and Kemna (2005). Data collected during and after tracer addition were inverted using the background resistivity distribution as a starting model. The background resistivity image was differenced from each of the images collected during and after the tracer study by calculating the percent change in resistivity ($\Delta\rho$) for each pixel. The percent difference tomograms show the low conductivity-labeled surface water mixing into the subsurface.

3. Results

3.1. In-channel conductivity

The conductivity in the surface water at each transect responded quickly to the beginning and end of tracer addition (Fig. 3). At T1, 20 m downstream of the tracer injection zone and upstream of BR80, the pre-test conductivity was 1800 μS and decreased to 861 μS within 40 min after tracer addition began. The conductivity at T1 continued its rapid decrease (to 597 μS after 90 min), then remained relatively constant for the next several hours and finally increased to ca. 1000 μS for the final 3 h of the tracer addition period. Conductivity measurements at T1 displayed greater variability as

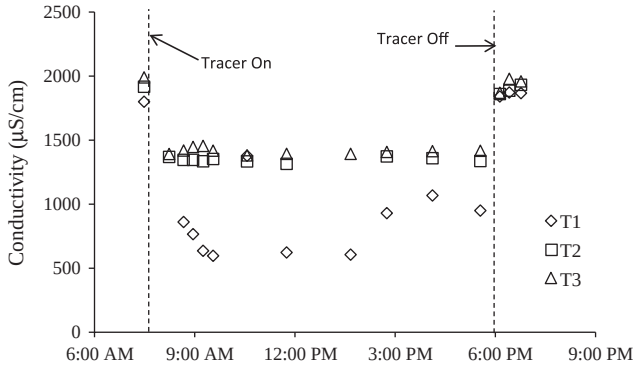

Fig. 3. In-stream conductivity measurements before, during, and after tracer addition. A 10 h constant rate addition of fresh water tracer began at 8:00 AM and ended at 6:00 PM (denoted by vertical dashed lines). Transect 1 (T1) was 20 m downstream of the tracer injection zone and upstream of the artesian spring BR80. Transect 2 (T2) was 46 m downstream of the tracer injection zone and 7 m downstream of BR80. Transect 3 (T3) was 58 m downstream of the tracer injection zone.

compared to the near-constant conductivity measurements at T2 and T3 during tracer addition. In-stream mixing of the tracer with the channel water may have been more homogeneous at T2 and T3 when compared to = T1, causing these differences. After tracer addition ceased, the conductivity at T1 returned to pre-test levels (1841 μS) by the first post-test measurement.

At T2, 46 m downstream of the tracer injection zone and 16 m downstream of BR80, the pre-test conductivity dropped from 1917 μS to 1369 μS within 14 min after tracer addition began and remained relatively constant for the 10 h duration of the test. Similar temporal patterns were observed at T3. The smaller extent of decrease in conductivity at T2 and T3, as compared to T1, was caused by the addition of high conductivity water from the artesian spring located at BR80.

Wading surveys conducted just below T3 before and during tracer addition confirmed that the entire added tracer flow was exiting the uni-directional channel during tracer addition. The measured flow at T3 before tracer addition was 15.8 L/s and then increased to 21.7 L/s after the start of tracer addition. This increase in flow nearly equaled the tracer flow (6.3 L/s), a quantity that was continuously measured during the test. Therefore, using an analogous flow balance at T1 and using conductivity as a conservative tracer, we used a flow-weighted summation to calculate the flow rate of water entering the uni-directional channel just upstream of BR100 (presented in Supplementary data). Based on this conductivity summation, we estimate approximately 3.5 ± 1.7 L/s was entering the channel upstream during tracer addition. In a similar manner, using conductivity values measured at BR80 and downstream of T3, we used a flow-weighted summation to calculate that approximately 12.5 ± 1.8 L/s of AMD entered the channel at BR80. Because of its artesian nature and physical location, the flow rate of BR80 was otherwise virtually impossible to measure directly.

3.2. Surface water chemistry

The geochemistry of the water at the top of the channel varied considerably compared to the headwater at the uphill spring. The uphill spring was anoxic, with Fe(II) as the predominant Fe valence state. As this water became aerated, biological low-pH Fe(II) oxidation occurred and Fe(III) produced from this process precipitated out of solution as schwertmannite and ferrihydrite (Burgos et al., 2012). Fe(III) precipitation consumed alkalinity and decreased the pH. Thus, the typical geochemical gradients downstream of

an acidic, anoxic, Fe(II)-rich spring will be for dissolved oxygen and ORP to increase; and for dissolved Fe(II), dissolved total Fe, and pH to decrease.

This generalization becomes more complicated in the current study because of the addition of the dilution tracer and the addition of BR80, a large anoxic, artesian source. The addition of BR80 into the channel effectively "reset" the geochemical gradients that had begun to establish in between the uphill spring and BR80. This was most evident with concentrations of dissolved Fe(II) (Fig. 4C). Dissolved Fe(II) concentrations increased in the channel due to the artesian spring at BR80 but immediately began to decease because of biological Fe(II) oxidation and Fe(III) precipitation in the channel. The addition of 6.3 L/s of the low conductivity tracer (42 μS, pH 6.2, 8.0 mg/L O_2, 450 mV ORP, <0.1 mg/L Fe) to the channel acutely modified the water chemistry and geochemical gradients in the channel (Fig. 4). While the tracer had a relatively high pH, this water had very little alkalinity such that the pH of the AMD in the channel during the test increased only by ca. 0.1 unit (uniformly along the whole channel length) during tracer addition (Fig. 4A). The ORP values measured during tracer addition were quite variable. In waters with high dissolved concentrations of Fe(II) and Fe(III), both Fe(II/III) and dissolved oxygen contribute to poise ORP. During tracer addition, ORP measurements were likely confounded by the blending of the tracer and surface water. As discussed above, the conductivity of the water decreased immediately downstream of the tracer injection zone, and then increased after the addition of BR80 (Fig. 3). Iron concentrations in the channel decreased during tracer addition, however, this was likely caused by dilution effects rather than changes in Fe(II) oxidation kinetics as Fe speciation (i.e., $[Fe(II)]/[Fe]_{TOT}$) remained essentially unchanged during the test.

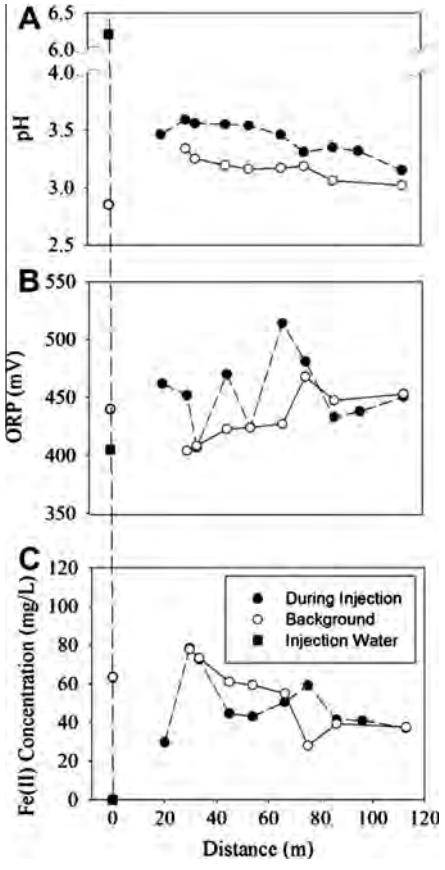

Fig. 4. Surface water geochemistry displayed as a function of distance from the tracer injection zone (0 m datum denoted with dashed vertical line). Open circles (○) are background measurements collected 1 h prior to tracer injection; closed circles (●) are measurements collected 5 h into the tracer experiment; and closed squares (■) are measurements of the tracer. The artesian spring at BR80 entered the channel at 30 m.

3.3. Electrical resistivity imaging

Time-lapse ERI results for each transect are presented in Fig. 5. Background resistivity values ranged from 10^{-1} to 10^{3} ohm-m across the three transects with lower values located within the channel. The spatial resolution of the ERI measurements cannot be quantified exactly, as it is dependent on the electrical conductivity of the subsurface and the geometry of electrodes used. Across all three transects, sensitivity values were greatest within 0–1.0 m below ground surface (b.g.s.) and decreased with depth, indicating greater reliability of imaging near the surface sediments. That is, the "trustworthiness" of data decreases with decreasing sensitivity. At T1, and T3 to a lesser degree, the sensitivity across the entire transect was uniform both laterally and vertically. At T2, low sensitivity values towards the left bank suggest a strong influence from the artesian source BR80 on resistivity measurements. From all of the ERI tomograms, the largest relative change of resistivity as compared to baseline (i.e., $\Delta\rho$) was 4.0%. While the range of relative $\Delta\rho$ was relatively small (0.23–4.0%) in this study, mean stacking errors for any transect never exceed 0.1%. The top-most row of pixels represents the net resistivity of the stream water and stream sediments within those domains.

The ERI tomograms reveal that hyporheic exchange is occurring along this stream reach. While hyporheic exchange involves the mixing of stream water and shallow groundwater, it is unique because the stream water that enters the subsurface (i.e., the hyporheic zone) eventually re-enters the stream at some point downstream (Gooseff, 2010). We operationally defined the extent of hyporheic exchange based on the penetration of the surface water tracer into the subsurface leading to measurable changes in apparent resistivity (Fig. 5). This system displays hyporheic exchange because the tracer added above T1 (Fig. 1) mixes into the subsurface beneath T1 and T2 and then re-enters the stream by T3. Detailed discussions of these transects are provided below.

The ERI tomograms displayed different characteristics at each transect. Across T1 (Fig. 5A), the tracer first arrived along the center of the channel. For T1 the largest $\Delta\rho$ value was 2.3%. As tracer addition continued, the tracer penetrated deeper into the subsurface and wider toward the stream banks. The radial expansion of tracer infiltration indicated the combination of advective and diffusive transport mechanisms within the hyporheic zone in this channel reach. The rapid infiltration of tracer indicated good connectivity between the surface water and shallow groundwater. After tracer addition ceased, the dilution tracer remained in the shallow groundwater for up to 0.5 h.

ERI tomograms for T2 (Fig. 5B) were more complicated as compared to T1, likely due to the addition of BR80 into the channel (16 m upstream of T2). For T2 the largest $\Delta\rho$ value was 4.0%. As with T1, the area of tracer infiltration expanded radially deeper into the ground and towards the stream bank. However, there were at least three important differences between the ERI tomograms collected at T1 as compared to T2. First, the expansion of the tracer signal beneath the center of the channel at T2 was non-uniform with abrupt differences in resistivity between adjacent pixels. Second, a strong transient tracer signal was observed several meters to the left of the left bank of the channel at T2. After 2.5 h of tracer addition, $\Delta\rho$ increased up to 2.5% in this region outside of the channel. After 5.5 h, the $\Delta\rho$ in this region had relaxed back to baseline levels. This suggests that the transient storage beneath the left bank endorsed preferential flow paths. Third, a large "dark void" was observed beneath the left bank of the channel where the

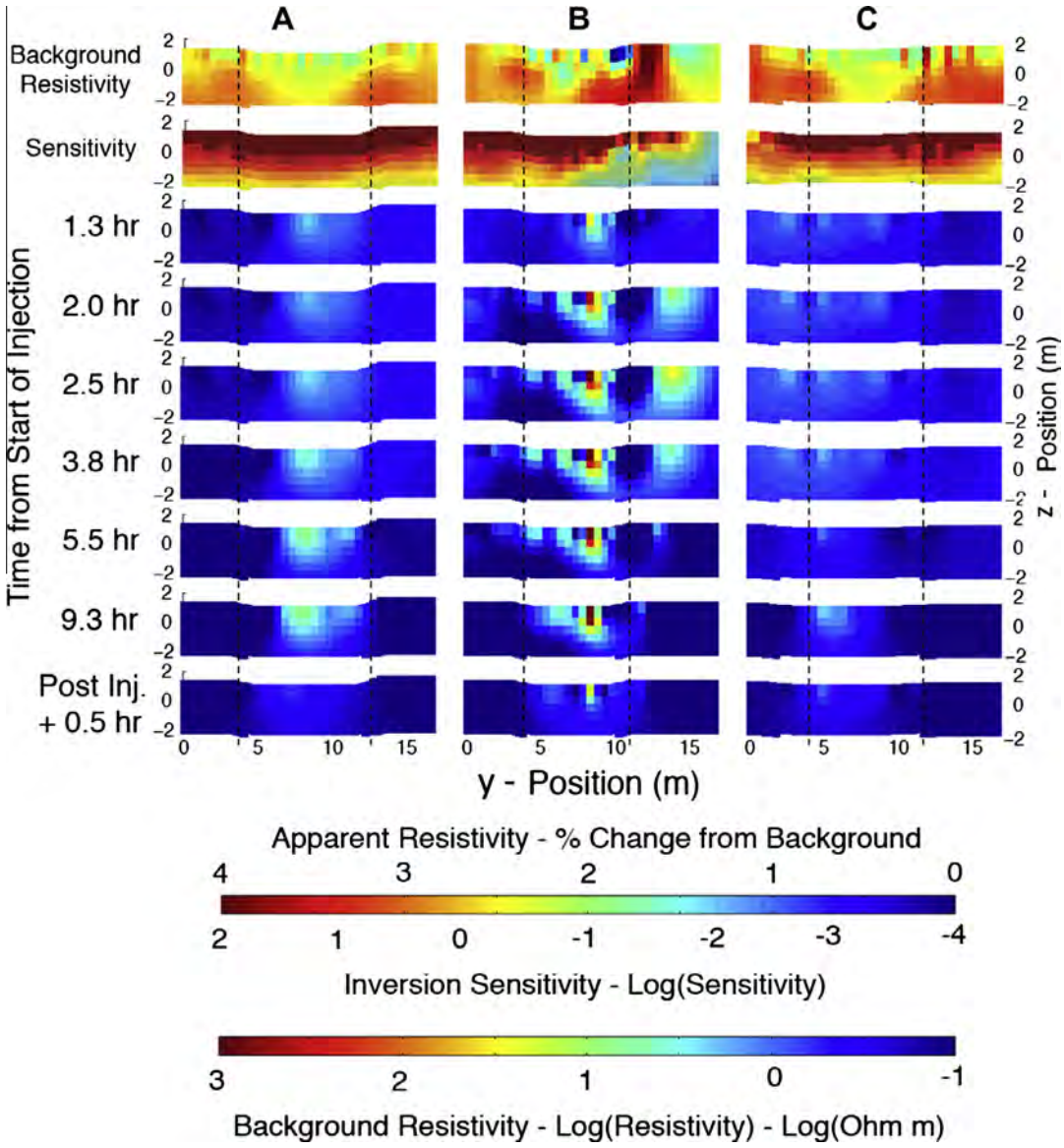

Fig. 5. Electrical resistivity imaging (ERI) tomograms from the three electrode transects: Left column – Transect 1 (T1); Middle column – Transect 2 (T2); and Right column – Transect 3. T1, T2, and T3 were located 20, 46, and 58 m, respectively, downstream of the injection zone. The artesian spring BR80 entered the stream ca. 30 m downstream of the injection zone. Top row – Pre-injection electrical resistivity background values. Transects are shown perpendicular to the stream with flow directed out of the page. The channel banks are identified by the dashed lines for each cross-section (R-bank on left; L-bank on right). *y* and *z* positions are assigned relative for each transect. 2nd row – Model sensitivity. 3rd – 8th row – Time-lapsed ERI results, at time elapsed after start of tracer addition. 9th row – Final ERI results collected after tracer addition ceased.

relative resistivity never substantially deviated from baseline values during the first 5.5 h of tracer addition. We propose the dark void was caused by water emerging from BR80 that overwhelmed or inhibited tracer penetration into this region, due to its proximity to T2. After 9.3 h of tracer addition, mixing between the tracer and BR80 appeared to decrease the influence of BR80 on hyporheic exchange occurring across T2. To the best of our knowledge, this represents the first time an artesian spring has been successfully imaged using ERI techniques.

ERI tomograms for T3 (Fig. 5C) were not as heterogeneous as those collected for T1 and revealed limited hyporheic exchange along this channel reach. Over the first 5.5 h of tracer addition the maximum $\Delta\rho$ for any single pixel never exceeded 2.1%. No physical pattern developed to resemble preferential infiltration of the tracer beneath the center of the channel. Interestingly, T3 was only 12 m downstream of T2 yet the complex distributions of varying subsurface resistivity observed at T2 had been homogenized by the time the tracer reached T3. This homogenization was not likely caused by greater dilution of the tracer between T2 and T3 because the relative decrease of in-stream conductivity was essentially the same at both of these locations (Fig. 3).

3.4. Flow path saturation

$\Delta\rho_{max}$ was defined as the greatest relative $\Delta\rho$ for a specified pixel area (Δy, Δz) at any given time as compared to the baseline resistivity. By analyzing the inversion data in terms of $\Delta\rho_{max}$, all time-lapse ERI images could be effectively collapsed into a single parameter that amplified the cross-section locations where the largest resistivity changes occurred (Fig. 6A). The highest and lowest $\Delta\rho_{max}$ values across T1 were 2.3% and 0.27%, respectively (Fig. 6A). The highest $\Delta\rho_{max}$ values occurred at the stream-bed surface along the center of the channel. High $\Delta\rho_{max}$ values also occurred in the subsurface, primarily beneath the center of the

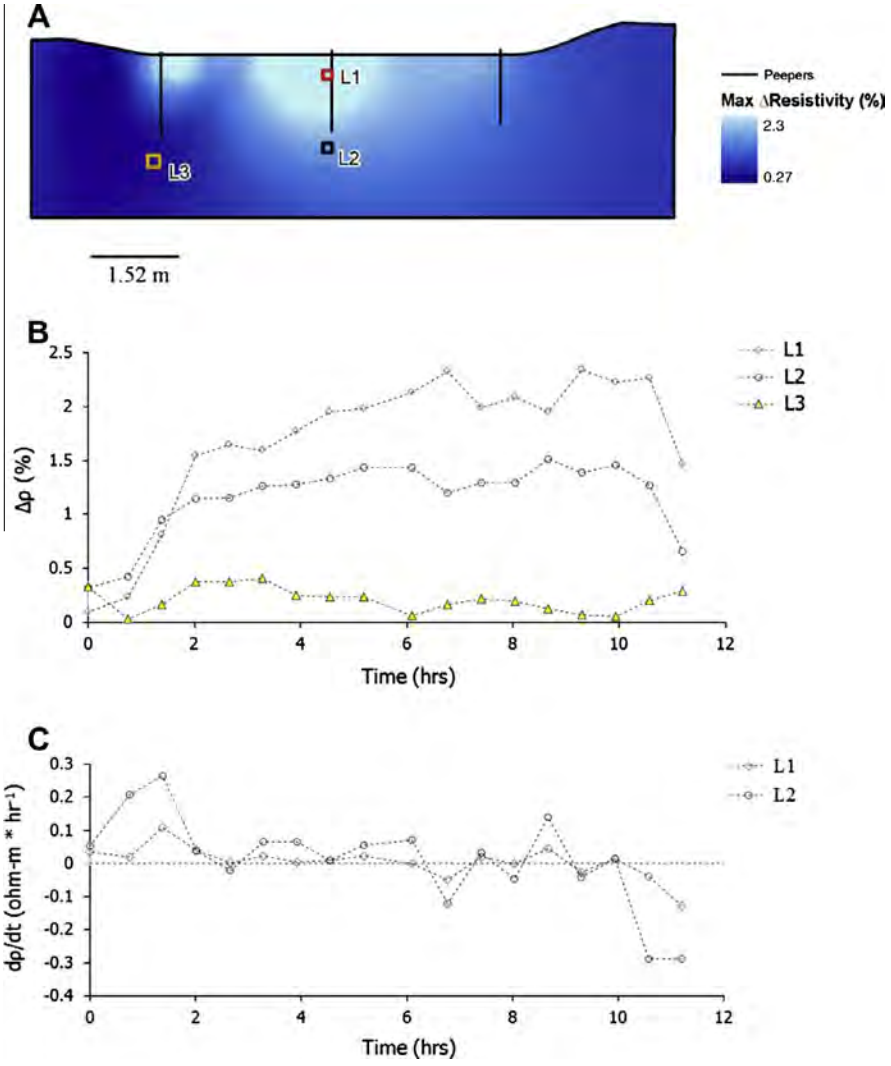

Fig. 6. (A) Maximum change in resistivity ($\Delta\rho_{max}$) resolved spatially at T1. The channel banks are identified by the indentation towards the top of the cross-section (R-bank on left; L-bank on right). (B) The corresponding temporal Δ resistivity at three finite element locations (L1, L2, and L3) shown in A. (C) Corresponding $d\rho/dt$ values as a function of time for finite elements L1 and L2.

channel, and represent substantial interactions between surface water and groundwater in the hyporheic zone. Because the tracer was injected for only 10 h, it was unknown whether, hypothetically, an infinite tracer addition time would result in a significant increase in the permeation radius of the tracer presented in Fig. 6A. Three pixel locations (L1, L2 and L3) in the 2-dimensional cross-section of T1 were compared over the duration of the test. Pixel locations were selected near the highest $\Delta\rho_{max}$ value (L1), an area of intermediate $\Delta\rho_{max}$ (L2), and an area presumably not influenced by the tracer (L3). At L1 and L2, comparable temporal trends were observed for the $\Delta\rho$ values (Fig. 6B). The $\Delta\rho$ values increased sharply in the first 2 h of tracer addition, stabilized to some extent over the next 8 h, and then decreased sharply after tracer addition ceased after 10 h. In contrast, L3 showed little to no change in $\Delta\rho$ versus time, confirming that the tracer had little to no influence at this location. The parameter $d\rho/dt$ was defined as the incremental relative $\Delta\rho$ for a specified pixel area between specified time intervals. Theoretically, as $d\rho/dt$ approaches zero, $\Delta\rho$ should approach a maximum value which indicates that the flow path through the pixel area has become saturated with the tracer. Saturated flow paths support the premise that the duration of tracer addition was adequate to visualize and quantify regions of preferential subsurface flow (e.g., hyporheic zones). Similar trends were observed for the parameter $d\rho/dt$ for locations L1 and L2 where $d\rho/dt$ was a positive value at the start of tracer addition, stabilized to near-zero values for the remainder of tracer addition, and then became negative after tracer addition ceased (Fig. 6C). The relatively higher magnitudes of $d\rho/dt$ at L2 suggest greater variability existed in this subsurface region as compared to L1. An interpretation of greater variability suggests the resistivity at L2 was approaching saturation slower relative to L1. Data from L3 were not presented in Fig. 6C; assuming no influence by the tracer.

Mean arrival time of the tracer was defined as the time when the $\Delta\rho$ for a pixel area first exceeded an arbitrary threshold value; indicating that the tracer had "arrived" at the specified location (Fig. 7A). Based on the range of $\Delta\rho_{max}$ values measured in the current study (0.27–2.3%), we used a threshold value ($\Delta\rho_{arrival}$) of 1.5%. This threshold value was chosen to confine the extent of radial change within the depth of trustworthy sensitivity. It was difficult, if not impossible, to assign quantitative values to these arrival times, as these 2-dimensional tomograms are generated by analyzing a 3-dimensional volume surrounding the transect. However, we propose that mean arrival times can serve as semi-quantitative proxies for relative groundwater velocities. In other

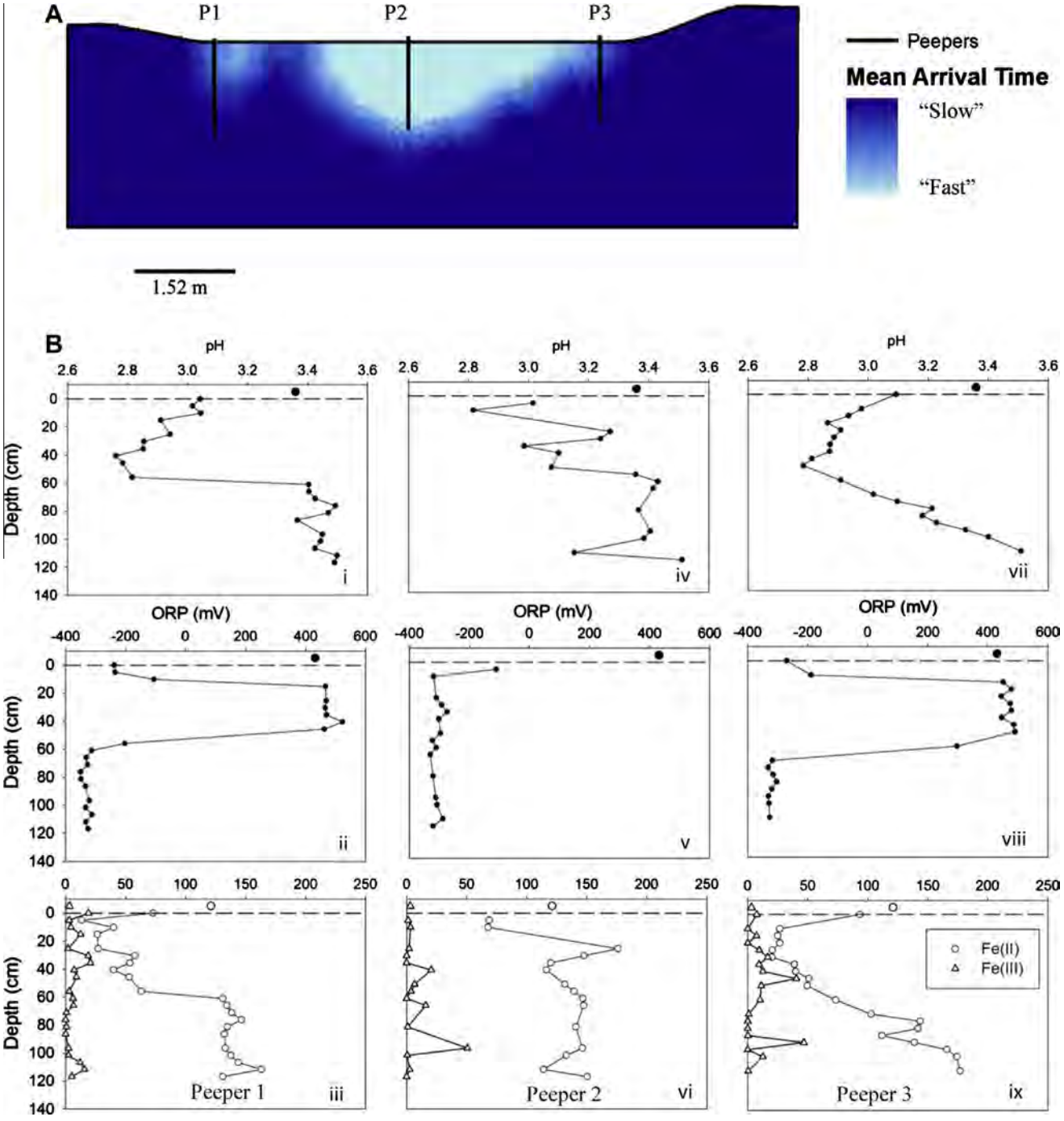

Fig. 7. (A) Relative mean arrival times resolved for transect 1 (T1). The channel banks are identified by the indentation towards the top of the cross-section (R-bank on left; L-bank on right). Black lines show the spatial locations of the subsurface porewater samplers (i.e., "peepers") to scale, and are labeled as P1, P2 and P3. (B) Geochemical results for pH (top row), oxidation–reduction potential (ORP) (middle row), and Fe speciation and concentration (mg/L) (bottom row) corresponding to P1, P2, and P3 (vertical columns). Surface water values are represented by larger symbols above the dashed line.

words, finite elements with shorter arrival times were located in regions of "fast" groundwater velocity while finite elements with longer arrival times were located in regions of "slow" groundwater velocity. Fast arrival times exceeded the threshold $\Delta\rho$ value during tracer addition. Slow arrival times exceeded the duration of tracer addition. Alternatively or additionally, pixels withshorter arrival times were located in regions of faster hyporheic exchange while finite elements with longer arrival times were located in regions of slower hyporheic exchange.

During this experiment, hyporheic exchange occurred predominantly as down-welling of the tracer and revealed hyporheic flow paths. During all other times, anoxic groundwater from the mine pool will likely up-well along these same hyporheic flow paths in this reach. Along T2, this up-welling manifests itself as the large artesian source at BR80. Along T1, this up-welling likely manifests itself along the radial distribution of flow paths visualized in Fig. 5A. The conceptual reversal of down-welling tracer (during ERI test) versus up-welling anoxic groundwater (during peeper

deployment months later) is important for interpreting subsurface geochemical depth profiles.

3.5. Subsurface pore-water chemistry

Vertical subsurface pore-water samplers were deployed across T1 for 28 d to investigate how subsurface geochemical profiles varied in regions of "fast" versus "slow" rates of hyporheic exchange (and groundwater velocity). The ERI methods identified that the most rapid exchange between surface and groundwater occurred near the center of the channel (Figs. 5 and 6A). The influence of the tracer was less substantial near the channel banks. Peepers 1 and 3 (P1 and P3) were installed in the streambed very close to the channel banks while peeper 2 (P2) was installed in the streambed directly in the center of the channel. Distinctly different geochemical depth profiles were found near the channel banks as compared to the channel center. At P1 the pH declined from 3.1 to <2.8 over the first 60 cm into the sediments, followed by a sharp increase in pH in between 60 and 65 cm, after which the pH stabilized between 3.4 and 3.5 from 65 cm to the final sample depth of 125 cm (Fig. 7B-ii). Also at P1, the ORP increased sharply from −220 mV nearest the surface to +450 mV at 15 cm into the sediments, stabilized at ca. +450 mV until 55 cm depth, decreased sharply to −350 mV at 60 cm depth, and then remained stable at ca. −350 mV from 65 cm to the final sample depth of 125 cm (Fig. 7B-iii). In-stream measurements for all parameters are presented as enlarged symbols just above 0 cm depth in all panels in Fig. 7B. At P1 the dissolved Fe(II) concentrations were below the in-stream concentration over the first 60 cm into the sediments; Fe(II) concentrations then increased sharply from 60 to 65 cm and stabilized at values above the in-stream concentration from 65 to 125 cm (Fig. 7B-iii). Similar subsurface geochemical trends were measured in P3 (Fig. 7-vii–ix); however, the increase in pH at depth was not a sharp gradient as compared to P1. While recognizing these differences, the more striking result was that the similar geochemical profiles at P1 and P3 could represent "symmetrical replicates" for the channel banks. Interpretations of these geochemical profiles are provided in Section 4.

Geochemical depth profiles beneath the center of the channel at P2 were distinctly different from the channel banks. At P2 the pH values changed inconsistently with depth but generally increased from ca. pH 2.9 to ca. pH 3.4 over the complete 125 cm profile (Fig. 7B-iv). No sharp pH gradient at any mid-depth location was observed (as seen at P1). At P2 the ORP decreased sharply from −100 mV at 5 cm into the sediments to −350 mV at 10 cm depth, and then remained stable at ca. −350 mV over the remainder of the profile (Fig. 7B-v). At P2 dissolved Fe(II) concentrations decreased to 65 mg/L at 5–10 cm into the sediments and then increased to 125–175 mg/L from 25 cm to the final sample depth of 125 cm (Fig. 7B-vi).

Collectively, these geochemical profiles demonstrated that subsurface zones of biological Fe(II) oxidation extended to greater depths beneath the channel banks as compared to the center of the channel. Biological Fe(II) oxidation will produce Fe(III) that will precipitate from solution (thus decreasing the dissolved Fe concentrations) and consume alkalinity (thus decreasing the pH). The presence of these sharp biogeochemical gradients, where sediments abruptly shift from Fe(II)-oxidizing to Fe(III)-reducing conditions, were also visually evident upon retrieval of the peepers. On P1 and P3, dark orange, Fe(III)-rich precipitates coated the peeper frames to an approximate depth of 60 cm. Below ca. 60 cm, the peeper frames were devoid of any mineral coatings. On P2 the Fe(III)-rich precipitates only coated the peeper frame to an approximate depth of 15 cm (photographs provided in Supplementary data). Low-pH biological Fe(III) reduction is expected to occur in these sediments based on previous studies (Senko et al., 2011). Many of the heterotrophic, acidophilic Fe(II)-oxidizing bacteria are also heterotrophic, acidophilic Fe(III)-reducers (Coupland and Johnson, 2008). Dissolved Fe(II) concentrations in the anoxic zones beneath the channel were typically higher than the in-stream Fe(II) concentrations, providing indirect geochemical evidence of Fe(III) reduction. While sulfide concentrations were not measured, no visual or olfactory evidence of sulfate reduction was observed in deep sediment samples.

4. Discussion

The physical conditions of Brubaker Run are important when trying to interpret subsurface geophysical and geochemical profiles. The large artesian spring uphill of the tracer injection zone provided the hydraulic head for both the surface water in the channel and the groundwater entering the channel. Prior to tracer addition, flow in the channel was 3.5 L/s at the top (0 m datum) and increased to 15.8 L/s at the bottom of the uni-directional channel (60 m downstream), due to contribution from BR80. The artesian spring at BR80 likely represents one large preferential flow path from the mine pool to the channel. ERI tomograms for T1 (Fig. 5A) demonstrate active hyporheic exchange in this reach (20 m downstream). Because the flow increases significantly from the top to the bottom of the channel, we presume that the channel near T1 is likely a gaining reach. Flow paths from the mine pool to this reach are likely more uniform, allowing the hyporheic zone to establish in a radial manner beneath the channel. The geochemistry of the groundwater that up-welled into the channel was essentially identical to the geochemistry of the uphill spring and the mine pool source. Because of the physical and hydrological complexities of this site, T1 provided an ideal setting to study the mixing of oxic surface water and anoxic groundwater and to measure subsurface geochemical profiles in areas of contrasting hyporheic exchange. Across T1, surface water hydrodynamics appeared to have a direct effect on the extent of hyporheic exchange beneath the channel. Surface water velocities were faster near the channel center (data not shown) while tracer penetration depths were greatest beneath the channel center (Fig. 5A). The extent of hyporheic exchange (Fig. 5A) and tracer arrival times (Fig. 7A) were lowest near the channel banks. Based on these 2-dimensional (Δy, Δz) representations of the system, flow paths from the groundwater to the channel banks are longer and slower as compared to flow paths to the channel center.

Subsurface pore-water chemistry (Fig. 7B) was directly influenced by the extent of hyporheic exchange (Fig. 5A) and rates of hyporheic exchange (Fig. 7A). Because of the greater mixing of anoxic groundwater with surface water, the subsurface pore-water beneath the channel center remained completely anoxic (Peeper 2; Fig. 7B-v). In contrast, a largevertical region (ca. 10–60 cm b.g.s.) of the subsurface pore-water beneath the channel banks was oxic (Peepers 1 and 3; Fig. 7B-ii and B-viii). One interpretation of these results is that because of less hyporheic exchange with the anoxic groundwater, $O_2(aq)$ in the surface water could penetrate to greater depths beneath the channel banks. However, measured values of low ORP in the near-surface sediments (0–10 cm b.g.s.) beneath the channel banks complicate this interpretation.

It is difficult to explain how $O_2(aq)$ can be delivered to intermediate depths of 10–60 cm b.g.s. and somehow bypass the overlying more reduced sediments. We are, however, confident in these measurements because they were observed in both Peepers 1 and 3 (symmetrical replicates of sorts). Based on visual observations of this site over several years, the accumulation of leaf litter and organic matter is not substantially variable between in-stream and on-land, nor between the stream bottom at the banks versus the center of the channel. Evidence of organic carbon cemented

into the sediments was found in all sediment cores collected from the site. We propose that the biological oxidation of this organic carbon, more so than dissolved Fe(II), created a highly reduced geochemical niche in the near-surface sediments. In other words, the rate of C oxidation exceeded the flux of $O_2(aq)$ into these sediments. A higher rate of C oxidation in these upper sediments may been due to the "fresher", more labile nature of this organic C as compared to organic C found deeper in the soil profile. We speculate that $O_2(aq)$ was then somehow delivered laterally into these deeper sediments (10–60 cm b.g.s.) from the dry land beyond the stream banks. Increased ORP values found deeper in the sediments represent a geochemical niche where the rate of Fe(II) oxidation did not exceed the flux of $O_2(aq)$. This geochemical niche is ideal for acidophilic, Fe(II)-oxidizing microbes. At even further depths (i.e., >80 cm b.g.s.), no $O_2(aq)$ penetrated into the sediments and little exchange of oxic surface water into the anoxic groundwater occurred. This deeper geochemical niche is ideal for acidophilic, Fe(III)-reducing microbes.

With respect to our applied objective of assessing the stability of Fe(III) sequestered in TIFs, it appears that (at least for this site) slow subsurface flow conditions may minimize the effect of Fe(III) reduction by minimizing the volume of its geochemical niche. Fe(III) reduction would lead to mineral dissolution and re-mobilization of Fe(II) and any associated trace metals or anions, compromising the effectiveness of TIFs for AMD treatment. Limiting the amount of organic matter that accumulates on and gets buried within the TIF should also help avoid the development of Fe(III)-reducing conditions. Provided that adequate land is available for an engineered TIF, slow flow conditions (both surface and subsurface) would also allow for greater Fe(II) oxidation and Fe removal.

With respect to our basic science objective, unique hydrogeochemical niches were identified in the subsurface beneath the AMD channel by overlaying tracer arrival times with pore-water chemistry profiles. Areas of relatively "fast" versus "slow" groundwater velocities were found beneath the center of the channel versus the channel banks, respectively (Fig. 7A). Areas of oxic versus anoxic conditions were found in shallow versus deep sediments, respectively, although the depth was strongly dependent on hyporheic exchange. When these data sets are combined, at least four unique hydrogeochemical niches can be identified: Fe(II)-oxidation in fast groundwater; Fe(II)-oxidation in slow groundwater; Fe(III)-reduction in fast groundwater, and; Fe(III)-reduction in slow groundwater.

Interstitial water velocities are known to influence redox processes in the hyporheic zone (Morrice et al., 2000). In a planimetric model of river meanders, the highest consumption of $O_2(aq)$ due to aerobic biogeochemical processes occurred in regions of relatively "slow" velocity or high sinuosity (Boano et al., 2010). In our system, where anoxic Fe(II)-rich water enters the hyporheic zone, regions of slow groundwater allowed for greater $O_2(aq)$ penetration. This in turn led to the highest consumption of Fe(II) (i.e., to greater depth) beneath the channel banks. It is still unknown how the different interstitial water velocities (i.e., fast versus slow) will affect the microbial communities in these subsurface environments.

In open channels, biofilm development and community structure are directly affected by hydrodynamic conditions. For example, in a study conducted on the development of microbial biofilms in microfluidic reactors, secondary flow features were shown to control biofilm architecture (Rusconi et al., 2011). In surface channels of AMD, Fe(II)-oxidizing bacteria capable of forming extracellular polymeric substances (EPS) have been observed to thrive in fast flowing waters (Hedrich and Johnson, 2012). Similarly, in subterranean streams in a sulfidic cave system, biofilm community structure appeared to be dependent on both primary (e.g., velocity) and secondary (e.g., eddy currents) hydrodynamic features (Macalady et al., 2008). It is likely that microbes that produce EPS and other hold-fast structures predominate in fast groundwater niches.

In the Fe(III)-reducing niches identified in our system, the mineral form of Fe(III) will likely exert an effect on Fe cycling and possibly on the microbial community structure. Several studies have shown that acidophilic Fe(II)-oxidizing bacteria are also capable of Fe(III)-reduction (Coupland and Johnson, 2008; Johnson et al., 2012; Lu et al., 2010). The potential for either process depends on geochemical conditions in the surrounding environment. Depending on the pH, schwertmannite precipitation will control Fe(III) solubility but will eventually transform to goethite (Schwertmann and Carlson, 2005). The kinetics of this transformation are relatively slow under low-pH conditions yet environmentally important over the time required for TIF maturation (months to years). Both minerals are used during dissimilatory Fe(III)-reduction, but Fe(III) in schwertmannite has been reported to be more bioavailable to heterotrophic iron(III)-reducing bacteria as compared to goethite (Lu et al., 2010). We would expect that sediments with a higher fraction of schwertmannite would support more Fe(III)-reducing activity. Future work will characterize the mineral assemblages and microbial communities found in these niches.

Acknowledgments

This research was supported by the Office of Surface Mining Reclamation and Enforcement under Cooperative Agreement (Grant) S11AC20005, and by the National Science Foundation Grant EAR-0911435. Any opinions, findings, and conclusions or recommendations expressed in this material are those of the author(s) and do not necessarily reflect the views of the National Science Foundation. Thanks to Dr. Scott Johnston, Southern Cross University, Australia, for loaning us the peepers used in this study.

Appendix A. Supplementary material

Supplementary data associated with this article can be found, in the online version, at http://dx.doi.org/10.1016/j.jhydrol.2013.08.007.

References

Baker, B.J., Banfield, J.F., 2003. Microbial communities in acid mine drainage. FEMS Microbiol. Ecol. 44 (2), 139–152.
Bigham, J.M., Schwertmann, U., Traina, S.J., Winland, R.L., Wolf, M., 1996. Schwertmannite and the chemical modeling of iron in acid sulfate waters. Geochim. Cosmochim. Acta 60 (12), 2111–2121.
Binley, A., Kemna, A., 2005. DC resistivity and induced polarization methods hydrogeophysics. In: Rubin, Y., Hubbard, S.S. (Eds.), Water Sci Technol. Library. Springer, Netherlands, pp. 129–156.
Boano, F., Demaria, A., Revelli, R., Ridolfi, L., 2010. Biogeochemical zonation due to intrameander hyporheic flow. Water Resour. Res. 46, W02511.
Bottacin-Busolin, A., Singer, G., Zaramella, M., Battin, T.J., Marion, A., 2009. Effects of streambed morphology and biofilm growth on the transient storage of solutes. Environ. Sci. Technol. 43 (19), 7337–7342.
Burgos, W.D. et al., 2012. Schwertmannite and Fe oxides formed by biological low-pH Fe(II) oxidation versus abiotic neutralization: impact on trace metal sequestration. Geochim. Cosmochim. Acta 76, 29–44.
Cardenas, M.B., Markowski, M.S., 2010. Geoelectrical imaging of hyporheic exchange and mixing of river water and groundwater in a large regulated river. Environ. Sci. Technol. 45 (4), 1407–1411.
Coscia, I., Greenhalgh, S.A., Linde, N., Doetsch, J., Marescot, L., Günther, T., Vogt, T., Green, A.G., 2011. 3D crosshole ERT for aquifer characterization and monitoring of infiltrating river water. Geophys. 76 (2), G49–G59.
Coupland, K., Johnson, D.B., 2008. Evidence that the potential for dissimilatory ferric iron reduction is widespread among acidophilic heterotrophic bacteria. FEMS Microbiol. Lett. 279 (1), 30–35.
Cravotta, C.A., 2008. Dissolved metals and associated constituents in abandoned coal-mine discharges, Pennsylvania, USA. Part 1: Constituent quantities and correlations. Appl. Geochem. 23 (2), 166–202.
DeSa, T., Brown, J., Burgos, W., 2010. Laboratory and field-scale evaluation of low-pH Fe(II) oxidation at Hughes Borehole, Portage, Pennsylvania. Mine Water Environ. 29 (4), 239–247.

Doro, K.O., Leven, C., Cirpka, O.A., 2013. Delineating subsurface heterogeneity at a loop of River Steinlach using geophysical and hydrogeological methods. Environ. Earth Sci., 1–14.
Ebraheem, A.M., Hamburger, M.W., Bayless, E.R., Krothe, N.C., 1990. A study of acid mine drainage using earth resistivity measurements. Ground Water 28 (3), 361–368.
Flores, G.E. et al., 2012. Inter-field variability in the microbial communities of hydrothermal vent deposits from a back-arc basin. Geobiol. 10 (4), 333–346.
Gooseff, M.N., 2010. Defining hyporheic zones – advancing our conceptual and operational definitions of where stream water and groundwater meet. Geogr. Compass 4, 945–955.
Hedrich, S., Johnson, D.B., 2012. A modular continuous flow reactor system for the selective bio-oxidation of iron and precipitation of schwertmannite from mine-impacted waters. Bioresour. Technol. 106, 44–49.
Hesslein, R.H., 1976. *In situ* sampler for close interval pore water studies. Limnol. Oceanogr. 21 (6), 912–914.
Johnson, D.B., Kanao, T., Hedrich, S., 2012. Redox transformations of iron at extremely low pH: fundamental and applied aspects. Front. Microbiol. 3.
Johnston, S.G. et al., 2009. Pore water sampling in acid sulfate soils: a new peeper method. J. Environ. Qual. 38 (6), 2474–2477.
Kirby, C.S., Cravotta, C.A., 2005. Net alkalinity and net acidity 1: theoretical considerations. Appl. Geochem. 20 (10), 1920–1940.
Lu, S., Gischkat, S., Reiche, M., Akob, D.M., Hallberg, K.B., Kusel, K., 2010. Ecophysiology of fe-cycling bacteria in acidic sediments. Appl. Environ. Microbiol. 76, 8174–8183.
Macalady, J.L. et al., 2008. Niche differentiation among sulfur-oxidizing bacterial populations in cave waters. ISME J. 2 (6), 590–601.
Merkel, R.H., 1972. The use of resistivity techniques to delineate acid mine drainage in ground water. Ground Water 10 (5), 38–42.
Morrice, J.A., Dahm, C.N., Valett, H.M., Unnikrishna, P.V., Campana, M.E., 2000. Terminal electron accepting processes in the alluvial sediments of a headwater stream. J. N. Am. Benthol. Soc. 19, 593–608.
Nyquist, J.E., Freyer, P.A., Toran, L., 2008. Stream bottom resistivity tomography to map ground water discharge. Ground Water 46 (4), 561–569.
Rucker, D.F., Glaser, D.R., Osborne, T., Maehl, W.C., 2009. Electrical resistivity characterization of a reclaimed gold mine to delineate acid rock drainage pathways. Mine Water Environ. 28 (2), 146–157.
Rusconi, R., Lecuyer, S., Autrusson, N., Guglielmini, L., Stone, H.A., 2011. Secondary flow as a mechanism for the formation of biofilm streamers. Biophys. J. 100, 1392–1399.
Sánchez España, J., Santofimia Pastor, E., López Pamo, E., 2007. Iron terraces in acid mine drainage systems: a discussion about the organic and inorganic factors involved in their formation through observations from the Tintillo acidic river (Riotinto mine, Huelva, Spain). Geosphys. 3 (3), 133–151.
Schwertmann, U., Carlson, L., 2005. The pH-dependent transformation of schwertmannite to goethite at 25 °C. Clay Miner. 40, 63–66.
Senko, J., Bertel, D., Quick, T., Burgos, W., 2011. The influence of phototrophic biomass on Fe and S redox cycling in an acid mine drainage-impacted system. Mine Water Environ. 30 (1), 38–46.
Stookey, L.L., 1970. Ferrozine – a new spectrophotometric reagent for iron. Anal. Chem. 42 (7), 779–781.
Toran, L., Hughes, B., Nyquist, J., Ryan, R., 2012. Using hydrogeophysics to monitor change in hyporheic flow around stream restoration structures. Environ. Eng. Geosci. 18 (1), 83–97.
Veysey Ii, J., Goldenfeld, N., 2008. Watching rocks grow. Nat. Phys. 4 (4), 310–313.
Ward, A.S., Gooseff, M.N., Singha, K., 2010. Imaging hyporheic zone solute transport using electrical resistivity. Hydrol. Process. 24 (7), 948–953.

PHILOSOPHICAL TRANSACTIONS OF THE ROYAL SOCIETY B

rstb.royalsocietypublishing.org

Review

Cite this article: Macalady JL, Hamilton TL, Grettenberger CL, Jones DS, Tsao LE, Burgos WD. 2013 Energy, ecology and the distribution of microbial life. Phil Trans R Soc B 368: 20120383.
http://dx.doi.org/10.1098/rstb.2012.0383

One contribution of 14 to a Discussion Meeting Issue 'Energy transduction and genome function: an evolutionary synthesis'.

Subject Areas:
microbiology, environmental science, ecology, bioinformatics

Keywords:
ecological niche, resource ratio theory, biogeography, biogeochemistry, environmental engineering, evolution

Author for correspondence:
Jennifer L. Macalady
e-mail: jlm80@psu.edu

†Present address: Department of Earth Sciences, University of Minnesota, Minneapolis, MN 55455, USA.

Royal Society Publishing
Informing the science of the future

Energy, ecology and the distribution of microbial life

Jennifer L. Macalady[1,2,3], Trinity L. Hamilton[1,2], Christen L. Grettenberger[1,3], Daniel S. Jones[1,2,†], Leah E. Tsao[1,2] and William D. Burgos[4]

[1]Department of Geosciences, Penn State University, University Park, PA 16802, USA
[2]Penn State Astrobiology Research Center (PSARC), Penn State University, University Park, PA 16802, USA
[3]Ecology Program, Penn State University, University Park PA 16802, USA
[4]Department of Civil and Environmental Engineering, Pennsylvania State University, University Park, PA 16802, USA

Mechanisms that govern the coexistence of multiple biological species have been studied intensively by ecologists since the turn of the nineteenth century. Microbial ecologists in the meantime have faced many fundamental challenges, such as the lack of an ecologically coherent species definition, lack of adequate methods for evaluating population sizes and community composition in nature, and enormous taxonomic and functional diversity. The accessibility of powerful, culture-independent molecular microbiology methods offers an opportunity to close the gap between microbial science and the main stream of ecological theory, with the promise of new insights and tools needed to meet the grand challenges humans face as planetary engineers and galactic explorers. We focus specifically on resources related to energy metabolism because of their direct links to elemental cycling in the Earth's history, engineering applications and astrobiology. To what extent does the availability of energy resources structure microbial communities in nature? Our recent work on sulfur- and iron-oxidizing autotrophs suggests that apparently subtle variations in the concentration ratios of external electron donors and acceptors select for different microbial populations. We show that quantitative knowledge of microbial energy niches (population-specific patterns of energy resource use) can be used to predict variations in the abundance of specific taxa in microbial communities. Furthermore, we propose that resource ratio theory applied to micro-organisms will provide a useful framework for identifying how environmental communities are organized in space and time.

1. Introduction

For all or most of the past 4 Gyr, life on Earth has depended on the activity of single-celled micro-organisms that harvest chemical (redox) and light energy from the environment. The evolution of diverse and complex biochemical mechanisms to accomplish this, combined with the revolutionary chemical transformation of the Earth's surface environment and the inexorable trend towards higher levels of biological diversity make for one of the most compelling stories in science. However, many missing pages remain. Among the mysteries are the mechanisms that allow and maintain the enormous taxonomic complexity of contemporary microbial communities. This question is far from academic. Astrobiologists would like to know, for example, whether Earth-like life on other habitable planets would show a similar march towards complexity and diversity, and whether or not this march depends on the types and amounts of energy available for life to harvest. On an even more practical level, environmental engineers use knowledge of relationships between microbial taxa and resource availability to design systems to purify wastewater, produce fuels and feedstocks, harvest ores and remediate polluted environments. Genetic engineers, not to mention politicians and the general public, would like to know under what conditions a genetically engineered microbial strain is competitive or invasive in nature, and why. Last but not least, revenues

© 2013 The Author(s) Published by the Royal Society. All rights reserved.

from genetically modified 'stuff' including drugs, agriculture, enzymes and plastics exceed 1 per cent of US $ GDP, and as of 2009 were growing at 10–20% per year [1]. Given that most of the genetic and metabolic diversity on Earth lies within the Bacterial and Archaeal domains of life (prokaryotes), microbial machines and their genetic templates represent a rich storehouse of 'bioengineered' solutions optimized over billions of years of evolution.

Our goal in this contribution is to explore the role of environmental selection, specifically selection based on the availability of energy resources, in controlling the distribution of microbial life.

2. Current knowledge of microbial taxonomic and metabolic diversity

Mechanisms that govern the coexistence of multiple biological species have been studied intensively by ecologists since the turn of the nineteenth century. Ecologists have long studied the mechanisms that underpin the biodiversity of plants and animals. By contrast, only since the late twentieth century have microbiologists possessed the tools to adequately determine microbial population sizes and community composition in nature. The methodological limitations faced by microbial ecologists have been further compounded by the lack of an ecologically coherent species definition, the vast taxonomic and functional breadth of micro-organisms as well as their limited morphological diversity. These challenges led to a gap between microbiology and the main stream of ecological theory. The gap is now gradually narrowing due to the accessibility of powerful culture-independent molecular methods. The same methods have sustained an intense and still ongoing period of discovery of new microbial taxonomic diversity (figure 1). Despite the growing potential of environmental genetics and genomics approaches, the number of sequences for which no coherent physiological or metabolic information is available is large and growing ever larger with respect to cultivated micro-organisms. Madsen [3] estimate that the number of uncultured species may be 10 000 times that of the cultured minority. Among prokaryotic phyla (having small subunit (SSU) 16S rRNA sequence divergence equivalent to eukaryotic 'kingdoms' such as fungi, animals, plants, etc.) between one-third and one-half have no cultivated representatives [2,4,5]. These recent statistics offer a staggering vista of the Earth's extant microbial diversity and highlight our relative ignorance about metabolic traits across vast swathes of microbial taxonomic diversity.

Although the array of chemical and physical environments colonized by microbial life on Earth is remarkable, the number of microbial taxa already discovered far outnumber the variety of possible energy-yielding chemical and light-harvesting metabolisms that can be identified based on thermodynamic considerations [6–8]. Thus, future findings that taxa in the uncultivated majority perform existing (known) metabolisms will not be entirely surprising. Many such discoveries are to be expected based on the scarcity of the so-called missing metabolisms versus the vast number of uncultivated microbial taxa. These future discoveries will nonetheless facilitate advances in bioengineering and biotechnology, environmental and agricultural sciences, geomicrobiology and biogeochemistry as well as astrobiology.

Recent research on ammonia oxidation (figure 2) provides an example of how new links between energy metabolisms

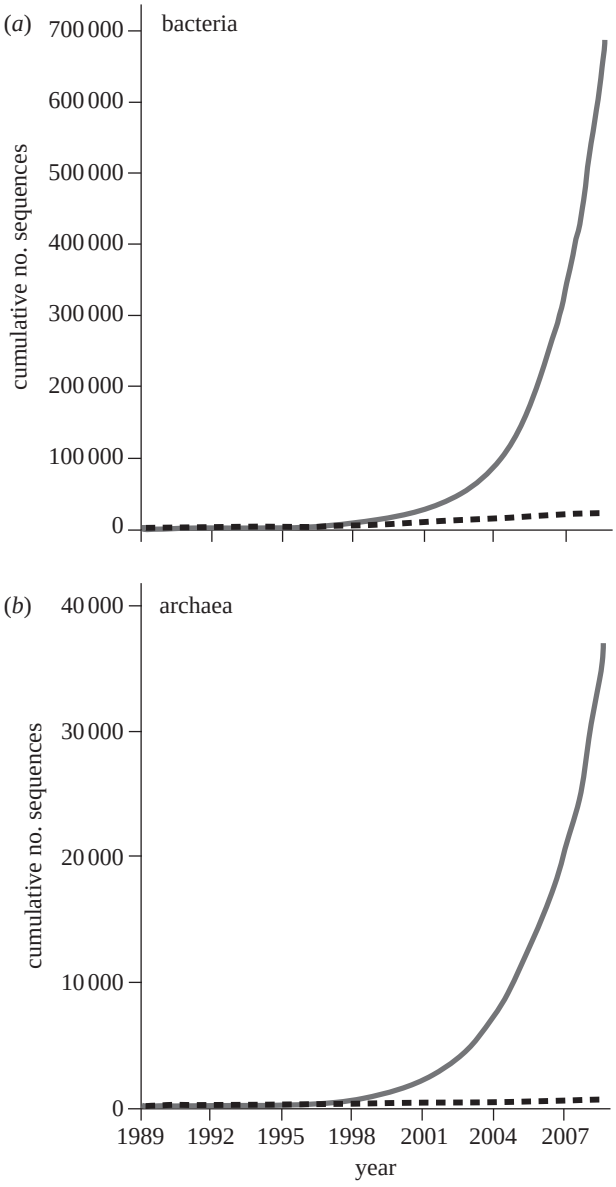

Figure 1. (*a*,*b*) Accumulation of biological sequence data in public databases originating from cultures versus environmental samples. Modified with permission from Pace [2]. Solid grey line denotes environmental; dashed line denotes cultured.

and microbial taxa spur advances in geobiology [10]. Although the fossil record of microbial life is considered poor, 'biosignatures' of past microbial life have been detected in rocks almost 4 Gyr old [10–13]. In addition to fossil cells and microbial biofilms (stromatolites), microbial biosignatures include hydrocarbons derived from cell membrane lipids, isotopic ratios of biologically processed elements such as C and N, and minerals produced as a result of biological activity or under the influence of microbial cells. Given sufficient data from the analysis of rocks, microbial physiology and nucleic acid as well as protein phylogenies, geobiologists have a chance to reconstruct the timing of the evolution of biogeochemical processes such as ammonia oxidation, including implications for the evolution of past Earth's environments. In practice, the scarcity and poor preservation of Archaean (more than 2.5 Ga) and Proterozoic (0.5–2.5 Ga) rocks may place limits on this exercise. Nonetheless, it is clear that an understanding of links between extant microbial diversity and the cycling of redox-active elements is

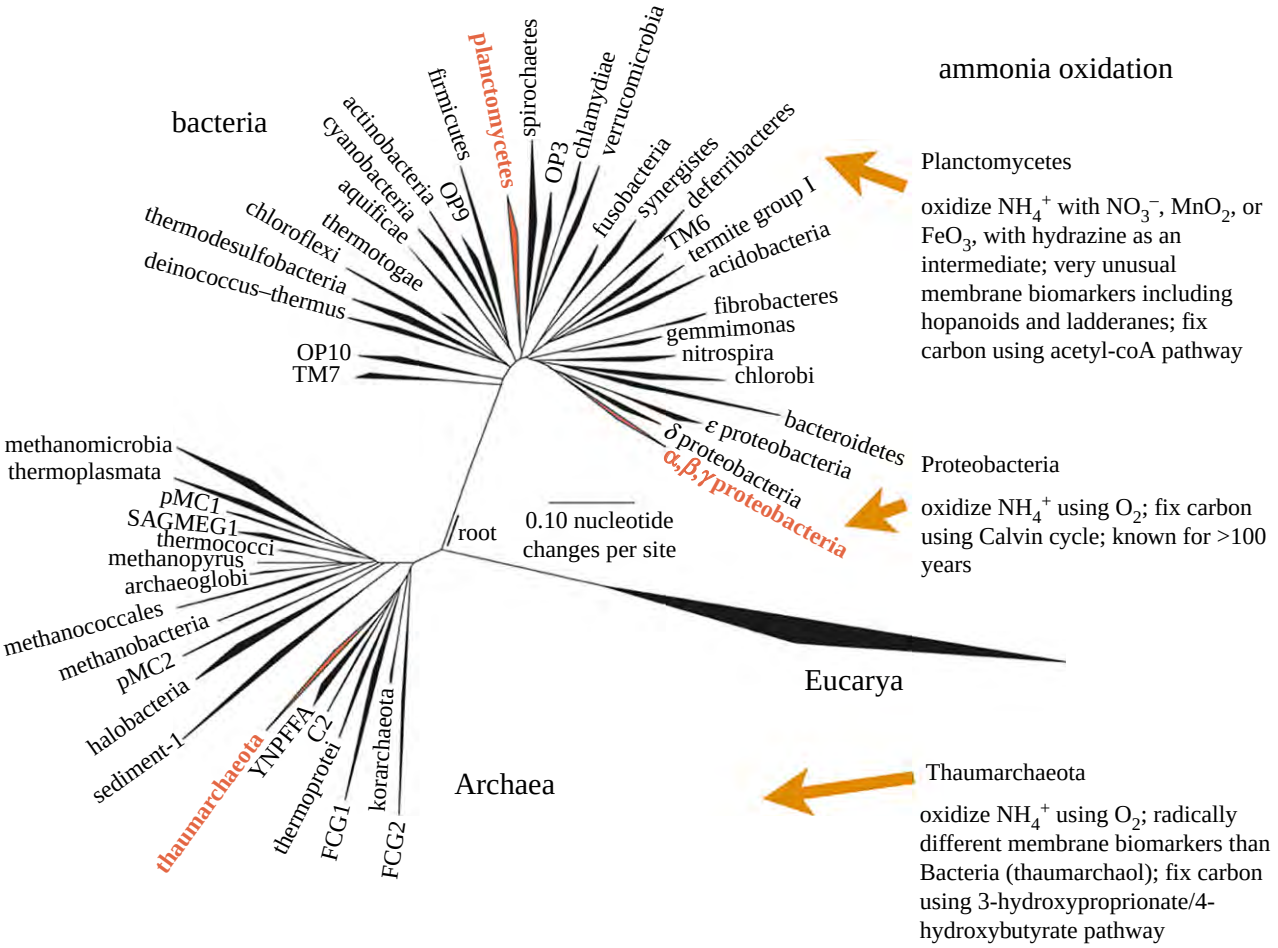

Figure 2. 16S rRNA gene phylogenetic tree illustrating lineages that contain canonical and recently discovered ammonia oxidizing prokaryotes. Highly divergent biosignatures associated with each group are shown, including organic biomarkers and carbon fixation pathways resulting in organic matter with different C isotopic ratios. Although the relative dominance of ammonia oxidizers from these lineages in the environment is still under investigation, one of the principal factors controlling the distribution of Thaumarchaeota versus Proteobacteria appears to be ammonium (electron donor) concentrations [9]. The relative abundance of Planctomycetes that carry out anaerobic ammonia oxidation, or 'annamox', is strongly governed by the availability of oxygen (electron acceptor). C2, FCG1, FCG2, OP3, OP9, OP10, pMC1, pMC2, SAGMEG1, sediment-1, TM6, TM7, termite group I, and YNPFFA represent candidate divisions with few or no cultured representatives [2,4,5]. (Online version in colour.)

essential to reconstructing Earth's history, and at present far from complete.

A more quantitative understanding of microbial distributions also has clear relevance for biotechnology and environmental engineering. Two examples related to iron oxidation serve to illustrate why. First, iron-oxidizing extreme acidophiles are used in metal extraction from low-grade ores (biomining), and have been heralded in biotechnology circles as the future of metal mining owing to the growing scarcity of high-grade ores that can be processed using conventional methods [14,15]. Members of the genera *Acidithiobacillus* and *Leptospirillum* (figure 3) are distantly related iron-oxidizing autotrophs with similar energy metabolisms but different evolutionary origins and physiological characteristics. Although *Acidithiobacillus* strains have served as model acidophiles for decades, *Leptospirillum* species have been studied only more recently. Genomic and genetic approaches including environmental omics [17–21] have begun to identify relationships between environmental parameters and *Acidithiobacillus* and *Leptospirillum* population distributions in natural and engineered systems [16,22]. These investigations are a first step toward engineering more efficient biomining operations.

Second, iron sulfides that are a major component of many metal ores are present in lower concentrations in coal deposits. They are also the source of persistent and globally significant environmental degradation in the form of acid mine drainage (AMD). The northern Appalachian Plateau of the eastern United States contains more than 8000 km of streams affected by acidic and heavy-metal laden drainage from abandoned coal mines (figure 4; [23]). Cost-effective treatment technologies for the remediation of these geographically dispersed and often remote sites are desperately needed. Conventional passive limestone treatment beds neutralize acidic water but promote the precipitation of Fe(III) oxides that coat the limestone surfaces ('armouring') and hydraulically clog the bed, requiring costly and frequent interventions to maintain treatment efficiency. A promising solution to this dilemma is to promote biological Fe oxidation at low pH, so that Fe(III) minerals precipitate before AMD reaches the limestone bed. At the relevant pH values (1.5–4.5), abiotic iron oxidation is kinetically inhibited and catalysed by acidophilic Fe-oxidizing bacteria [24–27].

Naturally occurring and engineered low-pH iron oxidation sites display a wide variety of physical, chemical and microbiological characteristics and have variable iron-removal efficiencies. For example, Heinzel *et al.* [28] found that specific iron oxidation rates in AMD treatment systems varied with the dominant microbial population, and Brown *et al.* [29] found that AMD sediment-hosted microbial communities

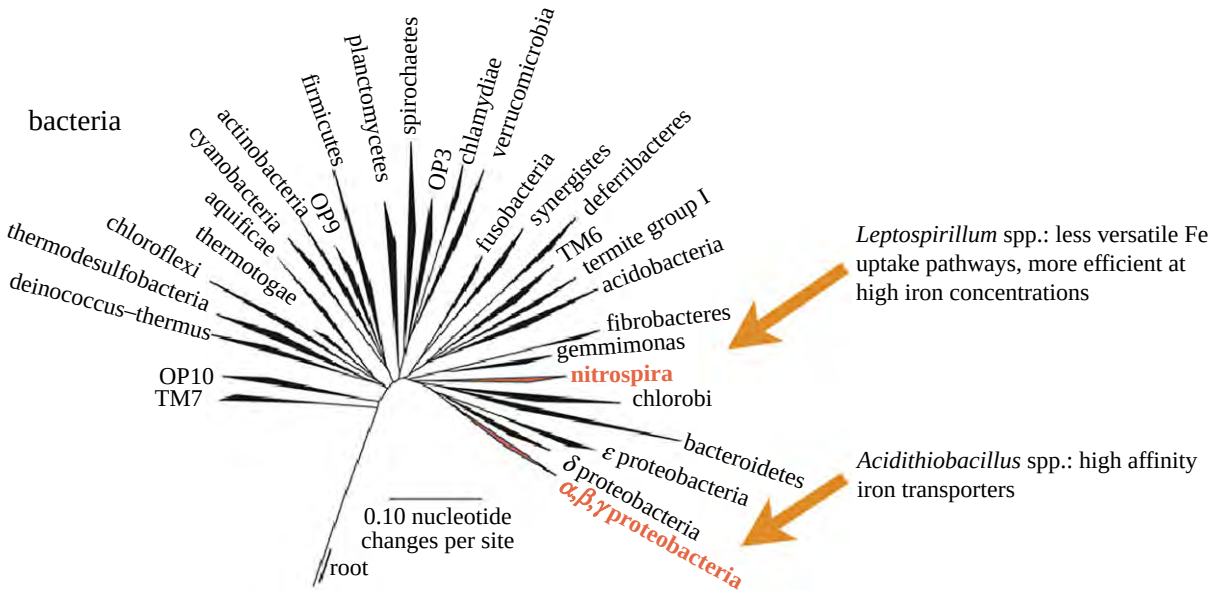

Figure 3. 16S rRNA gene phylogenetic tree illustrating two lineages that contain extremely acidophilic iron-oxidizing lithoautotrophs. Niches and ecological successions between biomining and bioleaching micro-organisms can be at least partially explained by changes in iron availability [16]. OP3, OP9, OP10, TM6, TM7, and termite group I represent candidate divisions with few or no cultured representatives [2,4,5]. (Online version in colour.)

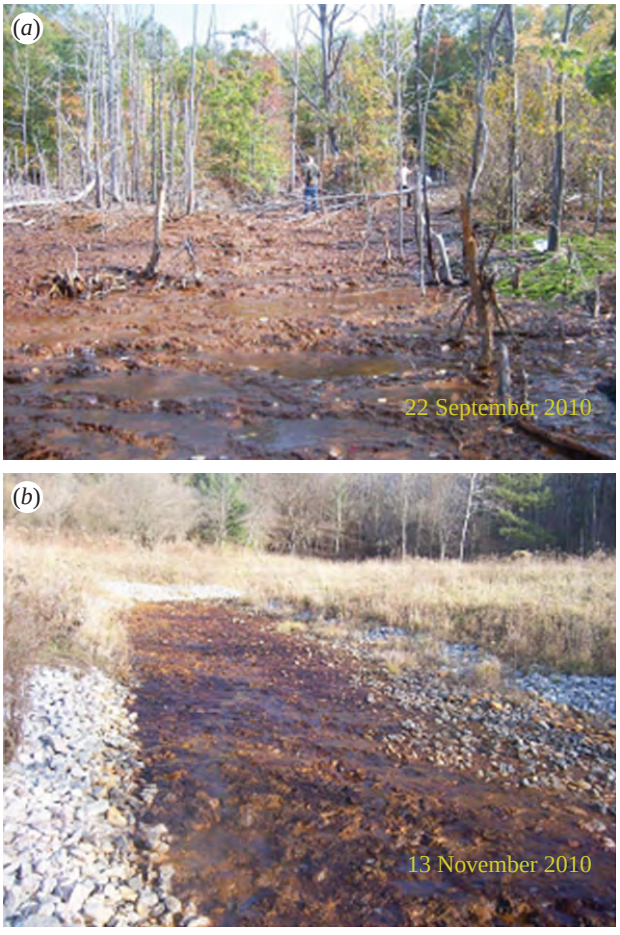

Figure 4. A natural iron oxide mound at Brubaker Run, Cambria County, PA (*a*), and an engineered 'oxidation/precipitation channel' at Dents Run, Elk County, PA (*b*). In both systems, the accumulation of Fe(III) minerals is due to low-pH Fe(II) oxidation by micro-organisms. (Online version in colour.)

dominated by *Ferrovum* spp. exhibited iron oxidation rates roughly twice that of sediments dominated by *Acidithiobacillus* spp. located nearby. Identifying the parameters that control the distribution of organisms with similar but ecologically differentiated patterns of resource use (in this case iron) is the first step in engineering AMD treatment systems that select for the desired microbial populations. These data underscore the need for both phylogenetic and ecological information to understand environmental controls on microbial distribution, especially among phylogenetically diverse and physiologically distinct coexisting populations that use the same core energy metabolic reactions.

3. Microbial distributions in space and time

Predicting the distribution of microbial life in space and time is a fundamental goal of microbial ecology. This endeavour, called microbial biogeography, is informed by a long tradition of research on macroscopic organisms in animal and plant communities [30–33], and more recently by a stimulating decade of biogeographic research specifically targeting microbial communities. According to current theory, a variety of contemporary and historical processes contribute to observed patterns in the spatial and temporal distributions of microbial populations. These processes include mutation, selection, dispersal and drift, and are expertly reviewed from a microbiology point of view by Martiny *et al.* [34] and Hanson *et al.* [35]. Historical processes include lingering effects of past environmental selection, distinct local histories of colonization and speciation, and dispersal barriers that restrict the flow of propagules to otherwise suitable habitats. To what degree does contemporary environmental selection drive distribution of contemporary microbial life? Although it is abundantly clear that historical processes are relevant for micro-organisms as well as macro-organisms [36,37], environmental selection appears to be more important over small spatial scales, and possibly overall [35,37,38]. Nonetheless, we stress that environmental selection is one of several independently operating contemporary and historical processes that potentially contribute to observed microbial biogeographic patterns.

The relationship between a species or population and contemporary environmental conditions is embodied by the concept of an ecological niche. A niche is defined as

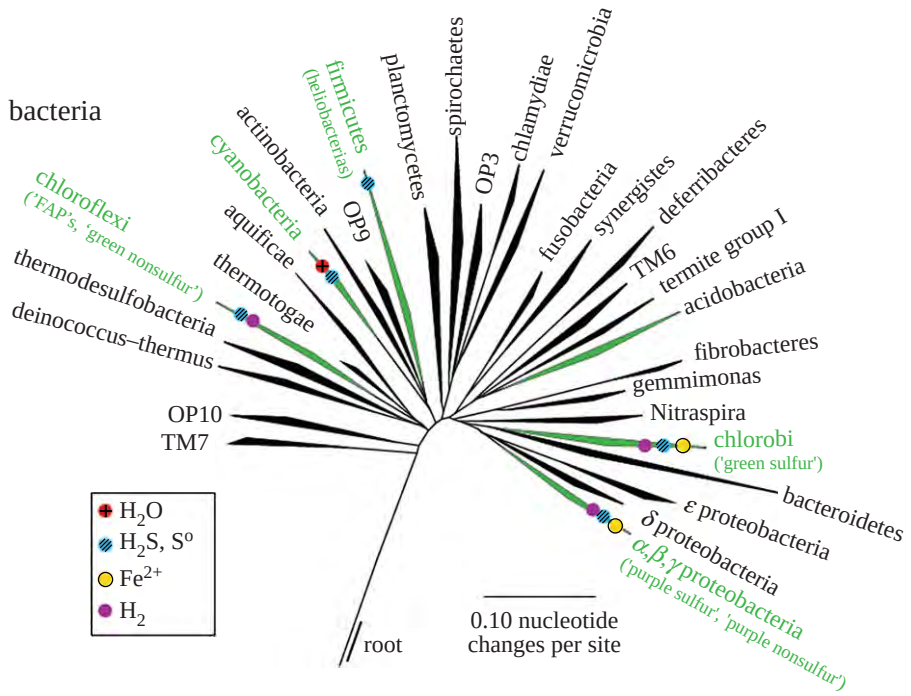

Figure 5. 16S rRNA gene phylogenetic tree illustrating lineages with representatives that harvest light energy using chlorophylls, i.e. chlorophototrophs, in green (not all members of these lineages are phototrophs). Reported photosynthetic electron donors are indicated by coloured dots. Pigment absorption spectra and carbon and nitrogen metabolism vary widely among phototrophs [46,47], indicating differential patterns of energy resource utilization at a variety of taxonomic scales. Notwithstanding significant evidence for lateral gene transfer among phototrophic lineages [48,49], some patterns of resource use are conserved within lineages that likely diverged billions of years ago [50–52]. OP3, OP9, OP10, TM6, TM7 and termite group I represent candidate divisions with few or no cultured representatives [2,4,5]. (Online version in colour.)

'the limits, for all important environmental features, within which individuals of a species can survive, grow and reproduce' [39, p. 31]. There is a notable tendency for coexisting taxa in communities to have different niche requirements, a phenomenon which has been termed variably 'niche separation', 'niche differentiation', 'niche segregation' or 'niche partitioning'. Niche separation is one of the processes commonly invoked to explain the enormous complexity of natural microbial communities, and yet is rarely explored in studies of micro-organisms in nature. It is useful to distinguish between theoretical niches, which conform to the definition above, and 'realized' niches, which correspond to the niche space occupied by a population in a specific environmental context. Inasmuch as environmental features may be said to include predators, phages and competing microbial populations, these definitions largely converge, but may lead to the observation that members of a given taxon occupy slightly different regions of their theoretical niche space in the environment depending on variations in community assembly and the taxonomic resolution of the methods used to gather data on microbial distributions.

The separation of microbial taxa into different niches is assumed to be a result of natural selection that drives competing populations into different patterns of resource use, such that they can coexist. This process has been observed in laboratory experiments [40], as well as in the environment [41,42]. Because relatively minor genetic changes are required to confer new phenotypes [43], small evolutionary steps are ecologically significant but not detectable using methods commonly used in environmental microbiology such as small subunit (SSU) rRNA gene cloning, pyrotags and fluorescence *in situ* hybridization (FISH). Enormous ecological complexity clearly exists within taxa having more than 97 per cent 16S rRNA gene similarity, the most common sequence similarity cut-off for microbial 'species', as well as among populations sharing identical 16S rRNA gene sequences [42,44,45]. The occurrence of ecologically distinct populations within taxa sharing high levels of 16S rRNA gene similarity appears to be the rule rather than the exception. Contemporary environmental selection-driving niche separation among closely related taxa (within-'species') is thus likely to be significant, and requires sensitive genetic and/or genomic methods to resolve.

However, niche separation observed in extant microbial communities is not exclusively due to adaptation and selection on closely related populations after communities are assembled. Environmental selection for differential resource use in the evolutionary past has led in some cases to stable and separate patterns of resource use in descendants of the original populations. Broad taxonomic patterns in energy-harvesting metabolisms are familiar and robust, including sulfate reduction in the *Deltaproteobacteria*, methanogenesis in Archaea and chlorophyll-based phototrophy (shown in figure 5), among others. Species with complementary patterns of energy resource use can thus be recruited from the environment, with the result that populations sharing similar energy resources in a given habitat may be distantly related to each other taxonomically. However, these qualitative patterns are not sufficient to predict the environmental distributions of genera, species, or populations.

4. Quantitative understanding of microbial niches

Given the inherent taxonomic and environmental complexity of natural microbial communities, quantitative frameworks to

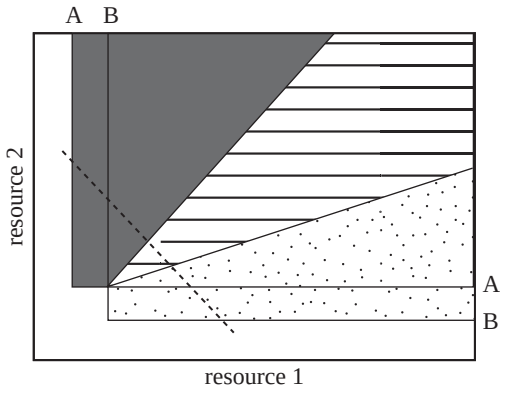

Figure 6. Illustration showing the basic features of resource ratio theory most relevant for autotrophs (after [54,56]). The field represents a range of habitats described by variations in the supply rates of two essential limiting resources (resource 1 and resource 2). Two populations (A and B) are shown that may be selectively enriched as a result of resource availability. Lines A–A and B–B represent zero net growth isoclines (ZNGI) for populations A and B. ZNGIs represent combinations of resources where growth rate is equal to death rate for each population. Below and to the left, population growth is negative. Population sizes are constant on the ZNGI. In the white area, no growth is observed for either population. In the grey area (high ratio of resource 2: resource 1), population A dominates, while in the stippled area (low ratio of resource 2: resource 1), population B is dominant. Populations A and B coexist in the striped area. The dashed line indicates the change in community structure as a function of changes in resource ratios [54,56].

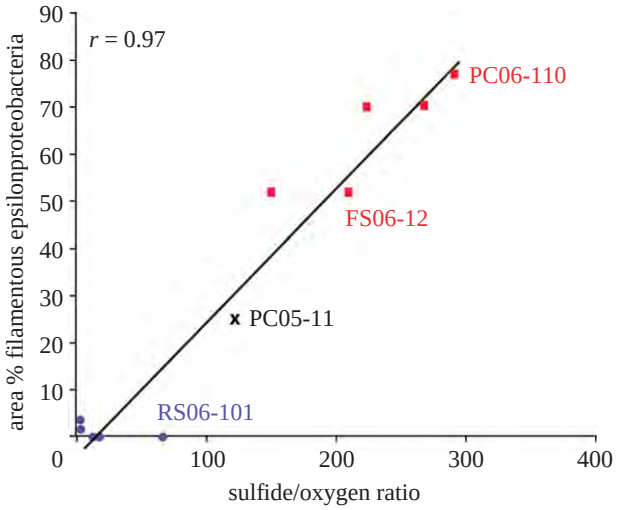

Figure 7. Correlation between dissolved sulfide : oxygen ratios and the abundance of cells hybridizing to a FISH (fluorescence *in situ* hybridization) probe targeting *Sulfurovumales* (filamentous Epsilonproteobacteria) in 12 biofilms from sulfidic cave groundwaters. Squares indicate biofilms with >50% *Sulfurovumales* biomass, whereas circles indicate biofilms dominated by *Thiothrix* populations. The black x (PC05-11) represents a biofilm comprised primarily of as-yet unidentified micro-organisms (not *Thiothrix* or *Sulfurovumales*), which likely have a distinct intermediate energy niche. Modified from Macalady *et al.* [59]. (Online version in colour.)

investigate patterns of microbial diversity and energy resource use are sorely needed. Resource ratio theory (RRT) was elaborated by Tilman [53,54] based on earlier work by MacArthur [55] as an alternative to non-mechanistic models of competition between species. The model is designed to explore patterns of species dominance or coexistence that emerge from competition between species sharing multiple resources (figure 6). Resources in the model have defined supply rates, and increases in their availabilities increase the growth rates of the populations that consume them. A central assumption of the theory is that there are unavoidable trade-offs in the ways that populations meet the challenge of acquiring resources, and therefore that no population can be a superior competitor for all the shared resources.

In the years since RRT was proposed, it has been largely successful at predicting autotrophic (mainly plant and algal) species' dominance based on ratios of limiting resource availabilities [57]. Two decades ago, an excellent review of the applicability of RRT to microbial ecology [58] concluded that the predictions of RRT are consistent with a large body of microbial competition data, including both autotrophs and heterotrophs. Despite these encouraging prospects, the theory has not been significantly explored by other microbiologists, with very few exceptions [56].

Our recent work on sulfide-oxidizing autotrophs in groundwater biofilms is consistent with a central prediction of RRT, namely that population dominance varies with the ratio of resources' availabilities (figure 7). Our data showed that populations belonging to the *Sulfurovumales* clade (*Epsilonproteobacteria*) always dominated in groundwaters with sulfide : oxygen ratios greater than 150, whereas *Thiothrix* populations dominated in groundwaters with sulfide : oxygen ratios less than 100 (figure 7; [59]). Based on this pattern, we successfully predicted the dominance of *Sulfurovumales* populations in high sulfide : oxygen biofilms collected at much higher temperatures (45 °C compared with 13 °C) approximately 100 km distant [60]. Data from the existing literature did not allow further tests of the pattern, because previous studies did not incorporate both sulfide and oxygen concentration data and quantitative measures of population sizes. Phylogenetic analyses of the *Sulfurovumales* populations from our sample sites showed that the populations were distantly related within the clade, suggesting the adaptation to high sulfide : oxygen ratios in these organisms occurred in the distant evolutionary past (figure 8).

Similar work on iron-oxidizing autotrophs in AMD suggests that RRT will prove to be a useful starting point for further investigations into patterns of microbial energy resource use and other ecological niche dimensions. We examined the composition of sediment microbial communities ($n = 61$) from five AMD sites using FISH. At most sites, communities were dominated by either *Acidithiobacillus*, acidophilic *Gallionella*-like, or *Ferrovum* populations. The taxonomy of the dominant populations appears to be largely predictable based on pH and ferrous iron concentrations (figure 9). Like the *Sulfurovumales* populations mentioned earlier, *Gallionella*-like and *Ferrovum* populations at these AMD sites are uncultivated. A greater understanding of their ecology may explain why some naturally occurring AMD sites are efficient at low-pH iron removal while others are not. Future bioengineering systems might manipulate pH, iron concentrations or other factors related to niche separation among these populations to increase the rate of iron removal and treatment efficiency and decrease the cost of AMD treatment. While pH is not a resource and thus this niche model does not fit easily into RRT, pH controls many other chemical variables in AMD systems (thus a proxy for an undiscovered resource dimension), and may be a direct energy tax [62,63]. Future research will be aimed at unravelling these aspects of the model.

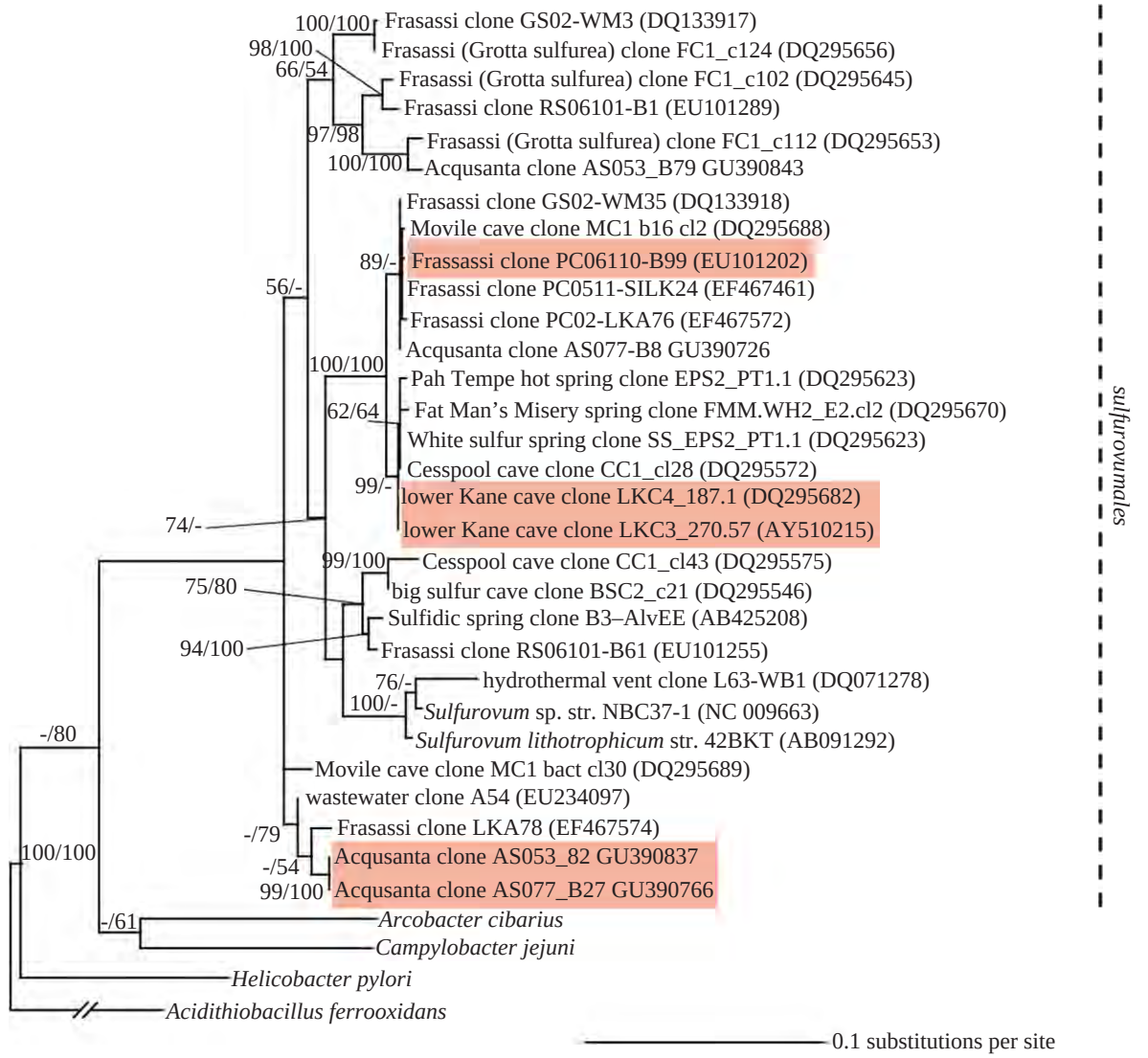

Figure 8. Maximum-likelihood phylogram of 16S rRNA sequences showing relationships among *Sulfurovumales* (*Epsilonproteobacteria*) clones retrieved from geographically distant sulfidic groundwaters in Italy and USA. Populations highlighted in red are known to be the dominant populations in waters with sulfide : oxygen ratios more than 150. Neighbour joining (left) and maximum parsimony (right) bootstrap values greater than 50 are shown for each node. Reprinted from Jones *et al*. [60], with permission. (Online version in colour.)

Although microbiologists rarely use RRT, aspects of the theory are inherent to microbial ecology and recent studies do ask whether coexisting populations have different niches with respect to energy resources. For example, Rocap *et al*. [64] found that *Prochlorococcus* genotypes have different optimum light intensities. Similarly, *Synechococcus* A/B types at Yellowstone hot springs are differently adapted to light quality and quantity [65]. Hatzenpichler [66] reviews literature suggesting that competition between bacterial and archaeal ammonia oxidizers is controlled by ammonium : oxygen ratios. Closely related sulfur-oxidizing autotroph populations within the genus *Achromatium* occupy different depth-defined sediment redox zones [67], which although not reported, would be expected to correlate with sulfide : oxygen ratios, iron availability and/or organic acid concentrations that would be expected to be essential resources for *Achromatium* growth. Based on these reports and our own research, we suggest that resources related to energy metabolism are a good place to begin mapping microbial niches, and that RRT should be explored in future studies.

We note in closing that other resources or even niche dimensions that may be difficult to assume within the framework of RRT are clearly also important for environmental selection. In our studies of sulfur-oxidizing autotrophs in sulfidic groundwater, *Beggiatoa* populations inhabited waters with a variety of sulfide : oxygen ratios (figure 7), but only in microenvironments with significantly slower water flow than *Thiothrix* and *Sulfurovumales* populations [59]. Fluid dynamical niche dimensions are often overlooked but have recently shown to be important for phytoplankton distributions in the ocean [68]. Temperature and pH have been shown to play an important role in niche separation in environments ranging from soils to hot springs. For example, although Yellowstone hot spring cyanobacteria show niche separation based on differential light adaptation (i.e. energy resource), temperature and presence/absence of phosphonate and phycocyanin (organic nutrient) acquisition pathways were also important niche dimensions controlling the distributions of *Synechococcus* strains and other phototrophs within microbial mats [65,69].

5. Conclusions

Continuing rapid taxonomic discovery enabled by molecular methods has revealed many new microbial phyla with no

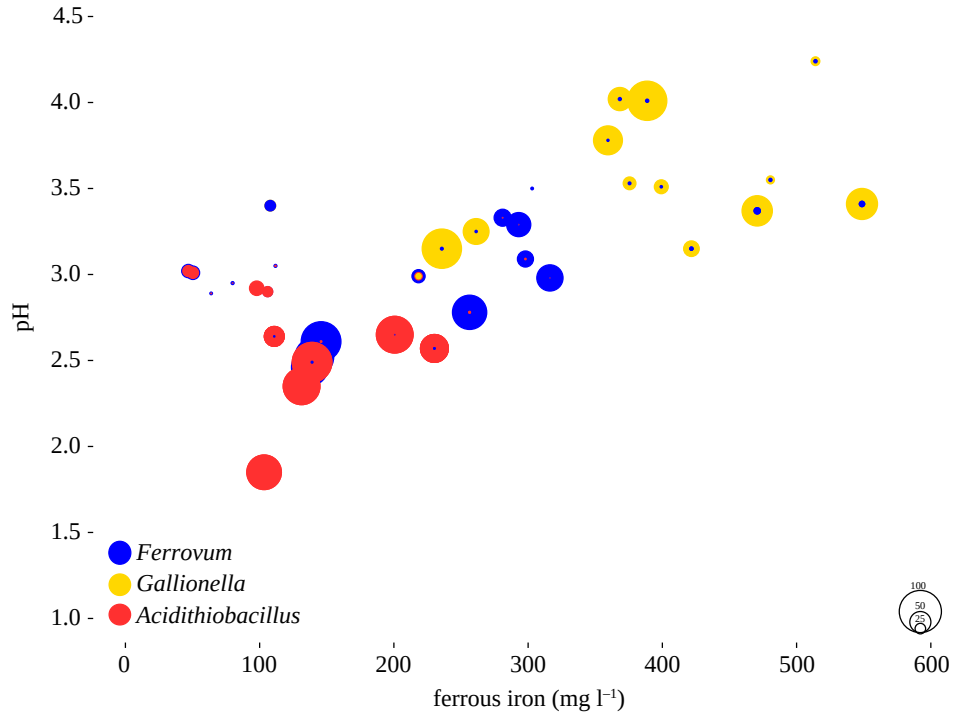

Figure 9. Dominant iron-oxidizing acidophiles in $n = 61$ microbial communities from five AMD sites. Colours indicate three genus-level taxa common in the communities: *Ferrovum*, *Gallionella*-like and *Acidithiobacillus*. Symbol diameters are scaled to the percentage of the community represented by each genus as indicated by the key at lower right. Community compositions were determined using fluorescence *in situ* hybridization (FISH), informed by 16S rRNA gene cloning. Methods follow those described in Brown *et al*. [29]. (Online version in colour.)

cultivated representatives. Environmental omics approaches enhance our ability to learn about the physiology of these unfamiliar taxa, and will play an increasing role in the discovery of their metabolic potential. It is likely that most of these enigmatic micro-organisms will make use of light and redox energy resources similar to those used by better-known micro-organisms, because there are far more novel taxa than 'missing' energy-yielding redox or light-harvesting reactions. There are nonetheless strong scientific and societal motivations to explore the ecological niches of the uncultivated majority, which may be novel even if their energy resources, broadly speaking, are not. Future discoveries of the metabolic capabilities of novel microbial groups will have important implications for engineering, environmental science, biotechnology and interpreting organic, mineral, and isotopic biosignatures in the rock record of Earth history.

In addition to revealing metabolic traits in the uncultivated majority, genetic data are gradually closing gaps between ecological theory and microbiology, and enable testing of ecological models and hypotheses in the absence of a defined microbial species concept. We suggest that RRT provides a useful and quantitative framework for exploring how energy resource availability in the environment controls the distributions of microbial populations and groups. One of the main predictions of RRT, that population dominance varies with the ratio of the availability of two or more essential limiting resources, is supported by our recent work on sulfur- and iron-oxidizing lithoautotrophs.

We are grateful to the Royal Society and to symposium organizers John Allen, Nick Lane and John Raven for their patience and encouragement during the preparation of this manuscript, and to external reviewers whose input substantially improved the manuscript. This research was supported by grants to J.L.M. from the National Science Foundation and the U.S. Department of Energy Joint Genome Institute, to J.L.M. and W.B. from the U.S. Department of Interior Office of Surface Mining, by the Penn State Astrobiology Research Center (PSARC, a node of the NASA Astrobiology Institute, NNA09DA76A), by a Penn State Biogeochemistry Programme fellowship to C.L.M., and by a NASA Astrobiology Institute postdoctoral fellowship to T.L.H. We thank J. Amend and L. Polerecky for interesting discussions about microbial niches, and undergraduate researchers J. Patel, A. Pearce, D. Mills and C. Kolesar for their enthusiasm and contributions to research on this topic in the Penn State geomicrobiology laboratory. J.L.M and D.S.J. especially thank A. Montanari at the Osservatorio Geologico di Coldigioco, S. Carnevali, S. Cerioni, S. Galdenzi, M. Mainiero and S. Mariani along with numerous members of the Gruppo Speleologico C.A.I. di Fabriano for years of collaboration during the exploration of sulfur-dependent microbial life in Italian sulfidic caves.

References

1. Carlson R. 2009 *The new biofactories in what matters.* McKinsey Quarterly. New York, NY: McKinsey and Company. See http://whatmatters.mckinseydigital.com/biotechnology/the-new-biofactories.
2. Pace NR. 2009 Mapping the tree of life: progress and prospects. *Mol. Microbiol. Rev.* **73**, 565–576. (doi:10.1128/MMBR.00033-09)
3. Madsen EL. 2008 *Environmental microbiology: from genomes to biogeochemistry*. Malden, MA: Blackwell Publishing.
4. Hugenholtz P. 2002 Exploring prokaryotic diversity in the genomic era. *Genome Biol.* **3**, 1–8. (doi:10.1186/gb-2002-3-2-reviews0003)
5. Rappe MS, Giovannoni SJ. 2003 The uncultured microbial majority. *Annu. Rev. Microbiol.* **57**, 369–394. (doi:10.1146/annurev.micro.57.030502.090759)
6. Shock EL, Holland ME. 2007 Quantitative habitability. *Astrobiology* **6**, 839–851. (doi:10.1089/ast.2007.0137)

7. Müller S, Strous M. 2011 Continuous cultivation and thermodynamic aspects of niche definition in the nitrogen cycle. *Methods Enzymol.* **486**, 33–52. (doi:10.1016/S0076-6879(11)86002-7)
8. Amend J, Shock EL. 2001 Energetics of overall metabolic reactions of thermophilic and hyperthermophilic Archaea and Bacteria. *FEMS Microbiol. Rev.* **25**, 175–243. (doi:10.1016/S0168-6445(00)00062-0)
9. Hatzenpichler R, Lebedeva EV, Spieck E, Stoecker K, Richter A, Daims H, Wagner M. 2008 Diversity and mode of transmission of ammonia-oxidizing archaea in marine sponges. *Environ. Microbiol.* **10**, 1087–1094. (doi:10.1111/j.1462-2920.2007.01515.x)
10. Shen Y, Buick R, Canfield DE. 2004 Isotopic evidence for microbial sulphate reduction in the early Archaean era. *Nature* **410**, 77–81. (doi:10.1038/35065071)
11. Rosing MT, Frei R. 2004 U-rich Archaean sea-floor sediments from Greenland – indications of >3700 Ma oxygenic photosynthesis. *Earth Planet. Sci. Lett.* **217**, 237–244. (doi:10.1016/S0012-821X(03)00609-5)
12. Van Kranendonk MJ. 2006 Volcanic degassing, hydrothermal circulation and the flourishing of early life on Earth: a review of the evidence from c. 3490–3240 Ma rocks of the Pilbara supergroup, Pilbara Craton, Western Australia. *Earth-Sci. Rev.* **74**, 197–240. (doi:10.1016/j.earscirev.2005.09.005)
13. Wacey D, Kilburn MR, Saunders M, Cliff J, Brasier MD. 2011 Microfossils of sulphur-metabolizing cells in 3.4-billion-year-old rocks of Western Australia. *Nat. Geosci.* **4**, 698–702. (doi:10.1038/ngeo1238)
14. Johnson DB. 2013 Development and application of biotechnologies in the metal mining industry. *Environ. Sci. Pollut. Res.* (doi:10.1007/s11356-013-1482-7)
15. Fecht S. 2011 Microbe miners: bacteria extract metals and clean up the mess afterward. *Sci. Am.* **305**, 46. (doi:10.1038/scientificamerican1211-46b)
16. Osorio H, Martínez V, Veloso FA, Pedroso I, Valdés J, Jedlicki E, Holmes DS, Quatrini R. 2008 Iron homeostasis strategies in acidophilic iron oxidizers: studies in *Acidithiobacillus* and *Leptospirillum*. *Geochim. Cosmochim. Acta* **94**, 175–179. (doi:10.1016/j.hydromet.2008.05.038)
17. Tyson GW *et al*. 2004 Community structure and metabolism through reconstruction of microbial genomes from the environment. *Nature* **428**, 37–43. (doi:10.1038/nature02340)
18. Ram RJ, VerBerkmoes NC, Thelen MP, Tyson GW, Baker BJ, Blake RC, Shah M, Hettich RL, Banfield JF. 2005 Community proteomics of a natural microbial biofilm. *Science* **308**, 1915–1920. (doi:10.1126/science.1109070)
19. Denef VJ, Mueller RS, Banfield JF. 2010 AMD biofilms: using model communities to study microbial evolution and ecological complexity in nature. *ISME J.* **18**, 1–12. (doi:10.1038/ismej.2009.158)
20. Mueller RS, Dill BD, Pan C, Belnap CP, Thomas BC, VerBerkmoes NC, Hettich RL, Banfield JF. 2011 Proteome changes in the initial bacterial colonist during ecological succession in an acid mine drainage biofilm community. *Geobiology* **138**, 2279–2292. (doi:10.1111/j.1462-2920.2011.02486.x)
21. Xie J, He Z, Liu X, Liu X, Van Nostrand JD, Deng Y, Wu L, Zhou J, Qiu G. 2011 GeoChip-based analysis of the functional gene diversity and metabolic potential of microbial communities in acid mine drainage. *Appl. Environ. Microbiol.* **3**, 991–999. (doi:10.1128/AEM.01798-10)
22. Quatrini R, Jedlicki E, Holmes DS. 2005 Genomic insights into the iron uptake mechanisms of the biomining microorganism *Acidithiobacillus ferrooxidans*. *J. Ind. Microbiol. Biotechnol.* **32**, 606–614. (doi:10.1007/s10295-005-0233-2)
23. Boyer J, Sarnoski B. 1995 *Progress report: statement of mutual intent strategic plan for the restoration and protection of streams and watersheds polluted by acid mine drainage from abandoned coal mines*. Philadelphia, PA: US EPA. See http://www.epa.gov/reg3giss/libraryp.htm.
24. Johnson DB, Kanao T, Hedrich S. 2012 Redox transformations of iron at extremely low pH: fundamental and applied aspects. *Front. Microbiol.* **3**, 1–13. (doi:10.3389/fmicb.2012.00096)
25. Baker BJ, Banfield JF. 2003 Microbial communities in acid mine drainage. *FEMS Microbiol. Ecol.* **4**, 139–152. (doi:10.1016/S0168-6496(03)00028-X)
26. Singer PC, Stumm W. 1970 Acid mine drainage: the rate-determining step. *Science* **167**, 1121–1123. (doi:10.1126/science.167.3921.1121)
27. Johnson DB, Hallberg KB. 2005 Acid mine drainage remediation options: a review. *Sci. Total Environ.* **338**, 3–14. (doi:10.1016/j.scitotenv.2004.09.002)
28. Heinzel E, Hedrich S, Janneck E, Glombitza F, Seifert J, Schloman M. 2009 Bacterial diversity in a mine water treatment plant. *Appl. Environ. Microbiol.* **75**, 858–861. (doi:10.1128/AEM.01045-08)
29. Brown JF, Jones DS, Mills DB, Macalady JL, Burgos WD. 2011 Application of a depositional *facies* model to an acid mine drainage site. *Appl. Environ. Microbiol.* **77**, 545–554. (doi:10.1128/AEM.01550-10)
30. Rosenzweig ML. 1995 *Species diversity in space and time*. Cambridge, UK: Cambridge University Press.
31. McGill B, Enquist B, Weiher E, Westboy M. 2006 Rebuilding community ecology from functional traits. *Trends Ecol. Evol.* **21**, 178–185. (doi:10.1016/j.tree.2006.02.002)
32. Westboy M, Wright IJ. 2006 Land-plant ecology on the basis of functional traits. *Trends Ecol. Evol.* **5**, 261–268. (doi:10.1016/j.tree.2006.02.004)
33. Shipley B, Vile D, Garnier E. 2006 From plant traits to plant communities: a statistical mechanistic approach to biodiversity. *Science* **314**, 812–814. (doi:10.1126/science.1131344)
34. Martiny JBH *et al*. 2006 Microbial biogeography: putting microorganisms on the map. *Nat. Rev. Microbiol.* **4**, 102–112. (doi:10.1038/nrmicro1341)
35. Hanson CA, Fuhrman JA, Horner-Devine MC, Martiny JBH. 2012 Beyond biogeographic patterns: processes shaping the microbial landscape. *Nat. Rev. Microbiol.* **10**, 497–506. (doi:10.1038/nrmicro2795)
36. Ramette A, Tiedje JM. 2007 Biogeography: an emerging cornerstone for understanding prokaryotic diversity, ecology, and evolution. *Microb. Ecol.* **53**, 197–207. (doi:10.1007/s00248-005-5010-2)
37. Whitaker RJ. 2006 Allopatric origins of microbial species. *Phil. Trans. R. Soc. B.* **361**, 1975–1984. (doi:10.1098/rstb.2006.1927)
38. Kuang JL, Huang LN, Chen LX, Hua ZS, Li SJ, Hu M, Li JT, Shu WS. 2013 Contemporary environmental variation determines microbial diversity patterns in acid mine drainage. *ISME J.* **7**, 1038–1050. (doi:10.1038/ismej.2012.139)
39. Begon M, Townsend CR, Harper JL. 2006 *Ecology: from individuals to ecosystems*, 2nd edn. Malden, MA: Blackwell Publishing.
40. Rainey PB, Travisano M. 1998 Adaptive radiation in a heterogeneous environment. *Nature* **394**, 69–72. (doi:10.1038/27900)
41. Stomp M, Huisman J, de Jongh F, Veraart AJ, Gerla D, Rijkeboer M, Ibelings BW, Wollenzien UIA, Stal LJ. 2004 Adaptive divergence in pigment composition promotes phytoplankton biodiversity. *Nature* **432**, 104–107. (doi:10.1038/nature03044)
42. Denef VJ, Banfield JF. 2012 *In situ* evolutionary rate measurements show ecological success of recently emerged bacterial hybrids. *Science* **336**, 462–466. (doi:10.1126/science.1218389)
43. Blount ZD, Barrick JE, Davidson CJ, Lenski RE. 2012 Genomic analysis of a key innovation in an experimental *Escherichia coli* population. *Nature* **7417**, 513–518. (doi:10.1038/nature11514)
44. Becraft ED, Cohan FM, Kuhl M, Jensen SI, Ward DM. 2011 Fine-scale distribution patterns of synechococcus ecological diversity in microbial mats of mushroom spring, Yellowstone National Park. *Appl. Environ. Microbiol.* **77**, 689–697. (doi:10.1128/AEM.05927-11)
45. Denef VJ, Kalnejais LH, Mueller RS, Wilmes P, Baker BJ, Thomas BC, VerBerkmoes NC, Hettich RL, Banfield JF. 2010 Proteogenomic basis for ecological divergence of closely related bacteria in natural acidophilic microbial communities. *Proc. Natl Acad. Sci. USA* **107**, 2383–2390. (doi:10.1073/pnas.0907041107)
46. Overmann J, Garcia-Piche IF. 2006 *The phototrophic way of life*. In *The prokaryotes*. (eds M Dworkin, S Falkow, E Rosenburg, KH Schleifer, E Stackebrandt), pp. 32–85, 3rd edn. New York, NY: Springer Science.
47. Maresca JA, Graham JE, Bryant DA. 2008 The biochemical basis for structural diversity in the carotenoids of chlorophototrophic bacteria. *Photosynth. Res.* **97**, 121–140. (doi:10.1007/s11120-008-9312-3)
48. Hohmann-Marriott MF, Blankenship RE. 2011 Evolution of photosynthesis. *Annu. Rev. Plant Biol.* **62**, 515–548. (doi:10.1146/annurev-arplant-042110-103811)
49. Raymond J, Zhaxybayeva O, Gogarten JP, Gerdes SY, Blankenship RE. 2002 Whole-genome analysis of photosynthetic prokaryotes. *Science* **298**, 1616–1620. (doi:10.1126/science.1075558)
50. Olson JM, Pierson BK. 1987 Origin and evolution of photosynthetic reaction centers. *Orig. Life* **17**, 419–430. (doi:10.1007/BF02386479)

51. Xiong J, Fischer WM, Inoue K, Nakahar M, Bauer C. 2000 Molecular evidence for the early evolution of photosynthesis. *Science* **289**, 1724–1730. (doi:10.1126/science.289.5485.1724)
52. Blankenship RE. 2010 Early evolution of photosynthesis. *Plant Physiol.* **154**, 434–438. (doi:10.1104/pp.110.161687)
53. Tilman D. 1977 Resource competition between plankton algae: an experimental and theoretical approach. *Ecology* **58**, 338–348. (doi:10.2307/1935608)
54. Tilman D. 1980 Resources: a graphical-mechanistic approach to competition and predation. *Am. Nat.* **16**, 362–393. (doi:10.1086/283633)
55. MacArthur RH. 1972 *Geographical ecology. Patterns in the distribution of species*. New York, NY: Harper and Row.
56. Curtis TP, Head IM, Graham DW. 2003 Are we standing on the threshold of a renaissance in designing biological systems? *Environ. Sci. Technol.* **37**, 64A–70A. (doi:10.1021/es0323493)
57. Miller TE, Burns JH, Munguia P, Walters EL, Kneitel JM, Richards PM, Mouquet N, Buckley HL. 2005 A critical review of twenty years' use of the resource-ratio theory. *Am. Nat.* **165**, 439–448. (doi:10.1086/428681)
58. Smith VH. 1993 Applicability of resource-ratio theory to microbial ecology. *Limnol. Oceanogr.* **38**, 239–249. (doi:10.4319/lo.1993.38.1.0239)
59. Macalady JL, Dattagupta S, Schaperdoth I, Jones DS, Druschel GK, Eastman D. 2008 Niche differentiation among sulfur-oxidizing bacterial populations in cave waters. *ISME J.* **2**, 590–601. (doi:10.1038/ismej.2008.25)
60. Jones DS, Tobler DJ, Schaperdoth I, Mainiero M, Macalady JL. 2010 Community structure of subsurface biofilms in the thermal sulfidic caves of Acquasanta Terme, Italy. *Appl. Environ. Microbiol.* **76**, 5902–5910. (doi:10.1128/AEM.00647-10)
61. Messerli MA, Amaral-Zettler LA, Zettler E, Jung SK, Smith PJS, Sogin ML. 2005 Life at acidic pH imposes an increased energetic cost for a eukaryotic acidophile. *J. Exp. Biol.* **208**, 2569–2579. (doi:10.1242/jeb.01660)
62. Krulwich TA, Sachs G, Padan E. 2011 Molecular aspects of bacterial pH sensing and homeostasis. *Nat. Rev. Microbiol* **9**, 330–343. (doi:10.1038/nrmicro2549)
63. Rocap G *et al*. 2003 Genome divergence in two *Prochlorococcus* ecotypes reflects oceanic niche differentiation. *Nature* **424**, 1042–1047. (doi:10.1038/nature01947)
64. Ward DM, Castenholz RW, Miller SR. 2012 Cyanobacteria in geothermal habitats. In *Ecology of cyanobacteria. II. Their diversity in space and time* (ed. BA Whitton), pp. 39–62. Berlin, Germany: Springer.
65. Hatzenpichler R. 2012 Diversity, physiology and niche differentiation of ammonia-oxidizing archaea. *Appl. Environ. Microbiol.* **78**, 7501–7510. (doi:10.1128/AEM.01960-12)
66. Gray ND, Howarth R, Rowan A, Pickup RW, Jones JG, Head IM. 1999 Natural communities of *Achromatium oxaliferum* comprise genetically, morphologically, and ecologically distinct subpopulations. *Appl. Environ. Microbiol.* **65**, 5089–5099.
67. d'Ovidio F, De Monte S, Alvain S, Dandanneau Y, Levy M. 2010 Fluid dynamical niches of phytoplankton types. *Proc. Natl Acad. Sci. USA* **107**, 18 366–18 370. (doi:10.1073/pnas.1004620107)
68. Boyd ES, Fecteau KM, Havig JR, Shock EL, Peters JW. 2012 Modeling the habitat range of phototrophs in Yellowstone National Park: Toward the development of a comprehensive fitness landscape. *Front. Microbiol.* **3**, 221. (doi:10.3389/fmicb.2012.00221)

Applied Geochemistry 47 (2014) 85–98

Contents lists available at ScienceDirect

Applied Geochemistry

journal homepage: www.elsevier.com/locate/apgeochem

Rates of low-pH biological Fe(II) oxidation in the Appalachian Bituminous Coal Basin and the Iberian Pyrite Belt

Lance N. Larson [a,1,*], Javier Sánchez-España [b], William Burgos [a]

[a] Department of Civil and Environmental Engineering, The Pennsylvania State University, University Park, PA 16802, United States
[b] Instituto Geológico y Minero de España (IGME), Tres Cantos, Spain

ARTICLE INFO

Article history:
Available online 23 May 2014
Editorial handling by M. Kersten

ABSTRACT

Low-pH Fe(II) oxidation can be exploited for the treatment of acid mine drainage (AMD). However, natural or engineered terraced iron formations (TIFs) are underutilized for AMD treatment because of uncertainties with respect to treatment performance. To address this problem we measured the rates of Fe(II) oxidation multiple times at eight sites in the Appalachian Bituminous Coal Basin and at three sites in the Iberian Pyrite Belt (IPB). Longitudinal geochemical transects were measured downstream of emergent anoxic AMD sources. Water velocities were measured at each sampling location and used to transform concentration versus distance profiles into concentration versus travel time for kinetic analysis of field data. Zero-order Fe(II) oxidation rates ranged from 8.60 to 81.3 $\times 10^{-7}$ mol L^{-1} s^{-1} at the Appalachian sites and 13.1 to 67.9 $\times 10^{-7}$ mol L^{-1} s^{-1} at the IPB sites. First-order Fe(II) oxidation rate constants ranged from 0.035 to 0.399 min^{-1} at the Appalachian sites and 0.003 to 0.010 min^{-1} at the IPB sites. Faster rates of Fe(II) oxidation were measured at two sites (one in Appalachia and one in IPB) where the emergent pH values were the lowest and little to no oxidative precipitation of Fe(III) occurred. Laboratory-based rates of Fe(II) oxidation were measured with TIF sediments and emergent AMD collected from seven Appalachian sites. First-order laboratory rate constants normalized to sediment biomass concentrations (measured by phospholipid fatty acids; PLFA) were positively correlated to first-order field rate constants. Biomass composition was relatively similar between all sites, and predominately comprised of proteobacteria and general PLFAs. A zero-order lab-based removal rate for dissolved Fe(T) was used to calculate area-based design criteria of 2.6–8.7 g Fe day^{-1} m^{-2} (GDM) for both natural and engineered TIFs.
©2014 Elsevier Ltd. All rights reserved.

1. Introduction

Active and historical mining activities threaten ecosystems throughout the world. It is estimated that 95–99.999% of earth material from Cu, Pb, Zn, Au, and Ag mining operations becomes waste material (Nordstrom, 2011). Acid mine drainage (AMD) occurs when physical and chemical weathering of sulfides in mine ores facilitate proton releasing reactions (Kirby and Cravotta, 2005; Nordstrom et al., 1999). The ensuing pH drop enhances the solubility of metals such as iron (Fe), aluminum (Al), manganese (Mn), metalloids such as arsenic (As), and sulfate (SO_4^{2-}), resulting in hazardous or toxic concentrations transported into aquatic systems. Some of the most notorious mining-impacted environments are associated with metal mining, such as the Berkley Pit in Montana(Gammons et al., 2010; Pellicori et al., 2005), Iron Mountain, California (Druschel et al., 2004; Edwards et al., 1999; Nordstrom et al., 1999), and Rio Tinto, Spain (Cánovas et al., 2008; Gammons et al., 2008; Sánchez España et al., 2007b). In the Appalachian region of the United States, AMD is the number one source of pollution to waterways (Pennsylvania Department of Environmental Protection (DEP), 2010). Although overall water quality in central Pennsylvania has improved since the 1970s, AMD pollution still impairs approximately 1930 km of streams (Trout Unlimited, 2011).

The oxidation of Fe(II) and the subsequent precipitation of Fe(III) are key reactions for AMD treatment. The kinetics of abiotic Fe(II) oxidation at circumneutral pH has been modeled according to (Stumm and Morgan, 1996):

$$\frac{d[\mathrm{Fe(II)}]_{\leftarrow}}{dt} = -k_{\mathrm{abiotic}}[\mathrm{Fe(II)}][\mathrm{O_2}][\mathrm{H^+}]^{-2}_{\leftarrow} \quad (1)$$

where $k_{abiotic}$ is the Fe(II) oxidation rate constant ($time^{-1}$), [Fe(II)] is the concentration of dissolved ferrous iron (M), [O_2] is the concentration of dissolved oxygen (M), and [H^+] is the concentration of protons (M). Due to the exponent on the [H^+] term in Eq. (1), small

* Corresponding author. Address: Department of Civil and Environmental Engineering, The Pennsylvania State University, 212 Sackett Building, University Park, PA 16802, United States. Tel.: +1 202 513 6279.
E-mail address: llarson@nrdc.org (L.N. Larson).
[1] Current address: Natural Resources Defense Council, 1152 15th Street NW, Suite 300, Washington, DC 20005, United States.

http://dx.doi.org/10.1016/j.apgeochem.2014.05.012
0883-2927/©2014 Elsevier Ltd. All rights reserved.

changes in solution pH greatly influence the rate of Fe(II) oxidation (where rate increases sharply as pH increases). Below pH ~5, the spontaneous abiotic Fe(II) oxidation rate is slow, although it can be influenced by a number of anions, organic ligands, and certain minerals (Cornell and Schwertmann, 1996). Under acidic conditions (pH <~4), Fe(II) oxidation is catalyzed by acidophilic organisms (Hallberg, 2010) as Fe(II) becomes an energetically favorable electron donor for microorganisms (Hedrich et al., 2011). As acidophilic organisms oxidize Fe(II), Fe(III) will precipitate from solution as various minerals, typically schwertmannite [nominally $Fe_8O_8(OH)_6(SO_4)$] or ferrihydrite (Bigham et al., 1996; Burgos et al., 2012; Sánchez España et al., 2007b; Yu et al., 1999). The precipitation of Fe(III)-minerals results in the development of terraced iron formations (TIFs) and the removal of dissolved total Fe(T) from solution (Brown et al., 2010; DeSa et al., 2010; Sánchez España et al., 2007a). For the applied purpose of using TIFs for AMD treatment, it remains unclear how site-specific geochemistry, hydrology, seasonal variability, and microbial diversity influence field-scale low-pH Fe(II) oxidation rates.

Rate expressions for biologically-catalyzed low-pH Fe(II) oxidation proposed in the literature are variable, ranging from multi-parameter, *n*th-order expressions (Kirby et al., 1999; Pesic et al., 1989) to pseudo first-order or zero-order expressions (Chen and Jiang, 2012; Sánchez España et al., 2007a). For ponds designed to collect low-pH Fe(II)-rich AMD, Kirby et al. (1999) modeled biological Fe(II) oxidation according to:

$$d[\mathrm{Fe(II)}]/dt = -k_{\mathrm{bio}} C_{\mathrm{bact}} [\mathrm{Fe(II)}][\mathrm{O_2}][\mathrm{H^+}] \leftarrow \qquad (2)\leftarrow$$

where k_{bio} is the biological rate constant ($L^3\ mg^{-1}\ mol^{-2}\ s^{-1}$), C_{bact} is the concentration of iron-oxidizing bacteria (mg L^{-1}), and [ ] represents dissolved concentrations (mol L^{-1}). In contrast to abiotic Fe(II) oxidation, the rate of biological Fe(II) oxidation increases as pH decreases. At a site in Pennsylvania, rotating biological contactors (RBCs) were used to treat AMD and Fe(II) oxidation was observed to be first-order with respect to the influent Fe(II) concentration. Treatment efficiency increased with temperature and hydraulic residence time (Olem and Unz, 1977). Rates of Fe(II) oxidation measured in wetlands designed for AMD treatment were better fit using a first-order versus zero-order model (Tarutis et al., 1999). Rates of Fe(II) oxidation measured in the Iberian Pyrite Belt (IPB) have been reported to be zero-order (Sánchez España et al., 2007a). Sánchez España et al. (2007a) also measured zero-order rates of Fe(II) oxidation in corresponding laboratory experiments but found the field rates were almost an order of magnitude faster than the laboratory rates.

Detailed rate laws for biological Fe(II) oxidation have been developed from laboratory studies using pure cultures of Fe(II)-oxidizing bacteria. Pesic et al. (1989) constructed a model to describe Fe(II) oxidation rates by *Thiobacillus ferrooxidans* as a function of Fe(II), pH, dissolved oxygen, and cell concentration (Williamson et al., 2006). An energetics-based model for *T. ferrooxidans* growth was developed by accounting for carbon fixation rates through the Calvin-Benson cycle (Nagpal, 1997). Rates of Fe(II) oxidation by *Acidithiobacillus ferrooxidans* were enhanced when Fe(III) (hydr)oxide precipitation was inhibited, presumably due to Fe solids interfering with cell proton diffusion (Meruane and Vargas, 2003). It remains unclear how biotic Fe(II) oxidation models can be scaled to predict field performance.

The ability of TIFs to remove dissolved Fe via low-pH Fe(II) oxidation represents an attractive passive treatment technology as little to no external energy inputs are required. Design guidelines for TIF-based AMD treatment are currently nonexistent. Remediation design is limited because reported rates of low-pH Fe(II) oxidation are highly variable, often spanning three to four orders of magnitude at a fixed pH value (Kirby and Elder-Brady, 1998). The objectives of this research were to (1) measure and compare low-pH Fe(II) oxidation rates across a number of TIFs that vary with respect to mine source (i.e., metal vs coal), AMD chemistry, hydrological and physical conditions, and seasonal variability; (2) simulate field conditions using controlled, laboratory flow-through experiments, and; (3) determine how laboratory rates and field scale observations can be used to predict the performance of engineered TIFs.

2. Materials and methods

2.1. Site locations and descriptions

Eleven mine-impacted sites were sampled. Eight sites were located in the Appalachian Bituminous Coal Basin of the United States and three sites were located in the IPB of southwestern Spain (Fig. 1). These sites were selected due to diverse geochemical and hydrological conditions (Table 1), and to compare rates of Fe(II) oxidation in Appalachian coal mine drainage versus IPB metal mine drainage. Sites in the US contained discharges associated with bituminous coal or clay mining that occurred in the mid-to-late twentieth century. A representative site photo is presented in Supplemental-1. Sites in the US were sampled three to six times between September 2010 and May 2013. Sites in Spain were sampled twice in March and May 2012, months that historically span a decline in rainfall and base flow (Sánchez España et al., 2005; Supplemental-2).

The US sites were divided into natural and engineered TIFs, the former formed below artesian AMD springs with no human intervention and the latter were shallow channels integrated into passive treatment systems. The natural TIFs included Brubaker Run (BR), Scalp Level (SL), Sulphur Run (SR), Summerlee-Natural (SUM-N), and Upper Red Eyes (UR). The engineered sites included Dents Run (DR), Greens Run (GR), and Summerlee-Engineered (SUM-E). Sites in the IPB contained discharges associated with metal mining that occurred since pre-Roman times until present-day (Leistel et al., 1997). The former ore deposits were always composed of massive sulfides with dominant pyrite. The IPB sites were identified as Rio Tintillo (RTL), La Zarza–Perrunal (LZP), and Peña del Hierro (PDH).

2.2. Field sampling

For each site, geochemical profiles were established as longitudinal transects downstream from the emergent source using a combination of field measurements, collection of water and sediment samples, and physical site characteristics, along a single flow path which conveyed the majority of the water across each TIF. Portable field meters were used to measure pH, oxidation–reduction potential (ORP), dissolved oxygen (DO), and temperature (Beckman BKA57201 ATC; HACH40d LDO portable meters). The pH meter was calibrated using pH 1.68, 4.0, and 7.0 standards, while the ORP meter was calibrated with a freshly prepared +228 mV Zobel standard solution. We also used a multiparametric probe (Hydrolab MS5, Hach Company) to measure pH, ORP, DO, temperature and specific conductance at the IPB sites. Water samples were collected at each location, filtered (0.2 μm), chemically preserved (according to each analyte), transported on ice, and stored at 4 C, until analysis (<7 d after collection). Rates of Fe(II) oxidation in the field were calculated using concentrations of dissolved Fe(II) versus travel time. Water velocities were measured at each sampling location and used to calculate travel times. Water velocities were measured using a food color dye as a tracer along with a stopwatch and tape measure. The rate of Fe(II) oxidation was modeled as first-order with respect to dissolved Fe(II) and

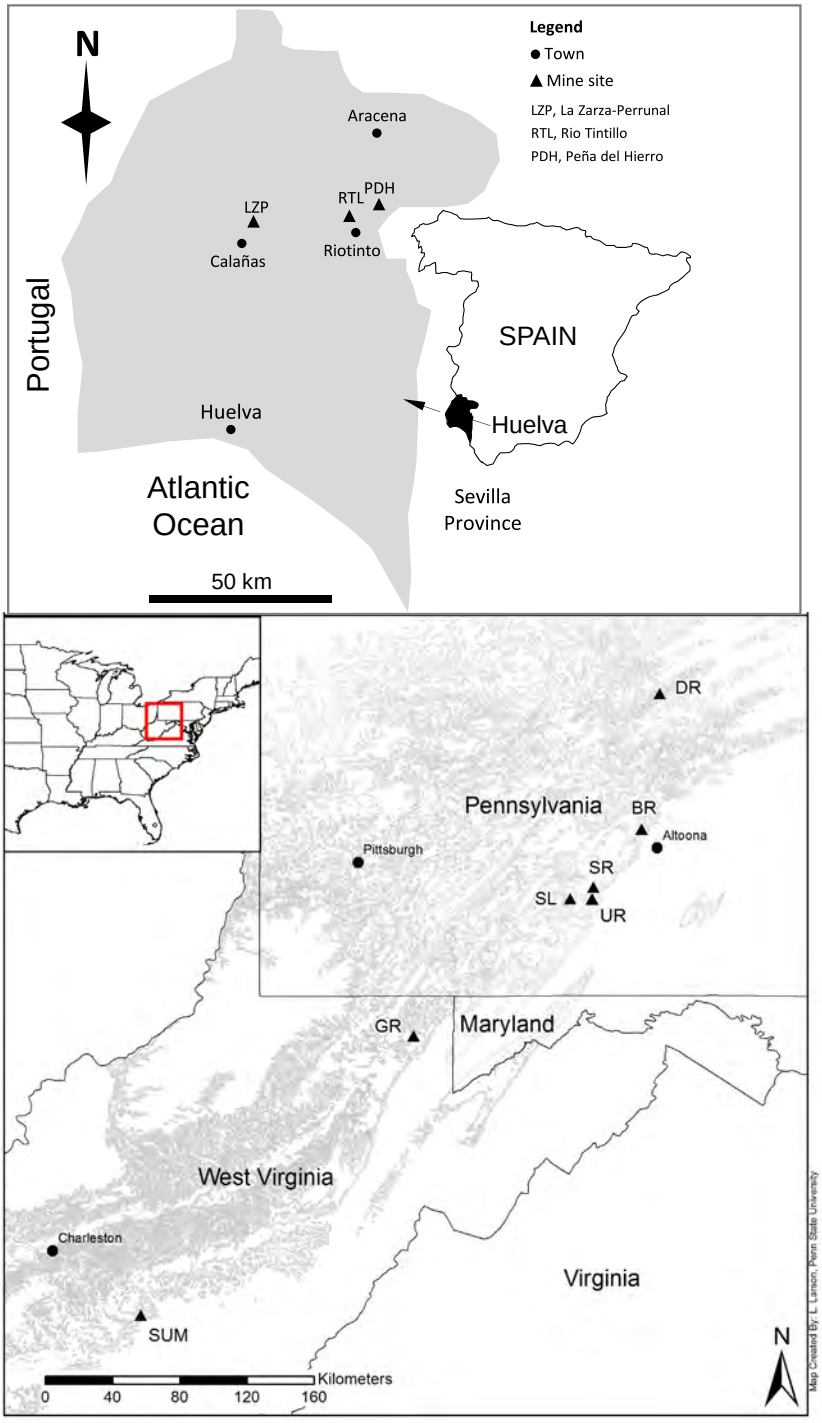

Fig. 1. Sampling locations for TIF sites in the Appalachian Bituminous Coal Basin in the US and the Iberian Pyrite Belt in Spain. Light gray zones show the location of coal fields in western Pennsylvania and West Virginia. SUM-E and SUM-N are located approximately 20 m apart and are collectively labeled as 'SUM'. Filled circles represent cities and filled squares represent field sites.

zero-order rates were calculated for comparisons to other studies (Table 2).

2.3. Laboratory experiments

Sediment pieces were cut from the TIFs and immediately placed into plastic containers similar to those used as the flow-through reactor vessels (13 cm × 8.2 cm × 6.4 cm; $l \times w \times d$). Sediment pieces were collected from the surface layer of the TIF, typically no thicker than 1 cm, and fashioned to similar shapes as the reactor vessel. Cemented sediments were extremely difficult to remove from the concrete channel at GR and shipping logistics precluded lab work with any of the Spanish sites. Water for flow-through reactors was collected from each AMD emergence into 38 L high density polyethylene (HDPE) plastic carboys and filled to eliminate or minimize headspace. Upon returning to the laboratory, the AMD was filtered (0.2 μm), flushed with N_2(g) for 1 h, capped and sealed with parafilm, and stored at 4 C for no more than one week.

Table 1
Geochemical characteristics of the emergent waters from the eleven acid mine drainage (AMD) study sites. Each site contained a terraced iron formation (TIF), either naturally occurring or engineered into an AMD passive treatment system. Values represent mean ± one standard deviation for *n* sampling events.

Parameter	United States – Appalachian region								Spain – Rio Tinto		
	Natural Sites					Engineered Sites			IPB		
	Brubaker run – BR	Scalp level – SL	Sulphur run – SR	Summerlee – SUM-N	Upper red Eyes – UR	Dents run – DR	Greens run – GR	Summerlee – SUM-E	La Zarza – LZP	Peña del Hierro – PDH	Rio Tintillo – RTL
Temp (C)	11.0 ± 0.26	13.3 ± 0.67	10.4 ± 0.15	14.6 ± 0.64	9.38 ± 0.46	11.2 ± 12.6	14.5 ± 7.5	17.3 ± 5.0	26.5 ± 0.4	16.9 ± 2.1	24.3 ± 0.3
DO (mg/L)	0.06 ± 0.05	0.30 ± 0.06	0.14 ± 0.03	0.53 ± 0.6	0.18 ± 0.04		9.1 ± 2.2	5.3 ± 1.8	1.18 ± 0.8	2.75 ± 3.66	2.6 ± 3.1
ORP (mV)	348 ± 37	386 ± 39	315 ± 34	194 ± 49	284 ± 41	440 ± 19	465 ± 36	364 ± 41	323 ± 14	423 ± 28	368 ± 8.5
Conductivity (uS)	1690 ± 236	2010 ± 24	859 ± 41	1890 ± 147	2647 ± 44		1270 ± 816	2440 ± 220	7440 ± 395		18,900 ± 117
pH	3.37 ± 0.15	2.89 ± 0.08	3.48 ± 0.07	4.32 ± 0.64	4.04 ± 0.03	2.47 ± 0.08	3.13 ± 0.88	3.38 ± 0.88	3.13 ± 0.04	2.36 ± 0.12	2.96 ± 0.01
Dissolved total Fe (mg/L)	118 ± 27.9	97.4 ± 9.43	105 ± 6.4	278 ± 57	395 ± 8.4	302 ± 32	379 ± 331	236 ± 64	2930 ± 294	1220 ± 32	2640 ± 151
Dissolved Fe(II) (mg/L)	114 ± 28.4	92.3 ± 11.9	102 ± 6.5	275 ± 57	383 ± 20	135 ± 27	210 ± 166	230 ± 75	2740 ± 229	1090 ± 61	2310 ± 50
Al (mg/L)	11.6 ± 1.6	19.4 ± 0.4	16.5 ± 3.1	20.3 ± 1.3	55.6 ± 2.9	96 ± 3.4	96 ± 125	24.4 ± 8.14	245 ± 32	137 ± 7.3	1940 ± 45
Mn (mg/L)	34.5 ± 10.4	3.3 ± 0.1	14.6 ± 3.3	15.45 ± 0.61	105 ± 11	16.8 ± 0.66	3.82 ± 4.59	14.1 ± 1.32	60.4 ± 7.2	14.4 ± 0.33	314 ± 17
Co (mg/L)	0.69 ± 0.15	0.045 ± 0.003	0.64 ± 0.12	0.22 ± 0.01	3.82 ± 0.36	0.24 ± 0.00	0.32 ± 0.39	0.23 ± 0.04	1.12 ± 0.08	1.01 ± 0.04	9.6 ± 0.35
Ni (mg/L)	1.47 ± 1.10	0.16 ± 0.06	1.67 ± 1.23	0.48 ± 0.24	9.01 ± 6.07	0.56 ± 0.008	1.26 ± 1.71	0.33 ± 0.07	0.68 ± 0.07	0.05 ± 0.005	5.72 ± 0.18
Zn (mg/L)	1.75 ± 0.32	0.23 ± 0.03	2.13 ± 0.39	0.39 ± 0.02	12.2 ± 0.66	1.02 ± 0.02	1.17 ± 1.51	0.46 ± 0.04	46.4 ± 8.96	54.2 ± 9.4	385 ± 127
SO_4^{2-}(mg S/L)	381 ± 89	429 ± 34	212 ± 44	547 ± 37	903 ± 100	655	496 ± 634	549 ± 8	2530	1180	8190
Si (mg/L)	10.4 ± 0.3	16.5 ± 1.14	14.4 ± 1.2	14.2 ± 0.16	13.9 ± 0.21	38.9 ± 1.5	23.4 ± 26.4	16.8 ± 2.1	52.3 ± 0.29	52.1 ± 3.5	55.3 ± 5.1
PO_4^{3-}(mg P/L)	1.32 ± 1.86	1.3 ± 1.7	1.5 ± 2.1	1.10 ± 1.56	2.95 ± 3.84	<.05	7.16 ± 10.1	0.11 ± 0.11	1.62	0.5	3.81
n (field chemistry)	7	4	5	5	5	3	5	4	2	2	2
n (trace metals)	3	2	2	2	2	2	2	2	2	2	2
Mean Acidity (mg/L as $CaCO_3$)*	360	357	325	642	1220	1420	1410	609	6910	3310	16,400

* Acidity calculated according to (Kirby and Cravotta, 2005).

Table 2
Physical characteristics of the eleven acid mine drainage (AMD) study sites, and summary of Fe(II) oxidation kinetics measured in the field.

Parameter	United States – Appalachian Bituminous Coal Basin								Spain – Iberian Pyrite Belt		
	Natural Sites				Engineered sites						
	Brubaker run – BR	Scalp level – SL	Sulphur run – SR	Summerlee – SUM-N	Upper red eyes – UR	Dents run – DR	Greens run – GR	Summerlee – SUM-E	La Zarza – LZP	Peña del Hierro – PDH	Rio Tintillo – RTL
GPS location (lat/long)	40 37′1.42″N 78 28′35.76″W	40 14′43.72″N 78 51′33.18″W	40 18′25.91″N 78 44′5.06″W	38 0′18.06″N 81 9′29.04″W	40 14′27.07″N 78 44′25.42″W	41 20′26.66″N 78 22′18.54″W	39 30′19.38″N 79 41′53.25″W	38 0′19.39″N 81 9′28.68″W	37 42′22.70″N 6 51′48.38″W	37 43′30.41″N 6 33′21.62″W	37 42′31.86″N 6 37′14.06″W
Linear TIF Length (m)	70	65	50	8	275	188	140	90	747	244	796
$k_{1st,field}$ (min^{-1})	0.070 ± 0.032	0.399 ± 0.132	0.066 ± 0.039	0.034 ± 0.015	0.038 ± 0.004	0.048 ± 0.003	ND	0.068 ± 0.033	0.003 ± 0.001	0.028 ± 0.003	0.01 ± 0.003
$k_{Zero,field}$ (mol/L * s) * 10^7	16.0 ± 6.10	81.3 ± 39.0	21.6 ± 10.2	29.1 ± 17.0	14.3 ± 3.40	8.60 ± 0.20	ND	36.3 ± 22.6	13.1 ± 9.40	67.9 ± 16.2	30.7 ± 1.10
n	5	4	3	4	3	3	–	3	2	2	2

The laboratory flow-through sediment reactors were modeled as tanks-in-series (TIS) to determine the pseudo first-order rate constant for Fe(II) oxidation ($k_{1st,lab}$). A conservative conductivity tracer (NaCl, 1410 μS) was injected into de-ionized water as a pulse input and measured every 30 s with the flow-through reactor operated at an 8 h residence time (residence time of the Fe(II) oxidation experiments). The conductivity results were analyzed using an exit age distribution ($E(\theta)$) to determine the non-ideality of the reactors (Crittenden et al., 2012). A TIS model was used to analyze the conductivity exiting the reactor according to:

$$E(\theta) = \frac{n(n\theta)^{n-1}}{(n-1)!} * \exp^{n\theta} \quad (3)$$

where θ was the normalized independent time variable, $E(\theta)$ was the exit age distribution, and n was the theoretical number of continuously stirred tank reactors (CSTR) in series. Theoretically, when $n = 1$, the reactor behaves as an ideal CSTR and as n approaches ∞, the reactor behaves as an ideal plug-flow reactor (PFR).

The conductivity tracer was performed with an empty reactor and repeated with a piece of non-reactive porous media (sponge) in the reactor. The best fits for the tracer breakthrough curves occurred with n ranging from 2 to 4 with an empty or filled reactor (Supplemental-3). A lower n value better modeled the tail of the tracer curve, while a higher n value better fit the rising portion of the tracer curve. An n value of 3 was selected for kinetic modeling as a compromise best-fit parameter.

Laboratory experiments were conducted using sediment and water collected from seven of the US sites (BR, SL, SR, SUM-N, UR, DR, and SUM-E). Sediment reactors similar to those described by Brown et al. (2010) used intact pieces of surficial sediments and emergent site water to measure rates of Fe(II) oxidation. Water height above the sediments was previously found to affect the rate of Fe(II) oxidation (Brown et al., 2010), therefore, water column height was fixed at 1.5 cm above the sediments. To maintain this fixed water column height, the water volume in each reactor varied slightly. Water volume was measured for every reactor and the flow rate was adjusted to maintain a hydraulic residence time of 8 h for all reactors. Water samples were collected from the inflow and outflow at the start of the experiment (time = 0), and after select pore volumes of fluid had been pumped through the reactors. Samples were immediately measured for pH (Mettler Toledo-InLab* Mini pH Electrode) and ORP (Mettler Toledo-InLab*- Redox Mini Electrode), filtered (0.2 μm), and filtrate was added into either 0.5 M HCl or 0.5 M hydroxylamine–HCl for determination of dissolved Fe(II) and dissolved total Fe(T), respectively, using the ferrozine assay (Stookey, 1970). Experiments were run in triplicate for 48–64 h and conducted in parallel with duplicate no-sediment control reactors. At the conclusion of each experiment, a single sediment reactor was re-started to measure pH and ORP continuously, in real-time within the reactor. Electrodes were located near the outflow drain, configured to record samples every 10–30 s for the entire duration of the experiment (up to 60 h), and were relayed and stored on a laptop computer.

Determination of laboratory Fe(II) oxidation rate constants were based on first-order kinetics. Once steady-state conditions were established in the reactor (i.e., when $[Fe(II)]_{out}/[Fe(II)_{in}$ remained constant), the first-order model was calculated according to:

$$[Fe(II)_{out}] = \frac{[Fe(II)_{in}]}{(1 + k_{1st*H})^{n}} \quad (4)$$

where k_{1st} was the first-order laboratory Fe(II) oxidation rate constant (min^{-1}), $[Fe(II)_{in}]$ was the steady-state inlet concentration of dissolved Fe(II) (M), $[Fe(II)_{out}]$ was the steady-state outlet concentration of dissolved Fe(II) (M), n was the equivalent number of CSTR

tanks in series (from Eq. (3), set constant to $n = 3$), and θ_H was the hydraulic residence time (min). Laboratory Fe(II) oxidation rate constants were normalized to reactor sediment mass and viable biomass concentrations according to:

$$k_{1st,lab} = \frac{k_{1st}}{m * X} \quad (5)$$

where $k_{1st,lab}$ was the normalized first-order laboratory rate constant (min^{-1} pmols-PLFA^{-1}), m was the sediment mass in the reactor (g), and X was the viable (active) sediment biomass concentration (pmols-PLFA g^{-1} sediment).

2.4. Analytical techniques

Dissolved Fe(II) and dissolved total Fe(T) (after reduction by hydroxylamine–HCl) were determined using the ferrozine assay with samples preserved with HCl. Dissolved Fe(III) concentrations were determined from the difference of dissolved total Fe(T) and dissolved Fe(II) measurements. Dissolved metals (Al, Co, Mn, Ni, Si, Zn), metalloids (As), and non-metals (Se) were analyzed on a Perkin–Elmer Optima 5300 ICP-AES with samples that had been preserved with HNO_3. Concentrations of As and Se were below detection limits for all US sites (50 μg/L). Sulfate was measured spectrophotometrically by barium sulfate precipitation with chemically unpreserved samples (Hach Method 8051).

Upon completion of the laboratory experiments, approximately 50 wet grams of sediment were immediately collected into whirl-pak® bags and stored at −80 C to minimize degradation of phospholipid fatty acids (PLFA). Samples were shipped on dry ice overnight and analyzed for PLFA by Microbial Insights, Inc. (Rockford, TN, US). PLFA measurements were performed only with sediments collected from the seven US sites used in the laboratory flow-through experiments. Upon cell death, membranes rapidly decay, and the concentration of total PLFAs represents the active or viable biomass concentration in the sample. The abundance of each type of PLFA provides information on microbial community structure. Active biomass concentrations (pmols-PLFA g^{-1} sediment) were used to normalize laboratory Fe(II) oxidation rates between sites (Eq. (5)). Upon arrival at Microbial Insights, sediments were thawed and lipids were extracted using a one-phase chloroform–methanol-buffer following a modified Bligh and Dyer method (White et al., 1979). Recovered lipids were fractionated into neutral lipids, glycolipids, and polar lipids using disposable silicic acid columns. The polar lipid fraction was transesterified by mild alkali methanolysis to recover the PLFAs as fatty acid methyl esters. PLFAs were determined on a gas chromatograph–mass spectrometer with electron ionization.

3. Results and discussion

3.1. Field sampling results

Because of the differences in acid-generating source rock, surrounding geologic strata, physical site conditions and the hydrogeological flow path from the source to the emergent discharge, water chemistry varied between all the sites (Table 1). Water chemistry for the few sites studied in each geologic region as compared to larger water chemistry databases are provided in Supplemental-4. Based on a simple rank analysis, our selected sites contained lower pH values and higher concentrations of dissolved total Fe(T) compared to median values in both regions. Sites were selected with low concentrations of dissolved oxygen (DO), low oxidation–reduction potentials (ORP), and a high proportion of dissolved Fe(II) to dissolved total Fe(T). These geochemical conditions were intentionally selected to study sites where low-pH Fe(II) oxidation was a dominant process downstream of the emergent springs.

Seasonal variations in water chemistry at any site may have been caused by changes in water table elevations that could impact pyrite oxidation (Nordstrom, 2011), and/or by complexities in underground conditions (Price, 2003). The temperature of emergent AMD varied between sites and reflected differences in site-specific hydrogeology and hydrogeochemistry. For the natural TIF sites in the US, emergent DO was typically less than 0.5 mg/L. Higher concentrations of DO were measured at the engineered sites in the US (5–9 mg/L) and at the Spanish sites (1–3 mg/L). Higher concentrations of DO and lower ratios of Fe(II)/Fe(T) were measured at these sites because the emergence (i.e., exposure to atmospheric P_{O2}) occurred upstream (e.g., in partially flooded mines or partially saturated spoils piles) of our most upstream sampling location.

Measured trace metal concentrations for all sites were above chronic Ambient Water Quality Criteria (AWQC) for aquatic life, which are as follows (μg/L): Al – 87, Cd – 0.25, Co – 3.06, Cu – 11.8, Fe – 1000, Mn – 80.3, Ni – 52, Pb – 3.2, Zn – 106 (Seal et al. 2010, US EPA 2013). The highest concentrations of Al for the US sites were measured at GR (96 ± 125 mg/L), DR (96 ± 3.4 mg/L), and UR (56 ± 2.9 mg/L). The IPB sites (RTL, LZP, and PDH) contained metal concentrations an order of magnitude higher than sites in the US. Notably, dissolved total Fe(T) concentrations ranged from 1223 to 2928 mg/L. Rio Tintillo (RTL) contained the highest concentrations of Al (1942 mg/L), Mn (314 mg/L), Co (9.6 mg/L), Ni (5.7 mg/L) and Zn (385 mg/L). Lower trace metal concentrations were observed at LZP and PDH, yet generally still exceeded any concentrations observed at US sites. Theoretical mean acidity values (calculated according to (Kirby and Cravotta, 2005)) for the US sites ranged from 325 to 1422 mg/L as $CaCO_3$, while calculated mean acidities for the IPB sites ranged from 3307 to 16,410 mg/L as $CaCO_3$. Periods of high flow substantially diluted the AMD at GR, which resulted in variable iron concentrations ([Fe(II)] = 210 ± 166 mg/L, [Fe(T)] = 379 ± 331 mg/L), trace metals, and sulfate (Table 1). Compared to cation and anion concentrations, the pH and ORP were less susceptible to seasonal changes at GR (pH – 3.13 ± 0.88, ORP – 465 ± 36 mV). Due to their physical proximity, emergent AMD from SUM-N and SUM-E had similar geochemistry and were presumably originating from the same coal refuse pile. The natural TIF sites, BR, SL, SR and UR, displayed relatively consistent emergent chemistry throughout all sampling events.

Longitudinal geochemical transects across the TIFs were measured on several seasonal sampling events for pH, ORP, DO, temperature, trace metals, and Fe speciation. For the majority of these sites, the general geochemical trends were for DO and ORP to increase, dissolved Fe(II) to decrease, dissolved total Fe(T) to decrease slightly, temperature to approach ambient conditions, and trace metals to remain unchanged. The trends for pH across the TIFs could not be generalized. For example, pH tended to decrease across four of the five natural TIFs in the US (Fig. 2), one of the three engineered TIFs (Fig. 3), and two of the three TIFs in the IPB (Fig. 4). Microbial-catalyzed Fe(II) oxidation can produce either soluble Fe(III) (Eq. (6)) or insoluble Fe(III) (Eq. (7)) according to:

$$Fe^{2+} + \frac{1}{4}O_2 + H^+ = Fe^{3+} + \frac{1}{2}H_2O \quad (6)$$

$$Fe^{2+} + \frac{1}{4}O_2\ (g) + \frac{7}{32}SO_4^{2-} + \frac{17}{16}H_2O = \frac{25}{16}H^+ + \frac{1}{8}Fe_8O_8(SO_4)_{1.75}(OH)_{4.5} \quad (7)$$

where $Fe_8O_8(SO_4)_{1.75}(OH)_{4.5}$ represents a nominal stoichiometry for schwertmannite (Regenspurg et al., 2004). In Eq. (6), acidity is

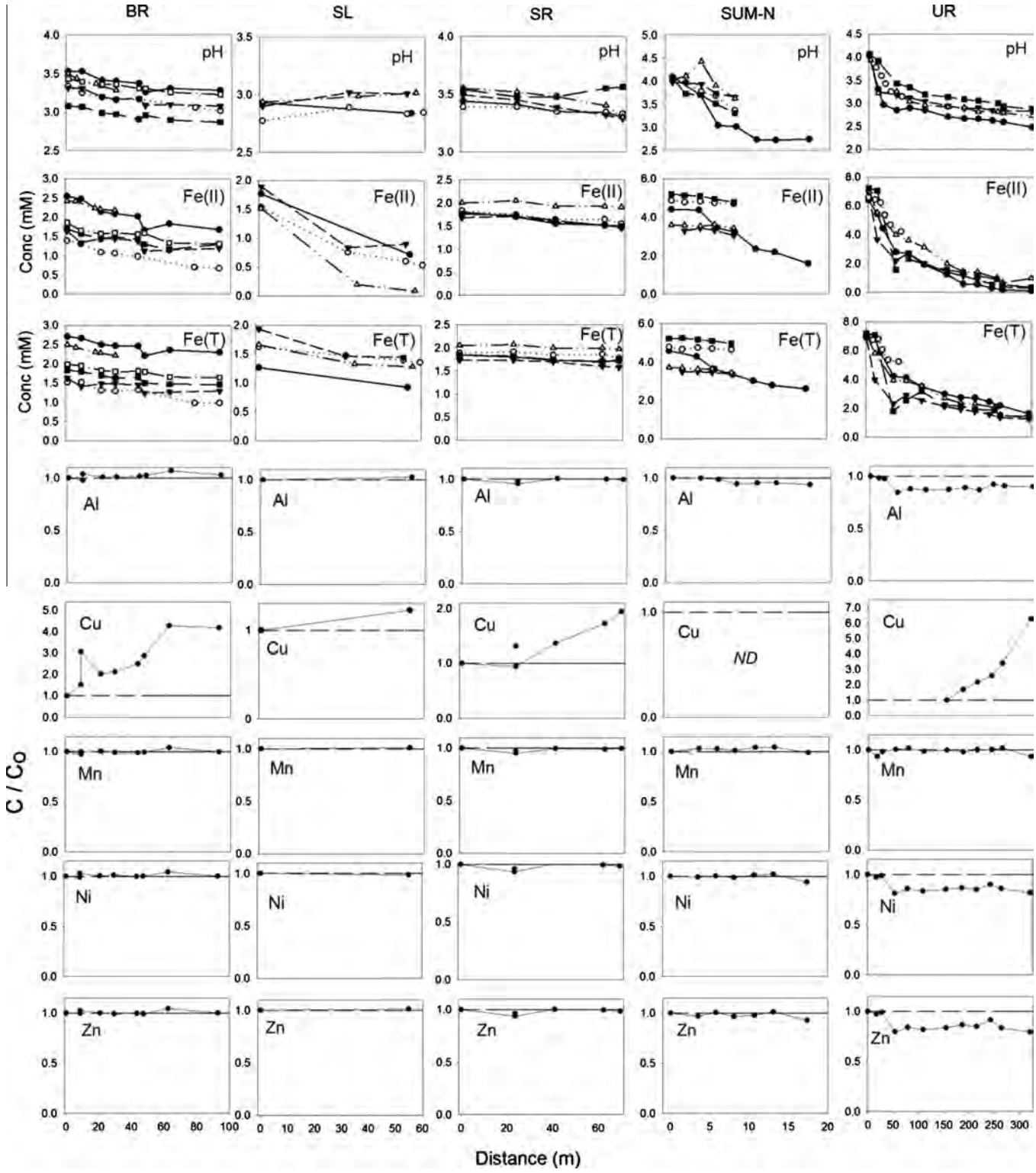

Fig. 2. Longitudinal geochemical transects for natural TIF sites in the US for pH, Fe speciation (mM), and trace metals. Data were collected 3–6 time at any given site. Trace metals are presented as the ratio of C/C_o to show changes relative to emergent metal concentrations. Trace metal transects were collected once.

consumed while in Eq. (7) acidity is produced. At virtually all sites, both dissolved Fe(II) and dissolved total Fe(T) decreased, and dissolved Fe(III) increased, indicating that both Eqs. (6) and (7) were operative. The removal of soluble Fe(III) is controlled by pH, the solubility of schwertmannite, and the kinetics of schwertmannite precipitation.

For presentation purposes, results have been divided into natural TIFs in the US (Fig. 2), engineered TIFs in the US (Fig. 3) and natural TIFs in Spain (Fig. 4). Trace metals across the TIFs were collected on one occasion, while pH and Fe speciation were collected two to six times. Comparisons of geochemical transects highlight important distinctions between the type of TIF (natural versus engineered)

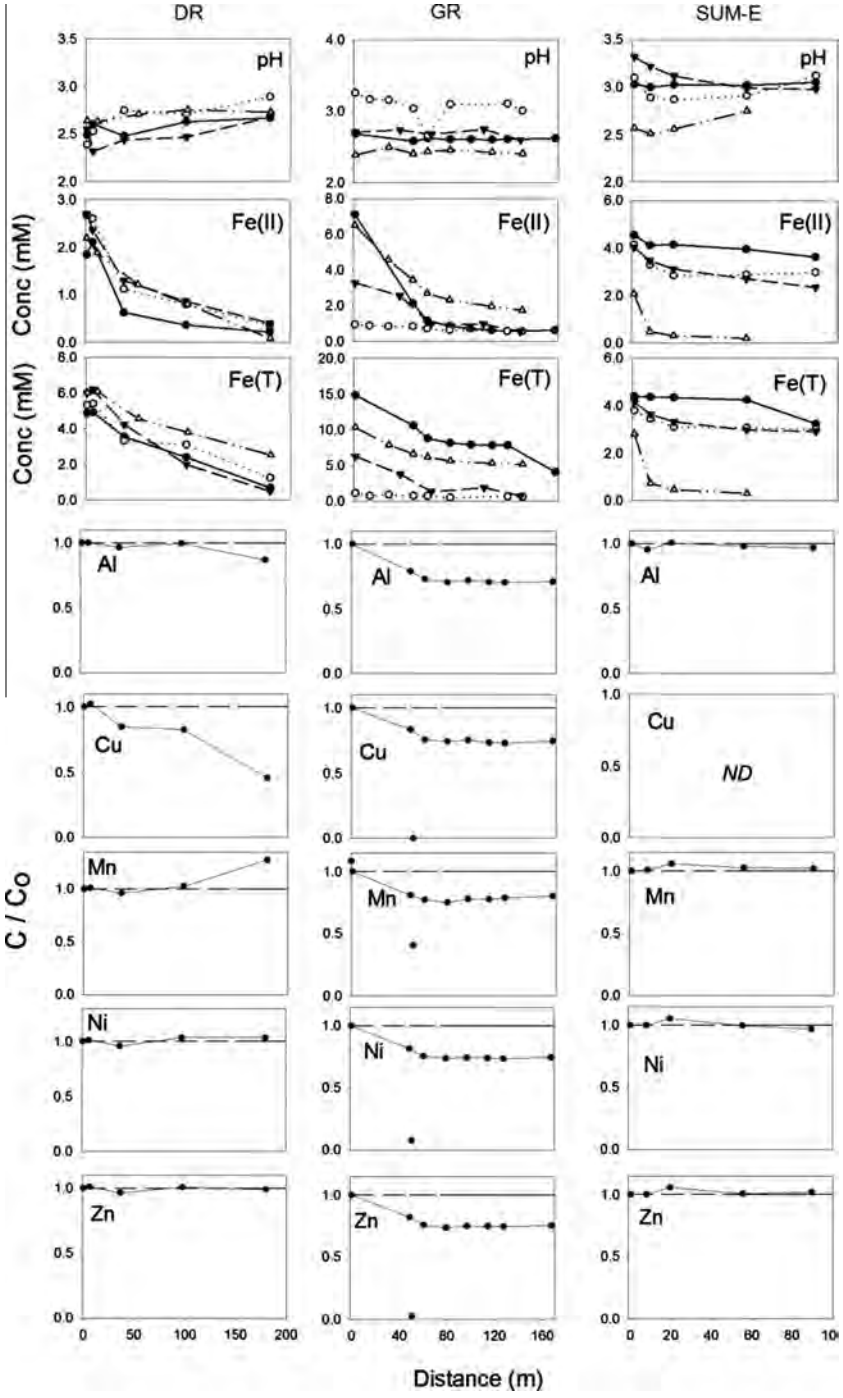

Fig. 3. Longitudinal geochemical transects for engineered TIF sites in the US for pH, Fe speciation (mM), and trace metals. Data were collected 4–5 times at any given site. Trace metals are presented as the ratio of C/C_o to show changes relative to emergent metal concentrations.

and AMD source (e.g., coal versus metal mines) on pH, Fe speciation, and trace metal mobility. These transects are plotted as a function of distance from the emergent AMD sources and some variations in geochemistry were dependent on the emergent flow rate and the local water velocity.

Longitudinal geochemical transects across most natural TIFs in the US displayed behavior consistent with Eq. (7) where dissolved Fe(II) and dissolved total Fe(T) decreased along with pH. Scalp Level (SL) was the one natural TIF site where pH did not drop but instead tended to increase. SL also had a lower emergent pH (2.51–2.90) as compared to the other natural TIFs (typically between pH 3.0 and 4.0). Even so, dissolved Fe(II) concentrations decreased from 50% to 90% of emergent Fe(II) concentrations while dissolved total Fe(T) decreased to a much lower extent. The geochemical transect at SL, therefore, displayed behavior more consistent with Eq. (6). Trace metal (Al, Cu, Mn, Ni, Zn) behavior for all natural TIF sites in the US were relatively similar (Fig. 3). In general, there was no significant removal of trace metals at any natural TIF. Decreases in Al, Mg, Ni, S and Zn were measured at UR. Decreases in metal concentrations at UR were likely caused by dilution with additional base flow entering this large TIF. Assuming concentrations of S and Fe from AMD sources are strongly correlated, and assuming S

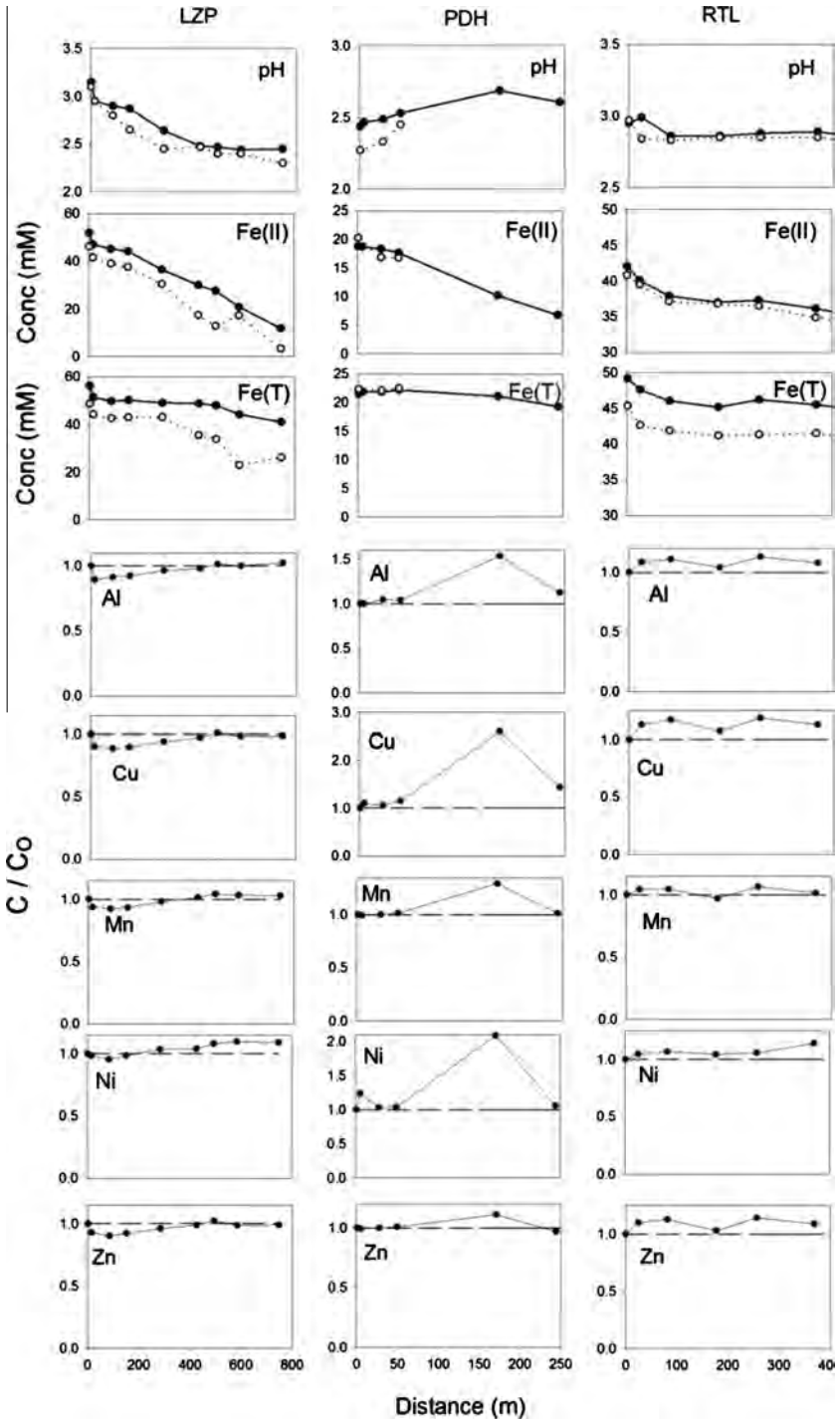

Fig. 4. Longitudinal geochemical transects for TIF sites in the IPB for pH, Fe speciation (mM), and trace metals. Data were collected twice at all sites. Trace metals are presented as the ratio of C/C_o to show changes relative to emergent metal concentrations.

and Mg act as conservative elements, we found that S and Mg decreased ~20% compared to their emergent concentrations suggesting base flow dilution. Increasing soluble Cu concentrations were measured at four sites, possibly due to decreased adsorption affinity of Cu to schwertmannite (Webster et al., 1998) and/or enhanced metal solubility of Cu-bearing minerals at lower pH values.

Longitudinal geochemical transects measured across engineered TIFs were rather variable (Fig. 3) compared to the natural TIF sites. Samples were collected from engineered channels at GR (concrete) and DR (limestone gravel), while SUM-E was designed to promote sheet flow across its clay-based "raceway". In contrast to natural sites, emergent AMD at the engineered sites was partially oxidized due to modified hydrogeochemical conditions at each site. Emergent pH values ranged from 2.4 to 3.4. On one occasion, higher pH values were observed at GR (pH 4.5; high flow condition) and SUM-E (pH 4.9; low flow condition) (transect data not shown in Fig. 3 and not included in Table 1). For three sampling events at GR, pH values remained relatively constant across the TIF while both dissolved Fe(II) and dissolved total Fe(T) decreased

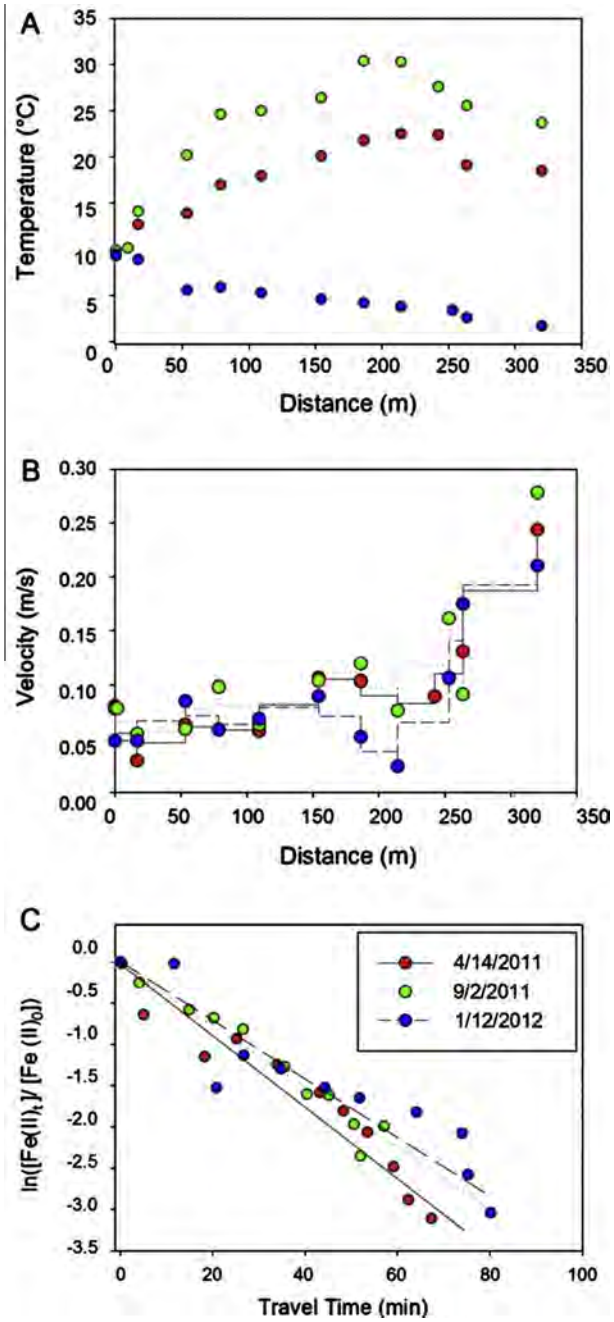

Fig. 5. Representative example from Upper Red Eyes (UR) showing data transformation of distance (m) to travel time (min) to calculate Fe(II) oxidation rates in the field. (A) Water temperature downstream of emergent AMD source. (B) Water velocity measured at discrete sampling locations (points) and the averaged velocity between any two sampling locations (lines). Travel times were calculated as the distance between two sampling locations divided by the averaged velocity. (C) Dissolved concentrations of Fe(II) versus cumulative travel time were used to calculate first-order Fe(II) oxidation rate constants. (For interpretation of the references to color in this figure legend, the reader is referred to the web version of this article.)

significantly. Dissolved concentrations of all trace metals (Al, Cu, Mn, Ni and Zn) at GR decreased approximately 30% compared to their emergent concentrations. Dilution from other point sources accounted for some of these decreases, as S and Mg decreased by ~20% compared to their emergent concentrations. We propose that additional trace metal removal was promoted by alkaline minerals in the concrete channel. While the pH at GR typically was less than 4, alkalinity generated via concrete dissolution could create localized zones of higher pH that facilitated precipitation of dissolved Fe(III) and co-precipitation of trace metals into the Fe(III) minerals. Ca concentrations remained constant along the channel even while Mg concentrations decreased, demonstrating that Ca dissolution was occurring, thus supporting our interpretation.

Similar to GR, substantial amounts of dissolved Fe(II) and dissolved total Fe(T) were removed in the engineered channel at Dents Run (DR). While oxidative precipitation of schwertmannite (Eq. (7)) should produce acidity, dissolution of the limestone gravel in the shallow channel at DR buffered the pH of this system such that it actually increased slightly (from pH 2.5 to pH 2.8) along this transect. Increasing calcium concentrations measured across this TIF support this hypothesis. Concentrations of dissolved Fe(III) were found to be slightly over-saturated with respect to ferrihydrite and schwertmannite (Supplemental-5). At DR, Cu and Al were the only trace metal concentrations to decrease along this transect. The extent of Fe(II) oxidation and removal of dissolved total Fe(T) was lowest at the Summerlee-Engineered (SUM-E) site as compared to the other engineered TIF sites. SUM-E also displayed the most inconsistent geochemical behavior. Both of these results, limited and variable oxidative precipitation of Fe, were likely because this was a newly constructed TIF that has yet to "mature".

Longitudinal geochemical transects at the IPB sites were measured on two occasions, March and May 2012 (Fig. 4). In general, emergent pH values were lower in the IPB as compared to the US sites, ranging from pH 2.3 to 3.1. Emergent concentrations of dissolved Fe(II) and dissolved total Fe(T) at the IPB sites were almost an order of magnitude higher than any US site (1223–2928 mg/L). Therefore, even modest changes in the [Fe(II)]/[Fe(T)] ratio amounted to substantial masses of Fe deposited onto these TIFs. For all of the IPB sites, no metal was removed other than Fe, while slight increases in Cu, Ni and Zn were measured downstream of RTL and PDH (Fig. 4). At RTL, increased metal concentrations could have been caused by additional AMD sources entering the study reaches. Similar to Scalp Level in the US, the pH increased downstream of Peña del Hierro (PDH) while dissolved Fe(II) decreased 64% compared to the emergent concentration but dissolved total Fe(T) decreased only 8%.

3.2. Rates of Fe(II) oxidation in the field

A representative data set from Upper Red Eyes (UR) shows the successive transformation of field data, using stream velocities, to estimate $k_{1st,field}$ (Fig. 5). The emergent temperatures were fairly constant (~10 C), while the downstream temperature gradients were controlled by the seasonal ambient temperature (Fig. 5A). Velocity measurements were averaged between sampling locations and were fairly consistent regardless of season for this site (Fig. 5B). Field rate constants were determined according to:

$$-d[\mathrm{Fe(II)}]/dt = k_n^*[\mathrm{Fe(II)}]^n \quad (8)$$

where $n = 0$ and $n = 1$ represent the zero- and first-order rate expressions, respectively. The slopes of the lines in Fig. 5C were used to calculate the first-order rate constants for each sampling event. First-order Fe(II) oxidation rate constants measured in the field ($k_{1st,field}$) for UR ranged from 0.035 min^{-1} (in January 2012) to 0.044 min^{-1} (in April 2011) (Fig. 5C).

For some field sites, the physical assumptions for our kinetic stream reach model were not met. We assumed the stream reach functioned as a plug flow reactor with no other inputs of flow or dissolved Fe(II). Rates of Fe(II) oxidation were not calculated at GR because additional point sources discharged directly into this engineered TIF, invalidating our model assumptions. At the largest natural TIF sites (UR, RTL), additional seeps and base flow did enter the systems but never from obvious point sources. If these diffuse

sources contained elevated concentrations of Fe(II), then our measured (i.e., apparent) field rates would be less than the actual rates. Conversely, if these diffuse sources contained relatively low concentrations of Fe(II), then our measured field rates would be greater than the actual rates. Assuming S acts as a conservative proxy for Fe, base flow dilution did occur at UR but did not occur at RTL. Thus, the measured rates at UR could be greater than the actual rates. Considering uncertainties with respect to model assumptions and hydrogeochemical variability between sampling events, the relative standard deviations of the field rates measured at UR and RTL were relatively low compared to all 10 sites (Table 2) providing confidence in these rate measurements. The measured field rates at UR and RTL were also near the median values for each region, neither exceptionally fast nor slow. Finally, because we tended to measure water velocity in stream reaches where our tracer was swept along via advective transport, our calculated travel times could be biased as relatively short compared to all the water flowing across each TIF. Thus, all of our calculated kinetic constants could be biased as relatively fast when compared to other studies. While we recognize the difficulty in measuring geochemical kinetics in the field, we propose that all of our rates are comparable within this study because we used identical methods at all sites.

Field-based Fe(II) rate constants and physical site characteristics are presented in Table 2. Physical site parameters (transect distance, surface area, and average slope) were obtained using geospatial processing of 3D digital elevation maps (DEM) in ArcGIS. Physical conditions were variable between sites. For example, UR was a relatively large TIF site that can be observed from satellite imagery, while SUM-N was only ~8 m in length. The fastest $k_{1st,field}$ for any natural US site was 0.497 min^{-1} (SL in April 2011) while the slowest $k_{1st,field}$ was 0.030 min^{-1} (SUM-N in December 2011). Excluding SL, the mean value for $k_{1st,field}$ from natural TIF sites in the US ranged from 0.035 to 0.070 min^{-1}.

Uncertainty with these kinetic analyses was most likely associated with the transformation of the independent variable of distance to travel time. Seasonally variable velocity measurements and the validity of assumptions used to calculate the average velocity between two sampling points could affect this transformation. Considering variable physical site characteristics, geochemical variability, and error and uncertainty associated with the first-order rate model, the calculated rate constants from the different sites were remarkably similar. First-order rate constants determined on each sampling event are provided in Supplemental-6. Rates of Fe(II) oxidation on engineered TIFs were comparable to rates of Fe(II) oxidation on natural TIF sites in the US (Table 2).

First-order rate constants of Fe(II) oxidation calculated for the IPB sites were ~10 times slower than first-order rate constants calculated at the US sites. First-order rate constants ranged from 0.003 to 0.01 min^{-1} (Table 2). However, zero-order Fe(II) oxidation rates ($k_{zero,field}$) calculated for the IPB sites were comparable to zero-order rates calculated for the US sites. In the IPB, $k_{zero,field}$ ranged from 13.1 $\times 10^{-7}$ to 67.9 $\times 10^{-7}$ mol L^{-1} s^{-1}. At the US sites, mean $k_{zero,field}$ ranged from 8.60 $\times 10^{-7}$ to 81.3 $\times 10^{-7}$ mol L^{-1} s^{-1}. It should be noted that interpretative discrepancies can be caused by the rate model used to describe the field results. First-order rate constants from the IPB sites may have been slower because of the higher conductance and trace metal concentrations in the waters of that geographic region (Table 1).

The fastest $k_{1st,field}$ were measured at sites with the lowest emergent pH values in both the US and the IPB (Fig. 6A). First-order rate constants grouped into distinct sets based on their geographic region. These correlations are consistent with the rate law for biotic Fe(II) oxidation proposed by Kirby et al. (1999) where the rate was proportional to $[H^+]$ (Eq. (2)). $k_{1st,field}$ were also fastest at sites where pH increased across the TIF (Fig. 6B). The change in pH across each TIF (ΔpH) was calculated as the pH at the bottom of the site minus the pH at the emergent spring at the top of site. If the pH increased across the site (ΔpH > 0), this would provide indirect evidence for the consumption of H^+ associated with the production of soluble Fe^{3+} (Eq. (6)). Similarly, if the pH decreased across the site (ΔpH < 0), this would provide indirect evidence for the production of H^+ associated with the precipitation of an Fe(III) mineral such as schwertmannite (Eq. (7)).

3.3. Rates of Fe(II) oxidation in the laboratory

Representative results from flow-through low-pH Fe(II) oxidation experiments using sediments and AMD from UR displayed a rapid decrease in the $[Fe(II)_{out}]/[Fe(II)_{in}]$ ratio between 0 and 10 h (Fig. 7A). No Fe(II) oxidation was observed in no-sediment control reactors, confirming that biotic processes were responsible for oxidizing Fe(II) within the sediment reactors. In similar previous experiments, Brown et al. (2010) showed that no Fe(II) oxidation occurred in gamma-irradiated, sterilized sediments. Approximately 24 h into the experiment (equivalent to three pore volumes), the $[Fe(II)_{out}]/[Fe(II)_{in}]$ ratio began to achieve a pseudo steady-state condition. Fe(II) oxidation rates in laboratory experiments were calculated and averaged over the whole duration of this pseudo steady-state period. Measurements of pH collected on a much more intensive time scale also demonstrated that pseudo steady-state conditions with respect to pH were established within 10 h (Fig. 7B). Steady-state conditions with respect to ORP took longer to establish, possibly because non-ideal mixing affected oxygen transfer (Fig. 6B).

Rate constants were normalized based on sediment mass and biomass concentration. The biomass-normalized Fe(II) oxidation rates ($k_{1st,lab}$) ranged from 10 $\times 10^{-11}$ to 68 $\times 10^{-11}$ min^{-1} pmol-$PLFA^{-1}$(Table 3). The fastest laboratory rate of Fe(II) oxidation was measured using sediments and AMD collected from SL. Relative standard deviations (RSD = standard deviation/mean value * 100%) were high in these experiments. For example, the RSD for the SL sediment experiments was 54%, the RSD for the SUM-E sediment experiments was 58%, and the RSD values for the remaining five sediments were <36%. Error and uncertainty associated with these experiments were most likely associated with sediment heterogeneity and non-ideal mixing in the reactors.

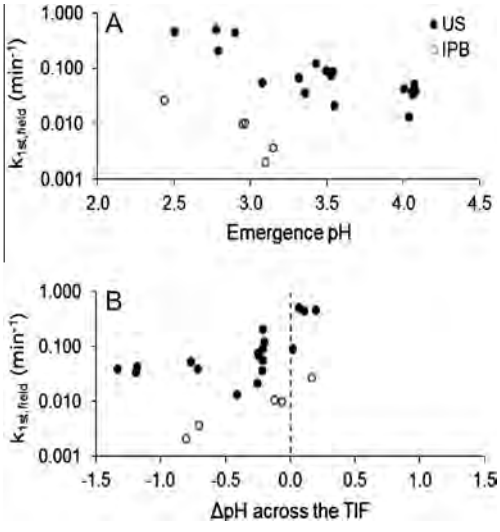

Fig. 6. Observed first order field Fe(II) rate constants ($k_{1st,field}$) at the US and IPB field sites displayed with (A) emergent pH and (B) ΔpH across the TIF. Positive values for ΔpH denote a net pH increase across the TIF and negative ΔpH values indicate a net pH decrease. Positive values for ΔpH are consistent with the oxidation of Fe(II) to soluble Fe(III) (Eq. (6)). Negative values for ΔpH are consistent with the oxidation of Fe(II) and precipitation of Fe(III) (Eq. (7)).

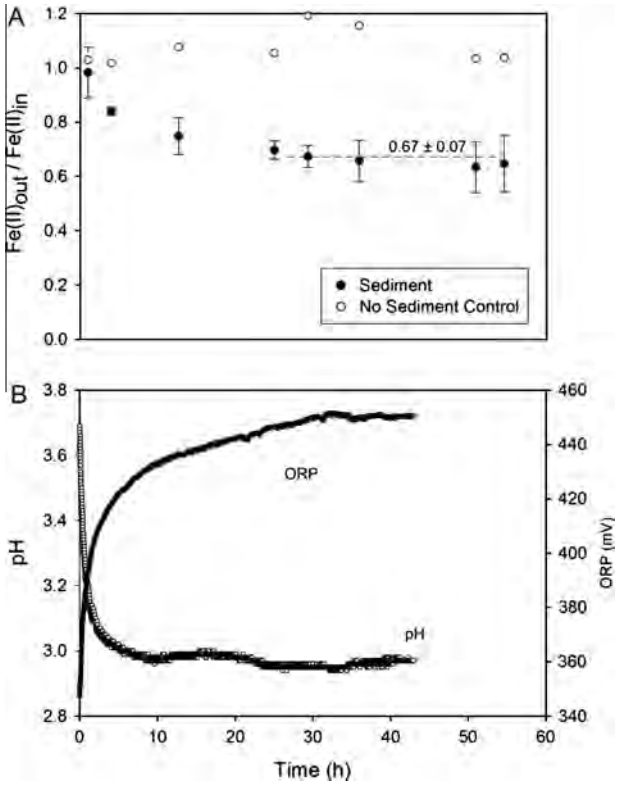

Fig. 7. Representative laboratory data for sediments and water collected from Upper Red Eyes (UR). (A) Laboratory rates of Fe(II) oxidation were calculated from concentrations of dissolved $Fe(II)_{out}/Fe(II)_{in}$ when pseudo steady-state conditions were established (dashed line). (B) Real-time pH and ORP results for sediments and water collected from UR. Real-time results for no-sediment controls showed no appreciable changes (data not shown).

The majority of the sediments had relatively low microbial diversity and contained a large abundance of proteobacteria and general PLFAs (Fig. 8). A complete PLFA profile for each site is provided in Supplemental-7. BR and SR contained the highest abundance of eukaryotes (10% and 6%, respectively), while SL contained the highest abundance of firmicutes (26%). There was a large range of biomass concentrations; DR contained the maximum (67,000 pmols-PLFA g^{-1} sediment) and SL the minimum (6500 pmols-PLFA g^{-1} sediment). Interestingly, SL had the highest observed field and lab Fe(II) oxidation rate constants, yet sediments collected from the site had the lowest active biomass concentration and a considerably different PLFA profile (i.e., much higher abundance of firmicutes, less abundance of proteobacteria). The other sites (UR, SUM-N, and SUM-E) contained similar biomass and abundances.

3.4. Environmental implications

Our results are consistent with several other studies that have reported Fe(II) oxidation rates. Zero-order oxidation rates from all eleven sites varied only by a factor of ~11 (Table 2), where $k_{zero,field}$ ranged from 8.60×10^{-7} to 81.3×10^{-7} mol L^{-1} s^{-1}. These values compare favorably with those reported by Brown et al. (2010) (0.6×10^{-7} to 1.6×10^{-7} mol L^{-1} s^{-1}), Kirby and Elder-Brady (1998) (1.0×10^{-9} to 3.3×10^{-6} mol L^{-1} s^{-1}), Nordstrom (1985) (3.6×10^{-7} to 9.7×10^{-7} mol L^{-1} s^{-1}) and Sánchez España et al. (2007a) (4.0×10^{-7} to 5.5×10^{-6} mol L^{-1} s^{-1}). First-order rate constants varied by a factor of ~130 between all eleven sites but were grouped much more closely when binned into their separate geographic regions. When considered as two separate data sets (one for US, one for IPB), $k_{1st,field}$ values increased with decreasing emergent pH (Fig. 6A). The fastest first-order rate constants also occurred at sites where the pH increased across the TIF (Fig. 6B), and little dissolved Fe(T) was removed from solution. Laboratory-based first-order rate constants were also fastest for sites where less dissolved

Table 3
Summary of Fe(II) oxidation kinetics measured in the laboratory for seven of the eleven study sites.

Parameter	United States – Appalachian Bituminous Coal Basin						
	Natural sites					Engineered sites	
	BR	SL	SR	SUM-N	UR	DR	SUM-E
Mass (g)	96	93	101	87	155	54	111
Biomass concentration (pmols PLFA g^{-1})	25,172	6464	20,124	18,678	20,117	66,871	10,258
Surface area (cm^2)	38	41	63	47	101	56	73
$k_{1st,lab}$ ($min^{-1} * pmol\text{-}PLFA^{-1}) * 10^{11}$	18 ± 4	68 ± 37	14 ± 5	11 ± 2	10 ± 1	21 ± 4	31 ± 18
GDM (g Fe d^{-1} m^{-2})	5.0	2.6	3.0	8.7	7.7	6.6	5.1

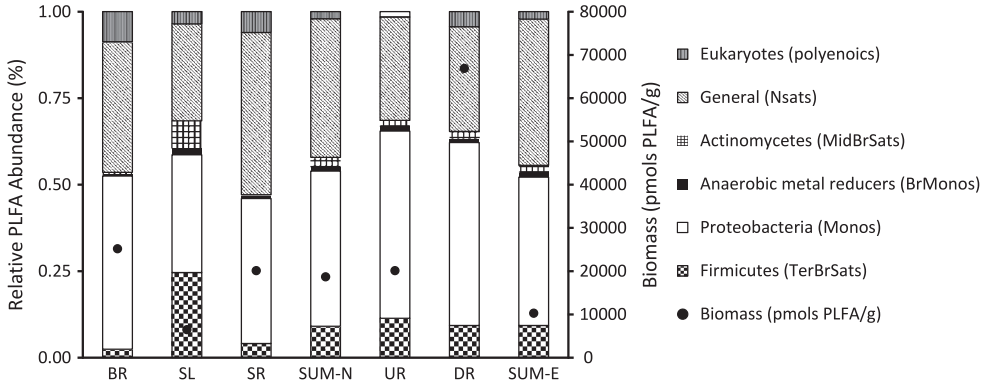

Fig. 8. Concentrations and distributions of phospholipid fatty acids (PLFAs) extracted from sediments used in laboratory experiments. The bar chart shows the relative distribution of each taxonomic group (%; left axis) and the filled circles show the total biomass concentration (pmols PLFA g^{-1}; right axis).

Fe(T) was removed from solution (Supplemental-8). In other words, faster Fe(II) oxidation rate constants occurred where less dissolved Fe(T) was removed from solution.

AMD passive treatment systems are often empirically sized on land area-based contaminant removal rates such as g Fe d^{-1} m^{-2} (Watzlaf et al., 2002; Ziemkiewicz et al., 1997). Using our flow-through laboratory sediment reactors we calculated area-based removal rates of 2.6–8.7 g Fe(T) d^{-1} m^{-2} (GDM) (Table 3). These results are consistent with Brown et al. (2010), who reported values of 3.4–6.3 GDM for similar laboratory reactors using sediments collected from several locations across the TIF at Upper Red Eyes (UR). In comparison, design guidelines for Fe removal from net-acidic coal mine drainage using aerobic wetlands range from 2 to 5 GDM (Hedin and Nairn, 1992). Our new data should support and solidify a design criteria of 4–8 GDM for low-pH Fe(II)-oxidizing TIFs.

The overarching goal of AMD treatment is neutralization of acidity and removal of metals. Therefore, an ideal treatment scenario would promote both Fe(II) oxidation and subsequent Fe(III) precipitation across a TIF. The engineered TIFs at GR and DR represent an ingenious (albeit serendipitous) modification to enhance the removal of Fe(T) and possibly other trace metals. Wider channels with lower water column depths will improve oxygen transfer and increase contact of AMD with the alkaline minerals lining the channel. Relatively low pH values were measured at GR and DR (2.4–3.1) yet substantial amounts of dissolved Fe(T) were removed from solution (Fig. 3). We propose that dissolution at the channel mineral-AMD interface created microenvironments with pH values higher than the bulk solution that promoted the precipitation of Fe(III). The relatively constant (or increasing) pH across the engineered TIFs at GR and DR was consistent with calcite dissolution balancing the acidity produced from Fe-hydrolysis and precipitation (Cravotta et al., 2004). Based on our field and laboratory results, the fastest rates of Fe(II) oxidation occurred in systems where relatively little Fe(T) was removed from solution. Therefore, we propose that natural and engineered features can be combined to maximize AMD treatment across a TIF. Natural TIFs would be retained to promote Fe(II) oxidation while a calcareous channel could be used to extend into an engineered TIF. This shallow channel would be similar to an oxidation ditch and distinct from a limestone bed. An oxidation ditch is shallow (0-cm bed depth with concrete, ~5-cm bed depth with gravel) as compared to a limestone bed (~1-m bed depth), and designed for open-channel flow as compared to flow through saturated porous media. This channel would not be intended to neutralize a large portion of the AMD acidity but instead serve as a substrate for Fe(II)-oxidizing bacteria and as an area for the accumulation of Fe(III) solids. Encouragingly, the armoring of the limestone at DR and the concrete at GR has not yet seemed to exert a negative effect on the performance of these engineering TIFs. The exact ratio of travel times across the natural and engineered sections would depend on site-specific conditions such as emergent geochemistry and land availability. This integration of natural and engineered TIFs will promote both Fe(II) oxidation and Fe(III) precipitation.

Acknowledgements

This work was partially supported by the US Office of Surface Mining Reclamation and Enforcement under Cooperative Agreement S11AC20005, by the Appalachian Research Initiative for Environmental Science (ARIES), and by the Spanish Ministry of Science and Innovation (project CGL2009-09070). ARIES is an industrial affiliates program at Virginia Tech, supported by members that include companies in the energy sector. The opinions and recommendations expressed herein are solely those of the authors and do not imply any endorsement by ARIES. The authors would like to thank Dr. Jenn Macalady, Christy Miller, Dr. Dan Jones, Carmen Falagán and Dr. Iñaki Yusta for their assistance in the field.

Appendix A. Supplementary material

Supplementary data associated with this article can be found, in the online version, at http://dx.doi.org/10.1016/j.apgeochem.2014.05.012.

References

Bigham, J.M., Schwertmann, U., Traina, S.J., Winland, R.L., Wolf, M., 1996. Schwertmannite and the chemical modeling of iron in acid sulfate waters. Geochim. Cosmochim. Acta 60, 2111–2121. http://dx.doi.org/10.1016/0016-7037(96)00091-9.

Brown, J.F., Jones, D.S., Mills, D.B., Macalady, J.L., Burgos, W.D., 2010. Application of a depositional facies model to an acid mine drainage site. Appl. Environ. Microbiol.. http://dx.doi.org/10.1128/aem.01550-10. AEM.01550-01510.

Burgos, W.D., Borch, T., Troyer, L.D., Luan, F., Larson, L.N., Brown, J.F., Lambson, J., Shimizu, M., 2012. Schwertmannite and Fe oxides formed by biological low-pH Fe(II) oxidation versus abiotic neutralization: Impact on trace metal sequestration. Geochim. Cosmochim. Acta 76, 29–44. http://dx.doi.org/10.1016/j.gca.2011.10.015.

Cánovas, C.R., Hubbard, C.G., Olías, M., Nieto, J.M., Black, S., Coleman, M.L., 2008. Hydrochemical variations and contaminant load in the Río Tinto (Spain) during flood events. J. Hydrol. 350, 25–40. http://dx.doi.org/10.1016/j.jhydrol.2007.11.022.

Chen, C.-J., Jiang, W.-T., 2012. Influence of waterfall aeration and seasonal temperature variation on the iron and arsenic attenuation rates in an acid mine drainage system. Appl. Geochem. 27, 1966–1978. http://dx.doi.org/10.1016/j.apgeochem.2012.06.003.

Cornell, R.M., Schwertmann, U., 1996. The Iron Oxides: Structure, Properties, Reactions, Occurence, and Uses, third ed. VCH, Weinheim, New York, Basel, Cambridge, Tokyo.

Cravotta, C.A., Kirby, C.S., District, N.C.C., 2004. Effects of abandoned coal-mine drainage on streamflow and water quality in the Shamokin Creek Basin, Northumberland and Columbia Counties, Pennsylvania, 1999–2001. US Department of the Interior, US Geological Survey.

Crittenden, J.C., Trussell, R.R., Hand, D.W., Howe, K.J., Tchobanoglous, G., 2012. MWH's Water Treatment: Principles and Design. Wiley.

DeSa, T., Brown, J., Burgos, W., 2010. Laboratory and field-scale evaluation of low-pH Fe(II) oxidation at Hughes Borehole, Portage, Pennsylvania. Mine Water Environ. 29, 239–247. http://dx.doi.org/10.1007/s10230-010-0105-5.

Druschel, G., Baker, B., Gihring, T., Banfield, J., 2004. Acid mine drainage biogeochemistry at Iron Mountain, California. Geochem. Trans. 5, 13.

Edwards, K.J., Gihring, T.M., Banfield, J.F., 1999. Seasonal variations in microbial populations and environmental conditions in an extreme acid mine drainage environment. Appl. Environ. Microbiol. 65, 3627–3632.

Gammons, C.H., Duaime, T.E., Parker, S.R., Poulson, S.R., Kennelly, P., 2010. Geochemistry and stable isotope investigation of acid mine drainage associated with abandoned coal mines in central Montana, USA. Chem. Geol. 269, 100–112. http://dx.doi.org/10.1016/j.chemgeo.2009.05.026.

Gammons, C.H., Nimick, D.A., Parker, S.R., Snyder, D.M., McCleskey, R.B., Amils, R., Poulson, S.R., 2008. Photoreduction fuels biogeochemical cycling of iron in Spain's acid rivers. Chem. Geol. 252, 202–213. http://dx.doi.org/10.1016/j.chemgeo.2008.03.004.

Hallberg, K.B., 2010. New perspectives in acid mine drainage microbiology. Hydrometallurgy 104, 448–453. http://dx.doi.org/10.1016/j.hydromet.2009.12.013.

Hedin, R.S., Nairn, R.W., 1992. Designing and sizing passive mine drainage treatment systems., 13th Annual WV Surface Mine Drainage Task Force Symposium. http://wvmdtaskforce.com/proceedings/1992.cfm.

Hedrich, S., Schlömann, M., Johnson, D.B., 2011. The iron-oxidizing proteobacteria. Microbiology 157, 1551–1564. http://dx.doi.org/10.1099/mic.0.045344-0.

Kirby, C.S., Elder-Brady, J.A., 1998. Field determination of Fe^{2+} oxidation rates in acid mine drainage using a continuously-stirred tank reactor. Appl. Geochem. 13, 509–520. http://dx.doi.org/10.1016/S0883-2927(97)00077-2.

Kirby, C.S., Cravotta, C.A., 2005. Net alkalinity and net acidity 1: theoretical considerations. Appl. Geochem. 20, 1920–1940. http://dx.doi.org/10.1016/j.apgeochem.2005.07.002.

Kirby, C.S., Thomas, H.M., Southam, G., Donald, R., 1999. Relative contributions of abiotic and biological factors in Fe(II) oxidation in mine drainage. Appl. Geochem. 14, 511–530. http://dx.doi.org/10.1016/s0883-2927(98)00071-7.

Leistel, J.M., Marcoux, E., Thiéblemont, D., Quesada, C., Sánchez, A., Almodóvar, G.R., Pascual, E., Sáez, R., 1997. The volcanic-hosted massive sulphide deposits of the Iberian Pyrite Belt Review and preface to the Thematic Issue. Miner. Deposi. 33, 2–30. http://dx.doi.org/10.1007/s001260050130.

Meruane, G., Vargas, T., 2003. Bacterial oxidation of ferrous iron by Acidithiobacillus ferrooxidans in the pH range 2.5–7.0. Hydrometallurgy 71, 149–158. http://dx.doi.org/10.1016/s0304-386x(03)00151-8.

Nagpal, S., 1997. A structured model for Thiobacillus ferrooxidans growth on ferrous iron. Biotechnol. Bioeng. 53, 310–319. http://dx.doi.org/10.1002/(sici)1097-0290(19970205)53:3<310::aid-bit10>3.0.co;2-o.

Nordstrom, D., 1985. The rate of ferrous iron oxidation in a stream receiving acid mine effluent. Selected papers in the hydrologic sciences: U.S. Geological Survey Water-Supply Paper 2270, p. 113-119.

Nordstrom, D.K., 2011. Hydrogeochemical processes governing the origin, transport and fate of major and trace elements from mine wastes and mineralized rock to surface waters. Appl. Geochem. 26, 1777–1791. http://dx.doi.org/10.1016/j.apgeochem.2011.06.002.

Nordstrom, D.K., Alpers, C.N., Ptacek, C.J., Blowes, D.W., 1999. Negative pH and extremely acidic mine waters from iron mountain, California. Environ. Sci. Technol. 34, 254–258. http://dx.doi.org/10.1021/es990646v.

Olem, H., Unz, R.F., 1977. Acid mine drainage treatment with rotating biological contactors. Biotechnol. Bioeng. 19, 1475–1491. http://dx.doi.org/10.1002/bit.260191006.

Pellicori, D.A., Gammons, C.H., Poulson, S.R., 2005. Geochemistry and stable isotope composition of the Berkeley pit lake and surrounding mine waters, Butte, Montana. Appl. Geochem. 20, 2116–2137. http://dx.doi.org/10.1016/j.apgeochem.2005.07.010.

Pennsylvania Department of Environmental Protection (DEP), 2010. 2010 Pennsylvania Integrated Water Qualiy Monitoring and Assessment Report; Clean Water Act, Section 305(b) Report and 303(d) List. Report, In Protection, D.o.E. (Ed).

Pesic, B., Oliver, D.J., Wichlacz, P., 1989. An electrochemical method of measuring the oxidation rate of ferrous to ferric iron with oxygen in the presence of Thiobacillus ferrooxidans. Biotechnol. Bioeng. 33, 428–439. http://dx.doi.org/10.1002/bit.260330408.

Price, W.A., 2003. Challenges posed by metal leaching and acid rock drainage, and approaches used to address them. In: Jambor, J.L., Blowes, D.W., Ritchie, A.I.M. (Eds.), Environmental Aspects of Mine wastes. In: Short Course Series, 31. Mineralogical Association of Canada, Vancouver, pp. 1–10.

Regenspurg, S., Brand, A., Peiffer, S., 2004. Formation and stability of schwertmannite in acidic mining lakes. Geochim. Cosmochim. Acta 68, 1185–1197. http://dx.doi.org/10.1016/j.gca.2003.07.015.

Sánchez España, J., López Pamo, E., Santofimia, E., Aduvire, O., Reyes, J., Barettino, D., 2005. Acid mine drainage in the Iberian Pyrite Belt (Odiel river watershed, Huelva, SW Spain): geochemistry, mineralogy and environmental implications. Appl. Geochem. 20, 1320–1356. http://dx.doi.org/10.1016/j.apgeochem.2005.01.011.

Sánchez España, J., López Pamo, E., Santofimia Pastor, E., 2007a. The oxidation of ferrous iron in acidic mine effluents from the Iberian Pyrite Belt (Odiel Basin, Huelva, Spain): field and laboratory rates. J. Geochem. Explor. 92, 120–132. http://dx.doi.org/10.1016/j.gexplo.2006.08.010.

Sánchez España, J., Santofimia Pastor, E., López Pamo, E., 2007b. Iron terraces in acid mine drainage systems: a discussion about the organic and inorganic factors involved in their formation through observations from the Tintillo acidic river (Riotinto mine, Huelva, Spain). Geosphere 3, 133–151. http://dx.doi.org/10.1130/ges00069.1.

Seal, R.R., Kiah, G.R., Nadine, M.P., Besser, J.M., Coles, J.F., Hammarstrom, J.M., 2010. Aquatic Assessment of the Ely Copper Mine Superfund Site, Vershire Vermont. US Geological Survey, Scientific Investigations Report 2010–5084.

Stookey, L.L., 1970. Ferrozine-–a new spectrophotometric reagent for iron. Anal. Chem. 42, 779–781. http://dx.doi.org/10.1021/ac60289a016.

Stumm, W., Morgan, J.J., 1996. Aquatic Chemistry: Chemical Equilibria and Rates in Natural Waters, third ed. John Wiley & Sons, New York.

Tarutis Jr, W.J., Stark, L.R., Williams, F.M., 1999. Sizing and performance estimation of coal mine drainage wetlands. Ecol. Eng. 12, 353–372. http://dx.doi.org/10.1016/s0925-8574(98)00114-1.

Trout Unlimited, 2011. The West Branch Susquehanna Recovery Benchmark Project. Trout Unlimited Eastern Abandoned Mine Program, Lock Haven, PA.

Watzlaf, G.R., Schroeder, K.T., Kleinmann, R.L.P., Kairies, C.L., Nairn, R.W., 2002. The Passive Treatment of Coal Mine Drainage. American Society of Mining and Reclamation, Lexington, Kentucky.

Webster, J.G., Swedlund, P.J., Webster, K.S., 1998. Trace metal adsorption onto an acid mine drainage iron(III) oxy hydroxy sulfate. Environ. Sci. Technol. 32 (10), 1361–1368.

White, D.C., Davis, W.M., Nickels, J.S., King, J.D., Bobbie, R.J., 1979. Determination of the sedimentary microbial biomass by extractible lipid phosphate. Oecologia 40, 51–62. http://dx.doi.org/10.1007/bf00388810.

Williamson, M.A., Kirby, C.S., Rimstidt, J.D., 2006. Iron dynamics in acid mine drainage. In: 7th Internat. Conf. Acid Rock Drainage. American Society of Mining and Reclamation, St. Louis, MO, pp. 2411–2423.

Yu, J.-Y., Heo, B., Choi, I.-K., Cho, J.-P., Chang, H.-W., 1999. Apparent solubilities of schwertmannite and ferrihydrite in natural stream waters polluted by mine drainage. Geochim. Cosmochim. Acta 63, 3407–3416. http://dx.doi.org/10.1016/s0016-7037(99)00261-6.

Ziemkiewicz, P.F., Skousen, J.G., Brant, D.L., Sterner, P.L., Lovett, R.J., 1997. Acid mine drainage treatment with armored limestone in open limestone channels. J. Environ. Qual. 26, 1017–1024. http://dx.doi.org/10.2134/jeq1997.00472425002600040013x.

Environmental Science & Technology

Article

pubs.acs.org/est

Thermodynamic Controls on the Kinetics of Microbial Low-pH Fe(II) Oxidation

Lance N. Larson,[†] Javier Sánchez-España,[§] Bradley Kaley,[†] Yizhi Sheng,[†,‡] Kyle Bibby,[⊥] and William D. Burgos*[,†]

[†]Department of Civil and Environmental Engineering, The Pennsylvania State University, University Park, Pennsylvania 16802, United States

[§]Instituto Geológico y Minero de España (IGME), c/Calera 1, 28760 Tres Cantos, Spain

[‡]School of Water Resources and Environment, China University of Geosciences, Beijing 100083 China

[⊥]Department of Civil and Environmental Engineering, University of Pittsburgh, 709 Benedum Hall, Pittsburgh, Pennsylvania 15261, United States

Supporting Information

ABSTRACT: Acid mine drainage (AMD) is a major worldwide environmental threat to surface and groundwater quality. Microbial low-pH Fe(II) oxidation could be exploited for cost-effective AMD treatment; however, its use is limited because of uncertainties associated with its rate and ability to remove Fe from solution. We developed a thermodynamic-based framework to evaluate the kinetics of low-pH Fe(II) oxidation. We measured the kinetics of low-pH Fe(II) oxidation at five sites in the Appalachian Coal Basin in the US and three sites in the Iberian Pyrite Belt in Spain and found that the fastest rates of Fe(II) oxidation occurred at the sites with the lowest pH values. Thermodynamic calculations showed that the Gibbs free energy of Fe(II) oxidation ($\Delta G_{oxidation}$) was also most negative at the sites with the lowest pH values. We then conducted two series of microbial Fe(II) oxidation experiments in laboratory-scale chemostatic bioreactors operated through a series of pH values (2.1−4.2) and found the same relationships between Fe(II) oxidation kinetics, $\Delta G_{oxidation}$, and pH. Conditions that favored the fastest rates of Fe(II) oxidation coincided with higher Fe(III) solubility. The solubility of Fe(III) minerals, thus plays an important role on Fe(II) oxidation kinetics. Methods to incorporate microbial low-pH Fe(II) oxidation into active and passive AMD treatment systems are discussed in the context of these findings. This study presents a simplified model that describes the relationship between free energy and microbial kinetics and should be broadly applicable to many biogeochemical systems.

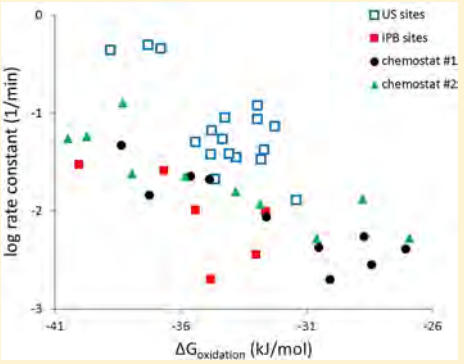

INTRODUCTION

Coal mine drainage (CMD) is the single largest cause of stream quality degradation in the Appalachian coal basins.[1] CMD can vary widely in its pH, acidity, and metal concentrations because of varied hydrogeochemical conditions. CMD sources also vary widely in their flow rates because of the relatively high, year-round rainfall in the Appalachian region and the presence of large underground mine pools. For example, in a study of 140 CMD sites (among thousands) in the Appalachian coal basins, Cravotta[2] reported that pH values ranged from 2.7 to 7.3, specific conductance ranged from 131 to 3,980 μS/cm, net acidity ranged from −326 to +1587 mg/L $CaCO_3$, total Fe ranged from 46 μg/L to 512 mg/L, and flow rate ranged from 0.028 to 2,210 L/s. Because of this great diversity in hydrogeochemical conditions, CMD remediation systems can be equally diverse in scale and biogeochemical processes employed for their treatment.

For acidic, Fe(II)-rich sources of CMD, microbial low-pH Fe(II) oxidation can be an effective component of an acid mine drainage (AMD) treatment system[3−5] At low-pH, abiotic Fe(II) oxidation by dissolved O_2 is slow. In contrast, the rate of microbial low-pH Fe(II) oxidation can be up to 5 orders of magnitude faster than abiotic oxidation.[6] However, the use of microbial low-pH Fe(II) oxidation for AMD treatment is limited because of uncertainties associated with its rate and ability to remove Fe from solution. For example, at a fixed pH of ~pH 3.0, rates of Fe(II) oxidation have been reported to vary by more than 3 orders of magnitude.[7] The solubility of schwertmannite, the predominant mineral stable under these geochemical conditions,[8,9] is also highly variable with respect to stoichiometry and log K_{sp} as values have been reported from 5.8 to 39.5.[8−12] Uncertainties with respect to Fe(II) oxidation kinetics and Fe(III) solubility confounds treatment design and performance prediction.

Received: March 18, 2014
Revised: July 28, 2014
Accepted: July 29, 2014
Published: July 29, 2014

 © 2014 American Chemical Society dx.doi.org/10.1021/es501322d | Environ. Sci. Technol. 2014, 48, 9246−9254

We hypothesized that the products of Fe(II) oxidation, that is, soluble versus insoluble Fe(III), contribute to the wide range in reported rates of low-pH Fe(II) oxidation. At many AMD sites, microbial low-pH Fe(II) oxidation has led to the formation of terraced iron formations[3,13,14] (TIFs). In acidic, sulfate-rich waters, schwertmannite[8] (nominally $Fe_8O_8(SO_4)_{1.5}(OH)_5(s)$[9]) is commonly found as the predominant mineral across the surface of these TIFs.[13,14] The oxidation of Fe(II) occurs by

$$Fe^{2+} + \frac{1}{4}O_2 + H^+ = Fe^{3+}(aq) + \frac{1}{2}H_2O \quad (1)$$

While the precipitation of Fe(III) as schwertmannite occurs by

$$8Fe^{3+} + \frac{3}{2}SO_4^{2-} + 13H_2O = 21H^+ + Fe_8O_8(SO_4)_{1.5}(OH)_5 \quad (2)$$

Such that the oxidative precipitation of schwertmannite at low-pH occurs by

$$Fe^{2+} + \frac{1}{4}O_2 + \frac{3}{16}SO_4^{2-} + \frac{9}{8}H_2O = \frac{13}{8}H^+ + \frac{1}{8}Fe_8O_8(SO_4)_{1.5}(OH)_5(s) \quad (3)$$

Acidophilic microorganisms are responsible for catalyzing reaction 1, while geochemical conditions (e.g., dissolved concentrations of Fe^{3+} and SO_4^{2-}, pH, temperature) control the extent of reaction 2. Pesic et. al[15] and Kirby et. al[16] have proposed a rate formulation for reaction 1 similar to

$$R_{Fe(II)} = -\frac{d[Fe(II)]}{dt} = k \cdot C_{bact} \cdot [O_2] \cdot [Fe(II)] \cdot [H^+] \quad (4)$$

where $R_{Fe(II)}$ is the rate of Fe(II) oxidation (mol Fe(II) L^{-1} s^{-1}), k is the rate constant (L^3 mg^{-1} mol^{-2} s^{-1}), C_{bact} is the concentration of Fe(II)-oxidizing bacteria (mg L^{-1}, dry weight), $[O_2]$ is the dissolved or atmospheric equivalent concentration of oxygen (mol L^{-1}), and Fe(II) and H^+ are in mol L^{-1}. Importantly, this rate formulation predicts that the kinetics of microbial low-pH Fe(II) oxidation will increase proportionally with decreasing pH. Consistent with this prediction, Larson et. al[17] found that field rates of Fe(II) oxidation measured at multiple sites in the Appalachian Bituminous Coal Basin and the Iberian Pyrite Belt (IPB) were fastest at the sites with the lowest pH values.

In the current study, we have developed a thermodynamic-based framework to describe how the kinetics of microbial low-pH Fe(II) oxidation increases as pH decreases under field and controlled laboratory conditions. We conducted a series of laboratory experiments using two separate chemostatic bioreactors operated at a range of pH values (pH 2.1−4.2) to compare to field measurements. Results obtained from these laboratory experiments and from geochemically distinct regions (i.e., Appalachia versus IPB) were all consistent with thermodynamic calculations. An applied objective of this research is to translocate the biogeochemical processes occurring on natural TIFs into more space-efficient bioreactors for AMD treatment and optimize reactor conditions to maximize Fe(II) oxidation rates. Design modifications for active and passive systems for AMD treatment are proposed based on this analysis.

METHODS AND MATERIALS

Laboratory Fe(II) Oxidation Experiments. Mixed cultures of naturally occurring microbes were enriched from two different sites in central Pennsylvania for use in chemostatic (with respect to pH and temperature) bioreactor experiments. Chemostat 1 used sediments and water collected from Brubaker Run (40° 37′ 1.42″ N, 78° 28′ 35.76″ W), a field site that displayed an "average" rate of Fe(II) oxidation (Table 1). Chemostat 2 used sediments and water collected from Scalp Level (40° 14′43.72″ N, 78° 51′33.18″ W), a field site that displayed the fastest rate of Fe(II) oxidation among all sites in this study. Sediments were collected from the top 2−3 cm of each TIF, 30−45 m downstream of the emergent AMD sources. Emergent AMD was collected in large plastic containers, filtered (0.2-μm) after transportation to the laboratory, then containers were wrapped in aluminum foil and stored at 4 °C. One hundred grams of moist sediment was mixed with 1 L of 0.1% (m/v) sodium pyrophosphate (adjusted to pH 3.5 with sulfuric acid) for 30 min at 400 rpm. The suspension was then allowed to settle and 900 mL of the cell-containing supernatant was transferred into a sterile 3-L chemostat reactor vessel (Eppendorf BioFlo/Celligen 115 Fermentor). The reactor volume was increased to 2 L by adding filtered site water. The chemostat was then operated in a no-flow, fed-batch mode for 6 weeks. During this time the pH set-point was pH 2.9 for chemostat 1 or pH 2.7 for chemostat 2, the stirring rate was 50 rpm, and the temperature was 20 °C. The headspace of the reactor was open to the ambient atmosphere. Ferrous sulfate was discontinuously added to the reactor as the primary substrate to enrich for Fe(II)-oxidizing microbes. Ferrous sulfate was added to yield 300 mg L^{-1} dissolved [Fe(II)] and added whenever the dissolved [Fe(II)] decreased below 30 mg L^{-1}. After less than a month, the enrichment cultures required a daily dose of Fe(II). The fed-batch enrichment mode continued until the reactor consistently maintained an Fe(II) oxidation rate of 10−14 mg Fe(II) L^{-1} h^{-1}.

The reactors were then switched to flow-through mode (hydraulic residence time of 6 h). During all flow-through experiments, influent water was flushed with 100% N_2(g) and $FeSO_4$ was added to yield an average influent dissolved Fe(II) concentration of 300 mg/L. For chemostat 1, the pH set-point was varied by starting at pH 2.9 and sequentially adjusting to pH 2.6, 2.3, 2.6, 2.9, 3.2, 3.5, 3.8, 4.1, 3.8, and 3.5. For chemostat 2, the pH set-point was varied by starting at pH 2.7 and sequentially adjusting to pH 2.4, 2.1, 2.4, 2.7, 3.0, 3.3, 3.6, 3.9, and 4.2. Automatic feedback controls maintained the pH set-point by adding either 0.1 M H_2SO_4 or 0.2 M NaOH. For each pH set-point, the chemostat was operated until it had achieved a pseudosteady state condition with respect to maintaining a near-constant effluent dissolved Fe(II) concentration. The operating time for each pH set-point ranged from 20 to 50 pore volumes for chemostat 1, but was fixed at 50 pore volumes for chemostat 2.

Influent and effluent Fe was measured as total and dissolved based on 0.2-μm filtration. Fe(II) was measured using the ferrozine assay.[18] Total Fe, Fe(T), was measured using the ferrozine assay after reduction by 0.5 M hydroxylamine in 0.5 M hydrochloric acid. Biomass samples were collected at the end of the fed-batch enrichment mode and at the end of each pseudosteady state condition. Biomass was collected from a unit area of the reactor wall (1 cm^2) and a unit volume of the

dx.doi.org/10.1021/es501322d | Environ. Sci. Technol. 2014, 48, 9246−9254

Table 1. Geochemical Characteristics of the Emergent Waters from the Eight Field Sites and Corresponding Fe(II) Oxidation Kinetics[a]

	Appalachian Coal Basin, United States				Iberian Pyrite Belt, Spain			
	Brubaker Run	Scalp Level	Sulfur Run	Summerlee	Upper Red Eyes	La Zarza	Pena del Hierro	Rio Tintillo
latitude/longitude	40°37′1.42″N 78°28′35.76″W	40°14′43.72″N 78°51′33.18″W	40°18′25.91″N 78°44′5.06″W	38°0′18.06″N 81°9′29.04″W	40°14′27.07″N 78°44′25.42″W	37°42′22.70″N 6°51′48.38″W	37°43′30.41″N 6°33′21.62″W	37°42′31.86″N 6°37′14.06″W
temp (°C)	11.0 ± 0.26	13.3 ± 0.67	10.4 ± 0.15	14.6 ± 0.64	9.38 ± 0.46	26.5 ± 0.4	16.9 ± 2.1	24.3 ± 0.3
DO (mg/L)	0.06 ± 0.05	0.30 ± 0.06	0.14 ± 0.03	0.53 ± 0.6	0.18 ± 0.04	1.18 ± 0.8	2.75 ± 3.66	2.60 ± 3.1
ORP (mV)	348 ± 37	386 ± 39	315 ± 34	194 ± 49	284 ± 41	323 ± 14	423 ± 28	368 ± 8.5
specific conductance (μS/cm)	1,690 ± 236	2,010 ± 24	859 ± 41	1,890 ± 147	2,647 ± 44	7,440 ± 395	4,650	18,900 ± 117
pH	3.37 ± 0.15	2.89 ± 0.08	3.48 ± 0.07	4.32 ± 0.64	4.04 ± 0.03	3.13 ± 0.04	2.36 ± 0.12	2.96 ± 0.01
dissolved total Fe (mg/L)	118 ± 27.9	97.4 ± 9.43	105 ± 6.4	278 ± 57	395 ± 8.4	2,930 ± 294	1,220 ± 32	2,640 ± 151
dissolved Fe(II) (mg/L)	114 ± 28.4	92.3 ± 11.9	102 ± 6.5	275 ± 57	383 ± 20	2,740 ± 229	1,090 ± 61	2,310 ± 50
sulfate (mg S/L)	381 ± 89	429 ± 34	212 ± 44	547 ± 37	903 ± 100	2,530	1,180	8,190
acidity (mg/L $CaCO_3$)[b]	360	357	325	642	1,220	6,910	3,310	16,400
total PLFA (pmol/g)	25,200	6,500	20,100	18,700	20,200	n.d.	n.d.	n.d.
$R_{Fe(II),field}$ ($\times 10^7$ mol L^{-1} s^{-1})	16.0 ± 6.1	81.3 ± 39.0	21.6 ± 10.2	29.1 ± 17.0	14.3 ± 3.4	13.1 ± 9.40	67.9 ± 16.2	30.7 ± 1.10
$k_{Fe(II),field}$ (min^{-1})	0.070 ± 0.032	0.399 ± 0.132	0.066 ± 0.039	0.034 ± 0.015	0.038 ± 0.004	0.003 ± 0.001	0.028 ± 0.003	0.010 ± 0.003
n	5	3	3	3	3	2	2	2

[a]Values represent mean ± one standard deviation for n sampling events. n.d. = not determined [b]Acidity calculated according to Kirby and Cravotta [45]using mean metal concentrations.

reactor contents (135 mL) to measure attached and suspended biomass concentrations, respectively. A colorimetric protein assay (Bio-Rad) was used to measure biomass and calculated as cells mL^{-1} based on the manufacturer's conversion factor and geometric features of the reactor vessel. Biomass samples from chemostat 1 were also characterized by pyrosequencing. Details of these laboratory experiments are provided in the Supporting Information and in Kaley.[19]

Assuming that the chemostat operated as a completely mixed flow-through reactor at steady state, the rate of Fe(II) oxidation in the laboratory ($R_{Fe(II),lab}$; mol Fe(II) L^{-1} s^{-1}) was calculated as

$$R_{Fe(II),lab} = -\frac{d[Fe(II)]}{dt} = \frac{([Fe(II)_{in}] - [Fe(II)_{out}])}{\theta_h} \quad (5)$$

where $[Fe(II)_{in}]$ is the influent dissolved Fe(II) concentration, $[Fe(II)_{out}]$ is the effluent dissolved Fe(II) concentration, and Θ_h is the hydraulic residence of the reactor. Assuming that the rate of Fe(II) oxidation was dependent on the dissolved Fe(II) concentration, the first-order rate constant for Fe(II) oxidation in the laboratory ($k_{Fe(II),lab}$; min^{-1}) was calculated as

$$k_{Fe(II),lab} = \frac{([Fe(II)_{in}] - [Fe(II)_{out}])}{[Fe(II)_{out}] \cdot \theta_h} \quad (6)$$

Field Measurements of Fe(II) Oxidation Rates. Eight mine-impacted sites with natural TIFs were sampled (Table 1). Five sites were located in the Appalachian Bituminous Coal Basin of the United States and three sites were located in the Iberian Pyrite Belt (IPB) of southwestern Spain. These sites were selected to ensure a broad spectrum of geochemical and hydrological conditions for our thermodynamic calculations, and to compare rates of Fe(II) oxidation in Appalachian coal mine drainage versus IPB metal mine drainage. Sites in the US contained discharges associated with bituminous coal or clay mining that occurred in the mid to-late twentieth century. Sites in the IPB contained discharges associated with metal mining that occurred since pre-Roman times until present-day, and the ore deposits were composed of massive sulfides dominated by pyrite.[20]

For each site, geochemical profiles were established as longitudinal transects downstream from the emergent source using a combination of field measurements, water samples, and physical site characteristics, along a single flow path which conveyed the majority of the water across each TIF. Portable field meters were used to measure pH, oxidation−reduction potential (ORP), dissolved oxygen (DO), and temperature. Dissolved Fe(II) and dissolved total Fe(T) (after reduction by hydroxylamine-HCl) were determined using the ferrozine assay[18] with filtered (0.2-μm) samples preserved with HCl. Dissolved Fe(III) concentrations were determined from the difference of dissolved total Fe(T) and dissolved Fe(II) measurements. Rates of Fe(II) oxidation in the field were calculated using concentrations of dissolved Fe(II) versus travel time. Stream velocities were measured at each sampling location and used to transform concentration-versus-distance plots into concentration-versus-travel time. Water velocities were measured using a food color dye as a tracer along with a stopwatch and tape measure. Assuming that each stream reach functioned as a plug flow reactor with no other inputs of flow or dissolved Fe(II), the rate of Fe(II) oxidation in the field ($R_{Fe(II),field}$; mol Fe(II) L^{-1} s^{-1}) was calculated as

$$R_{\mathrm{Fe(II),field}} = -\frac{\mathrm{d[Fe(II)]}}{\mathrm{d}t} = \frac{([\mathrm{Fe(II)}_{\mathrm{inflow}}] - [\mathrm{Fe(II)}_{\mathrm{outflow}}])}{t} \quad (7)$$

where $[\mathrm{Fe(II)}_{\mathrm{inflow}}]$ is the dissolved Fe(II) concentration at the inflow to the TIF (i.e., emergent source of AMD), $[\mathrm{Fe(II)}_{\mathrm{outflow}}]$ is the dissolved Fe(II) concentration at the outflow from the TIF, and t is the travel time of the water from the inflow to the outflow of the TIF. Assuming that the rate of Fe(II) oxidation was dependent on the dissolved Fe(II) concentration, the first-order rate constant for Fe(II) oxidation in the field ($k_{\mathrm{Fe(II),field}}$; min^{-1}) was calculated as

$$k_{\mathrm{Fe(II),field}} = \frac{-\ln\left(\frac{[\mathrm{Fe(II)}_{\mathrm{outflow}}]}{[\mathrm{Fe(II)}_{\mathrm{inflow}}]}\right)}{t} \quad (8)$$

Phospholipid fatty acids (PLFAs) were used to measure biomass concentrations in the sediments at the five US field sites. PLFAs were analyzed for PLFA by Microbial Insights, Inc. (Rockford, TN, US). Details of these field measurements are provided in the Supporting Information and in Larson et. al.[17]

Thermodynamic Calculations. On the basis of reaction 1, the Gibbs free energy for Fe(II) oxidation ($\Delta G_{\mathrm{oxidation}}$) was calculated as

$$\Delta G_{\mathrm{oxidation}} = \Delta G^0_{\mathrm{oxidation}} + RT\cdot\ln\left(\frac{\{\mathrm{Fe^{3+}}\}}{\{\mathrm{Fe^{2+}}\}\cdot\{\mathrm{O_2}\}^{1/4}\cdot\{\mathrm{H^+}\}}\right) \quad (9)$$

where $\Delta G^0_{\mathrm{oxidation}}$ was the standard state Gibbs free energy calculated from ΔG^0_{f} for all products and reactants,[21] and { } represents chemical activities for all dissolved species. $\Delta G^0_{\mathrm{oxidation}}$ was adjusted to different temperatures by assuming that $\Delta H^0_{\mathrm{oxidation}}$(298 K) and $\Delta S^0_{\mathrm{oxidation}}$(298 K) remained constant over the temperature range in this study[22] (9.3−26.2 °C). Ionic strength was calculated from conductivity using a correlation developed by the USGS based on 93 samples collected from 42 active mine water treatment plants in Pennsylvania, US that ranged from 250 to 13 000 μS/cm (Charles Cravotta III, 2014; personal communication). Activity coefficients for Fe^{2+} and Fe^{3+} were calculated with the Davies equation.[23] Measured values of pH equaled p{H^+}. The activity coefficient of O_2(aq) was assumed to equal 1 for all ionic strengths. Measured values of dissolved [Fe(II)], dissolved [Fe(III)], dissolved oxygen, pH, and temperature were then used in eq 9. On the basis of reaction 2, the standard state Gibbs free energy for schwertmanite precipitation ($\Delta G^0_{\mathrm{precipitation}}$) was calculated using an equilibrium constant of log K = 18.8 (25 °C).[9] The Gibbs free energy for the precipitation of schwertmannite ($\Delta G_{\mathrm{precipitation}}$) was calculated based on {H^+}, {Fe^{3+}}, and {SO_4^{2-}}. Details of these calculations are included in the Supporting Information.

RESULTS AND DISCUSSION

Evaluation of biogeochemical kinetics in the field is challenging because the microbial community often evolves in parallel with changing geochemical conditions. A sophisticated approach to measuring low-pH Fe(II) oxidation kinetics at field scale could attempt to account for biomass concentration (as in eq 4), microbial community composition, specific activity of community members, a suite of geochemical parameters (e.g., pH, O_2, Fe(II), Fe(III), sulfate, ...) and temperature, and then integrate all these factors across the stream reach. We have, instead, attempted to simplify our kinetic analysis and incorporate the effect of many system variables into a single first-order rate constant ($k_{\mathrm{Fe(II),field}}$ or $k_{\mathrm{Fe(II),lab}}$). There are several justifications for this approach. Geochemical gradients across these sites display similar trends,[13,14,17,24,25] microbial communities evolve in similar ways[13,25,26] (primarily controlled by pH[27]), biomass concentrations remain relatively constant along the reach,[13,24,25,28] and the specific activity of many Fe(II)-oxidizing bacteria (FeOB) are similar.[29]

Geochemical gradients are established downstream of each AMD source such that dissolved oxygen increases, pH decreases, Fe(II) decreases, Fe(III) increases, and total Fe decreases.[13,14,17,24,25] The microbial ecology shifts from photoautotrophs at the emergence to chemoautotrophs further downstream.[13,25−27] Microbes more tolerant of lower pH tend to become predominant as one moves downstream. As Fe(III) minerals and organic matter (algal biomass and leaf detritus) accumulate on the stream bottom, heterotrophic Fe(III) reduction also occurs at relatively shallow depths in the stream sediments.[30] The microbial community composition does not vary much from one site to another, being comprised primarily of some combination of *Ferrovum*, *Acidithiobacillus*, *Leptospirillum*, and *Acidiphilium*.[13,25,26] Measured cell abundance or cultivatable cell numbers along AMD-impacted streams remain relatively constant (within an order of magnitude).[13,24,25,28] In the current study, we found that total PLFAs in the sediments at four of the five U.S. sites were quite similar (Table 1). On the basis of these PLFA measurements, the microbial communities were also similar (Figure S1 of the Supporting Information). Finally, the specific rates of Fe(II) oxidation for eight different FeOBs, including *Ferrovum*, *Acidithiobacilli*, and *Leptospirillum*, have been shown to vary by less than a factor of 3.[29] One the basis of these previous studies and limited microbial characterizations of the US field sites, we have evaluated both field and laboratory kinetics using a first-order model (eqs 6 and 8) where $[H^+]$ is explicitly removed from the rate equation such that we can separately evaluate the effect of pH.

Rates of low-pH Fe(II) oxidation measured at the various field sites were consistently faster than previous studies[16,31−33] (Figure 1A). For each individual set of rates (US sites, IPB sites, chemostat 1, chemostat 2), the relatively fastest rates occurred at the lowest pH values. Rates from the US field sites ranged from 1.43×10^{-6} mol Fe(II) L^{-1} s^{-1} at pH 4.05 to 9.70×10^{-6} mol Fe(II) L^{-1} s^{-1} at pH 2.73 (Table 1). Rates from the IPB field sites ranged from 13.1×10^{-7} mol Fe(II) L^{-1} s^{-1} at pH 3.13 to 67.9×10^{-7} mol Fe(II) L^{-1} s^{-1} at pH 2.36. Rates from the chemostat experiments ranged from 1.05×10^{-7} mol Fe(II) L^{-1} s^{-1} at pH 3.50 to 2.44×10^{-7} mol Fe(II) L^{-1} s^{-1} at pH 2.40 (Tables 2 and 3). Laboratory rates were slower and, on a zero-order basis, less pH-dependent as compared to field rates. Sánchez Espana et al.[34] measured zero-order rates of Fe(II) oxidation in laboratory experiments and also found that the corresponding field rates were almost an order of magnitude faster than the laboratory rates.

The dotted line in Figure 1A is included to show how, when considering all the rates as one set of observations, these rates are consistent with the pH-dependency proposed in eq 4. The slope of −1·pH is derived directly from the stoichiometry of reaction 1, analogous to the slope of +2·pH for the rate-dependency of the oxidative precipitation of ferrihydrite ($Fe(OH)_3$(s)):

dx.doi.org/10.1021/es501322d | Environ. Sci. Technol. 2014, 48, 9246−9254

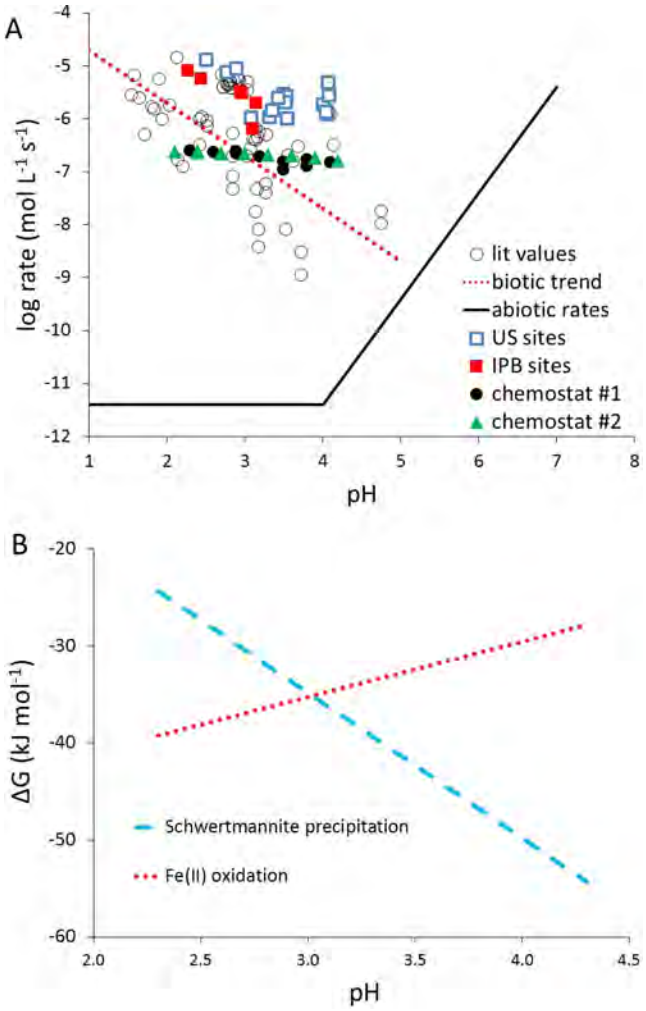

Figure 1. (A) Rates of Fe(II) oxidation reported from multiple studies and compared to the current study. Literature values compiled from Kirby and Elder Brady,[31] Sánchez-Espana et al.,[32] and Chen and Jiang.[33] Biotic trend included to show −1·pH dependency. Abiotic rates from Stumm and Lee.[43] (B) Gibbs free energy (ΔG) for microbial low-pH Fe(II) oxidation (reaction 1) and for schwertmannite precipitation (reaction 2). Conditions used for calculations are provided in the text and the Supporting Information.

$$Fe^{2+} + \frac{1}{4}O_2(aq) + \frac{5}{2}H_2O = 2H^+ + Fe(OH)_3(s) \quad (10)$$

shown by the rising solid line in Figure 1A. The dotted line in Figure 1B is the Gibbs free energy ($\Delta G_{oxidation}$) for Fe(II) oxidation (reaction 1) calculated using eq 9 and shows how this process becomes more favorable at lower pH. For the dotted line shown, $\{Fe^{3+}\}/\{Fe^{2+}\}$ was fixed at 10^{-2}, $\{O_2\}$ was fixed at 6.25 μM, temperature was 25 °C, and $\{H^+\}$ was the only variable. The values for the $\{Fe^{3+}\}/\{Fe^{2+}\}$ ratio and $\{O_2\}$ were selected to represent typical emergent AMD conditions. Thus, the pH-dependency of the rate of Fe(II) oxidation can be simply attributed to the amount of free energy available to the microbes catalyzing the reaction. Faster rates occur at lower pH values where $\Delta G_{oxidation}$ values are more negative.

In contrast to Fe(II) oxidation producing soluble Fe(III) (reaction 1), the precipitation of schwertmannite (reaction 2) becomes more energetically favorable as the pH increases between the pH range of 2.0−4.5 (Figure 1B). Microbes do not directly produce schwertmannite, instead a series of sequential abiotic reactions transform biogenic Fe(III) produced in reaction 1 into solid Fe(III). Assuming schwertmannite precipitation occurs according to reaction 2 and using an equilibrium constant of log K = 18.8 (25 °C),[9] $\Delta G_{precipitation}$ was calculated as a function of $\{H^+\}$ for fixed values of $\{Fe^{3+}\}$ and $\{SO_4^{2-}\}$ (per mol Fe). The dashed line in Figure 1B was calculated for $\{Fe^{3+}\}$ = 0.18 mM, $\{SO_4^{2-}\}$ = 10 mM, and 25 °C. The values for $\{Fe^{3+}\}$ and $\{SO_4^{2-}\}$ were selected to represent typical oxidized conditions for AMD that has been transported across a TIF.

First-order rate constants for Fe(II) oxidation were fastest at lower pH values (Figure 2A). Rate constants from the US field sites ranged from 0.034 min^{-1} at pH 4.07 to 0.465 min^{-1} at pH 2.73. Rate constants from the IPB field sites ranged from 0.002 min^{-1} at pH 3.10 to 0.030 min^{-1} at pH 2.27. Rate constants from the chemostat experiments ranged from 0.0020 min^{-1} at pH 3.50 with chemostat 1 (Table 2) to 0.128 min^{-1} at pH 2.40 with chemostat 2 (Table 3). Fe(II) oxidation kinetics measured in the field were 5-times slower at Brubaker Run (source of biomass for chemostat 1) as compared to Scalp Level (source of biomass for chemostat 2) (Table 1). However, differences in Fe(II) oxidation rates by the microbial communities enriched from these two sites were much smaller. Over the range of pH set-points tested, first-order rate constants for Fe(II) oxidation

Table 2. Biogeochemical Characteristics of the Laboratory Chemostat Reactor 1 (Brubaker Run) and Corresponding Fe(II) Oxidation Kinetics[a]

reactor pH	reactor O_2(aq) (mg L^{-1})	influent dissolved Fe(II) (mg L^{-1})	reactor biomass (×10^7 cell mL^{-1})	$R_{Fe(II),lab}$(×10^7 mol L^{-1} s^{-1})	$k_{Fe(II),lab}$ (min^{-1})	n
2.90	7.2 ± 1.1	346 ± 7.7	0.63	2.41	0.146	4
2.60	5.2 ± 0.3	313 ± 15	1.9	2.31	0.0226	3
2.30	5.9 ± 1.3	311 ± 15	0.94	2.43	0.0469	5
2.60	8.6	304	0.77	n.d.	n.d.	1
2.90	6.1 ± 0.3	299 ± 21	2.3	2.19	0.0212	2
3.20	6.4 ± 0.6	305 ± 5.5	1.1	1.92	0.0087	8
3.50	4.8 ± 0.3	306 ± 3.5	0.47	1.53	0.0042	3
3.80	4.1 ± 0.3	300 ± 2.5	1.2	1.65	0.0055	5
4.10	5.4 ± 2.1	301 ± 4.4	0.92	1.49	0.0041	5
3.80	3.9 ± 0.7	304 ± 0.0	0.48	1.27	0.0028	5
3.50	3.1 ± 0.7	303 ± 2.9	0.44	1.05	0.0020	6

[a]Values represent mean ± one standard deviation for n sampling points during pseudo-steady-state conditions. n.d. = not determined based on only one pseudo-steady-state time point.

dx.doi.org/10.1021/es501322d | Environ. Sci. Technol. 2014, 48, 9246−9254

Table 3. Biogeochemical Characteristics of the Laboratory Chemostat Reactor 2 (Scalp Level) and Corresponding Fe(II) Oxidation Kinetics[a]

reactor pH	reactor O_2(aq) (mg L^{-1})	influent dissolved Fe(II) (mg L^{-1})	reactor biomass ($\times 10^7$ cell mL^{-1})	$R_{Fe(II),lab}$ ($\times 10^7$ mol L^{-1} s^{-1})	$k_{Fe(II),lab}$ (min^{-1})	n
2.70	6.9 ± 0.4	314 ± 11.9	1.1	2.22	0.0161	5
2.40	7.5 ± 0.3	300 ± 12.0	1.8	2.44	0.128	2
2.10	7.8 ± 0.4	297 ± 12.5	0.94	2.36	0.0582	7
2.40	7.0 ± 0.1	295 ± 4.2	3.4	2.33	0.0556	2
2.70	7.9 ± 0.4	300 ± 4.2	4.9	2.22	0.0228	5
3.00	8.2 ± 0.3	297 ± 2.3	1.6	2.21	0.0245	4
3.30	8.1 ± 0.4	309 ± 9.4	1.4	2.08	0.0119	3
3.60	7.5 ± 0.3	292 ± 6.4	1.5	2.01	0.0135	6
3.90	7.7 ± 0.7	342 ± 11.7	2.3	1.86	0.00529	3
4.20	7.7 ± 0.3	299 ± 8.1	2.5	1.63	0.00536	5

[a]Values represent mean ± one standard deviation for n sampling points during pseudo-steady-state conditions.

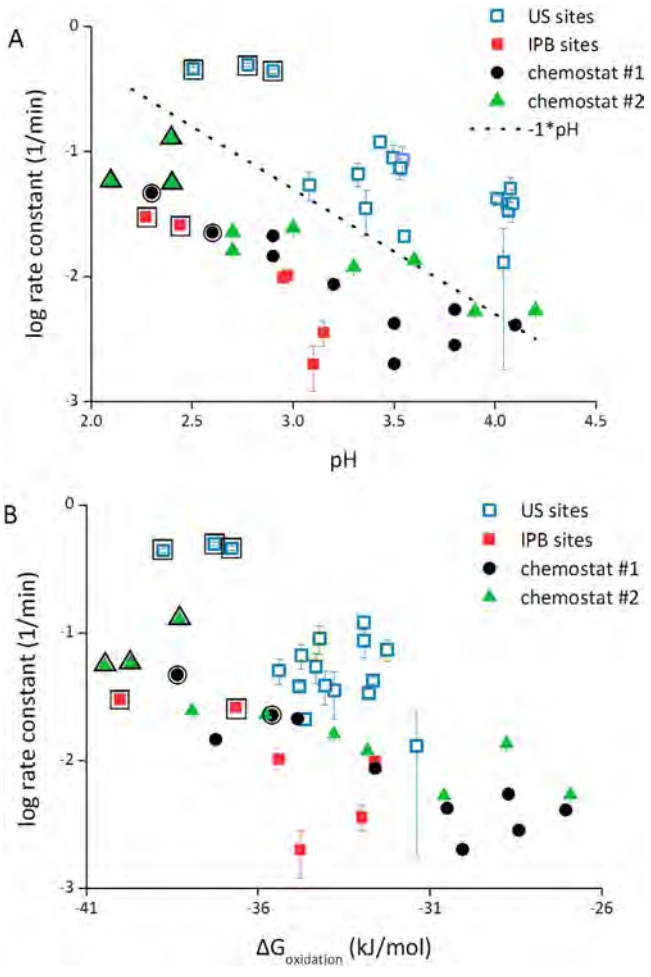

Figure 2. (A) First-order rate constants for Fe(II) oxidation versus pH. pH values for the field series were taken from the AMD emergence. pH values for the chemostat series were taken from the reactor set-point. The dotted line is included to show −1·pH dependency. Enlarged borders around select data points correspond to the same data in both panels A and B. Standard error shown with error bars, otherwise smaller than symbol. (B) First-order rate constants for Fe(II) oxidation versus Gibbs free energy for microbial low-pH Fe(II) oxidation ($\Delta G_{oxidation}$). $\Delta G_{oxidation}$ values were calculated based on site- and condition-specific geochemical measurements.

were 1.1-times slower in chemostat 1 as compared to chemostat 2. The convergence of these rates could have been caused by identical conditions used in the laboratory tests versus different physical and hydrodynamic conditions encountered at each field site. The −1·pH dotted line in Figure 2A is included only for visual reference.

The rate of microbial respiration has been shown to be dependent on the amount of free energy available to the microbes.[35,36] Jin and Bethke[35,36] proposed a rate law for microbial respiration that includes a thermodynamic factor (F_T) similar to a saturation index (Q/K_{sp}) term commonly used to adjust the kinetics of mineral precipitation/dissolution.[37] Their rate law was derived on the basis of chemiosmotic theory and accounts for forward and reverse fluxes through the electron transport chain and the energy required for ATP synthesis. Bethke et al.[38] validated this rate law by measuring and modeling the populations of sulfate reducers, iron reducers, and methanogens in long-term, energy-limited laboratory experiments. We hypothesized that the rate of low-pH Fe(II) oxidation in both the field and in our laboratory reactors were similarly controlled by free energy, in this case $\Delta G_{oxidation}$ as calculated by eq 9.

First-order rate constants for Fe(II) oxidation were dependent on the $\Delta G_{oxidation}$ calculated for each specific site and each specific chemostatic condition (Figure 2B). For the field sites, $\Delta G_{oxidation}$ was calculated based on the geochemical conditions (dissolved [Fe(II)], dissolved [Fe(III)], [O_2(aq)], pH, temperature, and conductivity) at the emergent source of AMD. For the chemostat experiments, $\Delta G_{oxidation}$ was calculated based on the geochemical conditions in the influent feed tank (dissolved [Fe(II)], dissolved [Fe(III)]) and in the reactor vessel ([O_2(aq)], pH, temperature, and conductivity). These geochemical conditions essentially represented the greatest potential energy for microbes to gain from oxidizing Fe(II). In contrast to the thermodynamic calculations presented in Figure 1B, only measured values were used for the data shown in Figure 2B.

Statistical analyses were employed to examine the significance of the relationships between the first-order rate constant versus pH (Figure 2A) and the first-order rate constant versus $\Delta G_{oxidation}$ (Figure 2B) for each series (US sites, IPB sites, chemostat 1, chemostat 2), and the difference of the regression slopes of each series by pairwise comparisons. t tests demonstrated that all regression equations for log rate constant-vs-pH described the data at a 95% significance level (Table S1 of the Supporting Information). All regression equations for log rate constant-vs-$\Delta G_{oxidation}$, except for the IPB sites, also described the data at a 95% significance level. Pair-

dx.doi.org/10.1021/es501322d | Environ. Sci. Technol. 2014, 48, 9246−9254

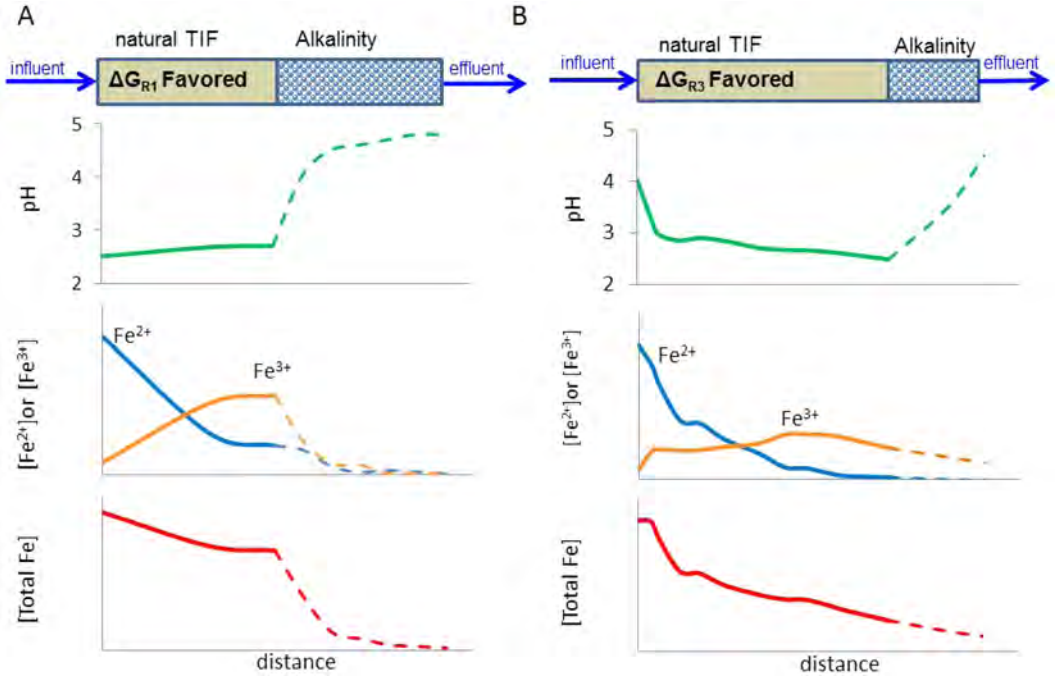

Figure 3. Conceptual schematics of passive treatment systems for anoxic, acidic, Fe(II)-rich acid mine drainage (AMD). An "engineered" terraced iron formation (TIF) would include a natural TIF followed by an alkaline channel. (A) Configuration for an extremely acidic discharge where the oxidation of Fe(II) to soluble Fe(III) (reaction 1) would be thermodynamically favored. Solid lines are observations from Scalp Level, dashed lines are conceptual predictions. (B) Configuration for a moderately acidic discharge where the oxidation of Fe(II) to insoluble Fe(III) (reaction 3) would be thermodynamically favored. Solid lines are observations from Upper Red Eyes.

wise comparisons of all the log rate constant-vs-pH regressions demonstrated that all slope coefficients were not significantly different at a 95% significance level (Table S2 of the Supporting Information). Similarly, all slope coefficients from the log rate constant-vs-$\Delta G_{oxidation}$ regressions were not significantly different.

The fastest rates of Fe(II) oxidation occurred at the lowest pH values and all corresponded with the most negative values of $\Delta G_{oxidation}$ (Figure 2). Enlarged symbols in Figure 2A and 2B are used to highlight the same data points in both panels for the four sets of rates. Less negative values of $\Delta G_{oxidation}$ for the chemostat experiments were caused by the partial oxidation of Fe(II) in the influent feed tank solutions. The fastest rates of Fe(II) oxidation also occurred under conditions where the production of soluble Fe(III) (reaction 1) was predominant versus the oxidative precipitation of schwertmannite (reaction 3). An increase in pH (i.e., consumption of H^+) is consistent with reaction 1 as compared to reaction 3. In the field, this was evident by a pH increase across the TIFs where the fastest rates of Fe(II) oxidation were measured (Table S3 of the Supporting Information). In the chemostat experiments, this was evident by titrant addition of acid to maintain the preset pH (Table S4 of the Supporting Information). The slower rates of Fe(II) oxidation occurred at higher pH values where schwertmannite precipitation became predominant as compared to the production of soluble Fe(III). In the chemostat experiments, this was evident by titrant addition of base to maintain the preset pH. In the field, this was evident by a pH decrease across the TIF and a decrease in dissolved Fe, plus the visual evidence of ocherous sediments deposited across the TIFs.

While $\Delta G_{oxidation}$ will become more negative as pH decreases (Figure 1B), we note that the correlation between field Fe(II) oxidation kinetics and pH will likely be valid over a limited pH range. In our study, pH values varied from 2.1 to 4.2 and span the great majority of pH conditions found in AMD systems worldwide.[39] We contend that the correlation between field Fe(II) oxidation kinetics and pH would likely apply from pH 2.0 to 5.0 for the following reasons. Low pH (<2.0) can be inhibitory to the growth and activity of FeOB, while precipitation of Fe(III) solids at higher pH (>4.0) can also inhibit FeOB.[40] We suspect that at extremely low pH values (<1.0), microbial diversity would be substantially less as compared to pH 2.1 to 4.2 because the optimum pH for growth of most acidophilic Fe(II) oxidizers is between pH 1.0 to 3.0.[41,42] Because biomass concentrations are incorporated into the first-order rate constant in our kinetic model (eq 8), slower rates would be measured at sites with lower biomass despite the high $\Delta G_{oxidation}$ available to the microbes. Because abiotic Fe(II) oxidation will become substantial above pH 5.0,[43,44] Fe(II) oxidation kinetics could increase even though $\Delta G_{oxidation}$ would decrease according to eq 9. Biomass concentrations remained relatively constant in the laboratory chemostat experiments (0.44×10^7 to 2.3×10^7 cell mL^{-1} in chemostat 1, Table 2; 0.94×10^7 to 4.9×10^7 cell mL^{-1} in chemostat 2, Table 3) supporting our approach to incorporate biomass into the first-order rate constant. On the basis of pyrosequencing of the biofilm samples collected from chemostat 1, the microbial communities remained relatively similar over the whole range of pH set-points (Figure S2 of the Supporting Information), also supporting our approach to incorporate the microbial community into the first-order rate constant.

■ ENVIRONMENTAL IMPLICATIONS

Microbial low-pH Fe(II) oxidation could be readily incorporated into passive treatment systems by enhancing natural TIFs

to create so-called engineered TIFs (Figure 3). Thermodynamic controls on the rates of low-pH Fe(II) oxidation and the predominant production of soluble Fe(III) versus insoluble Fe(III) solids would have important implications on how this process can best be exploited for AMD treatment. Regional geology and local hydrogeochemistry control the flow and geochemical conditions of the AMD that must be treated. Extremely acidic waters could be manipulated to promote the fastest rates of Fe(II) oxidation. The trade-off for exploiting faster rates at lower pH values is that less dissolved Fe will be removed. From field studies we have found that "oxidation channels" built from alkaline materials such as concrete or limestone remove significant amounts of dissolved Fe but with little change in pH.[17] Engineered TIFs, therefore, could be designed to use natural TIFs followed with an alkaline channel. The alkalinity in this channel would not be sized to neutralize the influent acidity but instead to counterbalance the acidity generated by Fe(III) precipitation within the channel. The hydrodynamics of the channel would be similar to the shallow sheet flow commonly seen across natural TIFs. The natural TIF would provide the microbial seed to colonize the downstream alkaline channel.

Conceptually, the relative sizes of the natural TIF and alkaline channel would be determined based on the thermodynamic favorability of the production of soluble Fe(III) (reaction 1) versus the production of schwertmannite (reaction 3). The solubility of schwertmannite (K_{sp}) and $\Delta G_{precipitation}$, and their noted uncertainties, will factor directly into the thermodynamic favorability of reaction 1 versus reaction 3. If an emergent AMD source was extremely acidic such that rapid production of soluble Fe(III) was favored, an equal-sized alkaline channel would be helpful to raise the pH and promote Fe(III) precipitation (Figure 3A). If an emergent AMD source had a pH that favored the oxidative precipitation of Fe(III), a relatively smaller sized alkaline channel would be used to help promote the removal of correspondingly lower concentrations of Fe(III). The geochemical trends shown as solid lines for the natural TIF portions in Figure 3 are from actual sites in the US; Figure 3A from Scalp Level, and Figure 3B from Upper Red Eyes. The geochemical trends shown as dashed lines for the alkaline channel portions are conceptual predictions.

Similarly, microbial low-pH Fe(II) oxidation could be incorporated into an active treatment system. In a pilot-scale three-chamber reactor system, pH was manipulated to optimize both Fe(II) oxidation and Fe(III) precipitation.[4] The first chamber was a suspended-growth bioreactor, the second chamber was used for pH adjustment to precipitate Fe(III), and the third chamber was an attached-growth bioreactor used to oxidize any remaining Fe(II). The fastest rate of Fe(II) oxidation occurred in the first chamber where the influent was pH 2.1 and the effluent increased to pH 2.3. The pH in the second reactor was adjusted with NaOH to pH 3.5 to rapidly precipitate schwertmannite from solution. A slower rate of Fe(II) oxidation occurred in the third chamber, where the influent was pH 3.5 and the effluent decreased to pH 3.3. In this example, the differing rates of Fe(II) oxidation as a function of pH were consistent with all of our field and laboratory studies—faster rates at lower pH where Fe(III) is more soluble.

AMD is a worldwide problem affecting important freshwater resources. Some of the areas most severely impacted by AMD are in arid and semiarid climates where water availability is an even greater issue. Low-pH Fe(II) oxidation can be incorporated into active or passive treatment systems for more cost-effective AMD treatment options. The treated water should be considered as an economic and natural resource for beneficial reuse. The geochemical conditions of the emergent AMD set thermodynamic conditions that influence both the rate and predominant products of Fe(II) oxidation. This simple linkage between thermodynamics and microbial kinetics should be broadly applicable to many other biogeochemical systems.

■ ASSOCIATED CONTENT

Supporting Information

Details of laboratory and field methods, details of thermodynamic calculations, regression equations, statistical comparison, change in pH across sites, titrant addition rates, and microbial characterizations. This material is available free of charge via the Internet at http://pubs.acs.org.

■ AUTHOR INFORMATION

Corresponding Author

*E-mail: wdb3@psu.edu.

Notes

The authors declare no competing financial interest.

■ ACKNOWLEDGMENTS

This work was partially supported by the US Office of Surface Mining Reclamation and Enforcement under Cooperative Agreement S11AC20005, by the Appalachian Research Initiative for Environmental Science (ARIES), and by the Spanish Ministry of Science and Innovation (project CGL2009-09070). ARIES is an industrial affiliates program at Virginia Tech, supported by members that include companies in the energy sector. The opinions and recommendations expressed herein are solely those of the authors and do not imply any endorsement by ARIES. This manuscript benefitted from comments and suggestions by three anonymous reviewers.

■ REFERENCES

(1) Trout Unlimited. *The West Branch Susquehanna Recovery Benchmark Project. A Watershed in Recovery*; Trout Unlimited: Lock Haven, PA, 2011; pp 1−12.

(2) Cravotta, C. A., III Dissolved metals and associated constituents in abandoned coal-mine discharges, Pennsylvania, USA. Part 1: Constituent quantities and correlations. *Appl. Geochem.* **2008**, *23*, 166−202.

(3) DeSa, T.; Brown, J.; Burgos, W. Laboratory and field-scale evaluation of low-pH Fe(II) oxidation at Hughes Borehole, Portage, Pennsylvania. *Mine Water Environ.* **2010**, *29* (4), 239−247.

(4) Hedrich, S.; Johnson, D. B. A modular continuous flow reactor system for the selective bio-oxidation of iron and precipitation of schwertmannite from mine-impacted waters. *Bioresour. Technol.* **2012**, *106*, 44−49.

(5) Janneck, E.; Arnold, I.; Koch, T.; Meyer, J.; Burghardt, D.; Ehinger, S. Microbial synthesis of schwertmannite from lignite mine water and its utilization for removal of arsenic from mine waters and for production of iron pigments. In *Proceedings of the International Mine Water Association*, Sydney, Nova Scotia, 2010; Wolkersdorfer, C.; Freund, A., Eds.; International Mine Water Association: Sydney, Nova Scotia, Canada, 2010; pp 131−134.

(6) Singer, P. C.; Stumm, W. Acidic mine drainage. Rate determining step. *Science* **1970**, *167*, 121−123.

(7) Nordstrom, D. *The Rate of Ferrous Iron Oxidation in a Stream Receiving Acid Mine Effluent*, Selected Papers in the Hydrologic Sciences, U.S. Geological Survey Water-Supply Paper 2270; U.S. Geological Survey: Reston, VA, 1985; pp 113−119.

(8) Bigham, J. M.; Schwertmann, U.; Traina, S. J.; Winland, R. L.; Wolf, M. Schwertmannite and the chemical modeling of iron in acid sulfate waters. *Geochim. Cosmochim. Acta* **1996**, *60* (12), 2111−2121.
(9) Sánchez-Espana, J.; Yusta, I.; Diez-Ercilla, M. Schwertmannite and hydrobasaluminite: A re-evaluation of their solubility and control on the iron and aluminium concentration in acidic pit lakes. *Appl. Geochem.* **2011**, *26* (9−10), 1752−1774.
(10) Caraballo, M. A.; Rimstidt, J. D.; Macías, F.; Nieto, J. M.; Hochella, M. F., Jr Metastability, nanocrystallinity and pseudo-solid solution effects on the understanding of schwertmannite solubility. *Chem. Geol.* **2013**, *360−361*, 22−31.
(11) Kawano, M.; Tomita, K. Geochemical modeling of bacterially induced mineralization of schwertmannite and jarosite in sulfuric acid spring water. *Am. Mineral.* **2001**, *86*, 1156−1165.
(12) Yu, J. Y.; Heo, B.; Choi, I. K.; Cho, J. P.; Chang, H. W. Apparent solubilities of schwertmannite and ferrihydrite in natural stream waters polluted by mine drainage. *Geochim. Cosmochim. Acta* **1999**, *63*, 3407−3416.
(13) Brown, J. F.; Jones, D. S.; Mills, D. B.; Macalady, J. L.; Burgos, W. D. Application of a depositional facies model to an acid mine drainage site. *Appl. Environ. Microbiol.* **2010**, *77*, 545−554.
(14) Sánchez Espana, J.; Santofimia Pastor, E.; López Pamo, E. Iron terraces in acid mine drainage systems: A discussion about the organic and inorganic factors involved in their formation through observations from the Tintillo acidic river (Riotinto mine, Huelva, Spain). *Geosphere* **2007**, *3*, 133−151.
(15) Pesic, B.; Oliver, D. J.; Wichlacz, P. An electrochemical method of measuring the oxidation rate of ferrous to ferric iron with oxygen in the presence of Thiobacillus ferrooxidans. *Biotechnol. Bioeng.* **1989**, *33* (4), 428−439.
(16) Kirby, C. S.; Thomas, H. M.; Southam, G.; Donald, R. Relative contributions of abiotic and biological factors in Fe(II) oxidation in mine drainage. *Appl. Geochem.* **1999**, *14* (4), 511−530.
(17) Larson, L. N.; Sánchez-Espana, J.; Burgos, W. Rates of low-pH biological Fe(II) oxidation in the Appalachian Bituminous Coal Basin and the Iberian Pyrite Belt. *Appl. Geochem.* **2014**, DOI: 10.1016/j.apgeochem.2014.05.012.
(18) Stookey, L. L. Ferrozine—A new spectrophotometric reagent for iron. *Anal. Chem.* **1970**, *42* (7), 779−781.
(19) Kaley, B. Low-pH Fe(II) oxidation using a bioreactor for the treatment of acid mine drainage. MS Thesis, The Pennsylvania State University, University Park, PA, 2013.
(20) Leistel, J. M.; Marcoux, E.; Thiéblemont, D.; Quesada, C.; Sánchez, A.; Almodóvar, G. R.; Pascual, E.; Sáez, R. The volcanic-hosted massive sulphide deposits of the Iberian Pyrite Belt review and preface to the thematic issue. *Miner. Deposita* **1997**, *33* (1−2), 2−30.
(21) Stumm, W.; Morgan, J. J. *Aquatic Chemistry: Chemical Equilibria and Rates in Natural Waters*, 3rd ed.; John Wiley and Sons: New York, 1996.
(22) Anderson, G. M. *Thermodynamics of Natural Systems*; Cambridge University Press: New York, 2008.
(23) Bethke, C. M. *Geochemical and Biogeochemical Reaction Modeling*, 2nd ed.; Cambridge University Press: New York, 2008.
(24) Walton, K. C.; Johnson, D. B. Microbiological and chemical characteristics of an acidic stream draining a disused copper mine. *Environ. Pollut.* **1992**, *76*, 169−175.
(25) Rowe, O. F.; Sánchez Espana, J.; Hallberg, K. B.; Johnson, D. B. Microbial communities and geochemical dynamics in an extremely acidic, metal-rich stream at an abandoned sulfide mine (Huelva, Spain) underpinned by two functional primary production systems. *Environ. Microbiol.* **2007**, *9* (7), 1761−1771.
(26) González-Toril, E.; Aguilera, A.; Souza-Egipsy, V.; López Pamo, E.; Sánchez Espana, J.; Amils, R. Geomicrobiology of La Zarza-Perrunal acid mine effluent (Iberian Pyritic Belt, Spain). *Appl. Environ. Microbiol.* **2011**, *77* (8), 2685−2694.
(27) Kuang, J.-L.; Huang, L.-N.; Chen, L.-X.; Hua, Z.-S.; Li, S.-J.; Hu, M.; Li, J.-T.; Shu, W.-S. Contemporary environmental variation determines microbial diversity patterns in acid mine drainage. *ISME J.* **2013**, *7*, 1038−1050.
(28) McGinness, S.; Johnson, D. B. Seasonal variations in the microbiology and chemistry of an acid mine drainage stream. *Sci. Total Environ.* **1993**, *132*, 27−41.
(29) Johnson, D. B.; Kanao, T.; Hedrich, S. Redox transformations of iron at extremely low pH: Fundamental and applied aspects. *Front. Microbiol.* **2012**, *3*, 96 DOI: 10.3389/fmicb.2012.00096.
(30) Coupland, K.; Johnson, D. B. Evidence that the potential for dissimilatory ferric iron reduction is widespread among acidophilic heterotrophic bacteria. *FEMS Microbiol. Lett.* **2008**, *279*, 30−35.
(31) Kirby, C. S.; Elder-Brady, J. A. Field determination of Fe^{2+} oxidation rates in acid mine drainage using a continuously-stirred tank reactor. *Appl. Geochem.* **1998**, *13* (4), 509−520.
(32) Sánchez Espana, J.; López Pamo, E.; Santofimia Pastor, E. The oxidation of ferrous iron in acidic mine effluents from the Iberian Pyrite Belt (Odiel Basin, Huelva, Spain): Field and laboratory rates. *J. Geochem. Explor.* **2007**, *92* (2−3), 120−132.
(33) Chen, C.-J.; Jiang, W.-T. Influence of waterfall aeration and seasonal temperature variation on the iron and arsenic attenuation rates in an acid mine drainage system. *Appl. Geochem.* **2012**, *27* (10), 1966−1978.
(34) Sánchez Espana, J.; López Pamo, E.; Santofimia Pastor, E. The oxidation of ferrous iron in acidic mine effluents from the Iberian Pyrite Belt (Odiel Basin, Huelva, Spain): Field and laboratory rates. *J. Geochem. Explor.* **2007**, *92*, 120−132, DOI: 10.1016/j.gexplo.2006.08.010.
(35) Jin, Q.; Bethke, C. M. A new rate law describing microbial respiration. *Appl. Environ. Microbiol.* **2002**, *69*, 2340−2348, DOI: 10.1128/AEM.69.4.2340-2348.2003.
(36) Jin, Q.; Bethke, C. M. Predicting the rate of microbial respiration in geochemical environments. *Geochim. Cosmochim. Acta* **2002**, *69*, 1133−1143, DOI: 10.1016/j.gca.2004.08.010.
(37) Lasaga, A. C. Rate Laws of Chemical Reactions. In *Kinetics of Geochemical Processes*; Lasaga, A. C., Kirkpatrick, R. J., Eds.; Mineralogical Society of America, BookCrafters Inc., Chelsea, MI, 1981; pp 1−68.
(38) Bethke, C. M.; Sanford, R. A.; Kirk, M. F.; Jin, Q.; Flynn, T. M. The thermodynamic ladder in geomicrobiology. *Am. J. Sci.* **2011**, *311*, 183−210.
(39) Nordstrom, D. K.; Alpers, C. N. Geochemistry of acid mine waters. In *The Environmental Geochemistry of Mineral Deposits, Part A. Processes, Techniques, and Health Issues*; Plumlee, G. S., Logsdon, M. J., Eds.; Society of Economic Geologists: Littleton, CO, 1999; Vol. *6A*, pp 133−156.
(40) Meruane, G.; Vargas, T. Bacterial oxidation of ferrous iron by *Acidithiobacillus ferrooxidans* in the pH range 2.5−7.0. *Hydrometallurgy* **2003**, *71*, 149−158.
(41) Baker-Austin, C.; Dopson, M. Life in acid: pH homeostasis in acidophiles. *Trends Microbiol.* **2007**, *15* (4), 165−171.
(42) Johnson, D. B. Biodiversity and ecology of acidophilic microorganisms. *FEMS Microbiol. Ecol.* **1998**, *27*, 307−317.
(43) Stumm, W.; Lee, G. F. Oxygenation of ferrous iron. *Ind. Eng. Chem.* **1961**, *53*, 143−146.
(44) Wehrli, B. Redox reactions of metal ions at mineral surfaces. In *Aquatic Chemical Kinetics*; John Wiley & Sons: New York, 1990.
(45) Kirby, C. S.; Cravotta, C. A. Net alkalinity and net acidity 1: Theoretical considerations. *Appl. Geochem.* **2005**, *20*, 1920−1940.

Geochemical niches of iron-oxidizing acidophiles in an acidic coal mine drainage

Daniel S. Jones[1,2†*], Courtney Kohl[1], Christen L. Grettenberger[1], Lance N. Larson[3,4], William D. Burgos[3], and Jennifer L. Macalady[1*]

[1]*Department of Geosciences, Penn State University, University Park, PA 16802, USA*

[2]*Current address: Department of Earth Sciences, University of Minnesota, Minneapolis, MN 55455, USA*

[3]*Department of Civil and Environmental Engineering, Penn State University, University Park, PA 16802, USA*

[4]*Current address: Natural Resources Defense Council, 1152 15th Street NW, Suite 300, Washington, DC 20005*

[*]*Correspondence: dsjones@umn.edu, jlm80@psu.edu*

Abstract

A legacy of coal mining in the Appalachians has provided a unique opportunity to study the ecological niches of iron-oxidizing microorganisms. Mine-impacted, anoxic groundwater with high dissolved metal concentrations emerges at springs and seeps associated with iron oxide mounds and deposits. These deposits are colonized by iron-oxidizing microorganisms that in some cases efficiently remove most of the dissolved iron at low pH, making subsequent treatment of the polluted stream water less expensive. We used full-cycle rRNA methods to describe the composition of sediment communities at two geochemically similar AMD discharges, Upper and Lower Red Eyes in Somerset County, PA, USA. The dominant iron-oxidizing microorganisms at both discharges were acidophilic *Gallionella*-like organisms, *"Ferrovum"* spp., and *Acidithiobacillus* spp. Archaea and *Leptospirillum* spp. were less than 2% of cells. The distribution of iron-oxidizing microorganisms at the two sites could be best explained by a combination of [Fe^{2+}] and pH. Populations of the *Gallionella*-like organism were restricted to locations with pH >3 and [Fe^{2+}] >4 mM, while *Acidithiobacillus* spp. were restricted to pH <3 and [Fe^{2+}] <4 mM. *"Ferrovum"* spp. were present at low levels in most samples, but dominated sediment communities where pH <3 and [Fe^{2+}] >4 mM. Our findings offer a predictive framework that could prove useful for describing the distribution of iron-oxidizing organisms in AMD, based on readily accessible geochemical parameters.

Introduction

Acid mine drainage (AMD) is the low pH, iron-rich discharge that occurs where pyrite (FeS_2) and other metal sulfide minerals in ore deposits or coal seams are exposed to atmospheric conditions by mining activity. AMD impacts over 10,000 km of streams in the Appalachian region of the United States alone, and the cost for AMD treatment worldwide may exceed US$100 billion using existing technologies (1-3). Widely applied treatment strategies include active and passive systems designed to accelerate iron oxidation and removal by raising the pH of the waste stream to circumneutral values (4). However, iron removal may also be achieved at low pH by promoting biological iron oxidation by acidophilic microorganisms. Low-pH biological iron oxidation could enhance existing passive treatment technologies, or be developed for novel alternative bioremediation strategies (e.g. 5, 6).

AMD generation by the oxidation of pyrite can be described with four reactions. Pyrite is initially oxidized by oxygen (equation 1) or Fe^{3+} (equation 2), which produces acid and Fe^{2+} ions.

$$FeS_2 + H_2O + \tfrac{7}{2}O_2 \rightarrow Fe^{2+} + 2SO_4^{2-} + 2H^+ \quad (1)$$

$$FeS_2 + 8H_2O + 14Fe^{3+} \rightarrow 15Fe^{2+} + 2SO_4^{2-} + 16H^+ \quad (2)$$

Fe^{2+} is subsequently oxidized to Fe^{3+} (equation 3), which may precipitate as iron oxyhydroxide minerals (equation 4) or act as an electron acceptor for further pyrite oxidation (equation 2).

$$Fe^{2+} + \tfrac{1}{4}O_2 + H^+ \rightarrow Fe^{3+} + \tfrac{1}{4}H_2O \quad (3)$$

$$Fe^{3+} + 3H_2O \rightarrow Fe(OH)_3 + 3H^+ \quad (4)$$

All four reactions can occur where the pyrite-bearing formation is exposed to oxygen, but iron oxidation and precipitation by equations 3 and 4 can continue to drive down pH values long after the discharge has been removed from the pyrite source. Iron is removed from solution by oxidation and Fe-oxide precipitation, but the abiotic oxidation of Fe^{2+} is very slow at pH values

63 <4 (7). Iron-oxidizing acidophiles can overcome this kinetic barrier and promote equation 3 even
64 under extremely acidic conditions, and thus play an important catalytic role in low-pH AMD
65 treatment.
66 Specific iron oxidation rates for acidophilic isolates range from 192-532 mg min^{-1} g
67 $protein^{-1}$ for autotrophic strains and 191-449 mg min^{-1} g $protein^{-1}$ for heterotrophic strains (8).
68 When different isolates were used to treat real and synthetic AMD in packed-bed bioreactors, a
69 betaproteobacterial isolate (later named "*Ferrovum myxofaciens*" (9)) achieved the fastest iron
70 oxidation rates while *Acidithiobacillus ferrooxidans* proceeded the slowest (10). Microbial
71 communities that develop naturally in AMD sediments also have different iron oxidation
72 capabilities. In experiments with sediments from Lower Red Eyes coal mine drainage in PA,
73 USA, cell-normalized iron oxidation rates were nearly twice as fast in reactors incubated with
74 *"Ferrovum"*-dominated sediments compared with *Acidithiobacillus*-dominated sediments (11).
75 In a subsequent study, cell-normalized iron oxidation rates determined for AMD sediments from
76 multiple drainages with different microbial assemblages varied by up to 7 times (12). Thus,
77 identifying and selecting for specific iron-oxidizing populations may improve the efficiency and
78 effectiveness of low pH bioremediation systems (e.g. 6).
79 Although diverse acidophilic iron-oxidizing organisms have been identified over the past
80 several decades, relatively little is known about what factors control their occurrence and
81 distribution in nature. pH seems to be especially important for controlling microbial distribution
82 in AMD (e.g. 13, 14). For example, a recent analysis of 59 AMD sites in China found that pH
83 was the most important explanatory variable across all sites (15). However, many taxa co-occur
84 in similar pH ranges, and other studies have found that environmental factors including dissolved
85 oxygen, conductivity, temperature, and iron and other metal concentrations are also important

controls on microbial community composition (14-20). In addition to contemporary environmental selection, microbial populations may also be affected by geographic isolation, which can maintain microbial communities independent of contemporary environmental factors by preserving the influence of past environmental factors or the history of stochastic microbial colonization (19, 21).

In this study we quantified microbial taxa across a geochemical gradient in two AMD springs, Upper and Lower Red Eyes, Pennsylvania, USA. Previous work at Lower Red Eyes showed that sediment microbial communities change with distance across the mound, and that distinct sediment communities exhibited different cell-normalized iron oxidation rates (11). In order to identify which variables controlled the distribution of acidophilic iron oxidizers at Upper and Lower Red Eyes, we performed a detailed analysis of microbial communities in and downstream from the two discharges including seasonal changes. We found that the distribution of the three most abundant iron-oxidizing populations could best be explained by a combination of pH and [Fe^{2+}].

Materials and Methods

Field sampling and geochemistry

Upper Red Eyes (URE) and Lower Red Eyes (LRE) drainages are located approximately 500 m apart in Somerset County, PA (URE, 40.2410 N, 78.7407 W, LRE, 40.2402 N, 78.7467 W). The AMD-impacted water at both locations is sourced from boreholes that channel underground drainage from nearby abandoned coal mines (11). The iron oxide mounds produced

by the drainages form a series of stepped pools and terraces as described in (11). Water flow is slow in pools and rapid where it cascades over vertical drops created by the terraces. The geochemistry of the sites is described in (11, 12).

We collected surface sediment and water samples in 2009-2011 at multiple locations along transects downstream from the springs. Samples for DNA extraction were immediately frozen in the field on dry ice and stored at -80^{o}C until analysis. Samples for FISH were fixed in 4% paraformaldehyde as described previously (22). Temperature, conductivity, dissolved oxygen, pH, and oxidation-reduction potential (ORP) were measured in the field using handheld meters (WTW, Weiheim, Germany; Oakton Instruments, IL, USA; or Beckman Coulter, CA, USA). Water samples for iron and trace metal analyses were filtered (0.2 μM) in the field and preserved with concentrated HCl and HNO_3, respectively. Total and ferrous iron were measured by the Ferrozine assay (23), and cations and trace metals were analyzed by inductively coupled plasma atomic emission spectroscopy (ICP-AES) at the Penn State Materials Characterization Laboratory.

Field ORP values measured against the standard calomel electrode were converted to standard hydrogen electrode (E_H) values as in (24), and converted to pe according to the relationship

$$pe = \frac{FE_H}{2.303RT}$$

in which F is Faraday's constant (C mol^{-1}), R is the gas constant (J mol^{-1} K^{-1}), and T is temperature (K). E_H values were only measured at URE, so we calculated E_H at LRE from activities of Fe^{2+} and Fe^{3+} according to the relationship

$$pe = pe^o - log\frac{\{Fe^{3+}\}}{\{Fe^{2+}\}}$$

in which pe^o is the empirically determined value at standard state (13 for the reaction Fe^{3+} + e- → Fe^{2+} (25)). Activity coefficients for Fe^{2+} and Fe^{3+} were calculated using the Davies equation (26). Ionic strength was calculated from specific conductivity values as in (27), using the average specific conductivities for URE and LRE (2.3 and 4.5 mS cm^{-1}, respectively). pe values from ORP field measurements at URE were in good agreement with calculated values from Fe^{3+}/Fe^{2+}, except at the emergent spring where oxygen is below detection and no Fe^{3+} was detectable (r^2=0.78, excluding values from the emergence) (Fig. S1).

DNA extraction and 16S rRNA gene sequencing

DNA was extracted from Red Eyes sediment samples as described in (28), after removing iron by repeated ammonium oxalate washes as described in (29). Environmental 16S rRNA genes were cloned from LRE sediment samples LRE21 and LRE22, collected 10.4 and 26.8 m downstream from the LRE emergence, respectively. Cloning was performed with bacterial primers 27f and 1492r as described in (28). Clones were end-sequenced at the Penn State Core Genomics Facility (ABI Hitachi 3730XL DNA analyzer with BigDye fluorescent terminator chemistry). An amplicon library was generated from sample LRE22 DNA extracts by pyrosequencing the hypervariable V6 region of the 16S rRNA gene. Amplification, barcoding and pyrosequencing (GS-FLX platform, Roche, Switzerland) were performed at the Marine Biological Laboratory (Woods Hole, MA) as in McCliment et al. (30).

Nearly full length 16S rRNA gene clones from this study were deposited in GenBank under accession numbers HQ420110-HQ420152 and KM488364-KM488407. The V6 amplicon library is available in VAMPS (http://vamps.mbl.edu) under the identifier LRE09_22_Bv6.

Fluorescence *in situ* hybridization

Fluorescence *in situ* hybridization (FISH) of AMD sediments was performed as described in (11). FISH probes and competitor oligonucleotides used in this study are listed in Table 1. The design and optimization of FISH probe FERRI643 was described in (11). We designed a new FISH probe (GAL177) to target the genus *Gallionella* and all *Gallionella*-like sequences retrieved from the study sites. We optimized GAL177 by testing a range of formamide stringencies from 0-45%, using a pure culture of *Acidithiobacillus thiooxidans* as a negative control (1 nucleotide mismatch). FISH was performed on multiwell Teflon®-coated glass slides, mounted with Vectashield (Vector Laboratories, CA, USA), viewed with a Nikon Eclipse 80i epifluorescence microscope, and photographed with a monochrome Photometrics Coolsnap ES2 CCD camera and NIS-Elements AS 3.0 software. The abundances of probe-labeled cells were obtained by counting at least 400 DAPI-stained cells for each sample and probe combination. The mean and standard deviation were calculated from counts of at least 8 microscope fields and at least two slide wells.

Phylogenetic, diversity, and other statistical analyses

Nearly-full length 16S rRNA gene clones were quality checked and assembled with CodonCode Aligner version 1.2.4 (CodonCode Corp., USA) and manually checked for ambiguities. Sequences were aligned to the 7,682-character Hugenholtz alignment using the NAST aligner at Greengenes (31). Clones were checked for chimeric sequences with Bellerophon 3 (32), and putative chimeras were removed. NAST-aligned sequences were loaded into an ARB database (33) containing over 500,000 nearly full-length sequences (base database from Greengenes (31), May, 2011). Alignments were manually refined using the ARB_Edit4

sequence editor. Prior to phylogenetic analyses, alignments were end-clipped to remove missing data, and positions with >50% gaps were filtered from the alignment (final alignment 1289 and 1383 positions for *"Ferrovum"* and *Gallionellaceae* analyses, respectively). Phylogenic analyses included the top BLAST matches to each sequences in Genbank, and their closest relatives in our ARB database. Neighbor joining analyses were performed in PAUP* v. 4b10 (34) with Jukes-Cantor-corrected distances and 2000 bootstrap replicates.

The LRE22 V6 amplicon library was uploaded to VAMPS (http://vamps.mbl.edu) and quality screened using the default VAMPS pipeline. Taxonomic assignments were performed using GAST software (35) and a 16S rRNA V6 reference database available at http://vamps.mbl.edu. Representative sequences for operational taxonomic units (OTUs) were extracted using mothur (36), and taxonomic assignments confirmed by BLASTN analysis (37) against the Silva 16S rRNA sequence database (38).

Non-metric multidimensional scaling (NMDS), canonical correspondence analyses (CCA), and other statistical analyses were performed using the vegan package (39) in R (40). Population data based on FISH were input as the average proportion of the total DAPI-stained cells labeled by each probe, as described above. Statistical analyses included the following two 'other' categories: 'other' *Gamma*- and *Betaproteobacteria* (GAMBET – (FERRI643 + GAL177 + THIO1)) and 'other' bacteria (EUBMIX – GAMBET). Prior to ordination analyses, environmental parameters were standardized to maximum values. Mantel tests (41) were performed in R using Bray-Curtis distance matrices and 999 permutations, with environmental parameters standardized by column maximum. Communities sampled from terrace sediments were compared to communities from the corresponding pool sample at LRE sites (indicated in Table 2) by ANOSIM analysis (41).

Results

Field observations and geochemistry

Upper and Lower Red Eyes drainages (URE and LRE) originate from anoxic springs with pH values between 4.0-4.5 and Fe^{2+} concentrations in excess of 6.5 mM (Fig. 1). Downstream from the springs, pH values and both Fe^{2+} and total Fe concentration decreased with distance. Downstream pH trends were generally consistent at different times of the year, but trends in water temperature and total Fe and Fe^{2+} differed according to season (Fig. 1). Dissolved oxygen was below detection at the springs, and approached saturation at all downstream sites (11, 12). In January 2011, thick ice prevented further downstream sampling at URE. Trace metal concentrations remained constant downstream at both sites (reported for LRE in (11), and URE in (12)).

Iron precipitates at URE and LRE form mounds characterized by stepped pools and terraces. Near the springs, iron-rich orange sediments were colonized by green benthic biofilms characteristic of the algae *Euglena* spp., which disappeared downstream. In stagnant pools, iron-oxide mineral precipitates exposed at the sediment-water interface were generally uncemented and easy to disturb. Well-cemented iron oxide precipitates were associated with water cascading over terrace rims. Iron oxide sediments at Red Eyes often display ‘cauliflower’ morphology characteristic of schwertmannite ($Fe_8O_8(OH)_6(SO_4)\cdot nH_2O$), consistent with the dominant mineralogy at the site reported in (11).

16S rRNA gene sequencing

We cloned 44 and 43 non-chimeric 16S rRNA gene sequences from samples LRE21 (10.4 m downstream of emergence) and LRE22 (26.8 m downstream of emergence), respectively. The most abundant phylotype in sample LRE22 (47% of clones) groups with the genus *"Ferrovum"* in the *Betaproteobacteria* (Fig. 2a). In contrast, the majority of sequences (84%) from LRE21 were >99% similar to chloroplasts of the algae *Euglena mutabilis*, and 12.5% were most closely related to a proteobacterial symbiont of another Euglenid, *Trachelomonas scabra* str. NJ T235. The remaining clone from LRE21 was from a sister group to the clade containing isolates of the neutrophilic iron-oxidizing genus *Gallionella* (Fig. 2b). For deeper characterization of sample LRE22, we created an amplicon library of the hypervariable V6 region of the 16S rRNA gene. We obtained 5,694 amplicons from sample LRE22, of which 77.2% were putative chloroplast sequences and 11.1% were mostly closely related to the same *Trachelomonas* sequence as above. The remaining 11.7% were from other bacteria, presumably representing the free-living bacterial community. Forty-two percent of those sequences were assigned to the *Gallionellaceae* family that includes the genus *Gallionella* and the single LRE21 clone (Fig. 2c).

The closest sequenced relatives to *Gallionellaceae* clones LRE21B36 and LRE22B18 (Fig. 2b) are environmental sequences from an acidic, iron-rich spa (42) and from an AMD treatment plant (43). These acidophilic sequences form a sister group to the clade containing *Gallionella ferruginea* and several environmental sequences from circumneutral iron-rich freshwater springs. We refer to these acidophilic organisms as "*Gallionella*-like" or as *Gallionellaceae*.

FISH probe design

Oligonucleotide probe GAL177 was designed to target the *Gallionellaceae* clade in the *Betaproteobacteria*, including the acidophilic clade containing Red Eyes clones LRE21B36 and LRE22B18 (Fig. 2b; Fig. 3). To ensure specificity of GAL177, we designed two competitor oligonucleotides, GAL177c1 and GAL177c2 (Table 1). The competitors bind to 1-mismatch sequences at probe position 14, which represent more than 95% of the 1-mismatch hits in our ARB database. The use of the competitors in an equimolar mixture with GAL177 consistently resulted in no visible signal from the 1-mismatch negative control cells at 20% formamide stringency.

The widely used FISH probes for *Betaproteobacteria* (BET42a) and *Gammaproteobacteria* (GAM42a) do not bind specifically to those clades (44). BET42a hits over 92% of the betaproteobacterial sequences but also 7% of the gammaproteobacterial sequences in a 23S rRNA gene database (Silva LSU ref database, version 115, (38)). Together, however, these two probes hit over 92% of the *Gamma-* and *Betaproteobacteria*, with only three mismatches outside of these groups. As it is now widely recognized that the *Betaproteobacteria* form a subgroup in the *Gammaproteobacteria* in rRNA gene phylogenies, we combined GAM42a and BET42a in an equimolar mixture (GAMBET) to target both groups (Table 1; Fig. 3).

Red Eyes sediment communities

Over 80% of cells in all samples stained with the bacteria-specific probe EUBMIX (Table 2; Fig. 4). Most samples were dominated by the *Gamma-* and *Betaproteobacteria* (probe GAMBET), except for the November transect at LRE, which had >40% other bacteria at all sites (Fig. 4b). The only other samples with <60% *Gamma+Betaproteobacteria* included the emergent

pool at LRE, which was dominated by bacteria with spirochete morphology (not shown), and the furthest downstream sites at URE, in which the proportion *Gamma+Betaproteobacteria* decreases with downstream distance (Fig. 4d).

Probes for the *Gallionellaceae* family (GAL177) and bacterial genera *Acidithiobacillus* (THIO1) and *"Ferrovum"* (FERRI653) each labeled over 80% of the cells in at least one sample (Table 2, Fig. 3). Probes for Archaea (ARCH915) and for the bacterial genus *Leptospirillum* (LF655) hybridized with less than 2% of cells in all samples. The relative abundance of THIO1, FERRI653, and GAL177-labeled cells changed downstream, with GAL177-positive cells generally most abundant near the springs, followed by FERRI643-positive cells, and finally THIO1-positive cells at some downstream sites (Fig. 4). Most samples contained over 5% FERRI643-positive cells, while GAL177- and THIO1-positive cells were absent from many samples (Table 2). THIO1-positive cells were abundant at downstream LRE sites (far from the spring), but never made up more than 3% of cells at URE. Groups present in rRNA gene libraries that we did not target using specific FISH probes include *Xanthamonadales* (*Gammaproteobacteria*), *Acidimicrobium* (*Actinobacteria*), and *Rhodospirallales* (*Alphaproteobacteria*).

Discussion

Microbial communities at Upper and Lower Red Eyes changed with distance downstream from the springs (Fig. 4). The microbial communities at each site also changed among sampling dates, as *Acidithiobacillus* became more abundant upstream at LRE in the fall relative to the spring, and the distribution of *Gallionellaceae* at URE was expanded in January as compared with April (Fig. 4). Dissimilarity among microbial communities was significantly correlated with

dissimilarity among sites based on all environmental parameters (Mantel test, r_M=0.41, p=0.001) and based on pH and Fe^{2+} concentration alone (Mantel test, r_M=0.42, p=0.001). Ordination analyses revealed that the major axes of variance among the Red Eyes microbial communities corresponded to changes in pH, Fe^{3+}, Fe^{2+}, and pe (Fig. 5). The abundance of *Gallionellaceae* was positively correlated with pH and Fe^{2+} (Spearman's ρ: pH = 0.68, $p < 0.001$; Fe^{2+} = 0.63, $p < 0.001$) and *Acidithiobacillus* was negatively correlated with pH and Fe^{2+} (Spearman's ρ: pH = -0.86, $p < 0.001$; Fe^{2+} = -0.76, $p < 0.001$). *"Ferrovum"* occurred at intermediate distances along stream transects and was not correlated with either (Spearman's ρ: pH = -0.04, p = 0.81; Fe^{2+} = 0.14, p = 0.46). At LRE, communities inhabiting terrace sediments were not statistically significantly different from communities inhabiting pool sediments (ANOSIM, R=-0.13, p = 0.78), which suggests that geochemical parameters affect the microbial community composition more than water flow velocity.

Because our sampling scheme effectively captured a wide range of pH, pe and Fe conditions, we were able resolve the effects of these individual parameters on microbial populations. We found that a combination of Fe^{2+} and pH better explains the distribution of microbial communities than any single parameter. Fig. 6 shows that the three most abundant iron oxidizers at Red Eyes occupied niches with distinct [Fe^{2+}] and pH values. *Gallionellaceae* were most abundant at locations with pH >3 and [Fe^{2+}] >4 mM, *"Ferrovum"* spp. predominated at sites with pH <3 and [Fe^{2+}] >4 mM, and *Acidithiobacillus* spp. were restricted to zones with pH <3 and [Fe^{2+}] <4 mM. pH alone does not explain the observed distribution of microbial populations. For example, both *Acidithiobacillus* and *"Ferrovum"* were abundant at pH values between 2.5 and 3, but *Acidithiobacillus* are restricted to areas with lower Fe^{2+}. The appearance of *Acidithiobacillus* spp. further upstream at LRE in October (cf. panel b vs. a in Fig. 4)

corresponds to lower [Fe^{2+}] at that time (Fig. 1). Indeed, the absence of *Acidithiobacillus* spp. at Upper Red Eyes is likely because pH remains close to 3 even at the most downstream sites (Fig. 1). Likewise, the abundance of *Gallionellaceae* populations downstream at URE in January versus April corresponds to higher [Fe^{2+}] in January. In a few samples, *"Ferrovum"* is abundant at pH >3 but low [Fe^{2+}], which suggests that it may also dominate under those conditions. However, further sampling will be required to describe the microbial communities that occur at pH >3 and low [Fe^{2+}].

Our analyses also showed that pH is inversely correlated with [Fe^{3+}], and [Fe^{2+}] is inversely correlated with pe (Fig. 5). This is likely because Fe-oxide precipitation has a strong impact on pH (equation 4), and because Fe^{2+} oxidation (equation 3) controls the redox potential in the AMD spring outflows (Fig. S1). Our results to do not exclude the possibility that pe, Fe^{3+}, or other parameters may play a role in determining microbial distributions at other AMD sites. The Red Eyes springs have only minor variations in dissolved trace metal and phosphorus concentrations (11, 12), a characteristic which may have allowed us to isolate the effects pH, pe and Fe on microbial community composition. Globally, AMD discharges are complex environments that encompass a much wider range in temperature, pH, conductivity, metal concentrations, and other environmental parameters that are potentially important for defining microbial niches.

Our finding that pH and Fe^{2+} explain the distribution of microbial populations at the Red Eyes AMD springs is consistent with physiological studies of acidophilic iron oxidizers. Iron is the primary energy source for lithotrophs in AMD, and the relative proportion of Fe^{2+} and Fe^{3+} is thought to select for certain AMD populations (e.g. 20). *"Ferrovum"* spp. occur in diverse AMD environments, including sites with extremely high [Fe^{2+}], up to 71 mM (9). pH is widely

336 considered an important variable in shaping AMD microbial communities, perhaps because it
337 reflects or controls other geochemical parameters. Additionally, acidity is an environmental
338 constraint that necessitates specific biological adaptations (45). Microbial acidophiles use a
339 variety of mechanisms to lower membrane permeability to H^+ ions, including reversed
340 membrane potential (46) and specialized membrane lipid structures (47, 48). pH also controls the
341 aqueous speciation of Fe-SO_4 complexes that impact ferrihydrite or schwertmannite
342 precipitation, which can impair cellular transport processes and impact the availability of Fe^{2+} to
343 microbial cells (49). Multiple studies have noted the role of pH in partially explaining microbial
344 community distribution in AMD (e.g. 13-15). Interestingly, in a study of pilot scale iron
345 oxidation bioreactors, a shift from *"Ferrovum"*- to *Gallionellaceae*-dominated communities
346 occurred with a slight increase in pH (to just above 3) and a slight decrease in Fe^{3+} during the
347 late stages of operation of one reactor (43). This study is consistent with the niches occupied by
348 *"Ferrovum"* and *Gallionellaceae* at our study sites.
349 Our results have implications for low-pH iron oxidation as a bioremediation strategy.
350 *"Ferrovum"* spp. have the highest specific iron oxidation rates of all strains reported measured
351 by (50), and Hedrich and Johnson (6) showed that *"Ferrovum"* biofilms were especially
352 effective in iron-oxidizing bioreactors. Indeed, in earlier work at LRE, *"Ferrovum"*-dominated
353 sediment communities outperformed *Acidithiobacillus*-dominated communities in flow-through
354 laboratory reactors (11). Little is known about the iron oxidation capabilities of the
355 *Gallionellaceae*-dominated communities, but perhaps geochemical conditions could be
356 manipulated in bioreactors or engineered treatment systems to preferentially select for
357 *"Ferrovum"* over *Gallionellaceae* to maximize Fe-oxidation rates or increase *"Ferrovum"*
358 biomass. More generally, a systematic framework like that presented here (Fig. 6), could help to

359 inform the design of future bioreactor and passive treatment systems and perhaps allow for the
360 selection of particular microbial communities or even specific iron-oxidizing strains.
361
362 **Acknowledgements**
363 This work was partially supported by the US Office of Surface Mining Reclamation and
364 Enforcement under Cooperative Agreement S11AC20005, and by NASA NAI (NNA04CC06A).
365 Special thanks to Linda Amaral-Zettler and Elizabeth McCliment for producing the rRNA gene
366 pyrotag library. We thank Juliana Brown, Daniel Mills, Trinh DeSa, Irene Schaperdoth and
367 Stephanie McPherson for assistance in the field and laboratory. D. Barrie Johnson kindly
368 provided us a culture of *"Ferrovum myxofaciens"* for the development of our FISH probe. We
369 thank Brent Means from the U.S. Office of Surface Mining and Malcolm Crittenden from the
370 Pennsylvania Department of Environmental Protection for insightful discussions and for
371 introducing us to the Red Eyes sites.
372
373
374

Figure captions

Table 1 Fluorescence *in situ* hybridization (FISH) probes used in this study

Table 2 FISH cell count and water chemistry data for Red Eyes sediment samples

FIG. 1 Changes in [Fe^{2+}] (black, top), total [Fe] (gray, top), pH (black, bottom), and temperature (gray, bottom) with distance at Lower and Upper Red Eyes.

FIG. 2 Neighbor joining phylograms of (a) the genus *"Ferrovum"*, and (b) the *Gallionellaceae*, including the *Gallionella*-like sequences from Red Eyes. Open circles indicate nodes supported by >90% bootstrap support. (c) Community composition of sample LRE21 based on pyrotag sequencing of the V6 region of 16S rRNA gene.

FIG. 3 Representative fluorescence *in situ* hybridization (FISH) photomicrographs of microbial communities in Red Eyes sediments. A *Euglena* cell is pictured in the upper left image. Autofluorescence in the lower left image is likely due to the presence of extracellular polymeric substances. White arrows in the upper right image indicate cells that do not hybridize with probe GAL177.

FIG. 4 Changes in the relative abundance of microbial taxonomic groups as a function of distance from the AMD springs at Upper and Lower Red Eyes. Points represent the relative abundance of FISH-labeled cells (as a percentage of total DAPI-stained cells), and error bars

represent one standard deviation. Panels A and B are Lower Red Eyes in April and November, 2009, respectively. Panels C and D are Upper Red Eyes in January and April, 2011, respectively.

FIG. 5 (A) Non-metric multidimensional scaling (NMDS) and (B) canonical correspondence analysis (CCA) ordinations of Red Eyes microbial communities, based on FISH data. Points are sample scores, vectors in (A) are environmental variables overlain on the NMDS (stress = 0.10 for the NMDS ordination), and vectors in (B) are constraining variables in the CCA. Parenthetical values in (B) are the percent of the total constrained variation explained by each axis. In total, 42.3% of total inertia is constrained in the CCA.

FIG. 6 Distribution of *"Ferrovum"*, *Acidithiobacillus,* and *Gallionella*-like organisms with respect to Fe^{2+} and pH. Points are scaled to the relative abundance of those organisms (as a percentage of total DAPI-stained cells). Black points indicate samples with <10% GAL177, FERRI643 and THIO1 hybridizing cells combined. Shaded regions indicate proposed niches for the respective organisms in the Red Eyes drainage.

References

1. **Herlihy AT, Kaufmann PR, Mitch ME, Brown DD.** 1990. Regional estimates of acid mine drainage impact on streams in the mid-Atlantic and southeastern United States. Water Air Soil Poll. **50:**91-107.
2. **Hudson-Edwards KA, Jamieson HE, Lottermoser BG.** 2011. Mine wastes: Past, present, future. Elements **7:**375-380.
3. **Tremblay G, Hogan C.** 2001. Mine Environment Neutral Drainage (MEND) Manual 5.4. 2d: Prevention and Control. Canada Centre for Mineral and Energy Technology. Natural Resources Canada, Ottawa.
4. **Johnson DB, Hallberg KB.** 2005. Acid mine drainage remediation options: a review. Sci. Total Environ. **338:**3-14.
5. **Burgos WD, Borch T, Troyer LD, Luan F, Larson LN, Brown JF, Lambson J, Shimizu M.** 2012. Schwertmannite and Fe oxides formed by biological low-pH Fe (II) oxidation versus abiotic neutralization: Impact on trace metal sequestration. Geochim. Cosmochim. Acta **76:**29-44.
6. **Hedrich S, Johnson DB.** 2012. A modular continuous flow reactor system for the selective bio-oxidation of iron and precipitation of schwertmannite from mine-impacted waters. Bioresour. Technol. **106:**44-49.
7. **Singer PC, Stumm W.** 1970. Acidic mine drainage: the rate-determining step. Science **167:**1121-1123.
8. **Johnson DB, Kanao T, Hedrich S.** 2012. Redox transformations of iron at extremely low pH: fundamental and applied aspects. Front. Microbiol. **3**.

9. **Johnson DB, Hallberg KB, Hedrich S.** 2014. Uncovering a microbial enigma: Isolation and characterization of the streamer-generating, iron-oxidizing, acidophilic bacterium "*Ferrovum myxofaciens*". Appl. Environ. Microbiol. **80:**672-680.

10. **Rowe OF, Johnson DB.** 2008. Comparison of ferric iron generation by different species of acidophilic bacteria immobilized in packed-bed reactors. Syst. Appl. Microbiol. **31:**68-77.

11. **Brown JF, Jones DS, Mills DB, Macalady JL, Burgos WD.** 2011. Application of a depositional facies model to an acid mine drainage site. Appl. Environ. Microbiol. **77:**545-554.

12. **Larson LN, Sánchez-España J, Burgos W.** 2014. Rates of low-pH biological Fe (II) oxidation in the Appalachian Bituminous Coal Basin and the Iberian Pyrite Belt. Appl. Geochem.

13. **Baker BJ, Banfield JF.** 2003. Microbial communities in acid mine drainage. FEMS Microbiol. Ecol. **44:**139-152.

14. **Lear G, Niyogi D, Harding J, Dong Y, Lewis G.** 2009. Biofilm bacterial community structure in streams affected by acid mine drainage. Appl. Environ. Microbiol. **75:**3455-3460.

15. **Kuang J-L, Huang L-N, Chen L-X, Hua Z-S, Li S-J, Hu M, Li J-T, Shu W-S.** 2012. Contemporary environmental variation determines microbial diversity patterns in acid mine drainage. ISME J. **7:**1038-1050.

16. **Edwards KJ, Gihring TM, Banfield JF.** 1999. Seasonal variations in microbial populations and environmental conditions in an extreme acid mine drainage environment. Appl. Environ. Microbiol. **65:**3627-3632.

17. **Schrenk MO, Edwards KJ, Goodman RM, Hamers RJ, Banfield JF.** 1998. Distribution of Thiobacillus ferrooxidans and Leptospirillum ferrooxidans: implications for generation of acid mine drainage. Science **279:**1519.

18. **Amaral-Zettler LA, Zettler ER, Theroux SM, Palacios C, Aguilera A, Amils R.** 2010. Microbial community structure across the tree of life in the extreme Rio Tinto. ISME J. **5:**42-50.

19. **Palacios C, Zettler E, Amils R, Amaral-Zettler L.** 2008. Contrasting microbial community assembly hypotheses: a reconciling tale from the Rio Tinto. PLoS One **3:**e3853.

20. **Rawlings D, Tributsch H, Hansford G.** 1999. Reasons why '*Leptospirillum*'-like species rather than *Thiobacillus ferrooxidans* are the dominant iron-oxidizing bacteria in many commercial processes for the biooxidation of pyrite and related ores. Microbiology **145:**5-13.

21. **Martiny JBH, Bohannan BJM, Brown JH, Colwell RK, Fuhrman JA, Green JL, Horner-Devine MC, Kane M, Krumins JA, Kuske CR.** 2006. Microbial biogeography: putting microorganisms on the map. Nat. Rev. Microbiol. **4:**102-112.

22. **Macalady JL, Jones DS, Lyon EH.** 2007. Extremely acidic, pendulous microbial biofilms from the Frasassi cave system, Italy. Environ. Microbiol. **9:**1402-1414.

23. **Stookey LL.** 1970. Ferrozine---a new spectrophotometric reagent for iron. Anal. Chem. **42:**779-781.

24. **Bourrié G, Trolard F, Jaffrezic J-MRG, Maître V, Abdelmoula M.** 1999. Iron control by equilibria between hydroxy-green rusts and solutions in hydromorphic soils. Geochim. Cosmochim. Acta **63:**3417-3427.

25. **Stumm W, Morgan J.** 1996. Aquatic chemistry, p. 1040, 3rd ed. Wiley, New York.

26. **Bethke CM.** 2010. Geochemical and biogeochemical reaction modeling, 2nd ed. Cambridge University Press, Cambridge.

27. **Larson LN, Kaley B, Sheng Y, Sánchez-España J, Burgos W.** *in review*. Thermodynamic Controls on the Kinetics of Microbial Low-pH Fe(II) Oxidation.

28. **Macalady JL, Dattagupta S, Schaperdoth I, Jones DS, Druschel GK, Eastman D.** 2008. Niche differentiation among sulfur-oxidizing bacterial populations in cave waters. ISME J. **2:**509-601.

29. **Senko JM, Wanjugi P, Lucas M, Bruns MA, Burgos WD.** 2008. Characterization of Fe (II) oxidizing bacterial activities and communities at two acidic Appalachian coalmine drainage-impacted sites. ISME J. **2:**1134-1145.

30. **McCliment EA, Nelson CE, Carlson CA, Alldredge AL, Witting J, Amaral-Zettler LA.** 2012. An all-taxon microbial inventory of the Moorea coral reef ecosystem. ISME J. **6:**309-319.

31. **DeSantis TZ, Hugenholtz P, Larsen N, Rojas M, Brodie EL, Keller K, Huber T, D D, Hu, Anderson GL.** 2006. Greengenes, a chimera-checked 16S rRNA gene database and workbench compatible with ARB. Appl. Environ. Microbiol. **72:**5069-5072.

32. **Huber T, Faulkner G, Hugenholtz P.** 2004. Bellerophon; a program to detect chimeric sequences in multiple sequence alignments. Bioinformatics **20:**2317-2319.

33. **Ludwig W, Strunk O, Westram R, Richter L, Meier H, Yadhukumar, Buchner A, Lai T, Steppi S, Jobb G, Förster W, Brettske I, Gerber S, Ginhart AW, Gross O, Grumann S, Hermann S, Jost R, König A, Liss T, Lüßmann R, May M, Nonhoff B, Reichel B, Strehlow R, Stamatakis A, Stuckmann N, Vilbig A, Lenke M, Ludwig T,**

Bode A, Schleifer K-H. 2004. ARB: a software environment for sequence data. Nucleic Acids Res. **32:**1363-1371.

34. **Swofford DL.** 2000. PAUP*: Phylogenetic analysis using parsimony and other methods (software). Sinauer Associates, Sunderland, MA.

35. **Huse SM, Dethlefsen L, Huber JA, Welch DM, Relman DA, Sogin ML.** 2008. Exploring microbial diversity and taxonomy using SSU rRNA hypervariable tag sequencing. PLoS Genet. **4:**e1000255.

36. **Schloss PD, Westcott SL, Ryabin T, Hall JR, Hartmann M, Hollister EB, Lesniewski RA, Oakley BB, Parks DH, Robinson CJ.** 2009. Introducing mothur: open-source, platform-independent, community-supported software for describing and comparing microbial communities. Appl. Environ. Microbiol. **75:**7537-7541.

37. **Altschul SF, Madden TL, Schäffer AA, Zhang J, Zhang Z, Miller W, Lipman DJ.** 1997. Gapped BLAST and PSI-BLAST: a new generation of protein database search programs. Nucleic Acids Res. **25:**3389-3402.

38. **Pruesse E, Quast C, Knittel K, Fuchs BM, Ludwig W, Peplies J, Glöckner FO.** 2007. SILVA: a comprehensive online resource for quality checked and aligned ribosomal RNA sequence data compatible with ARB. Nucleic Acids Res. **35:**7188-7196.

39. **Oksanen J, Kindt R, Legendre P, O'Hara R, Simpson GL, Stevens MHH.** 2008. Vegan: Community Ecology Package, R package version 1.11-0.

40. **R Core Development Team.** 2007. R: A language and environment for statistical computing. R Foundation for Statistical Computing, Vienna, Austria.

41. **McCune B, Grace JB.** 2002. Analysis of Ecological Communities. MjM Software Design, Gleneden Beach, OR.

42. **Hallberg KB, Coupland K, Kimura S, Johnson DB.** 2006. Macroscopic streamer growths in acidic, metal-rich mine waters in North Wales consist of novel and remarkably simple bacterial communities. Appl. Environ. Microbiol. **72:**2022-2030.

43. **Heinzel E, Janneck E, Glombitza F, Schlömann M, Seifert J.** 2009. Population dynamics of iron-oxidizing communities in pilot plants for the treatment of acid mine waters. Environ. Sci. Technol. **43:**6138-6144.

44. **Yeates C, Saunders AM, Crocetti GR, Blackall LL.** 2003. Limitations of the widely used GAM42a and BET42a probes targeting bacteria in the *Gammaproteobacteria* radiation. Microbiology **149:**1239-1247.

45. **Baker-Austin C, Dopson M.** 2007. Life in acid: pH homeostasis in acidophiles. Trends Microbiol. **15:**165-171.

46. **Cox JC, Nicholls DG, Ingledew W.** 1979. Transmembrane electrical potential and transmembrane pH gradient in the acidophile *Thiobacillus ferro-oxidans*. Biochem. J **178:**195-200.

47. **Macalady JL, Vestling MM, Baumler D, Boekelheide N, Kaspar CW, Banfield JF.** 2004. Tetraether-linked membrane monolayers in *Ferroplasma* spp: a key to survival in acid. Extremophiles **8:**411-419.

48. **Welander PV, Hunter RC, Zhang L, Sessions AL, Summons RE, Newman DK.** 2009. Hopanoids play a role in membrane integrity and pH homeostasis in *Rhodopseudomonas palustris* TIE-1. J. Bacteriol. **191:**6145-6156.

49. **Meruane G, Vargas T.** 2003. Bacterial oxidation of ferrous iron by *Acidithiobacillus ferrooxidans* in the pH range 2.5-7.0. Hydrometallurgy **71:**149-158.

50. **Hedrich S, Schlömann M, Johnson DB.** 2011. The iron-oxidizing proteobacteria. Microbiology **157:**1551-1564.

Table 1. Fluorescence *in situ* hybridization (FISH) probes used in this study

Probe name	Sequence (5'-3')	% formamide	specificity	label	source
EUB338	GCT GCC TCC CGT AGG AGT	0-50%	most Bacteria	FITC	Amann et al., 1990
EUB338-II	GCA GCC ACC CGT AGG TGT	0-50%	Planctomycetales	FITC	Daims et al., 1999
EUB338-III	GCT GCC ACC CGT AGG TGT	0-50%	Verrucomicrobiales	FITC	Daims et al., 1999
ARCH915	GTG CTC CCC CGC CAA TTC CT	20%	most Archaea	CY3	Stahl and Amann, 1991
THIO1	GCG CTT TCT GGG GTC TGC	35%	*Acidithiobacillus spp.*	CY3, CY5	Gonzalez-Toril et al. 2003
Ferri643	ACA GAC TCT AGC TTG CCA	35%	*Ferrovum spp.*	CY3	Brown et al., 2011
Gal177	TCC CCC TCA GGG CAT A	20%	*Gallionella spp.*	CY3	This study
Gal177c1	TCC CCC TCA GGG CTT A		competitor for gal177		This study
Gal177c2	TCC CCC TCA GGG CGT A		competitor for gal177		This study
LF655	CGC TTC CCT CTC CCA GCC T	35%	*Leptospirillum spp.*	CY3	Bond et al., 2001
BET42a	GCC TTC CCA CTT CGT TT	35%	most Betaproteobacteria, some Gammaproteobacteria	CY3	Manz et al., 1992
GAM42a	GCC TTC CCA CAT CGT TT	35%	most Gammaproteobacteria	CY3	Manz et al., 1992

EUBMIX is a mixture of EUB338, EUB338-II, and EUB338-III

GAMBET is a mixture of GAM42a and BET42a

GAM42a and BET42a target the 23S rRNA sequence. All other probes target the 16S rRNA sequence

Table 2. FISH cell count and water chemistry data for Red Eyes sediment samples

site	Date collected	Distance from emergence (m)	EUBMIX	GAMBET	GAL177	THIO1	FERRI643	Total Fe (mM)	Fe^{2+} (mM)	Fe^{3+} (mM)	pH	temp (°C)	pe[a]
URE	4/14/11	0	100.0 (±0.0)	86.6 (±3.1)	93.1 (±8.3)	0.0 (±0.0)	7.8 (±1.0)	6.90	6.96	0.00	4.01	9.5	10.04
URE	4/14/11	16.3	99.0 (±2.3)	74.9 (±9.2)	30.2 (±1.2)	0.0 (±0.0)	6.6 (±0.8)	6.69	6.73	0.00	3.53	11.1	10.05
URE	4/14/11	16.9	96.8 (±3.4)	93.8 (±3.3)	22.0 (±0.3)	0.0 (±0.0)	47.2 (±6.4)	3.98	3.67	0.31	3.26	12.7	11.56
URE	4/14/11	79.4	98.3 (±4.9)	73.1 (±14.1)	11.4 (±11.0)	1.0 (±2.3)	33.3 (±14.2)	2.93	2.75	0.19	3.13	17.0	11.46
URE	4/14/11	110.2	98.6 (±2.7)	54.3 (±13.2)	0.0 (±0.0)	2.8 (±5.3)	7.0 (±3.1)	2.56	2.00	0.56	3.05	18.0	12.07
URE	4/14/11	155.7	94.7 (±7.1)	32.9 (±12.9)	0.0 (±0.0)	1.1 (±2.9)	7.1 (±1.0)	2.14	1.43	0.71	2.95	20.1	12.33
URE	4/14/11	188	94.7 (±9.8)	20.3 (±11.7)	0.0 (±0.0)	1.5 (±2.9)	6.3 (±0.8)	1.93	1.14	0.79	2.89	21.8	12.47
URE	1/4/11	0	99.5 (±0.7)	71.7 (±2.5)	54.9 (±6.1)	0.0 (±0.0)	7.4 (±3.7)	7.09	6.60	0.49	4.02	8.7	11.50
URE	1/4/11	12.9	100.0 (±0.0)	82.2 (±5.9)	68.5 (±10.5)	0.0 (±0.0)	5.2 (±0.8)	6.74	6.44	0.30	3.78	6.2	11.30
URE	1/4/11	43.1	100.0 (±0.0)	96.7 (±3.6)	61.1 (±5.4)	0.0 (±0.0)	5.5 (±0.7)	5.36	4.68	0.68	3.25	3.1	11.79
URE	1/4/11	64.3	99.7 (±0.6)	97.1 (±1.4)	93.2 (±4.2)	0.0 (±0.0)	6.7 (±2.1)	5.23	4.22	1.01	3.15	0.9	12.01
LRE	4/21/09	0	99.4 (±1.0)	34.1 (±4.1)	0.0 (±0.0)	0.0 (±0.0)	0.0 (±0.0)	9.57	9.22	0.35	4.05	9.1	11.21
LRE	4/21/09	7	99.8 (±0.6)	76.0 (±2.8)	60.8 (±6.7)	0.0 (±0.0)	14.9 (±2.8)	8.50	8.43	0.07	3.37	13.3	10.57
LRE[b]	4/21/09	7	97.8 (±1.4)	93.5 (±7.7)	71.9 (±10.7)	0.0 (±0.0)	11.5 (±2.8)	8.50	8.43	0.07	3.37	13.3	10.94
LRE	4/21/09	10.4	96.9 (±3.6)	75.5 (±11.9)	73.6 (±8.2)	0.0 (±0.0)	12.7 (±5.6)	9.21	9.83	0.00	3.41	14.2	11.94
LRE	4/21/09	13.6	97.6 (±2.4)	78.9 (±5.0)	36.9 (±13.5)	0.0 (±0.0)	7.9 (±7.7)	9.09	7.55	1.54	3.15	12.0	12.29
LRE	4/21/09	26.8	99.7 (±0.9)	92.1 (±7.8)	13.8 (±8.9)	0.0 (±0.0)	77.9 (±5.7)	8.25	5.66	2.59	2.98	16.8	12.37
LRE[b]	4/21/09	26.8	98.6 (±1.4)	92.3 (±1.5)	35.7 (±10.9)	0.5 (±1.0)	62.2 (±11.2)	8.25	5.66	2.59	2.98	16.8	12.31
LRE	4/21/09	50.6	99.0 (±2.6)	86.7 (±5.5)	0.0 (±0.0)	4.2 (±5.8)	81.3 (±8.8)	7.13	4.59	2.54	2.78	17.1	10.57
LRE[b]	4/21/09	50.6	95.4 (±4.9)	90.7 (±4.9)	0.0 (±0.0)	4.1 (±4.4)	59.6 (±7.1)	7.13	4.59	2.54	2.78	17.1	12.29
LRE	4/21/09	58.8	94.0 (±3.8)	77.0 (±6.8)	0.0 (±0.0)	65.8 (±10.3)	3.5 (±3.5)	6.09	4.12	1.97	2.57	14.0	12.37
LRE[b]	4/21/09	58.8	97.2 (±3.4)	82.5 (±5.4)	0.0 (±0.0)	12.5 (±5.9)	59.0 (±6.2)	6.09	4.12	1.97	2.57	14.0	12.31
LRE	10/9/09	0	99.0 (±1.4)	56.3 (±4.7)	20.6 (±8.7)	0.0 (±0.0)	8.0 (±1.9)	9.56	9.21	0.36	4.24	9.0	11.22
LRE	10/9/09	7	100.0 (±0.0)	39.8 (±4.1)	18.9 (±5.7)	0.0 (±0.0)	7.6 (±2.8)	8.91	8.60	0.31	3.55	10.8	11.18
LRE	10/9/09	10.4	95.1 (±1.8)	45.4 (±8.5)	32.9 (±9.4)	0.0 (±0.0)	5.7 (±4.1)	8.72	7.15	1.57	3.51	12.7	11.97
LRE	10/9/09	13.6	92.9 (±2.8)	58.2 (±3.5)	18.0 (±6.5)	0.0 (±0.0)	29.5 (±6.1)	7.60	5.90	1.70	3.25	10.9	12.09
LRE	10/9/09	26.8	93.7 (±3.5)	55.5 (±6.4)	12.4 (±8.0)	17.6 (±9.0)	31.2 (±9.1)	6.33	3.91	2.42	2.99	13.5	12.42
LRE	10/9/09	50.6	89.1 (±3.7)	51.8 (±7.0)	0.0 (±0.0)	34.2 (±5.3)	6.8 (±4.0)	3.61	1.75	1.86	2.92	14.0	12.66
LRE	10/9/09	58.8	84.1 (±4.3)	54.7 (±6.8)	0.0 (±0.0)	47.2 (±6.0)	0.7 (±0.7)	4.14	1.99	2.16	2.64	13.6	12.66
LRE[b]	10/9/09	58.8	79.0 (±4.6)	53.7 (±4.9)	0.0 (±0.0)	46.4 (±7.8)	3.0 (±1.8)	4.14	1.99	2.16	2.64	13.6	12.66
LRE	6/7/09	58.8	99.5 (±0.6)	96.3 (±2.5)	0.0 (±0.0)	87.0 (±3.0)	0.8 (±1.2)	6.49	3.59	2.90	2.65	18.3	12.54

URE = Upper Red Eyes, LRE = Lower Red Eyes. Numbers in parentheses after FISH counts represent 1 standard deviation

[a]pe calculated from $\{Fe^{2+}\}/\{Fe^{3+}\}$

[b]samples collected from terrace sediments in fast-flowing water. (All other samples collected from pool sediments.) Terrace samples were collected just below the corresponding pool sample above.

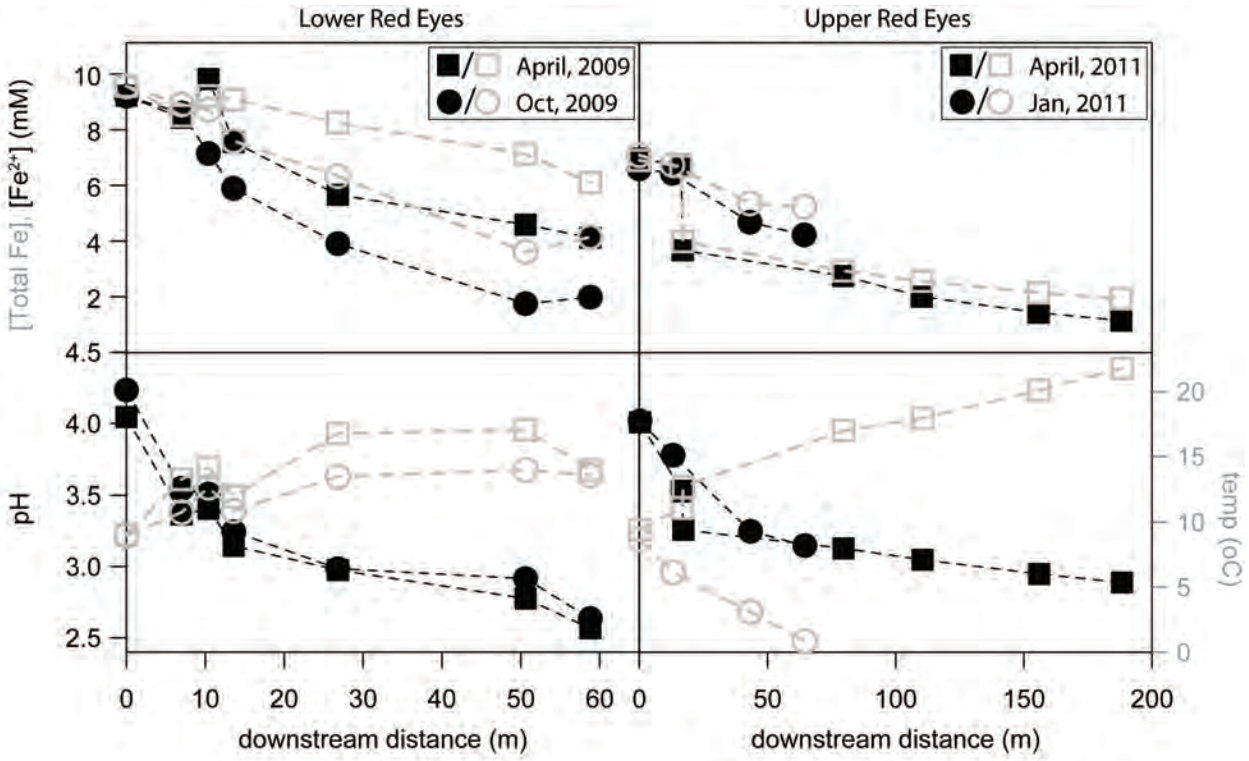

FIG. 1 Changes in [Fe^{2+}] (black, top), total [Fe] (gray, top), pH (black, bottom), and temperature (gray, bottom) with distance at Lower and Upper Red Eyes.

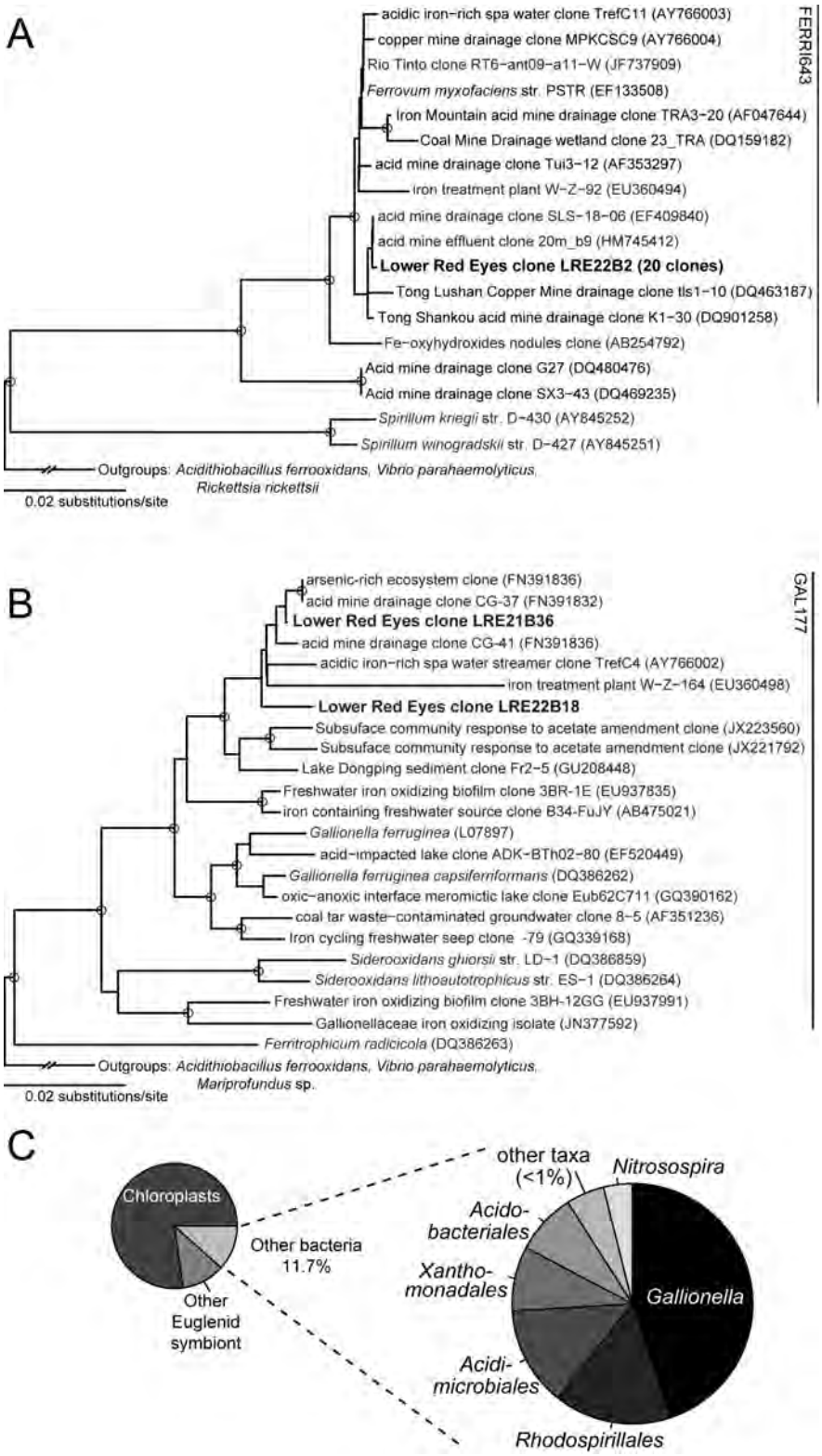

FIG. 2 Neighbor joining phylograms of (a) the genus "*Ferrovum*", and (b) the *Gallionellaceae*, including the *Gallionella*-like sequences from Red Eyes. Open circles indicate nodes supported by >90% bootstrap support. (c) Community composition of sample LRE21 based on pyrotag sequencing of the V6 region of 16S rRNA gene.

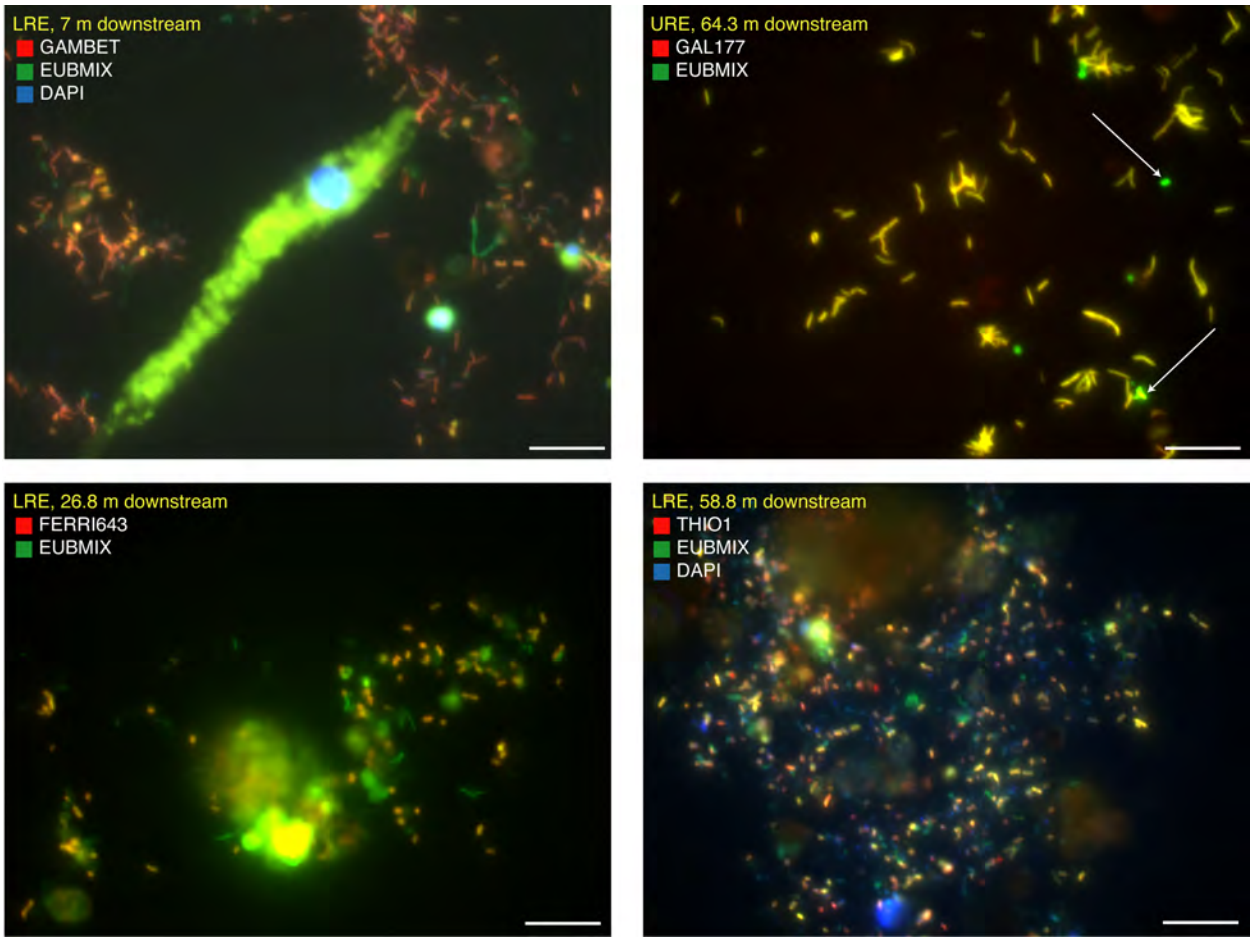

FIG. 3 Representative fluorescence *in situ* hybridization (FISH) photomicrographs of microbial communities in Red Eyes sediments. A *Euglena* cell is pictured in the upper left image. Autofluorescence in the lower left image is likely due to the presence of extracellular polymeric substances. White arrows in the upper right image indicate cells that do not hybridize with probe GAL177.

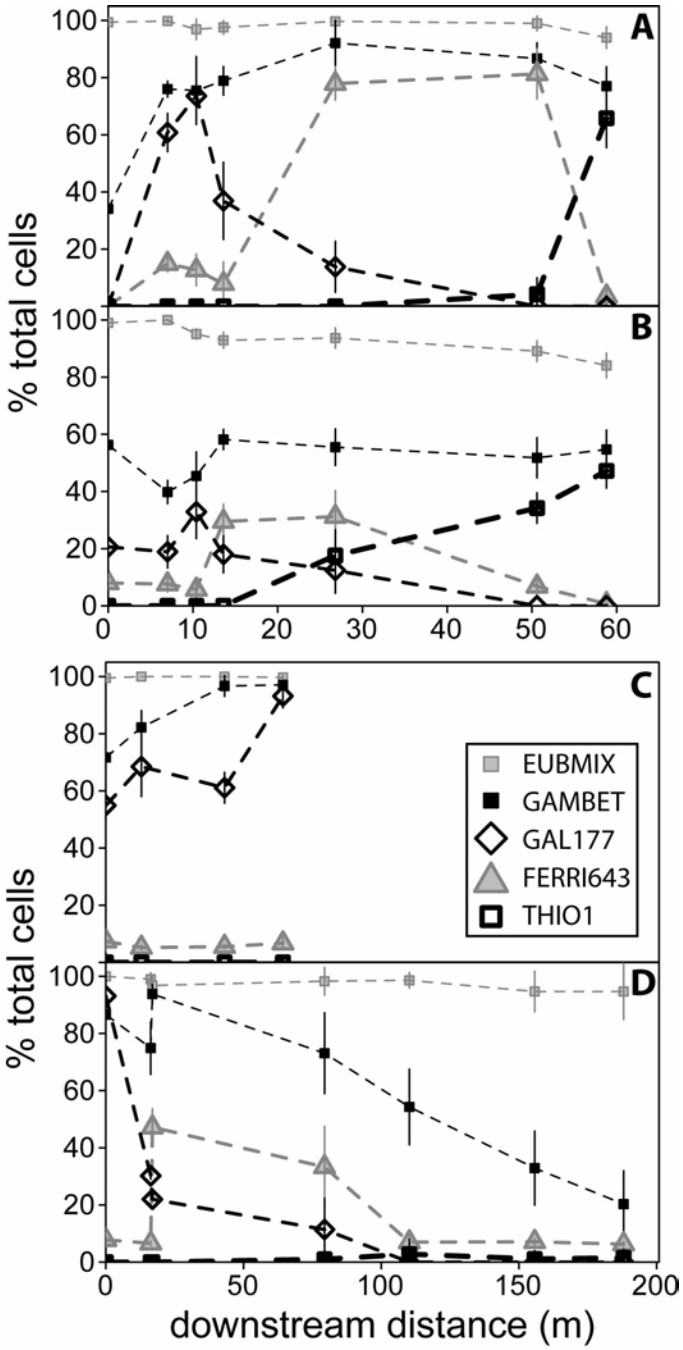

FIG. 4 Changes in the relative abundance of microbial taxonomic groups as a function of distance from the AMD springs at Upper and Lower Red Eyes. Points represent the relative abundance of FISH-labeled cells (as a percentage of total DAPI-stained cells), and error bars represent one standard deviation. Panels A and B are Lower Red Eyes in April and November, 2009, respectively. Panels C and D are Upper Red Eyes in January and April, 2011, respectively.

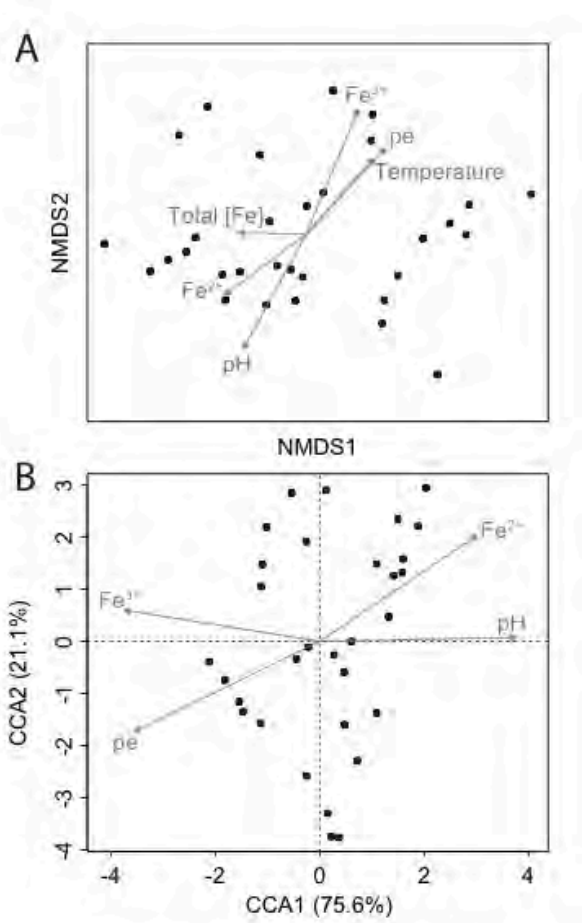

FIG. 5 (A) Non-metric multidimensional scaling (NMDS) and (B) canonical correspondence analysis (CCA) ordinations of Red Eyes microbial communities, based on FISH data. Points are sample scores, vectors in (A) are environmental variables overlain on the NMDS (stress = 0.10 for the NMDS ordination), and vectors in (B) are constraining variables in the CCA. Parenthetical values in (B) are the percent of the total constrained variation explained by each axis. In total, 42.3% of total inertia is constrained in the CCA.

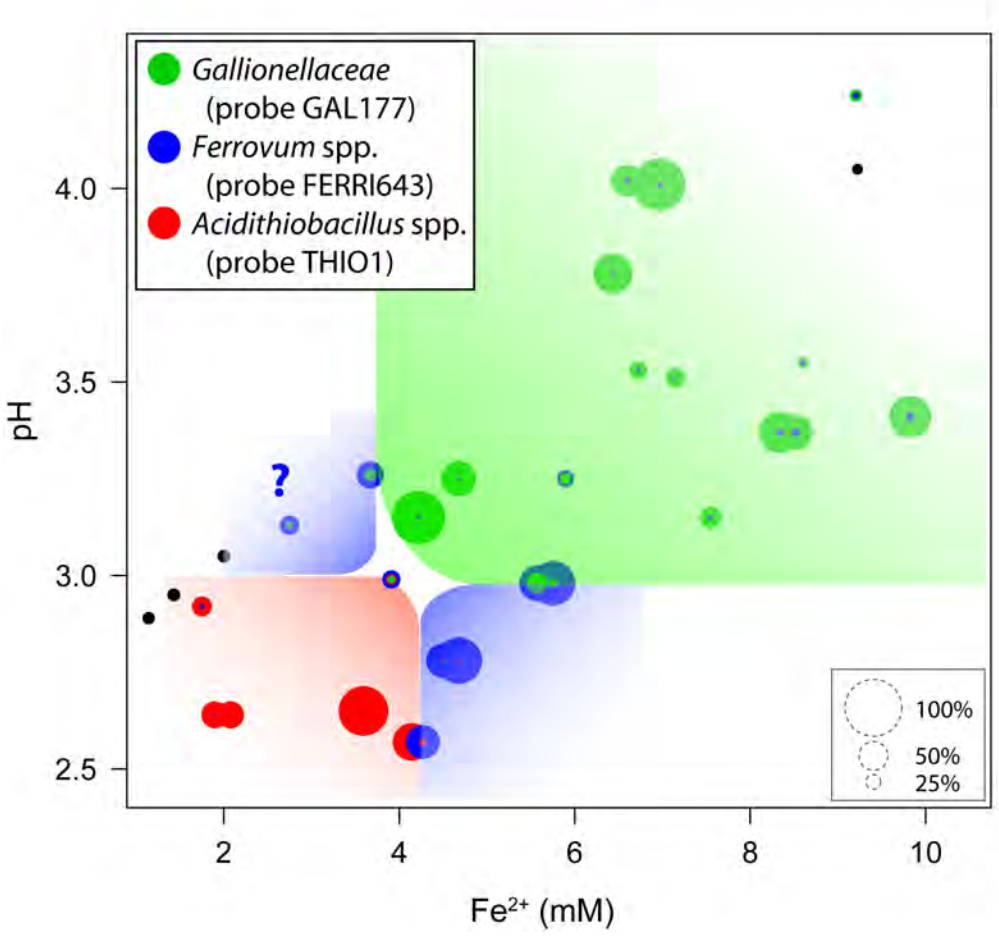

FIG. 6 Distribution of *"Ferrovum"*, *Acidithiobacillus*, and *Gallionella*-like organisms with respect to Fe^{2+} and pH. Points are scaled to the relative abundance of those organisms (as a percentage of total DAPI-stained cells). Black points indicate samples with <10% GAL177, FERRI643 and THIO1 hybridizing cells combined. Shaded regions indicate proposed niches for the respective organisms in the Red Eyes drainage.